INVESTIGATING THE STRUCTURE, STAR FORMATION AND STELLAR MASS OF THE $z = 0.9$ SUPERCLUSTER RCS 2319+00

Ashley J. Faloon

Doctor of Philosophy

Department of Physics

McGill University
Montréal, Québec
2013

A thesis submitted to McGill University in partial fulfillment of the requirements of the degree Doctor of Philosophy

Acknowledgements

First and foremost I wish to thank my supervisor Tracy Webb, whose contributions and encouragement have aided both my research and my overall graduate experience. I would also like to acknowledge my many collaborators through the RCS collaborations, whose generous sharing of data and advice were invaluable to the results presented in this thesis. My fellow graduate student group members deserve many thanks not only for their contributions to this work, but also for their valued friendship. Special thanks are due to Sebastien Guillot for graciously aiding in the translation of the abstract.

As any product is only the sum of its parts, so too is this PhD thesis the culmination of many years of learning in all levels of my education. I thank all of those teachers and professors who throughout these many years have nurtured and encouraged my love for learning; in physics and astronomy and beyond. Their dedication and passion for the art of teaching is commendable, inspirational and all too often overlooked.

To my friends, I offer many heartfelt thanks for their support and motivation. Especially for their ability to offer perspective when things get tough and to make me laugh when I need it most.

Finally, I would like to thank my family. Words cannot express how grateful I am for their ongoing encouragement throughout this crazy adventure we call grad school. Their endless love and support in all facets of my life have helped me to stay grounded and enjoy the journey. I owe them more than I can ever repay.

Abstract

The RCS 2319+00 supercluster is a massive supercluster at $z = 0.9$ comprising three optically selected, spectroscopically confirmed clusters separated by < 3 Mpc on the plane of the sky. This supercluster is one of a few known examples of the progenitors of present-day massive clusters ($10^{15}\,M_\odot$ by $z \sim 0.5$). RCS 2319+00 therefore allows us to witness the hierarchical buildup of large-scale structure in the Universe.

We present an extensive multiwavelength study carried out on the supercluster field. A spectroscopic campaign resulted in 302 structure members spanning three distinct redshift walls separated by ~ 65 Mpc ($\Delta\, z = 0.03$). We find evidence of substructure in the supercluster field, with a friends-of-friends (FOF) analysis identifying five infalling groups in addition to the three cluster cores. Various methods are presented to estimate the cluster and group masses, finding cluster masses of $\sim 10^{14.5}$–$10^{14.9}\,M_\odot$ and average masses of $\gtrsim 10^{13}\,M_\odot$ for the infalling groups. These group masses are in agreement with the halo sizes found to be important in cluster galaxy pre-processing in N-body simulation merger tree studies based on hierarchical formation models.

In conjunction with multiwavelength data, we use the spectroscopic members and their FOF associations as isolated, group or core galaxies to investigate the role of both the local and global environment on cluster galaxies' stellar mass and star formation. The $z = 0.9$ RCS 2319+00 supercluster is found to follow the local SFR-density relation, with the star formation primarily located in the lower density, infalling isolated and group regions. We see suggestions of both enhanced star formation activity and star formation quenching over the supercluster field. The densest regions of the groups and isolated outskirt galaxies show hints of enhanced star formation activity. There is evidence of a bimodal distribution in the SFRs with stellar mass: the known main sequence of increasing SFR with increasing stellar mass, and a sub-main sequence population of partially quenched star forming galaxies. The sub-main sequence itself seems to be divided between environment-quenching and mass-quenching effects.

We propose that the infalling groups in RCS 2319+00 are in varying stages of pre-processing, with their star formation activity level falling between that of the isolated supercluster galaxies and the less-active, more massive cluster cores. Overall, our results align with the theoretical models that predict galaxy pre-processing in group environments before final accretion onto cluster sized halos.

Abrégé

Le super-amas RCS 2319+00 est un super-amas massif à $z = 0,9$ comprenant trois amas sélectionnés optiquement et confirmés par spectroscopie. Ces amas sont séparés par < 3 Mpc dans le plan du ciel. Ce super-amas est l'un des rares exemples connus d'ancêtres d'amas massifs d'aujourd'hui ($10^{15}\,M_\odot$ par $z \sim 0.5$). RCS 2319+00 nous permet donc d'être témoin de l' accumulation hiérarchique de la structure à grande échelle dans l'Univers.

Nous présentons une vaste étude multi-longueurs d'ondes dans le champ du super-amas. Une campagne spectroscopique a donné lieu à 302 membres de la structure étalés sur trois sections de décalage vers le rouge (redshift z) distinctes séparés par ∼65 Mpc ($\Delta\, z = 0,03$). Nous trouvons des preuves de structure dans le champ du super-amas, avec une analyse dite "friends-of-friends" (FOF), identifiant cinq groupes retombants vers le coeur en plus des trois noyaux d'amas. Diverses méthodes sont présentées pour estimer les masses des amas et groupes. Nous trouvons des amas de masse $\sim 10^{14,5}$–$10^{14,9}\,M_\odot$ et de masses moyennes de $\gtrsim 10^{13}\,M_\odot$ pour les groupes retombants vers le centre. Les masses de ces groupes sont en accord avec la taille du halo jugée importante pour la prétraitement des galaxies d'amas dans les études de simulations n-corps basé sur des modèles de formation hiérarchique.

En conjonction avec les données multi-longueurs d'ondes, nous utilisons les membres spectroscopiques et leurs associations FOF comme des groupes ou noyaux de galaxies isolé pour étudier le rôle de l'environnement local et global sur la masse stellaire des galaxies de l'amas et leur taux de formation stellaire (SFR). Le super-amas RCS 2319+00 à $z = 0,9$ suit la relation locale SFR-densité, avec la formation d'étoiles principalement située dans les régions de plus faible densité, celle des galaxies isolées ou en groupe retombant vers le centre. Nous voyons des indications d'activité augmentée de formation stellaire et d'extinction de formation stellaire tous les deux dans le champ du super-amas. Les régions les plus denses des groupes et des galaxies isolées en périphérie de l'amas révèlent des notes d'augmentation de l'activité de formation stellaire. Il existe des preuves d'une distribution bimodale dans la relation de formation stellaire avec la masse stellaire: la séquence principale d'augmentation de la formation stellaire quand la masse stellaire augmente, et une population de séquence sous-principale des galaxies qui ont leur formation stellaire partiellement étouffée. La séquence sous-principale elle-même semble étre divisée entre les effets d'extinction de l'environnement et de masse.

Nous proposons que les groupes retombant vers le centre dans RCS 2319+00 sont à divers stades de pré-traitement, avec leur niveau de formation stellaire se situant entre celui des galaxies isolées et celui des noyau plus massives mais moins actifs des amas. Dans l'ensemble, nos résultats sont en accord avec les modèles théoriques qui prédisent le pré-traitement des galaxies dans les environnements de groupe avant l'accrétion finale sur les halos de taille des amas.

Statement of Originality

The research and results contained herein are the original work of the author, with contributions of advice and data from collaborators as outlined. The thesis has resulted in one peer-reviewed journal publication with two more pending. As a whole, the work in this thesis constitutes the largest study done to date on the RCS 2319+00 supercluster at $z = 0.9$.

Contributions of Co-authors

The following thesis is comprised of work presented in three papers.

Chapters 2 and 3 are based on:

> A.J. Faloon, T.M.A. Webb, E. Ellingson, R. Yan, D.G. Gilbank, J.E. Geach, A.G. Noble, L.F. Barrientos, H.K.C. Yee, M. Gladders and J. Richard, *The structure of the merging RCS 231953+00 supercluster at* $z \sim 0.9$, 2013, ApJ, 768, 104

Chapter 4 is based on:

> A.J. Faloon, T.M.A. Webb, D. O'Donnell, A.G. Noble, A. Delahaye, J.E. Geach, E. Ellingson, R. Yan, D.G. Gilbank, L.F. Barrientos, H.K.C. Yee, and M. Gladders, *Witnessing the assembly of a massive galaxy cluster: the distribution of stars and star formation in the merging supercluster RCS2319+00 at* $z \sim 0.9$, to be submitted to ApJ

Chapter 5 is based on:

> A.J. Faloon, T.M.A. Webb, D. O'Donnell, A.G. Noble, A. Delahaye, J.E. Geach, E. Ellingson, R. Yan, D.G. Gilbank, L.F. Barrientos, H.K.C. Yee, and M. Gladders, *The current and future mass content of the* $z \sim 0.9$ *RCS 2319+00 supercluster: Exploring the fate of the merged cluster*, to be submitted to ApJ

All writing and analysis done in the three papers, and thus this thesis, was completed by myself with helpful advice along the way from collaborators. I am indebted to my co-authors whose contributions of data sets, research guidance, and constructive feedback aided in all aspects of this work.

I was responsible for any of the data reduction not specifically listed below. The nature of observational astronomy at high redshift requires large amounts of data from a limited number of powerful telescopes and I am therefore very thankful to my collaborators for allowing me the use of their source catalogues for my research. The following lists the specific contributions of each of the co-authors:

- T.M.A. Webb provided indispensable guidance in all stages of the research and writing process as well as supplying the raw VIMOS spectroscopic data and the final MIPS and IRAC catalogues.
- E. Ellingson is the co-creator, along with myself, of the IDL-based interactive redshift program written for use with an associated spectroscopic survey, which was expanded and adapted for use in this work for the VIMOS, FMOS and GMOS-North spectroscopy. She was also a great help in figuring out the spectroscopic completeness of my catalogue and lead the University of Colorado, Boulder redshift finding team who found the redshifts for two of the IMACS masks and double-checked my redshift finding on the three other IMACS masks.

- R. Yan generously provided the reduced IMACS data, along with the `zspec` redshift finding program and endless help on its use.
- D.G. Gilbank provided the re-calibrated optical source catalogues from the RCS-1 survey, the red-sequence galaxy density maps and the raw GMOS-N spectroscopy data. He also provided helpful feedback and suggestions during the writing process.
- J.E. Geach helped with the FMOS proposal and observation set-up and contributed to the K_s imaging reduction, as well as providing suggestions throughout the analysis process.
- A.G. Noble was invaluable in aiding with the FMOS observations and provided the radio catalogue. She also contributed valuable discussion throughout the project.
- D. O'Donnell was responsible for the initial MIPS and IRAC imaging reductions.
- A. Delahaye is responsible for the reduction and catalogueing of the K_s imaging data, with the aide of J.E. Geach.
- L.F. Barrientos contributed the majority of the FORS2 redshifts as well as feedback during the writing process.
- H.K.C. Yee was very helpful in all aspects of the paper, providing great comments and suggestions throughout the research and writing process.
- M. Gladders is responsible, along with H.K.C. Yee, for the inception of the RCS-1 survey and therefore the discovery of the RCS 2319+00 supercluster on which this thesis is based.
- J. Richard provided FORS2 cluster member redshifts from a background survey.

Contents

List of Figures

List of Tables

Chapter 1

Introduction

1.1 Overview

The Universe is inhabited by massive sheets and filaments of galaxies that connect groups, clusters and superclusters of galaxies together in a vast cosmic web. To investigate the hierarchical formation and galaxy evolution that results in the universe around us, we can probe into the past to study the ancestors of present day structures. The high-redshift universe offers snapshots of the Universe as it was billions of years ago, when the massive clusters we observe in our cosmic neighbourhood were in their infancy. Distant superclusters, in particular, allow us to witness the predecessors of massive galaxy clusters at an important epoch in their evolution; when a collection of infalling galaxies, small groups and individual cluster cores are on a collision course to merge into the massive structures we observe today, such as the $\sim 10^{15}\,M_\odot$ Virgo and Coma clusters in our local universe.

In this thesis we motivate the study of a massive, redshift ~ 1 supercluster of galaxies, the RCS 2319+00 supercluster. The focus of the research is first to identify member galaxies of the supercluster and attempt to map out its structure. By identifying different global environments within the supercluster we can then look at the physical properties, such as mass and radius, of the different clusters and groups that make up the structure. With multiwavelength data, one can study different properties of galaxies within the supercluster, such as stellar mass, halo mass and star formation rate. These can then be investigated both as a function of the local galaxy density and the global environments (i.e., isolated, group or cluster core environments) in an aim to answer questions about the evolution of galaxies and whether their environment plays a role in their development. Studies of galaxy properties such as mass (e.g., Vulcani et al., 2012, 2013) and star-formation distribution (e.g., Finn et al., 2010; Feruglio et al., 2010; Muzzin et al., 2012) in different global environments generally compare field, group and cluster samples from different regions on the sky or by using cuts in local density (e.g., Patel et al., 2009; Koyama et al., 2010) that can suffer from cross-contamination between populations. By using a single large structure with well defined global populations we can test galaxy properties in a consistent way and compare results from different global environments at the same local densities. The RCS 2319+00 supercluster is a merging structure fated to become a massive galaxy cluster, which allows us to witness an intermediate stage in the formation of large structure and compare our results to current hierarchical formation models.

The following thesis provides a comprehensive study of the RCS 2319+00 supercluster at $z \sim 1$ and is laid out as follows: In Chapter 1 we provide a brief overview of the general theories and properties of galaxies and their evolution to lay the foundation for a study of the supercluster. More detailed information on the different theories or observational properties of galaxies are given throughout the thesis as needed for the analysis. Chapter 2 provides a spectroscopic study of the supercluster to compile a catalogue of members that are used in Chapter 3 to map out the substructure of RCS 2319+00 and estimate the cluster and group properties. In Chapter 4 we look at the distribution of stellar mass and star formation in the supercluster field in order to discuss the role, if any, that the environment plays on galaxies at this epoch. We attempt in Chapter 5 to investigate the fate of the final merged, $\sim 10^{15}\,M_{\odot}$ cluster predicted to occur by $z \sim 0.5$, comparing the current distribution of stellar and halo mass to those at $z \sim 0.5$ to once again investigate the possible role of the environment on galaxy evolution. In Chapter 6 we provide a brief summary of the thesis findings as well as discuss plans for future work on this object and others.

Throughout this thesis we assume cosmological parameters of $\Omega_\Lambda = 0.73$, $\Omega_m = 0.27$, and $H_o = 71$ km s^{-1} (Larson et al., 2011).

1.2 Hierarchical Structure Formation in the Universe

The formation of large structure in the Universe is accomplished through a bottom-up, hierarchical assembly. Galaxies accrete along high-density filaments and sheets to form groups and dense clusters. In a universe dominated by cold dark matter (CDM) small galaxies form first, followed by groups, clusters and superclusters, all linked in a 'cosmic web' of sheets and filaments (e.g., Bond et al., 1996; Springel et al., 2006). This CDM hierarchical structure formation theory and its accompanying simulations (e.g., Davis et al., 1985; Cen et al., 1994; Navarro et al., 1995, 1996) have been shown to be remarkably consistent with observations of the distributions of galaxies in the Universe with the Sloan Digital Sky Survey (SDSS; York et al., 2000) and the 2 degree Field Galaxy Redshift Survey (2dFGRS Colless et al., 2001).

According to the CDM hierarchical structure formation theory, small density fluctuations, seen as temperature fluctuations in observations of the Cosmic Microwave Background (CMB; e.g., Smoot et al., 1992; Spergel et al., 2003), are amplified through gravitational interactions and, once they are dense enough, collapse to form dark matter halos (e.g., Navarro et al., 1995; Ryden, 2003). If the potential wells of these dark matter halos are deep enough, gas can cool and condense at the bottom of dark matter potential wells to form galaxies and stars (e.g., White & Rees, 1978; Navarro et al., 1995; Kauffmann et al., 1999). Haloes assemble together along overdense filaments and sheets, merging into first groups and then clusters of galaxies (e.g., Bond et al., 1996; Springel et al., 2006; Jones et al., 2008). These galaxy clusters are themselves gravitationally bound in supercluster structures, the largest density enhancements in this cosmic web (e.g., Bond et al., 1996; Bahcall & Soneira, 1983; Wray et al., 2006). Theoretical modelling and observations suggest that superclusters are only just collapsing at present while individual galaxies are seen out to redshifts of $z \sim 6$ (e.g., Ryden, 2003; Wray et al., 2006; Jones et al., 2008), which again supports a CDM model of cosmological formation.

1.3 Superclusters

The largest known gravitationally bound structures in the Universe, clusters of clusters – or superclusters – comprise a mix of dynamical systems ranging from the densest cluster cores, through more relaxed group and filamentary structures and out to the isolated infalling galaxies on the outskirts of the systems. Superclusters represent the largest density enhancements in angular separation in the cosmic web and can reach scales of ∼100–200 h^{-1} Mpc. Clusters found to lie close together with their major axes aligned have the densest filamentary cluster–cluster bridges (e.g., Bond et al., 1996; Bahcall & Soneira, 1983; Wray et al., 2006).

As superclusters represent the largest component of the large-scale structure in the universe, they can be used to test cosmological models (e.g., Bahcall, 1988; Kolokotronis et al., 2002; Einasto et al., 2011b). They also offer a range of spatial and dynamical sub-environments from infalling galaxies, groups, and filaments to the high-density cluster cores and are therefore ideal laboratories in which to study the effects of the environment on galaxy evolution. In the nearby universe, superclusters have long been accessible for study (e.g., Gregory & Thompson, 1978; Gregory et al., 1981; Oort, 1983) and catalogues of superclusters in the low-redshift universe have been compiled through the large spectroscopic campaigns done by the SDSS (e.g., Einasto et al., 2003; Liivamägi et al., 2012) and the 2dFGRS (e.g., Einasto et al., 2007a).

The study of superclusters in the high-redshift universe, however, remains elusive.

In N-body simulations of hierarchical structure formation, the density of superclusters in the universe decreases with redshift, with few rich, compact superclusters found at high redshift (e.g., Wray et al., 2006). Though the number of superclusters found by Wray et al. (2006) decreased from $z \sim 0$ to $z \sim 1$ by only a factor of a few, their mean cluster separation increases, making them difficult to find observationally since typical high–redshift survey sizes are not large enough to recognize these immense structures and superclusters on smaller scales become more rare.

To date, only a handful of spectroscopically confirmed superclusters at high redshift have been published in the litterature. The CL0016 supercluster at $z = 0.55$ extends over 20 Mpc and includes three clusters along with companion groups and filamentary structures (Tanaka et al., 2009). At $z \sim 1$, three superclusters of varying scales have been reported. Lubin et al. (2000) identified a supercluster containing ten spectroscopically confirmed cluster and group candidates within a radial length of $\sim 100\ h_{70}^{-1}$ Mpc and transverse length of $\sim 13\ h_{70}^{-1}$ Mpc at $z = 0.9$ (Gal & Lubin, 2004; Gal et al., 2008). The Swinbank et al. (2007) supercluster at $z = 0.89$, found in the UK Deep Infrared Sky Survey (UKIDSS) Deep eXtragalactic Survey (DXS), contains five clusters ($\sim 10^{13.5-14.0}\,M_{\odot}$) spread over 30 Mpc on the sky. The RCS 231953+00 supercluster, the object of interest in this thesis, was first spectroscopically confirmed by Gilbank et al. (2008a) and contains three massive clusters at $z = 0.9$ with X-ray masses of $M_{X,\mathrm{tot}} \sim 4.7$–$6.4 \times 10^{14}\ M_{\odot}$ (Hicks et al., 2008) over an angular scale of only $\sim 6 \times 4$ Mpc. The highest redshift supercluster confirmed to date is the Lynx Supercluster of two X-ray emitting clusters at $z = 1.26$ and $z = 1.27$, first discovered by Rosati et al. (1999), with seven additional candidate groups and clusters identified through photometric redshifts (Nakata et al., 2005).

Superclusters allow for study of the effects of both the global and local environment on member galaxies. With identified cluster core, filament, group and outlying isolated member populations in superclusters, we can attempt to probe the environment in different ways to bridge the gap between studies of individual groups and clusters. This is done by looking at different galaxy properties and how they correlate with the local galaxy density while having the ability to separate out individual global density populations within the same density bins, i.e. cluster core members at larger radii versus members at the densest regions of the infalling groups.

Theoretical studies using semi-analytic techniques to retrieve galaxy merger tree information from N-body simulations give predictions for the accretion pathways of galaxies onto clusters in the current hierarchical formation model. Though the fractions of different sized group halos accreted throughout the lifetime of clusters differs for different final cluster masses, the fraction of galaxies accreted through groups versus the field are dependent on the epoch of observation rather than the final cluster mass (e.g. McGee et al., 2009).

1.4 The Red-sequence Cluster Survey

The RCS 2319+00 supercluster was found by the first Red-Sequence Cluster Survey (RCS-1; Gladders & Yee, 2005). The $\sim$ 90 square degree RCS-1 is an optical galaxy cluster survey that found $\sim$1000 clusters within a $0.3 \lesssim z \lesssim 1.1$ redshift range. The survey is based on the RCS cluster finding method, developed by Gladders & Yee (2000), which uses the well known fact that rich clusters contain red, early-type elliptical galaxies (e.g., Dressler, 1980). These early-type galaxies follow a distinct colour-magnitude relation known as the red-sequence that has been shown to have a tight, well-defined slope at low redshift (e.g., Visvanathan & Sandage, 1977; Bower et al., 1992; Lopez-Cruz et al., 2004).

Gladders & Yee (2000) found that two-filter optical imaging is all that is required to detect red cluster galaxies and their subsequent red-sequence. The 4000Å break

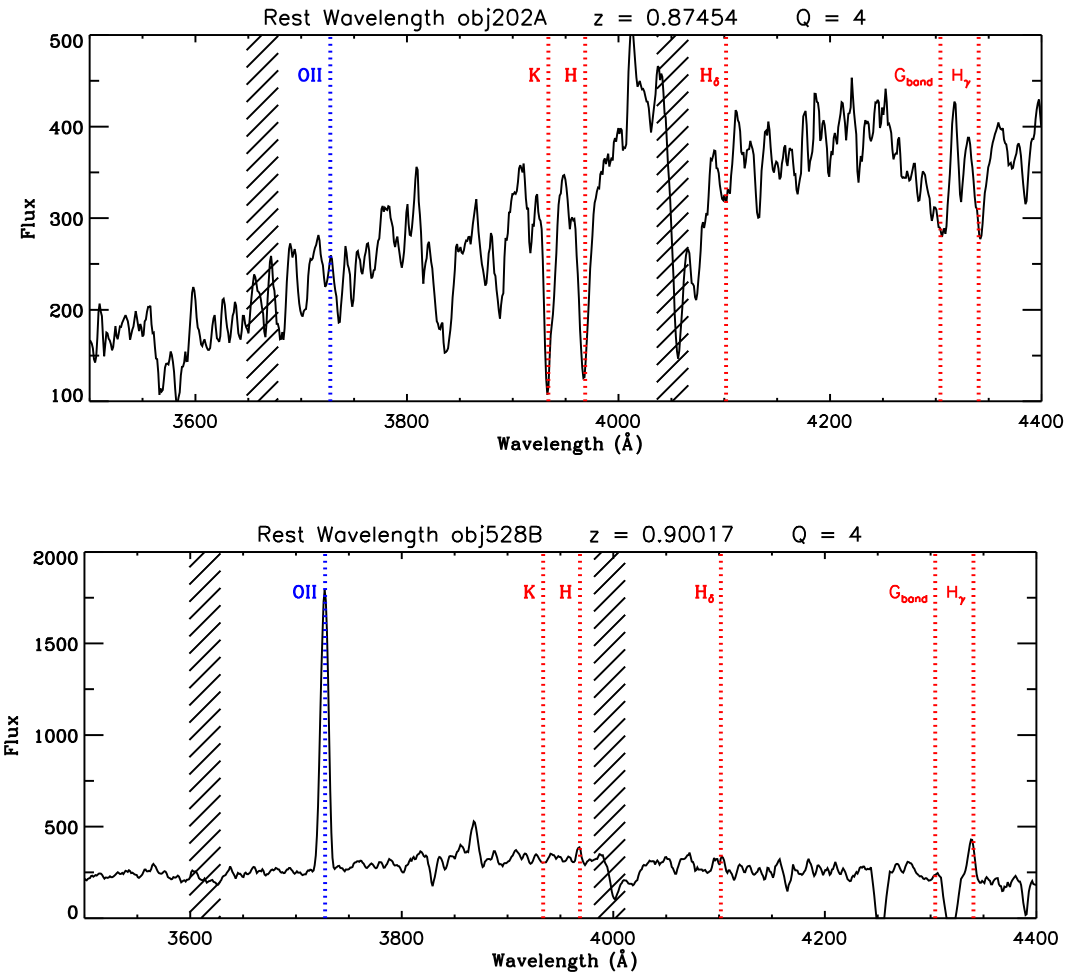

Figure 1.1 Example of early-type (top) and late-type (bottom) galaxy spectra of RCS 2319+00 supercluster members (See Chapter 3) over the rest wavelength range of 3500Å–4400Åwith flux given in arbitrary units. The difference in the 4000Å break is evident between the two populations. Blue dotted lines show the location of the [OII]λ3727 emission line while the red dotted lines show the location of the most common stellar absorption lines in early-type galaxies. These lines are seen as emission lines in late-type galaxies with strong star-formation. The black hatched areas are the locations of the atmospheric A and B-band absorption lines.

of the galaxy spectra, which is due to ionized metals, acts as an indicator of the age of galaxies. Old, metal rich, early-type galaxies show a stronger 4000Å break than young, late-type galaxies containing hot stars (Kauffmann et al., 2003b). Figure 1.1 shows examples of the rest wavelength spectra from an early-type and a late-type galaxy in the RCS 2319+00 supercluster, showing the 4000Å break evident in the early-type galaxy and lacking in the late-type galaxy.

The RCS-1 used the R_c (central wavelength ∼6500Å) and z' (central wavelength ∼9100Å) filters on the CFHT12K instrument (Cuillandre et al., 2000) as these filters span the rest-frame 4000Å break for early-type galaxies in clusters in a redshift range of $0.3 < z < 1.1$. At $z \sim 0.9$, the redshift of the RCS 2319+00 supercluster, the observed R_c and z' central wavelengths correspond to rest wavelengths of ∼3420Å and ∼4790Å. Figure 1.2 shows the simulated colour-magnitude diagrams for different galaxy types over a range of redshifts using the V and I_c optical filters, both at slightly lower wavelengths then their R_c and z' counterparts. These were used by Gladders & Yee (2000) as a proof of concept for the RCS cluster finding method and show that the red-sequence line can also be used to estimate the redshift of the galaxy clusters.

The observation strategy and reduction of the R_c and z' band data is described in Gladders & Yee (2005), with the object finding done using the Picture Processing Package (PPP; Yee, 1991). Dividing the colour-magnitude plane into slices congruent with smaller redshift ranges based on the know red-sequence slopes allowed for the detection of cluster cores through the presence of overdensities of red-sequence galaxies. Clusters are found as simultaneous overdensities in colour, magnitude and projected angular position (Gladders & Yee, 2000, 2005).

1.5 The RCS 2319+00 Supercluster

RCS 231953+0038.1 (hereafter referred to as Cluster A) at $z \sim 0.9$ was identified in the RCS-1 survey (Gladders & Yee, 2005) and shown to be a remarkable strong-lensing cluster by Gladders et al. (2003). Subsequent investigation of the RCS-1 catalogue identified two potential companion clusters (RCS 232003+0033.5: Cluster B and RCS 231946+0030.6: Cluster C) whose red-sequence peaks fall at a similar

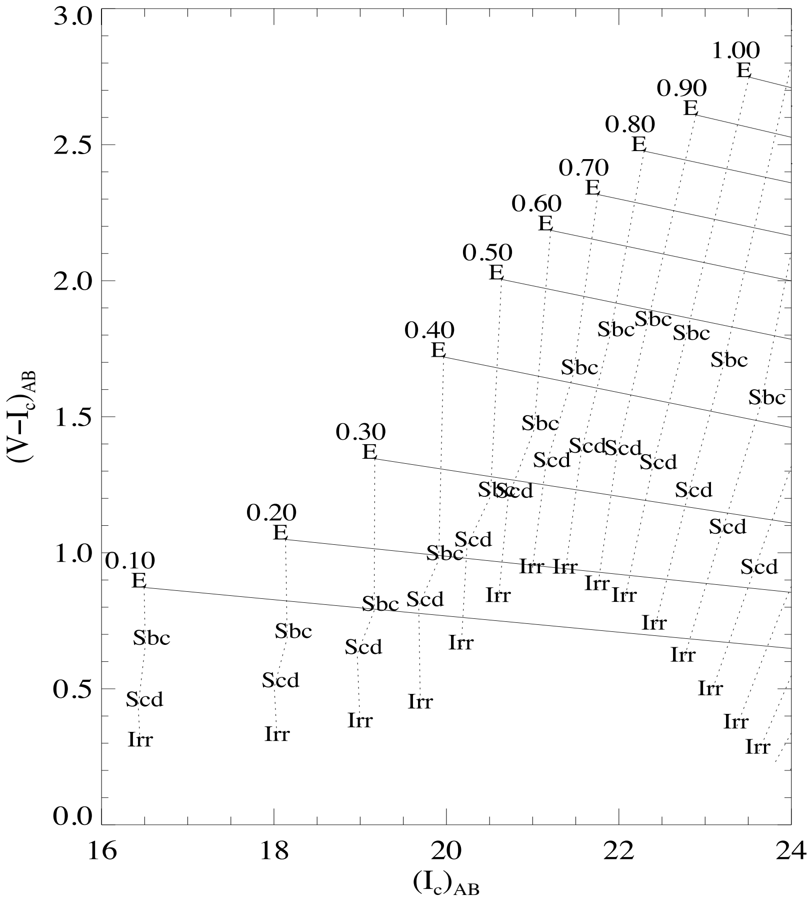

Figure 1.2 Colour–magnitude diagram showing the simulated slopes of the red-sequence relation (solid lines) for galaxies at different redshifts done by Gladders & Yee (2000) using the V and I_c optical filters. The different galaxy types, from elliptical through to irregular, are linked to their red-sequence slopes by the dotted lines.

photometric redshift to Cluster A. The density profiles of the red-sequence galaxies indicate that the three clusters are separated by $< 3\,\mathrm{Mpc}$ in the plane of the sky with each cluster core seemingly aligned toward its closest neighbour, further substantiating the claim that these clusters are bound to each other in a supercluster (as found by Binggeli (1982b) in a study of Abell clusters).

Chandra X-ray imaging confirmed the presence of three X-ray luminous cluster cores with $L_X \sim 3.6$–7.6×10^{44} erg s^{-1} and $M_{X,\mathrm{tot}} \sim 4.7$–$6.4 \times 10^{14}\ M_\odot$ (Hicks et al., 2008). Figure 1.3 shows the smoothed X-ray flux image from Hicks et al. (2008) that

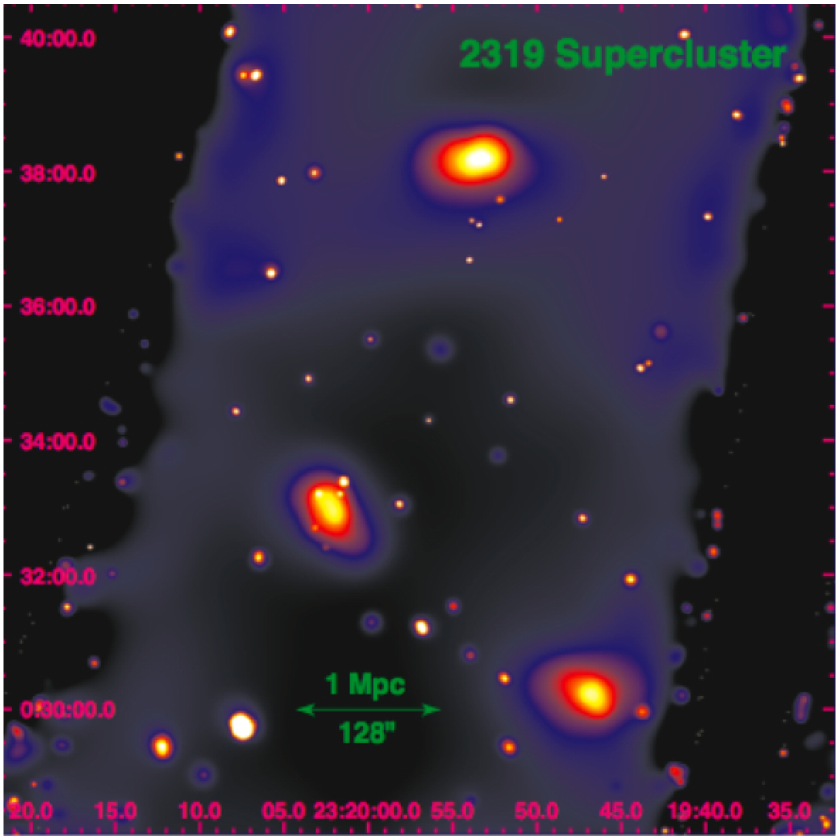

Figure 1.3 Smoothed X-ray flux image of the RCS2319+00 supercluster from Hicks et al. (2008) in the 0.3–7.0 keV band.

clearly indicates the presence of the three cluster cores. Cluster A is the northernmost cluster, Cluster B is offset to the east (recalling that astromonical positions show east at the left of the image) and Cluster C is found at the southwest corner of the image. Spectroscopic confirmation that the three clusters all lie at $z \sim 0.9$ was first shown in Gilbank et al. (2008a).

Using the methods of Sarazin (2002) to estimate the merger rate, Gilbank et al. (2008a) postulate that the three clusters will merge to form a Coma-sized cluster ($\sim 10^{15}\,M_{\odot}$) by $z \sim 0.5$, on order with the largest known clusters in the Universe. As the two other confirmed $z \sim 0.9$ superclusters of Swinbank et al. (2007) and Lubin et al. (2000) have lower mass cluster components that are spread over larger scales, they are therefore less likely to merge into as massive a cluster as RCS 2319+00 with longer merger rates (Gilbank et al., 2008a). Thus RCS 2319+00 is a rare example of a massive cluster caught in the process of forming through the merging of multiple cluster and group components and it is an ideal laboratory in which to study the role of the environment and hierarchical processes on galaxy evolution.

Extensive follow-up, including the results contained herein, is underway on the RCS 2319+00 supercluster to study the effect of this unique environment on its member galaxies. Cluster A has already been studied in several surveys: strong (Gladders et al., 2003) and weak-lensing (Jee et al., 2011) in massive galaxy clusters, the Sunyaev–Zel'dovich (SZ) effect of strong lensing clusters (Gralla et al., 2011), the submillimeter source counts of high-redshift clusters (Noble et al., 2012) and the stellar mass of brightest cluster galaxies in $z = 1$ clusters (Lidman et al., 2013). The X-ray properties of the three component clusters of the RCS 2319+00 supercluster have been investigated by Hicks et al. (2008). Using data from the *Herschel* Lensing Survey (HLS; Egami et al., 2010), Coppin et al. (2012) discovered an infrared-bright filament of galaxies in the *Herschel* 250-500 μm Spectral and Photometric Imaging REceiver (SPIRE) imaging. This filament projects 2.5 Mpc between component Clusters A and B with an estimated total star formation rate (SFR) $\simeq 900\,M_{\odot}\,\mathrm{yr}^{-1}$.

1.6 Galaxy Properties as a Function of Environment

Galaxy properties such as colour, morphology, stellar mass and star formation rate (SFR), have been shown to be correlated with the environment in which they reside as well as with redshift. In the local universe red, early-type galaxies dominate the dense cluster cores while blue, late-type galaxies prefer to reside in the lower density fields (e.g., Dressler, 1980). The highest stellar mass galaxies are found in the densest regions (Kauffmann et al., 2004).

An analytical model of hierarchical growth by Mo & White (1996) shows the distribution of dark matter halos having a higher fraction of massive dark matter halos in dense regions than in less dense environments, concurrent with the observations of stellar mass. Observational data from the VLT VIMOS Deep Survey of galaxies in the $0.2 < z < 1.4$ redshift range shows that, for high stellar masses, the magnitude of this mass segregation, with the highest mass galaxies in higher density regions, does not change significantly as a function of redshift (Scodeggio et al., 2009).

In galaxies in the local universe the specific SFR, or SFR per net total stellar mass ($\mathrm{SSFR} = \mathrm{SFR}/M_*$), has been found to decrease when going from lower to higher local densities, with the mid-mass galaxies showing a more prominent decrease at $\sim 10\times$ compared to the highest mass galaxies (Kauffmann et al., 2004). This implies that the efficiency of star formation activity is decreasing with local density.

As redshift increases, so to does the fraction of blue, star forming, spiral galaxies in clusters (Butcher & Oemler, 1978, 1984; Dressler et al., 1997; Ellingson et al., 2001). The cosmic star formation rate density has also been found to increase rapidly between the local universe and $z \sim 1-2$ (e.g., Madau et al., 1996; Lilly et al., 1996; Le Floc'h et al., 2005; Drake et al., 2013). The increasing data available on high-redshift clusters in recent years has facilitated the study of the evolution of star forming galaxies. The question of whether the increase in the star forming galaxy population in clusters is due to a reversal in the local SFR-density relation by $z \sim 1$ or to galaxies at this epoch (half the age of the local universe) being less evolved and more star forming overall, as seen with the increase in the cosmic SFR-density, has shown conflicting results.

Some recent studies have found no correlation between increased SSFRs and the environment at high redshift (e.g., Finn et al., 2010; Feruglio et al., 2010). Another set of studies finds that the local SFR-density relation, with the predominate sites for star forming galaxies being in the lower density fields, has reversed by $z \sim 1$ with star forming galaxies populating denser environments (e.g., Cooper et al., 2008; Elbaz et al., 2007; Tran et al., 2010; Bai et al., 2007; Marcillac et al., 2007). Contrasting results, with the primary location for star formation continuing to avoid the densest cluster cores, have also been found in many studies (e.g., Patel et al., 2009, 2011; Koyama et al., 2010; Muzzin et al., 2012; Webb et al., 2013; Noble et al., 2013). A series of papers on intermediate redshift clusters in the CNOC 1 survey found no excess of star formation in clusters over the field (Balogh et al., 1997, 1998, 1999). These studies observed that the cluster environment did not induce starbursts and was in fact responsible for suppressing the star formation of infalling galaxies, with galaxies evolving passively once they are accreted onto the cluster as their gas is exhausted.

Mechanisms that have been proposed in the truncation of star formation include strangulation (e.g., Larson et al., 1980) and ram-pressure stripping (e.g., Gunn & Gott, 1972). Tidal interactions (i.e. harrasment) and mergers are potential mechanisms through which enhanced starburst activity is triggered resulting in a short duration ($\lesssim 10^8$) of strong star formation that consumes the available gas, consequently shutting off further star formation activity (Barnes & Hernquist, 1991; Larson & Tinsley, 1978; Moore et al., 1998a). Studies of superclusters at intermediate redshift ($z = 0.55$; Geach et al., 2011) and high redshift ($z \sim 0.9$; Kocevski et al., 2011) have suggested that mergers and harassment are responsible for inducing the enhanced star formation seen in their infalling groups.

One issue that may be contributing to the conflicting results is the parameters used to define an enhancement or lack of star formation as well as the local density parameter used. One can look at the average SFR with respect to the local density (e.g., Cooper et al., 2008; Elbaz et al., 2007) or the SSFR versus local density (e.g., Cooper et al., 2008; Patel et al., 2009, 2011; Noble et al., 2013), both of which offer indications of the star formation activity but through slightly different means. The former looks only at total current output of star formation, while the latter takes into account the current stellar mass of the galaxy, offering insight into the relative SFR in different stellar mass bins. The fraction of star forming galaxies has also been used to study the SFR-density relation either as a function of the global environment (i.e. clusters versus the field; e.g., Bai et al., 2007; Marcillac et al., 2007; Webb et al., 2013) or the local environment (i.e. as a function of local density; e.g., Tran et al., 2010). The local density itself has been defined in different studies through many different means including, among others: using cluster centric radius, background-subtracted nearest neighbour counts, and volume density estimates through galaxy number counts in a given column space.

In the following thesis we aim to study the SFR-density relation of both the global and local environment through a combination of these methods to better determine the nature of the SFR-density relation at $z \sim 1$ and whether or not it is consistent with the local universe.

1.7 The Importance of Multiwavelength Data Sets

In order to define different parameters of galaxies including their colour, redshift, stellar mass, and SFR, we require multiwavelength imaging. The spectral energy distribution (SED) of galaxies defines the emission of stellar light from galaxies over the different wavelengths of the electromagnetic spectrum. In some areas the stellar light is detected directly (e.g., in the optical and ultraviolet), while at others the light seen has been remitted from the dust and gas of the interstellar medium (ISM) of the galaxies (e.g., in the mid-infrared) (Walcher et al., 2010). The different regions of the galaxy SED therefore contain information about the stellar and dust mass of the galaxy and the star formation present, either from direct light from specific emission lines or hidden behind a cloud of dust.

The following subsections give a brief outline of the multiwavelength data used in this thesis and the galaxy parameters which can be garnered from each. Figures 1.4 and 1.5 show cut outs of the 15×15 arcmin regions around the RCS 2319+00 supercluster for each of the wavelengths used in this work. They serve to illustrate the different emission present in the different observing bands, with sources dropping in and out of the images based on their properties. The specifics of the observations' instruments and reductions are described in more detail in Chapters 2 and 4.

1.7.1 X-ray

Clusters of galaxies contain not only hundreds of galaxies, full of stars, gas and dust, but also dark matter and hot gas. The hot intracluster gas, invisible at optical wavelengths, can be seen in the X-ray. Rich clusters typically have X-ray luminosities of $10^{43-45}\,\mathrm{ergs\,s^{-1}}$ and their X-ray emission, due to thermal bremsstrahlung radiation from the intracluster gas, is extended around the cluster core (Sarazin, 1988; Bahcall, 1999). Indeed this extended X-ray emission has allowed for the search of galaxy clusters in X-ray data, with surveys including the ROSAT-ESO Flux Limited X-ray galaxy cluster survey (REFLEX; Böhringer et al., 2004), the Local Cluster Substructure Survey (LoCuSS; Smith et al., 2010), the 2XMMi/SDSS Galaxy Cluster Survey (Takey et al., 2011), and the XMM Cluster Survey (XCS; Mehrtens et al., 2012). The extended X-ray emission from the three cluster cores in the RCS 2319+00 supercluster are shown in Fig 1.3, taken from the *Chandra* X-ray study of RCS-1 clusters done by Hicks et al. (2008).

In addition to the extended X-ray emission from the intracluster medium, X-ray point source emission has been found to be an excellent indication of the presence of significant active galactic nuclei (AGN) activity. Hard X-ray emission has been

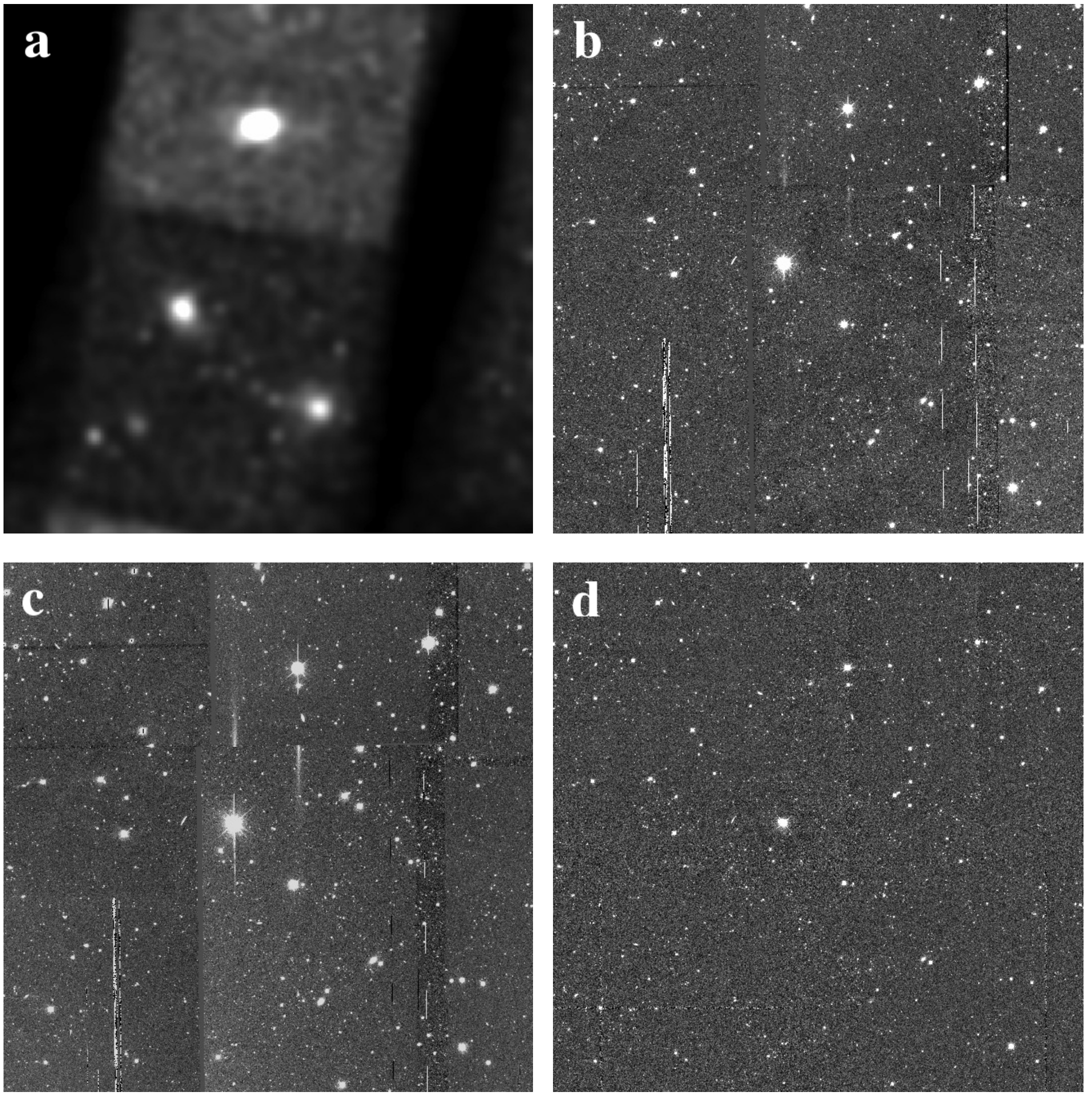

Figure 1.4 Multiwavelength imaging of a 15×15 arcminute region around the RCS 2319+00 supercluster. (a) 0.3–0.7 keV X-ray, (b) z' optical, (c) R_c optical, (d) K_s NIR.

linked to the accretion disks close to black holes, resulting from inverse Compton scattering from UV photons (Haines et al., 2012). X-ray detection of AGN also carries the advantage of lacking the obstruction commonly plaguing optical and UV AGN detections. In this thesis, the X-ray point source catalogue of the RCS 2319+00 supercluster field is used to help investigate possible AGN contamination in star

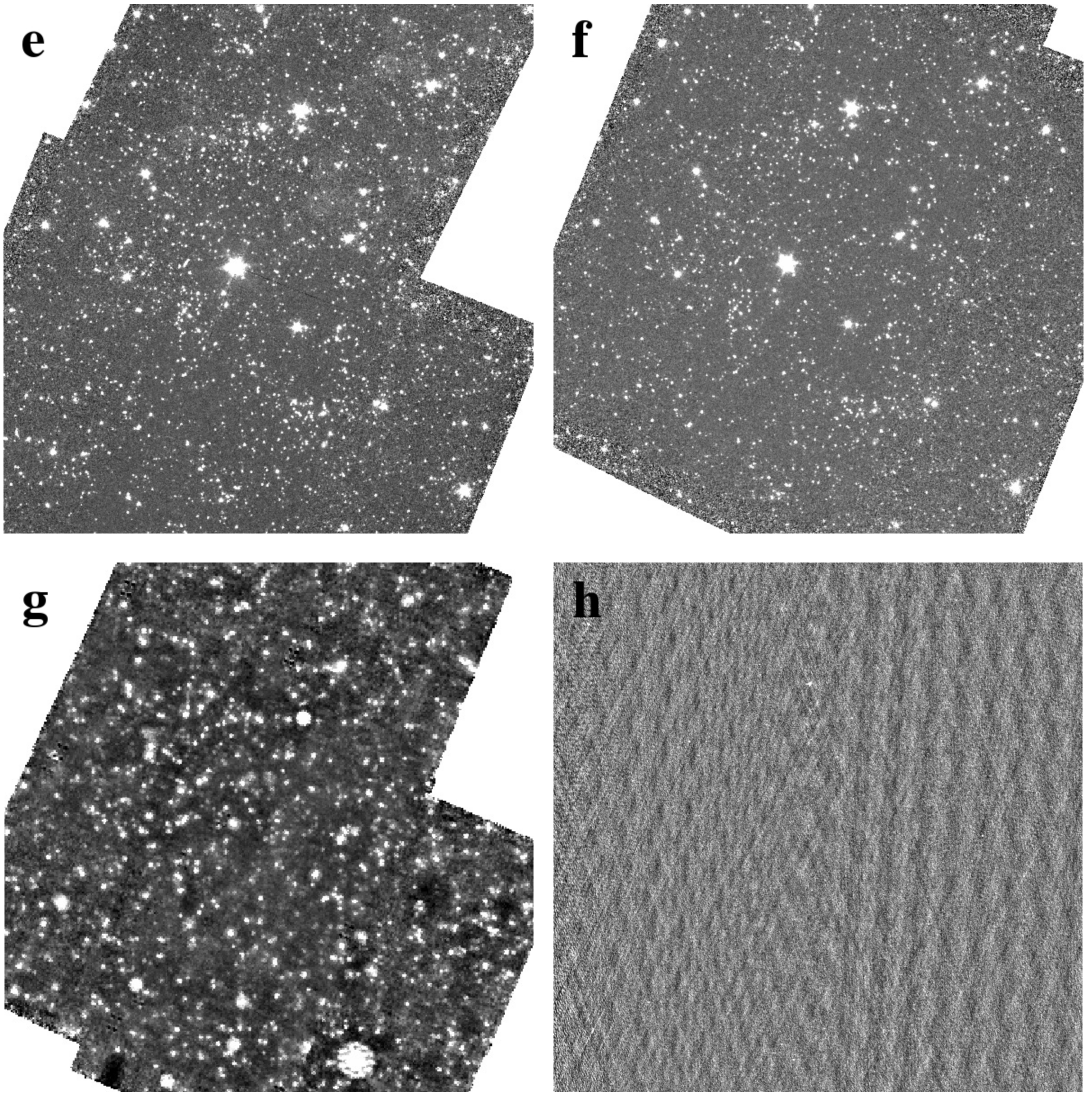

Figure 1.5 Same as Figure 1.4. (e) 3.6 μm, (f) 4.5 μm, (g) 24 μm, (h) 1.4 GHz

forming galaxies.

1.7.2 Optical

Optical data can provide information about the positions, colours and morphologies of galaxies. The R_c and z' imaging from the RCS-1 survey (Gladders & Yee, 2005) yielded galaxy catalogues with information on the positions of optical sources in the field. As well, the R_c and z' magnitude of sources results in $R_c - z'$ colour information. This colour and magnitude information can be used to create a colour-magnitude diagram, as seen in the simulations in Figure 1.2. These diagrams are used to estimate the redshift of clusters from the position of the red-sequence line. They also aid in pinpointing probable cluster core galaxies using the known relation that early-type, elliptical cluster core galaxies are found to lie predominantly along the red-sequence (e.g., Dressler, 1980). Late-type, star forming galaxies are known to be predominantly bluer in colour and found in the blue-cloud region below the red-sequence line.

The current study uses the colour-magnitude diagram of galaxies identified in the RCS 2319+00 supercluster to investigate the colours of members of different density groups within the structure, and therefore at different evolutionary stages within the supercluster environment.

1.7.3 Near–Infrared

The near-infrared (NIR) region of galaxy SEDs can be used to estimate galaxy stellar masses. This is done using ratios of the stellar light to stellar mass. At wavelengths of $\sim 2.2\,\mu$m (the position of the K-band NIR filter), the light emitted from galaxies has been found to be mostly unaffected by any recent or current star formation activity (Kauffmann & Charlot, 1998; Kodama & Bower, 2003). The NIR therefore provides an opportunity to estimate the current stellar mass of a galaxy, unobstructed by other possible activity.

As redshift increases so to does the wavelength at which we can observe the rest frame K-band. We can therefore use data from higher in the NIR range to estimate galaxy stellar masses. In this study we use $3.6\,\mu$m and $4.5\,\mu$m data as a proxy for rest-frame K-band at higher redshifts to estimate stellar masses. As well, the higher wavelength NIR data can be used to calibrate the observed K-band data in order to estimate stellar masses for higher redshift galaxies.

1.7.4 Mid–Infrared

Galaxies detected in the mid-infrared (MIR) are radiating stellar light that has been absorbed by dust in the galaxy and is being re-emitted in the thermal infrared (Kennicutt, 1998). These dusty MIR galaxies often have much of their star formation obscured at optical and UV wavelengths. The MIR is therefore an ideal bandwidth in which to detect current SFR activity in galaxies that would otherwise go undetected or underestimated using other tracers of star formation.

Here we use the $24\,\mu$m band, corresponding to $\sim 13\,\mu$m in the rest-frame at the $z \sim 0.9$ redshift of our target supercluster, to estimate galaxy SFRs and investigate the overall SFR activity and distribution in the various supercluster environments.

1.7.5 Radio

Radio emission in galaxies is dominated either by star formation or AGN activity. In star forming radio galaxies, the star formation results from young, massive stars with supernovae remnants that accelerate their electrons and emit synchrotron radiation (Condon, 1992; Condon et al., 2002). The division between the star forming radio population and the AGN dominated radio population is aided through use of the know MIR/Radio correlation of star forming galaxies (e.g., Appleton et al., 2004; Ibar et al., 2008; Beswick et al., 2008; Huynh et al., 2010a; Rieke et al., 2009; Boyle et al., 2007). Using the known correlation between the MIR and radio populations, we can isolate the AGN galaxy population to avoid contamination in studies of star forming galaxies. The 1.4 GHz radio data found herein is primarily used for this reason, to estimate the possible AGN contamination of MIR star forming galaxies.

1.7.6 Spectroscopy

Accurately determining the redshifts of galaxies and therefore their membership in a group, cluster or background/foreground population is done using either spectroscopic methods or multiband photometric SED fitting for photometric redshifts. These redshifts can also be used to estimate cluster velocity dispersions, radii, and virial masses. Both methods carry advantages and disadvantages.

The advantage of photometric redshift estimates is in the wide-field results that can be obtained using comparatively low observation times to obtain multiple photometric images. Photometric redshifts require accurate photometry from ultraviolet (UV) to near-infrared (NIR) wavelengths. Their accuracy is determined based on the number and range of filters available and the accuracy of the photometry, with care given to errors from zero-points, seeing differences, reddening, galactic extinction, k-corrections, the intrinsic accuracy of the given filter, etc. Photometric redshifts also rely heavily on galaxy templates, often from stellar population synthesis models. Redshift finding codes are calibrated using either spectroscopic redshift catalogues (e.g., HyperZ; Bolzonella et al., 2000) or through calibration with synthetic galaxy photometry based on theoretical galaxy formation and evolution models (e.g., EAzY; Brammer et al., 2008). For photometric redshift estimates in the RCS-1 catalogues using four bands, Hsieh et al. (2005) estimated rms errors of $\sim$0.2 in the redshifts calculated for $z \sim 0.8$ galaxies when compared to spectroscopic redshifts, with the errors increasing with increasing redshift. Bolzonella et al. (2000) found that photometric redshift errors reduce drastically by increasing the number of filters used in the estimates.

Spectroscopic redshifts, while they can be very accurate, come with their own disadvantages. The main set-back in compiling large spectroscopic redshift catalogues is the overhead, both observationally and in the reduction processes. Multi-object spectrographs (MOS), used to target a large number of objects simultaneously, range in field of view size from square detectors several arcmins across to large spectrographs $\sim$30 arcminutes in diameter (e.g., Hook et al., 2004; Appenzeller et al., 1998; Le Fevre et al., 2003; Kimura et al., 2010; Dressler et al., 2011). These MOS instruments allow for tens to several hundreds of target slits per mask. While the numbers of targets on some instruments are large, they are significantly less than the tens to hundreds of thousands of objects detected in wide-field imaging.

Spectroscopic redshifts are found using the spectrum of a target source often cross-correlated to template spectra and then checked by eye for distinct emission and absorption features in the spectrum (e.g., Gal & Lubin, 2004; Gilbank et al., 2007, 2008a). At higher redshifts, longer integration times are needed in order to obtain spectra with the same S/N as lower redshift sources. Higher redshifts also mean that common prominent emission features of galaxies such as the distinct $[\mathrm{H}_\beta]\lambda4861$–$[\mathrm{OIII}]\lambda4959, 5007$ and the $[\mathrm{H}_\alpha]\lambda6563$–$[\mathrm{SII}]\lambda6716, 6731$ patterns are often redshifted out of the range of optical spectra or appear in areas with high CCD fringing effects. The advent of NIR multi-object spectrographs is beginning to bridge this gap with the Fibre Multi Object Spectrograph (FMOS; Kimura et al., 2010) recently beginning observations. The lack of prominent emission line features in higher redshift galaxies causes redshift detections to rely on a combination of lower wavelength, often less prominent emission lines as well as absorption lines. This again requires higher S/N spectra to accurately detect confident redshifts.

Looking for spectroscopic redshifts of cluster galaxies is further complicated by the lower frequency of emission-line galaxies in clusters compared to the field, due to the higher fraction of early-type, elliptical galaxies associated with cluster cores (e.g., Osterbrock, 1960; Gisler, 1978; Dressler, 1980). Other complications include the presence of cosmic rays in the spectral observations that, if they are not carefully removed from the 2D spectra, can appear as strong emission lines in the final 1D spectrum (e.g.; Gilbank et al., 2007). Despite its difficulties, this thesis uses the more accurate, though less numerous, redshifts found through spectroscopic analysis.

Chapter 2

An Extensive Spectroscopic Survey of RCS 2319+00

THE FOLLOWING CHAPTER IS BASED ON:

The structure of the merging RCS 231953+00 supercluster at $z \sim 0.9$

A.J. Faloon, T.M.A. Webb, E. Ellingson, R. Yan, D.G. Gilbank, J.E. Geach, A.G. Noble, L.F. Barrientos, H.K.C. Yee, M. Gladders and J. Richard, 2013, ApJ, 768, 104

2.1 Introduction

In this chapter we present the results of a large spectroscopic campaign on the RCS 2319+00 supercluster field at $z \sim 0.9$. The aim of the survey is to compile a large supercluster membership catalogue for use in further analysis. The chapter is organized as follows. Section 2.2 details the extensive spectroscopic campaigns that have been completed on the supercluster along with brief descriptions of their reductions and redshift finding methods. Section 2.3 summarizes the output of the combined redshift catalogue. In Section 2.4 we attempt to quantify the cluster properties including the redshifts, velocity dispersions, virial radii and masses of the three main component clusters. Section 2.5 offers a summary of the findings in this chapter.

2.2 The Spectroscopic Data

The spectroscopic catalogue emanates from six different observing runs with five different Multi-Object Spectrographs (MOS): Magellan-IMACS, VLT-VIMOS, Subaru-

Table 2.1 Spectroscopic Mask Observations on the RCS 2319+00 Supercluster Field

Instrument	Mask	RA	DEC	Date/ID	Total Int time (s)	# slits
IMACS	231953+A	23 19 53.00	+00 38 00.00	2006 Oct 29	7200	722
IMACS	231953+B	23 19 53.00	+00 38 00.00	2007 Oct 9	7200	708
IMACS	231953+C	23 19 53.00	+00 38 00.00	2007 Oct 10	7200	644
IMACS	2319NE	23 18 31.00	+00 34 12.00	2007 Oct 9	7200	751
IMACS	2319W	23 21 02.00	+00 50 30.00	2007 Oct 10	7200	740
VIMOS	RCS2319P1	23 19 32.93	+00 42 26.10	2005 Jul 9	2500	341
VIMOS	RCS2319P2	23 19 32.43	+00 33 55.44	2005 Aug 13	2500	337
VIMOS	RCS2319P3	23 20 13.13	+00 32 11.90	2006 Aug 22	1920	355
VIMOS	RCS2319P4	23 20 13.70	+00 41 09.60	2006 Oct 16	2880	339
FMOS	RCS2319P1	23 19 49.83	+00 34 41.90	2011 Oct 16	7200	171
FMOS	RCS2319P2	23 19 54.30	+00 35 11.60	2011 Oct 16	7200	174
GMOS-N	RCS2319+0039	23 19:53.40	+00:38:13.80	2003 Sept 30	10800	27
FORS2	RCS231953+0038.0	23 19 53.00	+00 38 00.00	70.A-0378(B)	10800	29
FORS2	R2319M01	23 19 53.00	+00 37 13.00	2011 Oct 30	1800	21
FORS2	R2319M01	23 19 53.00	+00 39 27.00	2011 Nov 1	2700	20

Note. Units of right ascension are hours, minutes, and seconds and units of declination are degrees, arcmins, and arcsecs.

FMOS, Gemini-GMOS, and VLT-FORS2. Table 2.1 summarizes the central coordinates of each of the spectroscopic masks, the dates or program ID of the observations, the total integration time, and the number of target slits per mask.

The observation setup and data reduction techniques used for each instrument are detailed below. Figure 2.1 shows the coverage of the IMACS, VIMOS and FMOS masks over the supercluster field. The cluster positions are identified by their X-ray contours (see Figure 1 of Hicks et al. 2008 for a more detailed view of the X-ray flux distribution). The GMOS and FORS2 fields of view are smaller and fall within the larger instrument masks, centered on Cluster A.

2.2.1 IMACS Data

Wide-field MOS was taken with the Inamori Magellan Areal Camera and Spectrograph (IMACS; Dressler et al., 2011) on the Baade 6.5 m Magellan telescope using the University of Toronto's share of Magellan time. Three pointing positions of the 27′ diameter IMACS field of view were used. The data were taken as part of a large optical spectroscopic survey covering 42 RCS1 and 1 RCS2 clusters over eight

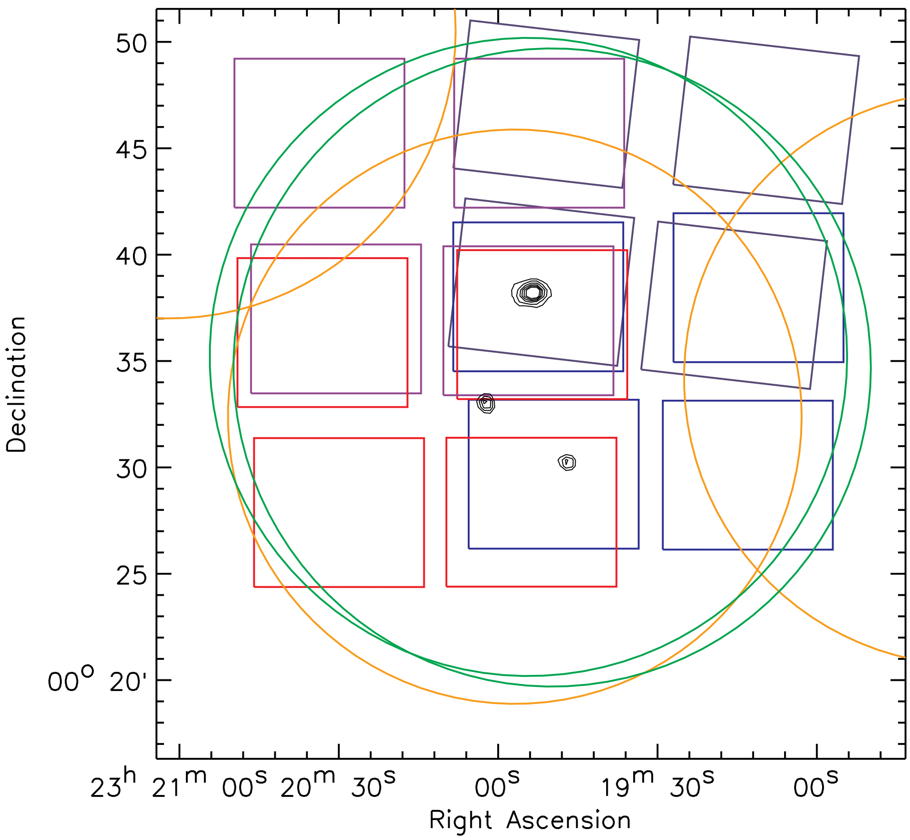

Figure 2.1 Spectroscopic mask coverage centered on $23^{\mathrm{h}}19^{\mathrm{m}}52^{\mathrm{s}}.8{+}00°34'12''$ over a 35 × 35 arcmin region with the three component cluster positions identified by the X-ray contours from Hicks et al. (2008). Rectangles denote the four VIMOS pointings with each colour representing the four quadrants of a single VIMOS observation. The orange circles show the three IMACS positions and green circles represent the FMOS field of view. The coverage with GMOS and FORS2 is not shown. Both instruments were centered on Cluster A, with GMOS targets covering ∼1 arcmin^2 and FORS2 targets over a ∼6 × 6 arcmin region.

observing runs from 2004 October to 2007 October (R. Yan et al. 2013, in preparation). Three masks were centered on the RCS 2319+00 supercluster field (masks 231953+A, 231953+B, and 231953+C). Two additional masks covering the nearby RCS 231831+0034.2 (2319NE) and RCS 232102+0050.5 (2319W) RCS-1 cluster candidates overlap the supercluster field region. Each mask was observed in 4 × 1800 s exposures with ∼ 650–750 slits per mask. The g150 grism was used with the $f/2$ camera and 1 arcsec slit widths, yielding a spectral resolution of R=555. A custom band-limiting filter was used to restrict wavelength coverage to 6050-8580 Å encompassing the [O II]λ3727 to G-band (~4304 Å) spectral features and slightly beyond at the supercluster redshift. In total, there are 2138 unique IMACS spectroscopic targets in a 35×35 arcmin region around the supercluster, with duplicates used to check the redshift accuracy of the IMACS sample (see R. Yan et al. 2013, in preparation).

The full details of the IMACS reduction and redshift finding are discussed further in the R. Yan et al. (in preparation) paper detailing the large IMACS RCS survey. Briefly, the IMACS spectroscopy was reduced using a modified version of the DEEP2 DEIMOS reduction pipeline (Davis et al., 2003). The redshift finding was done using the IDL-based `zspec` program, which uses chi-squared fitting to template spectra. It was adapted from the DEEP2 software for use with the RCS IMACS spectroscopy sample by R. Yan. All redshift assignments were checked by eye and assigned a quality flag: $Q \geq 3$ for a secure redshift, $Q = 2$ for a potential redshift, $Q = 1$ for bad spectra, and Q = -1 for stars. Using high-quality spectra of repeated targets, the redshift error for the IMACS sample was calculated to be $\Delta z \sim$ 0.000388, or ~60 km s^{-1} at $z \sim 0.9$. The initial discovery paper of the RCS 2319+00 supercluster (Gilbank et al., 2008a) used preliminary redshifts from the 231953+A IMACS mask, which have been refined and updated for this work.

2.2.2 VIMOS Data

Optical spectroscopy was taken with the Visible Multi-Object Spectrograph (VIMOS; Le Fevre et al., 2003) on the 8.2 m Unit Telescope 3 of the Very Large Telescope (VLT UT3). VIMOS contains four detectors, each with a 7×8 arcmin field of view, separated by 2 arcmin gaps between quadrants. Four VIMOS pointings were designed to cover a ~25×25 arcmin region centered on RCS 2319+00 Cluster A (see Figure 2.1). At the time of the spectroscopic proposal, Clusters B and C had not yet been identified. No colour or magnitude selection was applied to the mask design; however, the highest priority was given to sources with radio and submm counterparts (Noble et al., 2012). The low resolution red grism (LR_red), with a wavelength range of 5500-9500 Å, was used to cover the [O II]λ3727 to [O III]λ5007 spectral features at $z \sim 0.9$. This setup resulted in a spectroscopic resolution of R=210 with a dispersion of 7.3 Å pixel^{-1}.

The VIMOS spectroscopy was run through the standard VIMOS data reduction pipeline. We decided to re-extract the 1D spectra from the 2D sky-subtracted, flat-fielded, wavelength-calibrated spectra in order to (1) verify that the correct primary object spectra was extracted when multiple sources appeared in a single slit, (2) improve the trace of faint continuum sources and (3) allow for better removal of contamination from cosmic rays, zeroth-, first-, and second-order contamination and fringing in the spectra. The IRAF `noao` package was used to trace and extract the 1D spectra, with additional background subtraction performed and bad pixels replaced using model points. Spectra of separate observations were then co-added with `imarith` and checked for any residual bad pixels, which were removed manually. The full details of the reduction of the VIMOS spectroscopy and the initial redshift finding, done by eye with manual measurements of the spectroscopic emission lines, are found in Faloon (2008). For the current study, we decided to refine the redshift results using a correlation program and an interactive redshift fitting program in order to increase the number of confident redshifts through template matching.

To prepare the spectra for redshift finding the continuum was fitted and subtracted

Table 2.2 Spectroscopic Galaxy Templates Used for the Cross-Correlation of Target Galaxies.

Template	Galaxy Type
1	Mix of F & K type stars
2	Elliptical galaxy
3	Bruzual & Charlot (2003) post-starburst model
4	SA type spiral galaxy with emission and absorption lines
5	SC type spiral galaxy with strong emission lines

using `fit1d` and stacked with a weighted spectrum to remove the *A*-band absorption line. Redshifts were found by first running the final 1D spectra through a cross-correlation program adapted for IDL (Blindert, 2006) from the CNOC1 technique using five template galaxy spectra (Yee et al., 1996a) and then interactively checking and, if necessary, re-fitting the redshifts using an IDL-based redshift program written for use with the output of the cross-correlation program.

The IDL-based program first assigns redshifts based on the best correlation to the five template galaxies, listed in Table 2.2, as well as listing the best redshift for each galaxy template spectrum along with their correlation value, with higher values denoting better fits. The interactive program shows the source spectrum with the most common galaxy emission and absorption lines identified for the chosen redshift (see Figure 2.2). The vertical grey bands denote the A-band and B-band Fraunhofer atmospheric absorption lines. Below the source spectrum the correlations for all redshifts for the selected template spectrum is plotted with the x-axis scale of $log(1+z)$ and the correlation peak corresponding to the chosen redshift identified with a green line. The redshifts were assigned the same quality flags as the IMACS data. The VIMOS redshifts carry errors of $\Delta z \sim 0.002$ ($\sim$300 km s^{-1}) based on the wavelength calibration and dispersion of the data, the widths of the correlation peaks and matched targets between the IMACS and VIMOS samples.

2.2.3 FMOS Data

Near-Infrared spectroscopy were obtained with the Fiber Multi Object Spectrograph (FMOS) on the 8.2 m Subaru telescope (Kimura et al., 2010). FMOS contains 400 fibers with an accuracy of 0.2 arcsec rms in a 30 arcmin diameter field of view. Two pointings were centered on the supercluster field. We used the Cross-Beam-Switching (CBS) mode, which uses nodding for better sky subtraction by allocating two fiber

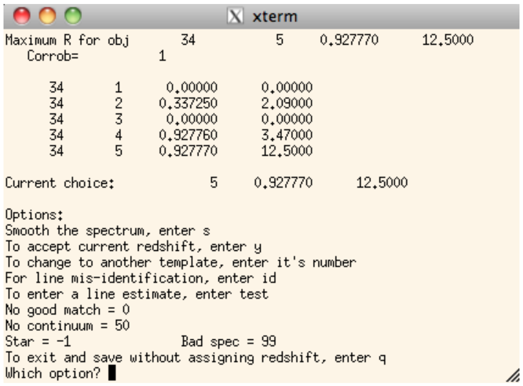

```
Maximum R for obj      34          5     0.927770      12.5000
   Corrob=           1

      34       1      0.00000      0.00000
      34       2     0.337250      2.09000
      34       3      0.00000      0.00000
      34       4     0.927760      3.47000
      34       5     0.927770      12.5000

Current choice:             5     0.927770      12.5000

Options:
Smooth the spectrum, enter s
To accept current redshift, enter y
To change to another template, enter it's number
For line mis-identification, enter id
To enter a line estimate, enter test
No good match = 0
No continuum = 50
Star = -1               Bad spec = 99
To exit and save without assigning redshift, enter q
Which option? █
```

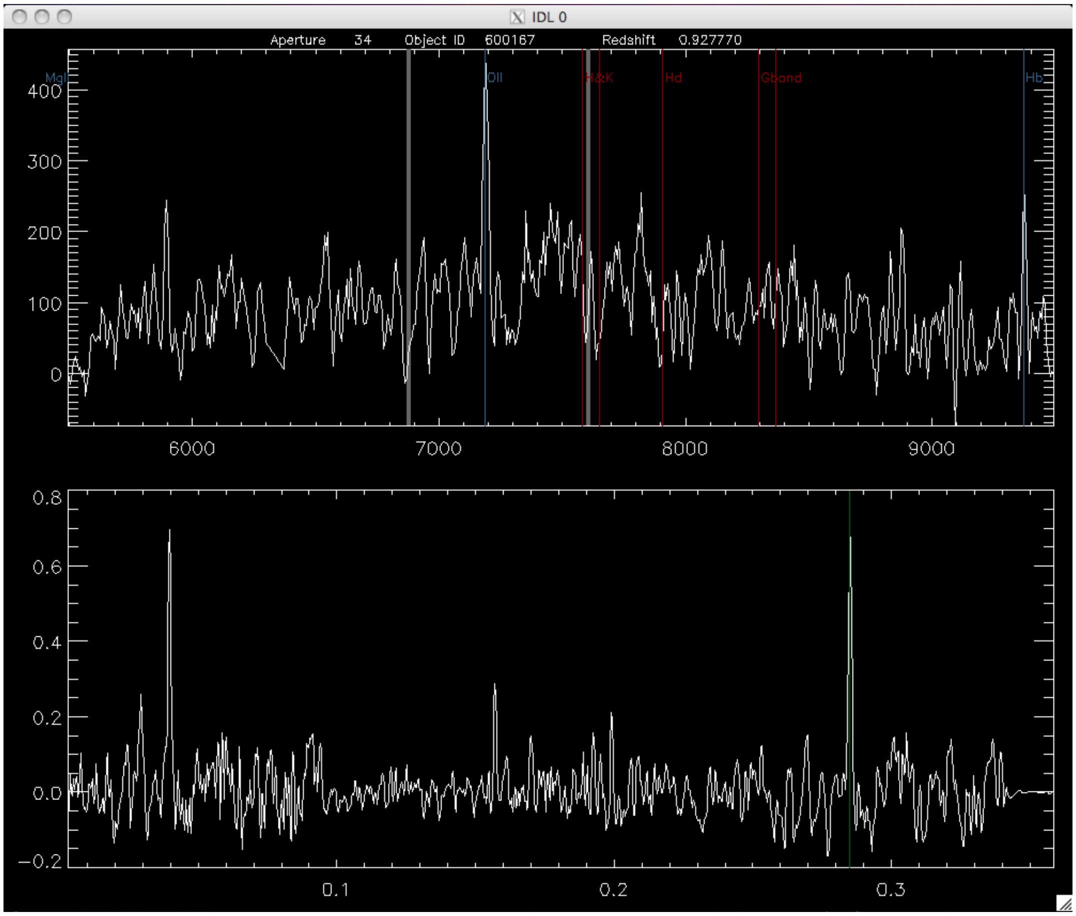

Figure 2.2 Screen grab of the interactive IDL-based redshift finding program written for use with the VIMOS, FMOS and GMOS spectra. The observed spectrum is shown with the most common galaxy emission (blue) and absorption (red) lines for the given test redshift. The bottom panel shows the correlation peaks against the given galaxy spectrum, with the x-axis scale of $log(1+z)$.

spines per target: one that is initially on target and one that is initially on the nearby sky. This results in only $\lesssim$200 science targets per pointing but allows each target to be observed for 100% of the exposure time and provides more accurate sky subtraction. We used the low-resolution mode (R=600, $\Delta\lambda \sim 20\,\text{Å}$) with a wavelength range of 0.9–1.8 μm, which allows coverage of H_α (6563 Å) and the S I (~6716/6730 Å) doublet features and beyond at the supercluster redshift.

Spectroscopic targets were chosen based on our Canada-France-Hawai'i Telescope WIRCam K_s catalogue, with priority going to mid-infrared 24 μm counterparts from our *Spitzer* MIPS catalogue (Webb et al., 2013). Previously identified ($Q\geq3$) and suspected (Q=2 redshifts) luminous infrared galaxy (LIRG) supercluster members from the IMACS and VIMOS redshift lists were targeted for further confirmation of their redshifts and for use in further studies of their spectral features. Overall 345 targets, including 121 targets not previously observed by other instruments, were observed with FMOS.

The FMOS spectroscopy was run through the FMOS preliminary data reduction and calibration package, fiber-pac: FMOS Image-Based Reduction Package (Iwamuro et al., 2012), which uses IRAF scripts and C programs based on CFITSIO to produce 1D spectra. The reduction includes flat-fielding, bad pixel removal, spatial distortion correction, spectral distortion correction, background subtraction, bias correction, wavelength calibration and flux calibration. The resulting spectra have a dispersion of 5 Å pixel^{-1}.

Final 1D spectra were prepared in the same way as the VIMOS spectra for use with the cross-correlation and redshift confirmation programs, with redshifts having the same quality flags and errors as the previous data. The redshift errors were again taken to be $\Delta z \sim 0.002$ to account for the wavelength dispersion and correlation peak widths. For any target with a previous, low-confidence spectra from IMACS or

VIMOS, the estimated FMOS redshift was checked with the lower wavelength range spectra in an effort to confirm the FMOS redshift and/or increase the confidence of the previous redshift. As FMOS is still in shared risk mode and the fiber-pac reduction package is still in development, the data were noisier than anticipated, despite photometric observing conditions, with only ∼30% redshift success.

2.2.4 GMOS North Data

Spectra from the 5.5×5.5 arcmin field-of view Gemini Multi-Object Spectrograph (GMOS; Hook et al., 2004) on the 8.1 m Gemini North Telescope were obtained in an effort to identify the redshift for the strong lensing arc in Cluster A (Gilbank et al., 2008a). The data were observed in the band-shuffle nod-and-shuffle mode, resulting in 27 targets in a ∼1 arcmin^2 region. The R150_G5306 red grism was used with a band-limiting filter (GG455 G0305) and 2×2 detector binning for a wavelength range of ∼4500–10000 Å, allowing coverage of [OII]λ3727 to [OIII]λ5007 at $z \sim 0.9$ and giving a resolution of 11.48 Å and a dispersion of 3.564 Å pixel^{-1}.

The GMOS spectroscopy was reduced in IRAF with the help of the `gemini` package tasks to bias-subtract, flat-field, and wavelength-calibrate the data. The positive and negative spectra for each object from the nod-and-shuffle observations were co-added and 1D spectra were extracted using the IRAF `apall` task with residual bad pixels removed manually. The spectra were prepared and redshifts found as in the VIMOS and FMOS data, with the same errors and quality flags assigned.

2.2.5 FORS2 Data

Spectroscopy taken with the Focal Reducer and low dispersion Spectrograph (FORS2; Appenzeller et al., 1998) of the Very Large Telescope were obtained from two separate observation runs. In the first observation run (mask RCS231953+0038.0) spectra of

29 target galaxies was taken as part of the larger spectroscopic follow-up of RCS-1 clusters. FORS2 was used in MXU multi-object spectroscopy mode with the 300I grism in conjunction with the OG590 filter to give a dispersion of 108 Å mm^{-1} and wavelength coverage from 6000 to 11000 Å. The target galaxies were selected primarily using a fixed magnitude limit. The observations totalled three hours per mask, including overheads, split into individual observations to improve cosmic ray rejection. Redshifts were found using cross-correlation with the IRAF `rvsao` package and interactively checked and, where necessary, refitted using the `emsao` task. Quality flags have been adjusted to be consistent with our larger redshift catalogue.

The second FORS2 data set consisted of a total of 43 slits over two masks (R2319M01 and R2319M02) taken as a follow up of *Herschel*-selected sources from the Herschel Lensing Survey (HLS; Egami et al., 2010). The data were taken using the 300V grism combined with the GG435 filter to give a wavelength coverage of 445–865 Å with a 112 Å mm^{-1} dispersion. Redshifts were found manually using the peak of the [OII]λ3727 emission line. The targets in this run comprised mainly background galaxies lensed by Cluster A of the RCS2319+00 supercluster, however six fell within the supercluster redshift range, with three having no previous spectroscopy.

2.3 The RCS 2319+00 Redshift Catalogue

2.3.1 The Combined Spectroscopic Data Set

In total, our spectroscopic campaign in the 35×35 arcmin field around the supercluster contains 3305 unique spectroscopic targets. Where there are duplicate targets present between masks or different instruments, the redshift with the higher quality factor is used. If the quality factor is the same between spectrographs, then priority is given to IMACS redshifts since it is the instrument with the smallest error.

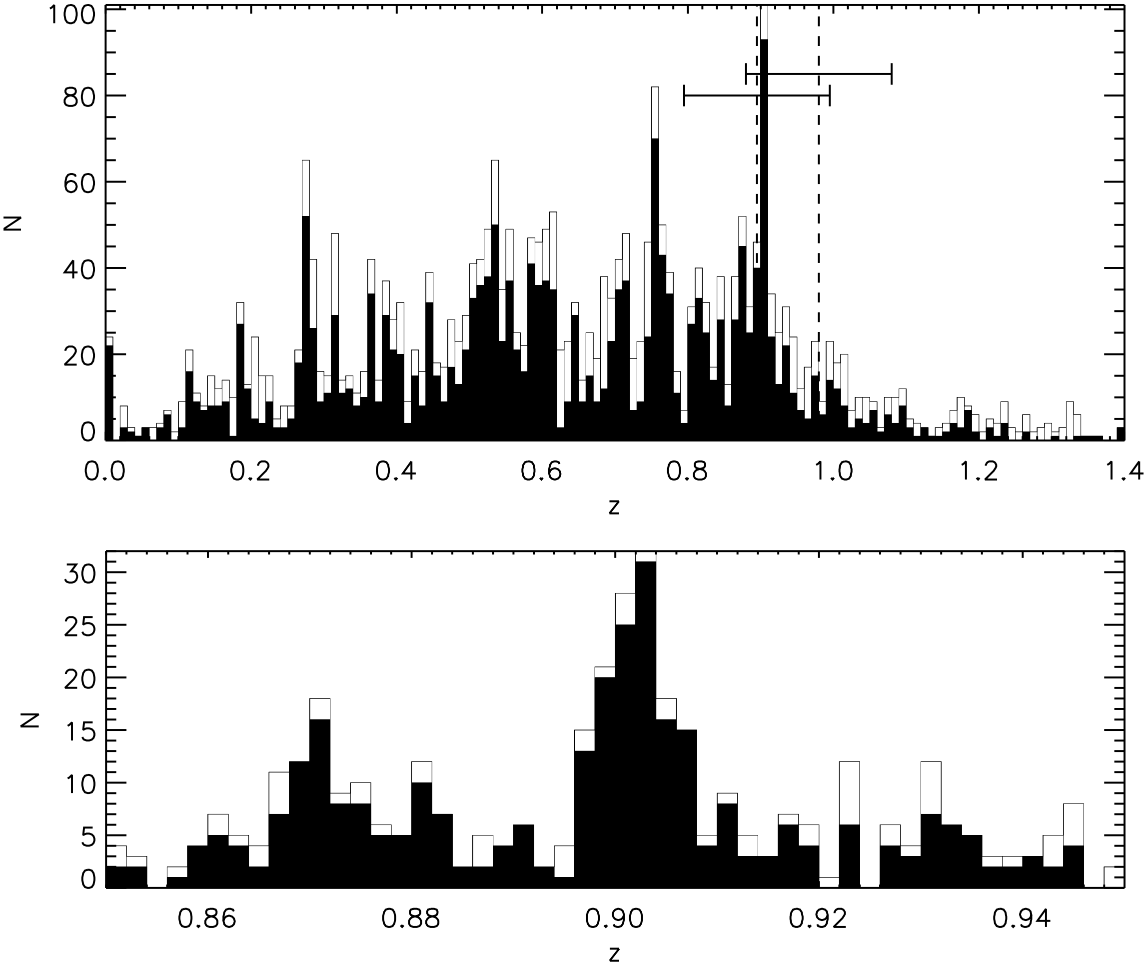

Figure 2.3 Top: spectroscopic redshift distribution in the 35 × 35 arcmin region around the RCS 2319+00 supercluster field with a bin size of $z = 0.01$ ($\sim$ 1500 km s^{-1} at $z \sim 0.9$). The filled histogram represents good confidence redshifts while the white histogram shows all redshift results. Potential foreground structures are visible in the histogram, as well as a clear peak at $z \sim 0.9$. The dashed lines indicate the photometric redshifts for the three component clusters of RCS 2319+00 (A & B: $z_{\mathrm{phot,RS}} = 0.984$, C: $z_{\mathrm{phot,RS}} = 0.895$; L.F. Barrientos et al., in preparation). The 1σ error on the RCS-1 photometric redshifts at $z \sim 0.9$ is $\Delta z \sim 0.1$ and is shown by the horizontal error bars. Bottom: zoomed in redshift histogram around the supercluster redshift of $z \sim 0.9$ with a bin size of $z = 0.002$ ($\sim$ 300 km s^{-1} at $z \sim 0.9$), consistent with the largest redshift error in our catalogue.

In total, there are 66 duplicate targets between the IMACS and VIMOS samples that have confident redshifts with both instruments. Of these, 9% had redshifts that did not fall within 3σ of each other. This implies that, in the worst case scenario, 8 of the VIMOS structure members listed in Table 2.3 have been mis-identified. This error may be due to updates in the calibration of the astrometry of the optical catalogues after the initial spectroscopic targeting resulting in a few very close neighbouring sources being identified with the same optical source in the updated catalogue.

The average redshift error on the IMACS/VIMOS matched galaxies is $\Delta z \sim 0.002$. The redshifts of overlapping targets between the combined IMACS/VIMOS spectroscopic catalogue and the FMOS data were found with the aid of the previous spectra and consequently they all match within errors. The redshifts of the duplicate sources in the FORS2 spectroscopy matched to the combined redshift list to within $\Delta z \sim 0.001$ and the two duplicates from the GMOS sample matched to within $\Delta z \sim 0.003$.

The full redshift distribution of the RCS 2319+00 supercluster region is shown in the top panel of Figure 2.3. Our catalogue contains 2000 good confidence redshifts, with 1961 galaxy spectra and 39 stars. There is a clear peak at the supercluster redshift of $z \sim 0.9$ along with potential foreground peaks at $z \sim 0.28$, 0.45, 0.53 and 0.76. The photometric redshifts of the RCS 2319+00 clusters, as identified by overdensities of red galaxies in this field (L.F. Barrientos et al., in preparation), are shown as dashed lines in the top panel of Figure 2.3 (A and B: $z_{\rm phot,RS} = 0.984$, C: $z_{\rm phot,RS} = 0.895$). The red-sequence redshifts were found to carry errors of $\Delta z \lesssim 0.05$ over the majority of the RCS-1 survey range, increasing to $\Delta z \sim 0.1$ at the highest redshifts due to larger uncertainties in the photometric data and poorer sampling of the 4000 Å break in the R_c and z' bands. Possible foreground clusters and structures are discussed in the Appendix A.

The bottom panel of Figure 2.3 shows the zoomed in redshift histogram covering a redshift range of $0.85 \leq z \leq 0.95$. Three distinct redshift peaks are apparent, separated by ~ 4700 km s^{-1} ($\Delta z \sim 0.03$) from one another, ~ 65 Mpc assuming Hubble flow. To determine membership in the RCS 2319+00 supercluster field we

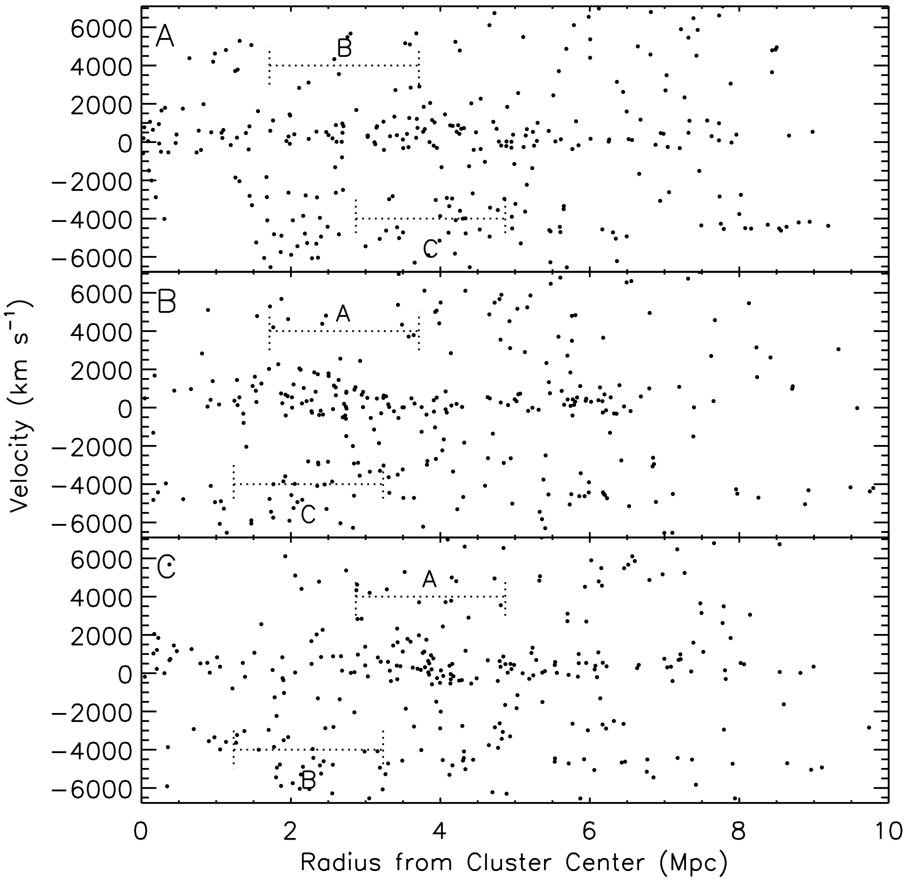

Figure 2.4 Velocity vs. radius of all spectroscopically confirmed galaxies in the RCS 2319+00 supercluster field within the redshift range $0.848 \leq z \leq 0.946$. In each panel the galaxies' radial positions are plotted relative to the specified cluster center. All velocities are plotted relative to an arbitrary $z = 0.9$. The dotted lines denote the ± 1 Mpc radii for the neighbouring cluster centers relative to their radial position from the center of the specified cluster to demonstrate the difficulty in assigning cluster membership to specific cluster cores.

use a broad membership range of $0.858 \leq z \leq 0.946$ based on the bottom panel of Figure 2.3. This is done to encompass any infalling groups, filaments or walls in redshift space. This is the range over which we search for substructure in the supercluster and may contain isolated galaxies not connected to the supercluster structures (see Section 3.2).

A different view of this redshift range is shown in Figure 2.4, where each of the three panels represents the velocity versus radius of all spectroscopically confirmed galaxies from the center of each cluster relative to $z = 0.9$. The dotted lines indicate

Table 2.3 Spectroscopic Target Numbers in the RCS 2319+00 Supercluster Field

Spectroscopic Source	Targets	Secure Redshifts	Stars	Galaxies	Structure Members
IMACS	2133	1325	33	1292	185
VIMOS	962	562	6	556	85
FMOS	181	87	0	87	25
GMOSN	14	11	0	11	4
FORS2	15	15	0	15	4
TOTAL	3305	2000	39	1961	302

Note. All numbers listed are for unique spectroscopic targets only. Any duplicate targets have been attributed to the instrument with the highest redshift quality and/or the lowest redshift error.

the positions of the ± 1 Mpc radii from the neighbouring cluster centers relative to their radial position from the center of the specified cluster. The transverse proximity of the clusters highlights the difficulty in assigning cluster membership over the field to specific cluster cores. The three separate velocity walls can be seen in all three panels at $z \sim 0.87, 0.90, 0.93$. These redshift sheets may or may not belong to a single, gravitationally bound structure. For the purpose of investigating substructure around the supercluster region, we retain all spectroscopically confirmed galaxies within the broader redshift range.

Table 2.3 gives a summary of the number of unique spectroscopic targets and the good confidence redshifts for each spectrograph along with the number of good confidence stars, galaxies and overall structure members. For the rest of this paper we use only secure spectroscopic redshifts. We find 302 members in the broad supercluster range of $0.858 \ \leq \ z \ \leq \ 0.946$.

2.3.2 Spectroscopic Completeness and Success Rates

Due to the large survey area of the supercluster field, targeting all sources with spectroscopy is unrealistic. The 5σ magnitude limits of the RCS survey are $z' = 24.05\,\mathrm{mag}$ and $R_c = 24.7\,\mathrm{mag}$ (Gladders & Yee, 2005), resulting in costly time overheads to obtain high signal-to-noise (S/N) spectroscopy for the faintest sources in our catalogue. From Figure 2.1 it can be seen that the spectroscopic coverage of the three cluster

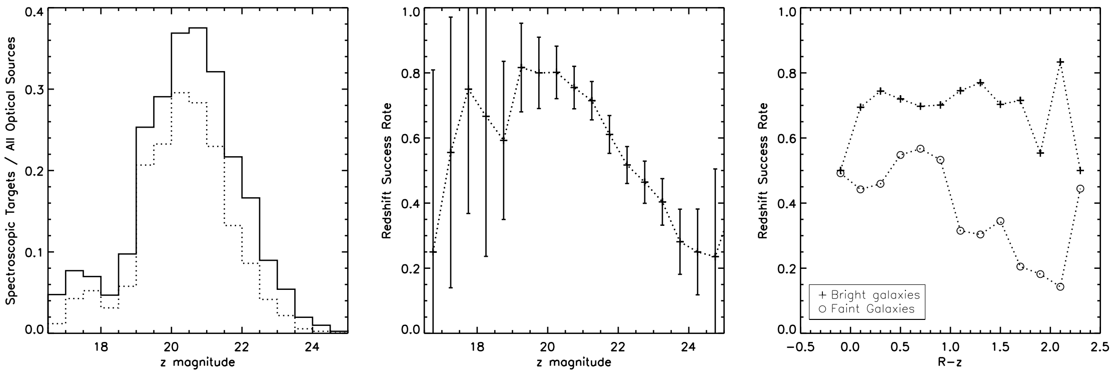

Figure 2.5 Left: spectroscopic target coverage completeness for the 35×35 arcmin catalogue region. The solid line shows spectroscopic targets representing all slits, including those that did not yield reliable redshifts, compared to the full optical catalogue with 5σ depth of $z' = 24.05$ mag. The dotted line shows the coverage completeness when only the secure redshifts are taken into account. Middle: spectroscopic redshift success for all targets based on z' magnitude. Right: redshift success based on R_c–z' colour for bright ($z' \leq 22$ mag) and faint ($z' > 22$ mag) targets.

cores varies, with Cluster A having the most mask coverage from all instruments including the additional GMOS and FORS2 data. Cluster B has the least amount of spectroscopic coverage, with its core falling outside or along the edges of the VIMOS mask coverage.

The completeness of the spectroscopic target coverage over the entire optical catalogue for magnitude bins of 0.5 in z' magnitude over the 35×35 arcmin area is shown in the left panel of Figure 2.5. The solid line shows the target completeness for all spectroscopic targets, regardless of redshift success, while the dashed line shows only those targets that yielded a secure redshift. Despite our 3305 independent spectroscopic targets, our highest target completeness, for 20–21 magnitude sources, is only ∼37%, decreasing to ∼30% coverage for secure redshifts.

Spectroscopic selection functions and weights were calculated for each source with a spectroscopic redshift following the method used in the two Canadian Network for Observational Cosmology (CNOC) surveys (see Yee et al. (1996a, 2000) for a detailed explanation). Briefly, the magnitude selection function (S_m) of each spectroscopically confirmed supercluster member is found by taking all galaxies within the photometric catalogue in a magnitude bin centered around the desired galaxy and calculating the ratio of galaxies in that bin having a measured redshift to those without a redshift. The geometric distribution selection function (S_{xy}), used as a correction to the primary magnitude selection function, was also computed. The geometric selection function corrects for different target densities over the larger field and uses only sources within two arcmins of the desired galaxy, within ± 0.5 mag bins to compute a local magnitude selection function. This is then divided by the previously found S_m. The spectroscopic weight of each galaxy is the inverse of its total selection function ($S = S_m S_{xy}$).

The spectroscopic redshift success rates for the targeted sources is shown in the middle panel of Figure 2.5 and represents all instruments combined, with ∼80% of the brighter targets yielding confident redshifts and success rates dropping to only ∼30% at our 5σ depth of $z' = 24.05$ mag. The S/N, wavelength dispersion and reduction methods all affect the quality of the final spectra and therefore the redshift success rate. Most spectra were not taken under photometric conditions and the S/N varies between different spectra from the same instrument based predominantly on the weather conditions throughout the observations. The success rate of bright ($z' \leq 22$ mag) and faint ($z' > 22$ mag) sources, based on R_c–z' colour is also shown (Figure 2.5, right). For bright sources, the redshift success is fairly consistent at 70%–80% for all colours, with the lowest and highest colour bins affected by small numbers. The faint sources have variable success rates depending on their colours. At the bluer R_c–z' colours of < 1 the faint sources have a success rate of ∼50%, dropping to an average of ∼25% for the redder sources.

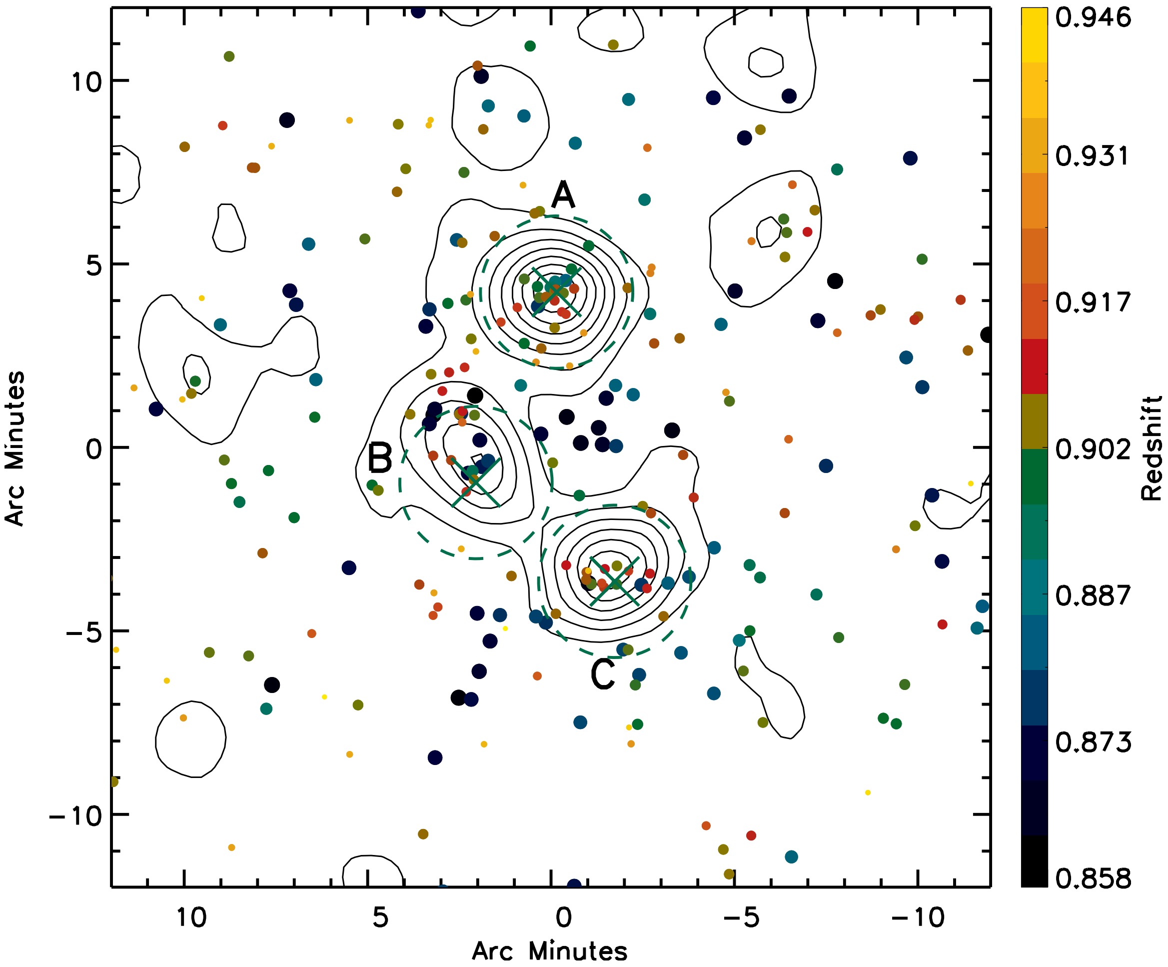

Figure 2.6 Redshift distribution of RCS 2319+00 supercluster members ($0.858 \leq z \leq 0.946$) centered on $23^{\rm h}19^{\rm m}52^{\rm s}.8 + 00^\circ 34' 12''$ and plotted over the significance contours of the red-sequence galaxy density profile at a photometric redshift of $z \sim 0.9$. Spectroscopically confirmed members are plotted as circles, the size and colour varying with redshift, with circle size decreasing with redshift and the colours varying from black through to yellow with increasing redshift. The dashed green circles denote the 1 Mpc radii around each clusters' X-ray center, indicated with large green X marks and seen to be offset from the red-sequence significance peaks.

2.4 Cluster Properties

2.4.1 Determining the Proper Cluster Centers

Figure 2.6 shows the distribution of galaxies within the RCS 2319+00 supercluster field over the $0.858 \leq z \leq 0.946$ range discussed above, plotted over the den-

Table 2.4 Cluster Center Positions

	Red-sequence (RS) Center	X-Ray Center	BCG Position	RS/X-Ray Offset	X-Ray/BCG Offset
A	23 19 52.8 +00 38 03.5	23 19 53.2 +00 38 12.5	23 19 53.42 +00 38 13.65	13.9	3.5
B	23 20 02. +00 33 29.6	23 20 02.1 +00 32 57.6	23 20 02.33 +00 33 03.10	32.5	6.5
C	23 19 46.1 +00 30 37.5	23 19 46.8 +00 30 14.3	23 19 46.60 +00 30 09.54	25.5	5.6

Note. Offsets are in units of arcseconds.

sity profiles of the red-sequence galaxies map at a photometric redshift of $z \sim 0.9$ (L.F. Barrientos et al., in preparation). The symbol size and colour varies with the redshift of the galaxies: larger, darker symbols are blueshifted relative to the mean redshift; smaller, lighter symbols are redshifted. The X-ray contours seen in Figure 2.1 (from Hicks et al., 2008) are not plotted but their peaks are shown with large green X marks and show an offset to the red-sequence peaks (see Table 2.4 for coordinates and offset distances). These offsets are most likely due to the contamination from the lower redshift wall seen in Figures 2.3 and 2.4 causing the cluster peak positions in the red-sequence density profile, which spans a broad redshift bin, to shift. The RCS 2319+00 supercluster is already visible in the red-sequence density profile maps with central redshifts as low as $z \sim 0.758$ (see Figure A.1a–d in the Appendix). As our spectroscopic coverage is not complete, the galaxies in this lower redshift peak, whose spatial distribution can be seen in Figure 2.6, represent a lower limit on the red-sequence density profile contamination.

We look to the brightest cluster galaxy (BCG) in each cluster core to aid in isolating the correct cluster center. The BCGs were found by first isolating all galaxies less than 0.5 Mpc from the red-sequence cluster centers in the photometric catalogue. From the reduced source lists, the brightest z'-band galaxy within ± 0.2 of the $R_c - z'$ red-sequence line for each cluster was selected as the BCG. The identified BCGs for the three clusters are all found ≤ 6.5 arcsecs from the cluster X-ray peaks, closer than the 13.5–32.5 arcsecs between the X-ray and red-sequence cluster center positions. We therefore use the X-ray centers in calculating the dynamical properties of the

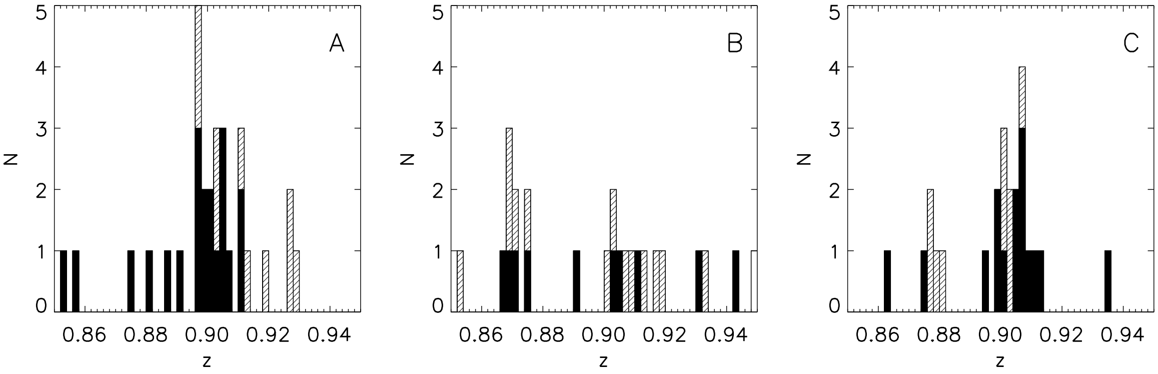

Figure 2.7 Histograms of the spectroscopic redshifts within a 1.0 Mpc radius of each cluster's X-ray peak. Solid histograms show confident redshift within 0.5 Mpc of the cluster centers and hatched histograms extend the radius to 1.0 Mpc.

clusters.

2.4.2 Determining the Cluster Core Members

To calculate the velocity dispersions and spectroscopic redshifts of the component clusters (Section 2.4.3) we use all confident redshifts within radii of 0.5 and 1.0 Mpc of the X-ray peak positions in each cluster. Due to the close separation distance between the three component cluster centers, a 1.0 Mpc radius is the largest used to avoid double counting of galaxies between component clusters. The green dotted circles in Figure 2.6 shows the 1.0 Mpc radii from the X-ray centers. An initial cut of $0.85 \leq z \leq 0.95$ around the supercluster redshift peak was used and the redshift histograms for the three cluster cores are shown in Figure 2.7. All secure redshifts within 1.0 Mpc of the center positions are shown as hatched histograms, with the solid histograms including only those galaxies within 0.5 Mpc of the centers. The histograms were examined for obvious outliers not consistent with a Gaussian curve that could falsely broaden the velocity distribution.

For Cluster A, no sources were removed as the redshift distribution, while broad, does not show any obvious irregularity and an iterative interloper clipping method is used in Section 2.4.3 when determining the cluster redshifts and velocity dispersions. We again look to the BCG of Cluster A for comparison to ensure that the redshift distribution in the region around the cluster core is tracing the proper cluster redshift. The BCG is found to have a confident spectroscopic redshift of 0.901, consistent with the approximate peak of the redshift distribution in the left-hand panel of Figure 2.7.

Clusters B and C seem to show double peaks in their redshift distributions, with lower redshift peaks at $z \sim 0.868$ and $z \sim 0.877$, respectively, and higher redshift peaks consistent with the overall supercluster redshift peak at $z \sim 0.9$ visible in all three cluster cores. This could possibly be due to under sampling of the cluster cores, especially for B, which falls at the edges or in the gaps of the VIMOS spectroscopy masks (Figure 2.1). However, if this were correct and the true redshift of the cores falls between the two peaks, the resulting velocity dispersions would lead to cluster virial masses much too large to be consistent with the measured X-ray masses (Hicks et al., 2008). Another, more probable possibility is that the lower redshift peaks in Clusters B and C belong to filaments and groups of the potential foreground structure seen in Figure 2.4. We investigate this further by looking at the spatial distribution of all members having redshifts consistent with the separate peaks in the 1.0 Mpc regions around Clusters B and C. As well, we use the spectroscopic redshifts of the BCG in each cluster core to corroborate our choice of approximate cluster redshift.

For Cluster C, the redshift peak of $0.874 < z < 0.882$ (Figure 2.8, center) shows that the members of this peak are inconsistent with the red-sequence significance contours of the cluster core. However, the members of the higher redshift peak of $0.894 < z < 0.914$ (Figure 2.8, right), present in all three cluster cores, are consistent with the red-sequence density contours. The BCG in Cluster C also validates the choice of the higher redshift peak as the correct one, with a spectroscopic redshift of 0.899.

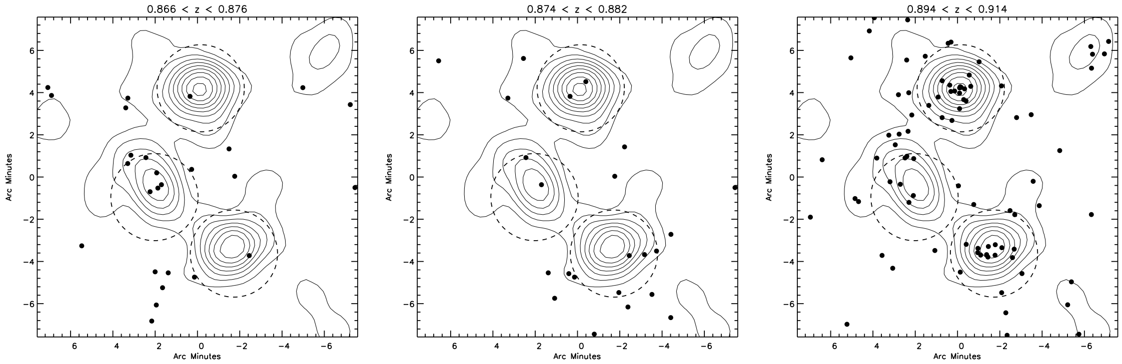

Figure 2.8 Distribution of galaxies in the three component cluster cores within three redshift slices corresponding to the lower redshift peaks in the histograms of Clusters B (left) and C (middle) and the higher redshift peak present in all three clusters (right). The dashed circles denote the 1 Mpc radii from the X-ray peaks. The contours show the significance contours of the red-sequence galaxy density profile at a broad photometric redshift slice around $z \sim 0.9$

The case of Cluster B is more difficult to disentangle. While there are similar numbers of galaxies in the two redshift peaks, neither the higher, broader peak nor the lower, sharper peak at $0.866 < z < 0.876$ (Figure 2.8, left) seem to have members significantly more clustered within the red-sequence over-density contours. Again, this is most likely due to the spectroscopic undersampling of Cluster B compared to the other cluster cores. We rely on the cluster BCG, with a spectroscopic redshift of 0.903, to isolate the correct redshift peak for this cluster as the higher of the two at $z \sim 0.9$, consistent with both Clusters A and C.

The presence of a strong X-ray peak corresponding to the position of the red-sequence over-density for Cluster B argues in favour of the existence of a massive cluster at this position rather than two less massive clusters or groups in the same line of sight. Though massive groups and lower mass clusters can emit in the X-ray, we would expect to see evidence of other substructure in the supercluster region in the X-ray if the emission were due to line of sight groups. The apparent alignment of both the red-sequence overdensities and the X-ray emission of the three peaks towards their nearest neighbour also implies the presence of three cluster cores rather than

Table 2.5 Spectroscopic Redshifts and Velocity Dispersions within Two Different Radii of the Cluster Centers

	0.5 Mpc			1.0 Mpc		
	N	z_{spec}	σ (km s^{-1})	N	z_{spec}	σ (km s^{-1})
A	17	0.900 ± 0.008	1253 ± 306	23	0.901 ± 0.008	1202 ± 233
B	···	···	···	9	0.905 ± 0.007	1154 ± 367
C	11	0.906 ± 0.005	759 ± 203	15	0.905 ± 0.005	714 ± 180

two cores at the positions of Clusters A and C and a two low mass clusters or high mass groups in the line-of-sight of the area denoted as Cluster B.

We manually remove the lower redshift peaks from the histograms of Clusters B and C so as not bias the cluster dynamics determinations.

2.4.3 Cluster Redshifts and Velocity Dispersions

The reduced galaxy redshift lists from the cluster core histograms, with the lower redshift peaks in Clusters B and C removed as described, were used to determine the cluster redshifts and velocity dispersions from within the 0.5 and 1.0 Mpc radii. We follow the method described by Postman et al. (1998), using the biweight mean estimate (Beers et al., 1990) to iteratively calculate the mean spectroscopic redshift and velocity dispersion of the cluster cores. At each iteration, all galaxy rest frame relative velocities to the biweight mean cluster redshift are calculated as $\Delta\nu = c(z-\bar{z})/(1+\bar{z})$. Any galaxy falling outside of the mean dispersion by more than 3σ or 3500 km s^{-1} is removed from the list and the biweight mean is recalculated. The biweight mean is used as it is less susceptible to outlying interlopers that may otherwise disproportionally shift the value of the mean.

The results of the mean redshift and velocity dispersion measurements within the two different radii from the cluster centers are listed in Table 2.5. The larger number of cluster galaxies used for the dynamical property measurements within 1 Mpc of the cluster centers result in smaller errors and more reliable values. For Cluster B, there are not enough galaxies within a 0.5 Mpc radius of the center coordinate to calculate the dynamical properties. We therefore use the values derived from the 1 Mpc radii. Cluster B again has the fewest galaxies within this radius with only nine galaxies remaining after the iterative interloper clipping, making the velocity dispersion unreliable, as seen by the large error. The 15 galaxies remaining within 1Mpc of Cluster C offer a better estimate of the properties but would still benefit from additional spectroscopic members for a more dependable measurement. Cluster A has 23 galaxies remaining after interloper clipping, though there remains a significant error of ~20% due to the broad distribution. This may indicate that we are not sampling a virialized population in this cluster and are instead witnessing a cluster merger. We discuss this possibility below when looking for substructure both in the multiwavelength and spectroscopic data (see Sections 2.4.5 and 3.2).

2.4.4 Virial Radius and Mass

Using the measured velocity dispersions we can estimate the dynamical mass and radius of the component cluster cores. The cluster virial mass can be approximated by calculating the mass at which the overdensity of the cluster is 200 times the critical density (ρ_c). We use the method of Carlberg et al. (1997) to calculate M_{200} from the velocity dispersion using,

$$M_{200} = \frac{3\sqrt{3}\,\sigma^3}{H(z)\,G}, \tag{2.1}$$

where $H(z) = H_o\sqrt{\Omega_\Lambda + \Omega_M(1+z)^3}$ and σ is the one-dimensional velocity dispersion. The virial radius is then approximated from $M_{200} = (4/3)\pi r_{200}^3 \times 200\rho_c$, which can be simplified as,

$$r_{200} = \frac{\sqrt{3}}{10} \frac{\sigma}{H(z)}. \tag{2.2}$$

The calculated r_{200} and M_{200} values are found in Table 2.6.

Another method of determining the mass of clusters within r_{200} from their velocity dispersions is to employ the method of Evrard et al. (2008), who used hierarchical clustering simulations to determine a virial scaling relation for massive dark matter halos of

$$M_{200} = \frac{10^{15}\,M_\odot}{h(z)} \left(\frac{\sigma_{\rm DM}}{\sigma_{15}}\right)^{1/\alpha}, \tag{2.3}$$

where the logarithmic slope is $\alpha = 0.3361 \pm 0.0026$ and the normalization at a cluster mass of $10^{15}\,M_\odot$ is $\sigma_{15} = 1082.9 \pm 4.0$ km s^{-1}. The dark matter halo velocity dispersion is related to the velocity dispersion of galaxies by the velocity bias, $b_v = \sigma_{\rm gal}/\sigma_{\rm DM}$. The current best estimate is $\langle b_v \rangle = 1.00 \pm 0.05$ (Sifon et al., 2012). We assume the non-bias case of $b_v = 1$, as done in previous cluster studies (e.g., Brodwin et al., 2010; Sifon et al., 2012). From the derived mass, we can compute the related r_{200} value for each cluster. The results of the dynamical mass and radius using this method are listed in Table 2.6.

The results for the cluster masses using the two methods agree within errors; however, the masses derived using the virial theorem are $\sim 50\%$ larger than those found using the dark matter scaling relation. Carlberg et al. (1996) found that masses measured using the virial theorem are dependent on the boundary within which the cluster properties are determined and should be corrected with a surface pressure term, which requires a knowledge of the mass profile of the cluster. For cases where only the interior of the cluster's profile is being measured with no surface pressure correction, as is the case here, they found that the overestimation of the cluster mass

Table 2.6 Dynamical Properties of the Component Clusters Found with Two Different Methods from Spectroscopic Velocity Dispersions

	Carlberg et al. (1997) Method		Evrard et al. (2008) Method	
	r_{200} (Mpc)	M_{200} (10^{14} $M_\odot$)	r_{200} (Mpc)	M_{200} (10^{14} $M_\odot$)
A	1.82 ± 0.35	18.4 ± 10.7	1.58 ± 0.30	11.9 ± 6.9
B	1.75 ± 0.55	16.2 ± 15.5	1.51 ± 0.48	10.5 ± 10.0
C	1.08 ± 0.27	3.8 ± 2.9	0.94 ± 0.24	2.5 ± 1.9

should be less than 50%.

With this in mind, and the results for the mass and virial radius found using the method of Evrard et al. (2008) being $\sim 50\%$ lower than those found with the virial theorem, we estimate that the masses of the clusters are closer to those calculated using the dark matter scaling relation. However, as the velocity dispersion measured for Cluster B is based on only nine spectroscopic galaxy redshifts it, along with the resulting cluster properties, must be corroborated with the values determined for this cluster from additional supporting data before it can be deemed as a reliable estimate. In the following section we compare the cluster parameters found using the spectroscopic data to estimates from multiwavelength data.

2.4.5 Comparison with Other Mass Estimators

We can compare our results for the velocity dispersions and mass estimates of the three clusters to those found by other methods where available. We use the X-ray temperatures reported in Hicks et al. (2008) and the σ–T_X relation from Xue & Wu (2000) of $\sigma = 10^{2.49\pm0.02}\, T_X^{0.65\pm0.03}$ to predict the velocity dispersions of the three clusters. The cluster masses extrapolated directly from the X-ray data are also available. Jee et al. (2011) calculated weak lensing values for Cluster A from *Hubble Space Telescope* (*HST*) ACS/WFC data. Using an SZ scaling relation, Gralla et al. (2011) found an M_{500} value for Cluster A of $\sim 0.5\times$ the X-ray derived $M_{500,X}$ value.

Table 2.7 Dynamical Properties from Multiwavelength Data

	X-Ray[a]			Weak Lensing[b]		
	T_X	$M_{200,X}$	σ	σ	r_{200}	M_{200}
	keV	($10^{14}\ M_\odot$)	(km s^{-1})	(km s^{-1})	(Mpc)	($10^{14}\ M_\odot$)
A	$6.2^{+0.9}_{-0.8}$	$6.4^{+1.0}_{-0.9}$	1012^{+107}_{-97}	898^{+67}_{-71}	$1.22^{+0.15}_{-0.13}$	$5.8^{+2.3}_{-1.6}$
B	5.9^{+2}_{-1}	$4.7^{+0.9}_{-1.4}$	980^{+102}_{-93}	...	...	...
C	6.5^{+1}_{-1}	$5.1^{+0.8}_{-0.8}$	1043^{+112}_{-101}	...	...	...

[a] X-ray mass estimates ($M_{200,X}$) were extrapolated to r_{200} by Gilbank et al. (2008a). We use the X-ray temperatures reported in Hicks et al. (2008) and the σ–T_X relation from Xue & Wu (2000) of $\sigma = 10^{2.49\pm0.02}\, T_X^{0.65\pm0.03}$ to predict the velocity dispersions of the three clusters.

[b] Parameters are derived through weak lensing analysis of *HST* ACS/WFC data by Jee et al. (2011) and not through dynamical methods.

They noted that the SZ derived masses are lower than those previously published for a number of the clusters in their sample from various multiwavelength methods and therefore we do not include the SZ mass estimate for Cluster A in our discussion. Table 2.7 lists the known multiwavelength measurements of the masses and velocity dispersions of the three cluster cores.

The velocity dispersions measured from the spectroscopic data and those predicted from the X-ray temperatures agree well within errors for Clusters A and B. The values for Cluster C are less consistent, varying by about 1.5σ between the two values. This would suggest that the dynamical mass estimates based on the measured velocity dispersions should be reasonable, even for Cluster B with its low spectroscopic galaxy numbers. In fact, the dynamical masses measured using the Carlberg et al. (1997) virial mass method, which is known to overestimate the cluster mass by up to 50% (Carlberg et al., 1996), overestimates the X-ray extrapolated mass by only 1.12σ and 0.74σ for A and B and underestimates the mass by 0.45σ for Cluster C from the dynamical mass errors only. The masses estimated using the dark matter scaling relation of Evrard et al. (2008) are all consistent with the X-ray masses, which are also based on a scaling relation to extrapolate the mass based on the temperature of the cluster cores (Hicks et al., 2008). The X-ray data therefore confirm that the dynamical properties found from the spectroscopic data using the Evrard et al. (2008) dark matter scaling relation, with their large errors, are reasonable estimates for the cluster cores' mass and radius. For Cluster A, the velocity dispersion found from the weak lensing analysis is lower than that found using the spectroscopic and X-ray data, though just consistent within errors of the two measurements. The weak lensing mass estimate is consistent with both dynamical mass estimates as well as with the X-ray mass.

In an effort to resolve the proper mass estimates of our cluster cores, we look at the possible sources of error for the different mass estimates. White et al. (2010) used simulated clusters to test the effect of the line-of-sight on various cluster mass indicators, including richness, weak lensing and velocity dispersion. They found that the distributions of velocity dispersions measured from 10 000 randomly selected lines-of-sight on the same clusters were significantly non-Gaussian due to the triaxial shape of clusters and the anisotropic nature of infall. This results in a ∼40% inferred error on the mass estimate where $M \propto \sigma^3$, as is the case for both the virial theorem method (Equation 2.1) and the dark matter scaling relation (Equation 2.3).

Using the spectroscopically measured velocity dispersion of a cluster to estimate the cluster mass can also introduce biases if the cluster is in the process of accreting a large group or is not in a relaxed state. A non-Gaussian distribution of velocities, as we see in Cluster B (middle panels, Figure 2.7), can be an indicator of this non-virialized condition (Girardi & Biviano, 2004). In their simulated clusters, White et al. (2010) saw this effect by tracing halos as they fell into larger hosts and witnessing that the subhalos and even groups of subhalos retained their association for several gigayears, causing the host structure to lose its virialization.

The X-ray data can provide insight into the possibility of merging activity in the cluster cores. There is evidence in the X-ray data that Cluster B may contain significant substructure or have undergone a recent merger, as the peak of the X-ray emission is not consistent with the center of the extended X-ray emission (see Figure 1 in Hicks et al., 2008). The X-ray data for Cluster A also seem to indicate the presence of some possible substructure in the radial surface brightness profile, but not enough to show evidence of a significant merger or verify if the population we are sampling is virialized or not (see Figure 2 in Hicks et al., 2008). Both methods used to find the mass of the clusters in RCS 2319+00 from the spectroscopic velocity dispersions assume a virialized population, with Evrard et al. (2008) noting that only ∼10% of their simulated clusters, used to constrain the dark matter scaling relation, were strongly interacting, unrelaxed systems.

Systematic errors in the X-ray mass may also exist. Rasia et al. (2006) used high resolution hydrodynamical solutions to test the systematic errors associated with X-ray mass estimates of clusters. They found that the isothermal β–model, which was used by Hicks et al. (2008) to determine the X-ray masses of the member clusters in the RCS 2319+00 supercluster, can underestimate the cluster mass by up to ∼40%. This is due to the gas density profile of the cluster not being sufficiently characterized by the β–model and from possible errors in fitting the model parameters.

If the X-ray derived masses are indeed underestimated by up to ∼40% and the velocity dispersions from the spectroscopic redshifts overestimate the mass by up to ∼40% then the two methods of cluster mass determination would agree more strongly within errors for Clusters A and B and the true cluster masses would lie at ~ 8 and $\sim 6 \times 10^{14}\ M_\odot$ respectively. As we suspect that there is significant substructure present in Clusters A and B, with recent and ongoing merger activity, the velocity dispersion derived estimates for those clusters are likely to be overestimates.

This estimate for Cluster A is also consistent with the highest end of the weak lensing mass estimate range for Cluster A. Of the estimators we have available, White et al. (2010) found that the correlation to mass is tighter for weak lensing, followed by velocity dispersion, so we take the $\sim 8 \times 10^{14}\ M_\odot$ estimate, which is enclosed within both the weak lensing and velocity dispersion methods, as a reasonable value.

For Cluster C, whose X-ray and spectroscopically derived masses agree within errors but with the X-ray velocity dispersion seemingly overestimating the spectroscopic dispersion by $\sim 45\%$, we use an estimate of $\sim 3 \times 10^{14}\ M_\odot$, averaged between the two velocity dispersion estimates. Therefore, from the multiwavelength data currently available we estimate the masses of the three clusters to be $\sim 8, \sim 6$ and $\sim 3 \times 10^{14}\ M_\odot$ for Clusters A, B and C, respectively, or a range of $\sim 10^{14.5}$–$10^{14.9}\ M_\odot$.

2.5 Summary of the Spectroscopic Campaign

In this chapter we have outlined the results of an extensive spectroscopic campaign to map out the substructure of the RCS 2319+00 supercluster at $z \sim 0.9$. The following summarizes the results of the redshift survey.

- From 1961 good confidence spectroscopic galaxy redshifts in a 35×35 arcmin region around the three main component clusters of the supercluster, we have found 302 structure members in a redshift range of $0.858 \leq z \leq 0.946$.

- The three clusters were found to lie at redshifts of 0.901, 0.905, and 0.905, a separation of only 630 $\mathrm{km\,s^{-1}}$. Combined with the ≤ 3 Mpc transverse separation of each component cluster to its nearest neighbour, the three clusters of RCS 2319+00 represent the most compact supercluster found to date at this redshift.

- Three distinct walls in redshift space are apparent in the spectroscopic data, with the main supercluster peak surrounded by lower and higher redshift walls separated by ~65 Mpc ($\Delta z \sim 0.03$).

We attempt to measure accurate velocity dispersions from the spectroscopically confirmed galaxies for the three main cluster components with the aim of determining the mass of each cluster.

- *Cluster A*: from 23 spectroscopically confirmed galaxies within 1 Mpc of the cluster center, we find a velocity dispersion of 1202 ± 233 km s^{-1}. This results in a dynamical cluster mass of $\sim 10^{15} M_{\odot}$, consistent within errors with the lower mass estimates from the X-ray and weak lensing data of $\sim 8 \times 10^{14} M_{\odot}$.
- *Cluster B*: there are not enough cluster members left within 1 Mpc of the cluster center after interloper clipping to calculate a reliable velocity dispersion and we looked to the X-ray data to corroborate our dynamically derived properties. The X-ray predicted velocity dispersion is consistent with the measured spectroscopic value of 1154 ± 367 km s^{-1} and the resulting dynamical mass is consistent with the X-ray mass of $5.9 \times 10^{14} M_{\odot}$.
- *Cluster C*: we believe that this cluster is in a relaxed state and that our measured velocity dispersion of 714 ± 180 km s^{-1} and mass estimate of 2.5–$3.8 \times 10^{14} M_{\odot}$ is accurate.

The large spectroscopic redshift catalogue compiled here provides a basis for the research that follows in this thesis as well as concurrent studies by collaborators. Searches for substructure in the RCS 2319+00 supercluster, performed in Chapter 3, are based on the spectroscopically confirmed supercluster member list. In Chapter 4, we study the stellar mass and star formation of supercluster members and in Chapter 5 we look at the possible fate of these galaxies. The overall redshift catalogue is used in Appendix A in the search for foreground and background structures.

Chapter 3

Mapping the Substructure of the Supercluster

The following chapter is based on:

The structure of the merging RCS 231953+00 supercluster at $z \sim 0.9$

A.J. Faloon, T.M.A. Webb, E. Ellingson, R. Yan, D.G. Gilbank, J.E. Geach, A.G. Noble, L.F. Barrientos, H.K.C. Yee, M. Gladders and J. Richard, 2013, ApJ, 768, 104

3.1 Introduction

The following chapter uses the spectroscopic member catalogue defined in Chapter 2 to map out the substructure of the RCS 2319+00 supercluster. We endeavour to divide the confirmed supercluster members into regions of various densities within the field from the densest cluster cores through to group densities and the individual, infalling galaxies. We trace the substructure of the supercluster in Section 3.2 using two methods, testing our structure finding method with Monte Carlo simulations and against the Millennium Simulation light cones. The recovered structure is used to investigate the colour-magnitude relation and galaxy colour distribution in different density environments in Section 3.3. In Section 3.4 we attempt to place constraints on the masses of the potential infalling groups and put them in context with current theories of group infall in clusters. In Section 3.5 we summarize the main results from the chapter.

3.2 The Substructure of the RCS 2319+00 Supercluster

Due to the close proximity of the three cluster cores, both in angular separation and redshift space, designating galaxies as unique members of one of the particular cluster cores is difficult, as seen in Figure 2.4. We therefore chose to study the cluster member properties as a function of their distribution within the overall structure and their apparent local density environment within the supercluster. The spectroscopically confirmed members have allowed us to begin tracing the supercluster structure and identifying spatial and dynamical sub-environments within it.

3.2.1 The Dressler–Shectman Test for Substructure

As an initial trial to identify the distribution of the underlying structure in the RCS 2319+00 supercluster field we performed the Dressler & Shectman (1988, DS) test. The DS test looks for inconsistency between the locally measured velocity dispersion and velocity mean with the parameters measured over the whole structure field. Deviations from the global velocity parameters of the cluster indicate the likely presence of substructure. The DS test was used with the RCS 2319+00 data to begin tracing the locations of possible groups and filaments within the supercluster before attempting to assign specific galaxies to these potential groups. We follow Dressler & Shectman (1988) to compute, for each galaxy in our structure, the deviation δ from the global mean as

$$\delta^2 = \left(\frac{1+N_{\mathrm{nn}}}{\sigma^2}\right)\left[(\bar{v}_{\mathrm{local}} - \bar{v})^2 + (\sigma_{\mathrm{local}} - \sigma)^2\right], \tag{3.1}$$

where N_{nn} is the number of nearest neighbours used to compute the local variables. We use 10 nearest neighbours, as done by Dressler & Shectman (1988) in their cluster study. The Δ statistic is defined as the sum of all deviations δ_i and a cluster is said to have substructure if $\Delta/N_{\mathrm{members}} > 1$.

To test for false positives, we shuffle the redshifts between galaxy positions and perform 25000 Monte Carlo (MC) tests. If the substructure detected in the real data is indicative of true substructure, then the probability that the shuffled data gave a higher Δ statistic than the real data will be low. The probability of false structure detection is

$$P = \frac{N(\Delta_{\mathrm{shuffle}} > \Delta_{\mathrm{real}})}{N_{\mathrm{shuffle}}}, \tag{3.2}$$

where N_{shuffle} is the number of MC shuffling tests performed.

The DS test was done both on the full redshift range of our larger structures and on the three separate redshift walls with ranges of ± 2000 km s^{-1} for each to avoid significant overlap. For the full redshift range, we find $\Delta/N_{\mathrm{members}} = 2.02$, while the three redshift peaks yield values of $\Delta/N_{\mathrm{members}} = 2.00, 2.76$ and 2.64 for the redshift walls centered on $z \sim 0.87, 0.90$, and 0.93, indicating the presence of substructure in each case. The MC shuffled tests find P-values of < 0.006 for the full redshift range, and <0.05, 0.0002 and 0.003 for the three separate redshift walls, leading us to believe there is real substructure in each of the redshift peaks in our supercluster field and prompting a search for the specific sub-environments within our spectroscopic galaxy catalogue in the following sections.

The results of the test for the lower and central-redshift walls are shown in Figure 3.1 in DS test bubble diagrams, with each galaxy represented by a circle whose size scales with e^{δ} for that galaxy. The three cluster cores are indicated by the 1 Mpc radius dashed circles on the each of the panels. Though the highest redshift slice has a high $\Delta/N_{\mathrm{members}}$ of 2.64, it has the lowest number of galaxies, causing the 10 nearest neighbours to be spread over a large region in most cases and so we do not find any evidence of substructure in concentrated regions.

In the $z \sim 0.87$ redshift slice, we find that both Clusters B and C show deviations

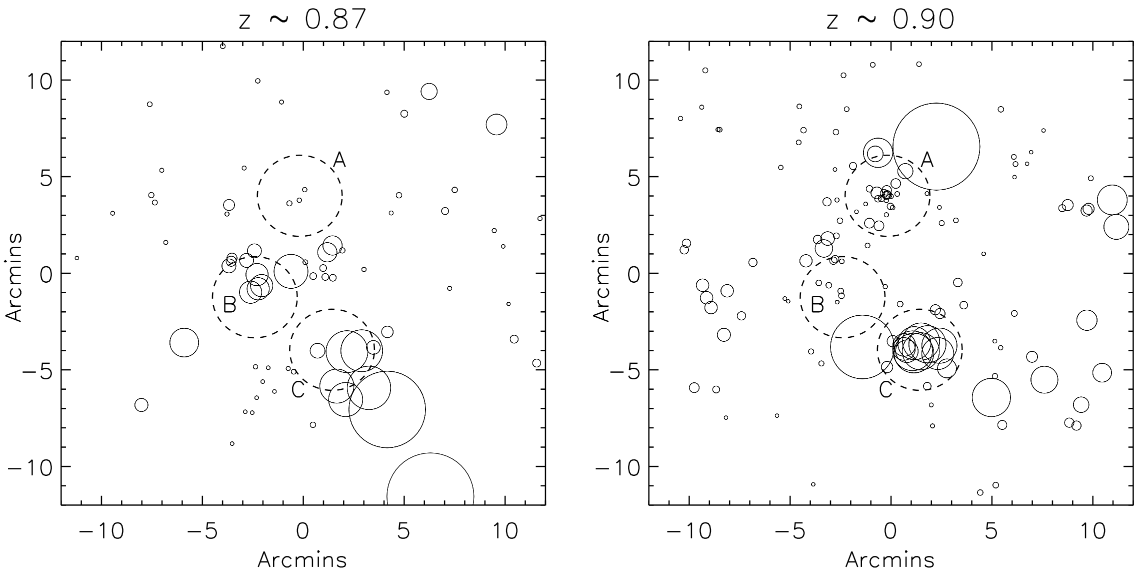

Figure 3.1 DS test bubble diagrams with each galaxy in our structure catalogue denoted by a circle whose radius scales with e^{δ}. Dashed circles show the 1 Mpc radius around each cluster center. Results from the DS test on the ± 2000 km s^{-1} region around the lower $z \sim 0.87$ redshift wall (left) and the $z \sim 0.9$ redshift structure (right).

from the overall mean parameters, with substructure extending from the centers of both cluster core positions. Deviations are found to extend from the center of Cluster B slightly to the northeast as well as a more elongated deviation northwest towards the middle of the three clusters. These areas of broad redshift distribution can be seen in the top panel of the velocity versus radius plot in Figure 2.4 as a wide grouping of galaxies, both in radius and velocity, $\sim$ 1.5–2.5 Mpc from the center of Cluster A. Whether the deviations that extend in the two directions outward from Cluster B belong to the same substructure or to separate overdensities in the supercluster will be explored in the following section. In Cluster C, evidence of substructure is shown to extend southwest of the cluster core, with the largest deviations from the mean present in this region.

The redshift slice around $z \sim 0.9$ also shows indications of substructure in the area of Cluster C, though in a more concentrated region and with lower deviation than seen in this cluster in the lower redshift slice. There are also regions of potential substructure east of Cluster B and west of Clusters A and C. An interesting area to note is the region between Clusters A and B, where there seems to be some evidence of substructure consistent with a previously confirmed infrared bright filament found in the *Herschel* 250-500 μm Spectral and Photometric Imaging REceiver (SPIRE) map by Coppin et al. (2012). The complementary detection of this structure in the IR provides support for our claim of a substructure detection in this area.

Both Clusters B and C were seen to show two redshift peaks in Figure 2.7 within the central 1 Mpc around the clusters, one in each of the lower and middle redshift slices. For Cluster B, the signs of deviation from the mean parameters in the core region in the lower redshift wall at $z \sim 0.87$ in contrast to the lack of deviation in the DS test of the central, overall supercluster redshift slice around $z \sim 0.9$ give further evidence that the cluster core lies in the higher $z \sim 0.9$ redshift slice since we expect cluster core galaxies to show little deviation from the mean parameters. In the case of Cluster C, the DS test on both redshift slices show signs of substructure emanating from the center, with the larger deviations present in the lower redshift slice. In Section 2.4.2 we motivated the choice of the $z \sim 0.9$ peak in the Cluster C plot of Figure 2.7 as the one corresponding to the cluster core given its agreement with both the spectroscopically confirmed BCG and the distribution of the red-sequence galaxies significance contours. The deviations seen in the core of Cluster C in this redshift slice could therefore be an indication that there is a line-of-sight group falling towards the cluster core (Einasto et al., 2012; Pinkney et al., 1996). The following search for individual groups will explore this possibility in more detail.

3.2.2 Friends-of-Friends Search for Substructure in RCS 2319+00

The distribution of possible substructure in our supercluster field found with the DS test lead us to attempt to recover the substructure in a more tangible way. We used a modified friends-of-friends (FOF) algorithm (Huchra & Geller, 1982) with linking lengths of D_L and V_L, representing distance and velocity separations, to identify associations of three or more linked galaxies. Briefly, the algorithm uses each of our spectroscopically confirmed cluster members and searches for friends within the two linking lengths. The test galaxy and its friends are removed from the main source list, and each friend is then tested against the remaining galaxies in the list. This is done iteratively until there are no new friends found. If the final candidate friends list has three or more members then it is considered an FOF association, or else the galaxies are returned to the isolated galaxy list. We chose three member associations to compensate for the incompleteness of the spectroscopic data in an effort to identify regions that may be undersampled spectroscopically but still contain signs of structure. MC simulations are performed in Section 3.2.3 to help determine the membership number above which we believe the FOF associations are tracing real structures.

The linking lengths were determined through trial and error, with the aim of recovering structure while not linking all three cluster cores together. MC simulations (Section 3.2.3) and Millennium Simulation data (Section 3.2.4) were also used to test the FOF linking lengths, again to ensure that linking lengths were large enough to recover structure while not linking broad redshift walls across the test region. A more thorough method of determining the linking lengths would have been to construct a mock catalogue from N-body simulations to test our linking lengths based on completeness and recovery purity, as done by Farrens et al. (2011) in their search for groups and clusters in the 2SLAQ catalogue (2dF-SDSS Large Red Galaxy and

QSO survey). However, a search of the existing Millennium simulation light cones (Lemson & the Virgo Consortium, 2006) for a similar structure to the RCS 2319+00 supercluster did not yield any comparable structures and attempting to model this superstructure with our own simulations falls outside the scope of this thesis. Instead, we use three individual large clusters found at $z \sim 0.9$ in the Millennium Simulation light cones (see Section 3.2.4 for details).

We found that the spatial linking length, D_L, was more influential in linking all three cluster cores as each cluster is separated by <3 Mpc from its nearest neighbour and D_L was thus limited to 0.5 Mpc. The velocity separation, V_L, had more subtle effects on the group recovery rate and membership. We tested several different velocity separations, from 600 to 1500 km s^{-1} ($\sim$ 2–5× our spectroscopic redshift error of $\Delta z = 0.002$). For the lowest velocity separations, the core groups of the clusters are recovered as several separate, small groups, even for members of the prominent peak in Cluster C. We found that in our real data and MC tests (Section 3.2.3) the difference in group recovery between V_L lengths of 1000 and 1500 km s^{-1} were minimal, recovering the same groups on average, with only one or two members missing from two of the larger groups. Since we suspect recent merger activity is present in some regions of the supercluster field and therefore expect our substructures may not be virialized, we choose to use the larger linking length of 1500 km s^{-1} to look for extended structures.

One limitation of the FOF method would be in the case where substructure is collapsing and deviates from the Hubble flow with two or more substructures falling along the same line of sight with infalling galaxies having large relative velocities that overlap in redshift space. If the difference in redshift between members on the outskirts of the line of sight structures is small enough, i.e., within the 1500 km s^{-1} linking length, and fall within 0.5 Mpc on the sky, then the structures would be

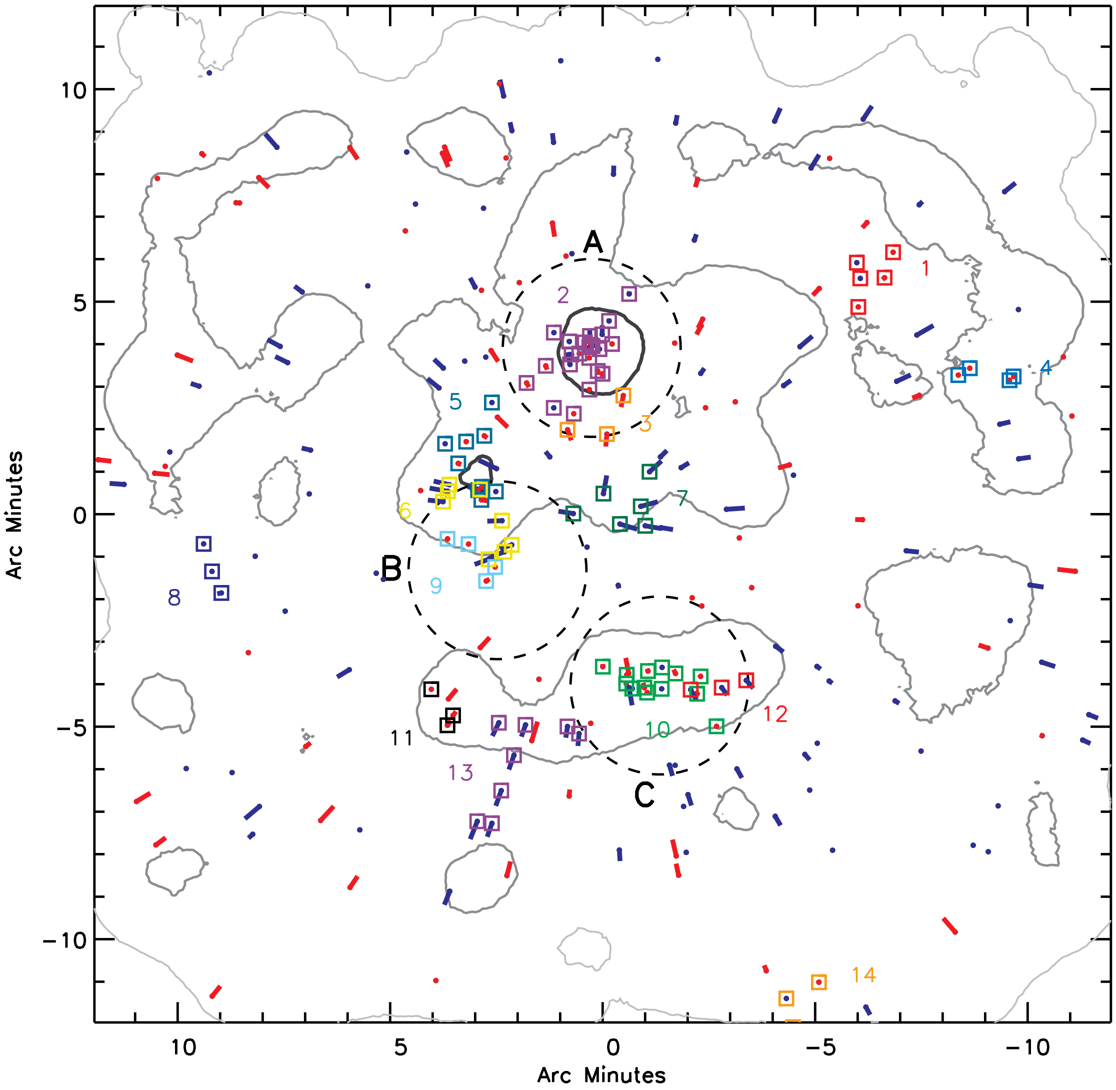

Figure 3.2 Friends-of-friends associations identified with the linking lengths of 0.5 Mpc and 1500 km s^{-1} are surrounded by like-coloured boxes. Red and blue arrows represent redshifted/blueshifted velocities of spectroscopically identified cluster members relative to a midpoint redshift of 0.897 in the $0.858 \leq z \leq 0.946$ range and directed toward an arbitrary center position. Dotted circles represent 1 Mpc radii around the X-ray centers of the three cluster cores. Gray contours show the spectroscopic target density relative to the full optical source catalogue, with higher target densities having thicker, darker gray contours (i.e. the ∼0.5 Mpc region around Cluster A is a high target density region).

identified as a single structure. In this case, plots of the relative velocity versus angular separation would aid in identifying line of sight structures.

Figure 3.2 shows the results of the friends-of-friends test using the linking lengths of 0.5 Mpc and 1500 km s^{-1}, with linked FOF associations identified by same coloured boxes. The red and blue lines on the plot indicate all supercluster member positions with the colour and length of the lines representative of the relative velocity of the galaxies to a median redshift of z=0.897. The lines are oriented arbitrarily towards a center position on the plot, with the galaxy located at the end pointing towards the center for blue-shifted galaxies and at the end pointing away from the center for red-shifted galaxies. This was done to retain some redshift information in order to better visualize the layout of the FOF associations within supercluster field. The gray contours represent the smoothed spectroscopic target density relative to the full optical catalogue, with the higher target densities having darker, thicker contours.

Due to an incomplete spectroscopic sample, some of our isolated superstructure 'field' galaxies may in fact belong to infalling groups or filaments. We note, however, that FOF associations are still found in regions of lower spectroscopic density and some high target density regions contain few cluster members and no FOF associations. As such we do not suspect that our recovered structure is simply tracing the areas of high spectroscopic targeting. We identify 14 FOF associations, with 7 having more than three members. Figure 3.3 shows the number of groups for each membership number (hatched histogram).

3.2.3 Monte Carlo Simulations

To test the veracity of our group finding method and look for spurious groups in our identified FOF associations we performed MC simulations. All 1961 confident galaxy redshifts were first randomly shuffled between their positions and then the new supercluster field members in the redshift range of $0.858 < z < 0.946$ were selected, now with their new positions. We then performed the same FOF test as done on our non-shuffled data. This was repeated 1000 times and the average number

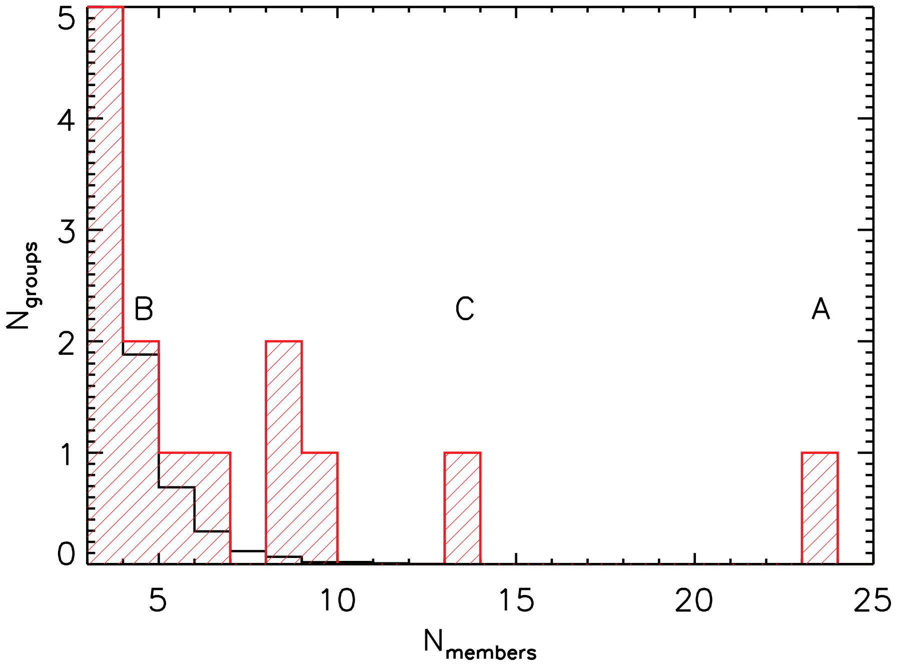

Figure 3.3 Number of FOF associations found for each membership bin for the real supercluster data (red hatched histogram) and the MC test data described in Section 3.2.3 (averaged over all tests – black outlined histogram) recovered using the FOF method. The letters indicate the bins in which the groups corresponding to the three cluster cores are found.

of FOF associations and membership number per association was compared with our real data.

The average number of FOF associations returned in the MC tests was 8.8, compared to the 14 recovered overdensities in the real data. Figure 3.3 shows the number of FOF associations in each membership bin for the real data (red hatched histogram) versus the average numbers over all shuffled MC tests (black outlined histogram). The bins containing the FOF associations identified as the main cluster cores (see Section 3.2.5 for details) are labeled with their corresponding cluster ID. This shows that larger FOF associations are recovered only in the real data, including the cores of clusters C and A at 13 and 23 members, but not in the randomly shuffled data, leading us to believe that FOF associations with ≥ 5 members are tracing real group and core structures. Also, since the positions of the spectroscopic sampling are consistent between the real data and the MC test data, we are not recovering large structures simply due to highly targeted regions.

3.2.4 Comparison with Millennium Simulation Data

In order to further test our friends-of-friends parameters we searched the Croton et al. (2006) semi-analytic catalogue of galaxies in the Millennium Simulation light cones (Lemson & the Virgo Consortium, 2006) for structures similar to the RCS 2319+00 supercluster. No such high mass, multiple cluster structures with small cluster separations were found at high redshift in the simulation data. Instead, we found three separate cluster halos with masses of 1.4-$2.7 \times 10^{14} M_{\odot}$ at $z = 0.94$, 0.89 and 0.92. Though these will not be representative of our superstructure, we aim to test if the FOF method employed on our data will recover the simulated clusters and their infalling structure.

For each of the three light cones we first shifted the catalogue so that the most massive halo was centered in a similar field of view as our real data, with the central cluster of each light cone positioned over one of the three real cluster cores. We then adjusted the redshift of each galaxy in the Millennium catalogues so that the cluster fell at a redshift of $z \sim 0.9$ and cut the catalogue down to the broad cluster membership range used for the RCS 2319+00 supercluster of $0.858 \leq z \leq 0.946$. In order to simulate our spectroscopic coverage, we applied a magnitude filter according to the magnitude distribution of our real cluster members before running the new, reduced catalogue of cluster members through the FOF algorithm. This was repeated 100 times for each of the three light cones.

We found that, though we recover groups at the positions of massive halos in the simulated light cones, when we trace each member galaxy back to its parent halo, we

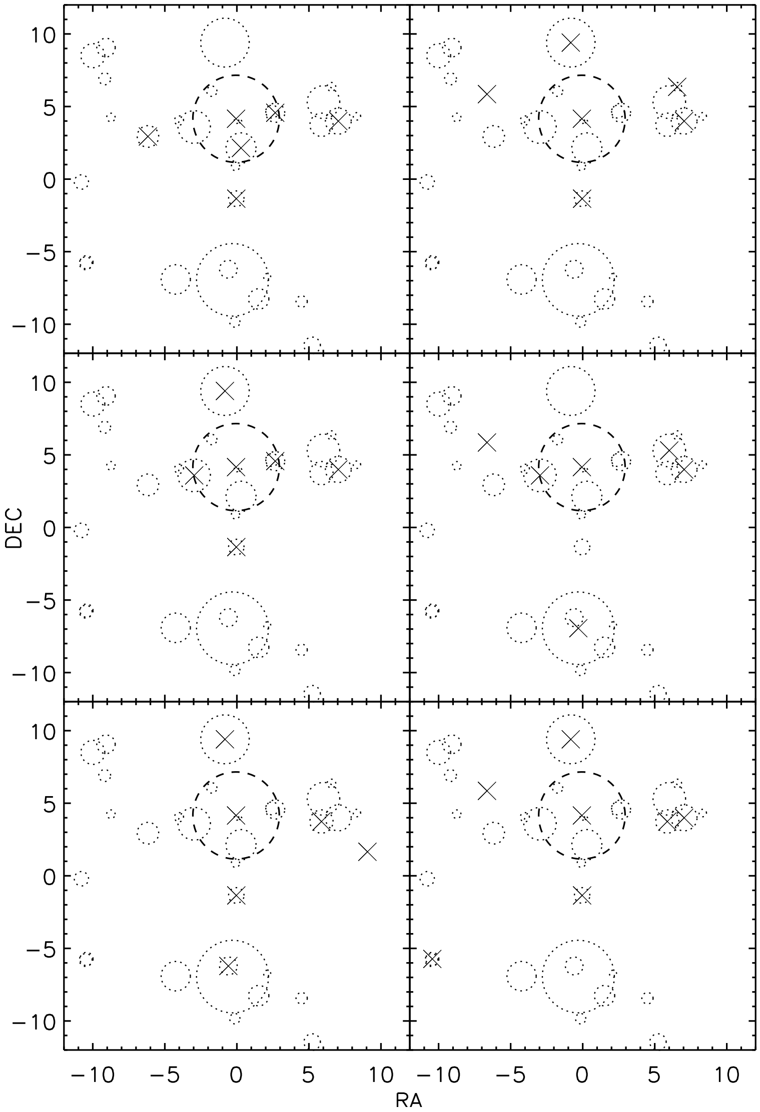

Figure 3.4 Plot of the halo positions in data from a Millennium Simulation light cone with the main cluster halo identified by the dashed circle and all other halos having ≥ 5 members plotted as dotted circles, increasing in size with increasing halo mass. The X's mark the position of FOF recovered groups using reduced samples of halo galaxies magnitude–filtered to simulate the real spectroscopic cluster member sampling. Recovered groups not centered on a visible halo have been identified with halos having < 5 member galaxies.).

find that members from a mixture of halos are recovered as belonging to the same group. This was also seen by Farrens et al. (2011) in their FOF tests on their mock 2SLAQ simulation. As they have done, we have assigned the recovered group the identification of the halo with the most number of recovered members, which in all cases was also the most massive. Where there are no repeated halo members within a recovered group, we have assigned the identification of the most massive halo in the region of the recovered group, with preference going to halos with at least one recovered member. This ability to recover the position but not the unique members of the massive halos may be an example of the subhalos retaining their identity long after falling into the more massive host halos, as seen by White et al. (2010).

Using our FOF linking lengths of 0.5 Mpc and 1500 km s^{-1} with the halo identification method described above, we were able to recover the most massive halo in ∼83% of the tests for all three light cones. Halos with masses $> 10^{13}\ M_{\odot}$ were recovered in ∼59% of the tests on average. A sample of the results from the light cone data of the most massive halo is shown in Figure 3.4 with the group sized halos in the catalogue plotted with dotted circles of increasing size for increasing halo mass. The main cluster is plotted with the dashed circles. The positions of recovered FOF associations in each test are shown with X marks. From these tests we believe that, though we may associate multiple halos as single groups in our real data, we are identifying areas of real substructure.

3.2.5 Recovered Structures in the RCS 2319+00 Supercluster Field

Taking into account the results of the MC simulations, we designate all FOF associations with ≥ 5 members recovered from the FOF test on our real data as a lower estimate on the true substructure of the RCS 2319+00 supercluster, noting that the simulations show the possibility that one of the recovered 5-8 member groups may still be a spurious detection (see Figure 3.3).

Several structural features are immediately discernible in Figure 3.2. The cluster cores all comprise groups that seem to extend in an elongated fashion pointing to the neighbouring core, with 23 and 13 members in the core groups in Clusters A and C.

This alignment towards the nearest cluster neighbour was previously observed in the red-sequence galaxy overdensity plots (see Figure 2.6). The galaxies in the core group of Cluster A (Group 2) span a redshift range of ∼6000 km s^{-1} and have a dispersion of 1404 ± 249 km s^{-1}, with no interloper clipping. This is slightly higher, though within errors, than the dispersion we calculated in Section 2.4.3 from the spatial distribution and interloper clipping. In Cluster C, the main core group (Group 10) contains galaxies spanning ∼960 km s^{-1} with an estimated dispersion of 722 ± 182 km s^{-1}, very close to the dispersion calculated in Section 2.4.3 with interloper clipping.

Figure 3.5 shows the relative velocity of the galaxies in groups from the average redshift of Cluster A as a function of the spatial distance from Cluster A, with the identified ≥ 5 member groups highlighted against all confirmed members. The numbers and colours plotted for each group correspond to the same numbers and colours as Figure 3.2. The top panel highlights the groups consistent with the spatial centers of the cluster cores and shows that the core group of Cluster A is elongated in velocity space as well as in its spatial distribution, while the core group of Cluster C is more tightly bound. The lower redshift galaxies in the core group of Cluster A may be interlopers from the lower redshift structure, from which they seem to extend.

Once again, Cluster B presents some difficulties. The two redshift peaks that were apparent in Figure 2.7 fall into two separate groups with eight members at an average redshift of 0.870 and four members in a group ∼5700 km s^{-1} away at $z = 0.906$. Again, we suspect that more galaxies belong to the higher redshift group in this core, corresponding to the red-sequence density, X-ray contours and BCG, that have yet to be targeted with spectroscopy. Figure 3.5 again shows that the smaller group in Cluster B (Group 9) lies along the same velocity space as Clusters A and B. It can also be seen in Figure 3.2 that this higher redshift group falls in the region of lower spectroscopic target density. In light of this, we assign the four-member

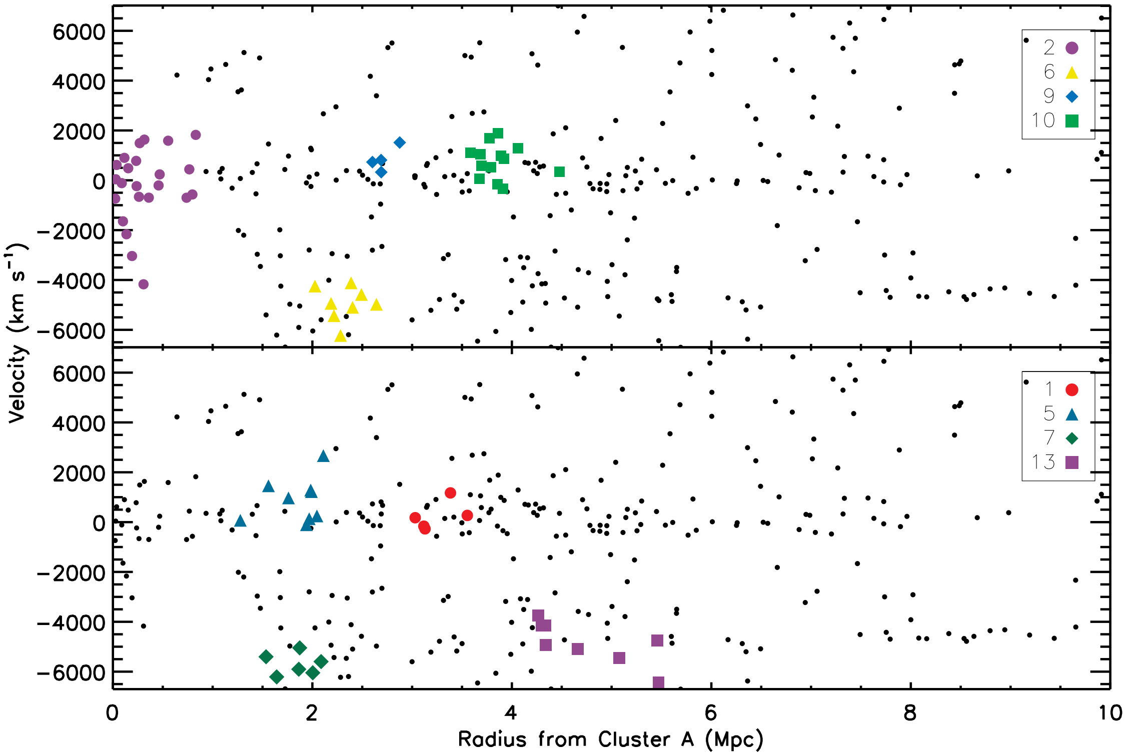

Figure 3.5 Velocity vs. radius for all confirmed cluster members in the RCS 2319+00 supercluster relative to Cluster A. Top panel: groups that correspond to the spatial positions of the three cluster cores are highlighted: Cluster A - Group 2, Cluster B - Groups 6 and 9, Cluster C - Group 10. The two groups near the spatial center of Cluster B lie on two of the distinct redshift walls that extend through the supercluster region. We assign Group 4 as the cluster core as it falls along the same velocity space as the two other cluster cores and corresponds to the red-sequence peak redshift in this region. Bottom panel: groups having ≥5 members outside of the cluster cores are highlighted. Two larger groups are seen to be potentially falling into the cluster from the lower redshift peak. The filamentary structure between Clusters B and C (Group 5) is shown to lie within the same redshift wall as the core groups.

Group 9 as the core group of Cluster B and the eight-member Group 6 is considered a potentially infalling group distinct from the core of the cluster. We attempt to correct for spectroscopic completeness in Section 3.4.

An interesting structure recovered through the FOF algorithm is an apparent nine-member filamentary structure (Group 5) stretching from Cluster B toward Cluster A, first hinted at in the results of the DS test around the $z \sim 0.90$ redshift wall

(Section 3.2.1, Figure 3.1). This structure has an average redshift of $z = 0.906$ with galaxies spanning $\sim$2800 km s^{-1} toward higher redshift (bottom panel, Figure 3.5). It corresponds well to the spatial position of the previously confirmed *Herschel* infrared bright filament that Coppin et al. (2012) found may be forming stars with an SFR $\simeq 900\,M_{\odot}$ yr^{-1} and building up significant stellar mass.

Other notable groups include a six-member group centered between the three component cluster cores (Group 7) as well as an eight-member filamentary group falling in toward Cluster C (Group 13). Both of these groups appear to be falling into the clusters from the lower redshift wall (bottom panel, Figure 3.5) and may represent infalling groups.

Comparing our recovered groups from the FOF method with the substructure detected with the DS test (see the DS test bubble diagram, Figure 3.1), we see that the central group (7), the filamentary structure (Group 5), and the eight-member group in the line of sight of Cluster B (Group 6) correspond to regions of deviation in the DS test. Cluster C has one large core group (Group 10), which is relatively compact in velocity space, and a small, three member FOF association (Group 12) found in the same line of sight. This small overdensity falls within the lower redshift wall and accounts for the deviation seen in the DS test of this redshift slice when tied with the other blueshifted galaxies seen southwest of the cluster core in Figure 3.2. This area and other areas of possible substructure in the DS test found to have small, 3–4 member overdensities with the FOF method (Groups 4 and 8), lack adequate members in the immediate area to confirm substructures. The addition of further spectroscopic redshifts may serve to confirm the DS substructures.

We find that of our 302 cluster members in the supercluster field $\sim$13% are found in the core cluster groups and $\sim$18% belong to the potential infalling groups. We note that these are rough estimates, since our supercluster 'field' galaxies may in fact be tied into groups given further spectroscopy. Areas of deviation from the global properties in the DS test that are not recovered with the FOF method may belong to structures whose linking members have not yet been confirmed spectroscopically, leaving them out of the FOF group list and currently identified as part of our superstructure 'field' population. Conversely, we may find a higher proportion of isolated galaxies given further spectroscopy. At low redshift Small et al. (1998) found that approximately one third of the galaxies associated with the Corona Borealis supercluster do not belong to the component clusters. At higher redshifts we would expect the number of galaxies in superclusters without specific cluster associations to increase as the clusters are less relaxed. This has already been seen by Gal et al. (2008) in their study of the structure of the CL1604 supercluster at $z \sim 0.9$, where they found that a large portion of galaxies were associated with the connecting large-scale filaments and not with the individual clusters and groups in their supercluster. As such, while we do expect that additional spectroscopically confirmed supercluster members will result in more discernible structures, the percentage of unassociated supercluster members will most likely remain high.

3.3 The Colour–Magnitude relation

A colour–magnitude relation (CMR) for elliptical field galaxies was first identified by Baum (1959), with bright ellipticals having redder colours then their fainter counterparts. In clusters, the CMR for early-type galaxies, the red-sequence, has been shown to have a tight, well-defined slope at low redshift (e.g., Visvanathan & Sandage, 1977; Bower et al., 1992; Lopez-Cruz et al., 2004) and the cluster cores are dominated by early-type galaxies (Dressler, 1980). At higher redshifts however, the dynamically younger clusters have shown an increasing scatter in their CMR and a deficit of red-sequence galaxies at the low-luminosity end of the slope (e.g., De Lucia et al., 2004b;

Tanaka et al., 2005; Mei et al., 2009; Lemaux et al., 2012). This is seen as a sign that the cluster red-sequence is still in the process of being built up at $z \sim 1$. Rudnick et al. (2012) propose that the lack of low-luminosity red-sequence galaxies may be due to the accretion of faint blue galaxies whose star-formation is suppressed in groups or in the cluster and experience mergers with other red-sequence galaxies, increasing their mass and moving them along the red-sequence. Recent studies of clusters at $z > 1$ differ over the basis for the scatter in the red-sequence at higher redshifts, with clusters at $z = 1.46$ and 1.62 found to be consistent with models of a single burst of star-formation (Hilton et al., 2009; Papovich et al., 2010, respectively) while more diverse star formation histories are needed to explain the width of the CMR in clusters at $1.0 < z < 1.5$ (Snyder et al., 2012).

3.3.1 Colour–Magnitude diagram

In this section we investigate the CMR in the RCS 2319+00 supercluster. The $R_c - z'$ versus z' colour–magnitude diagram for all spectroscopically confirmed galaxies within the supercluster redshift range of $0.858 \leq z \leq 0.946$ is shown in Figure 3.6, with the red-sequence slope at $z = 0.9$ (from Gilbank et al., 2008b) plotted for reference as a solid line, and dotted lines denoting ±0.2 mag from the red-sequence. The errors on the photometric catalogue range from 0.01 mag for the brightest galaxies, increasing to 0.62 mag for the faintest, $z' = 24.85$ mag cluster member and 0.73 mag for the faintest $R_c = 25.73$ mag member, with an average error of ~ 0.08 mag in both filters.

The two top panels of Figure 3.6 both show all of the spectroscopically confirmed RCS 2319+00 supercluster members plotted as black circles. The coloured symbols in each panel represent members of the identified groups from our FOF algorithm in Section 3.2. The numbers and colours plotted for each group corresponding to the same numbers and colours on the structure plot (Figure 3.2) separated into the

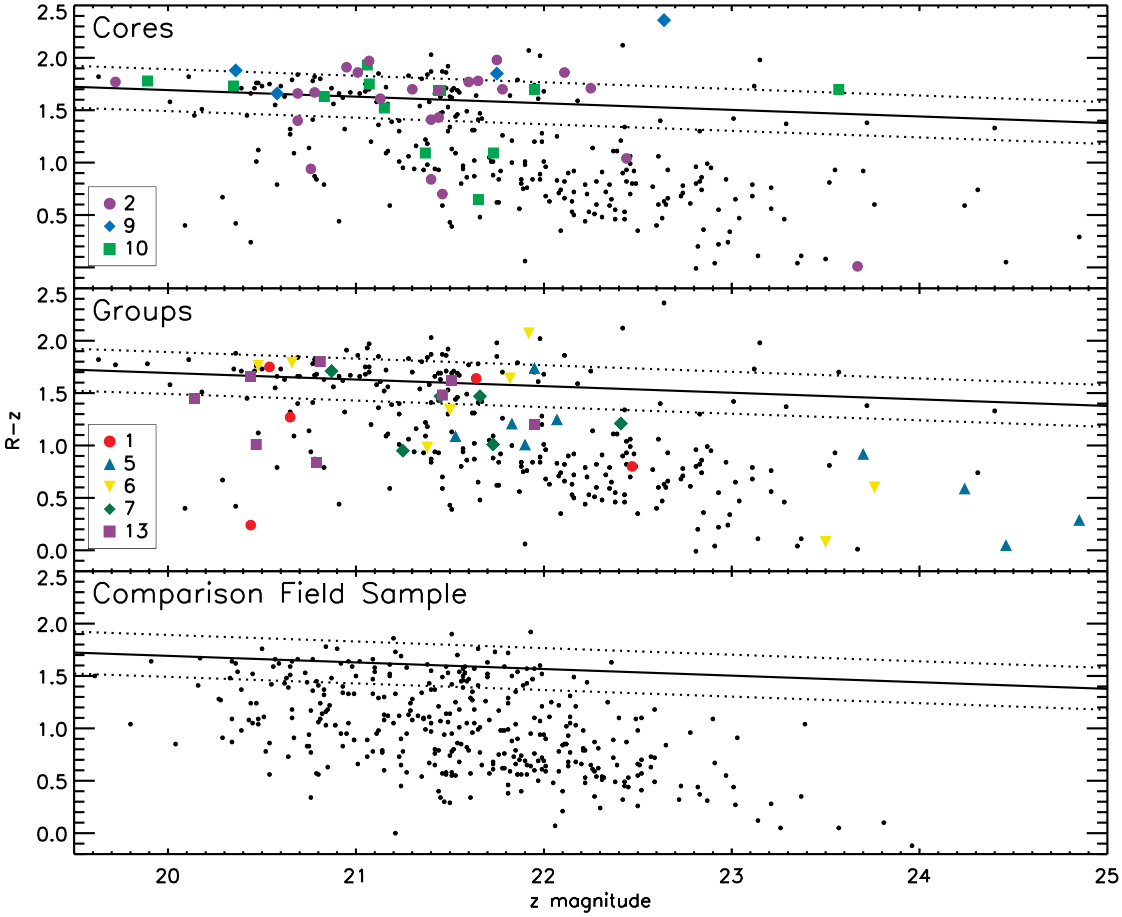

Figure 3.6 $R_c - z'$ vs. z' colour–magnitude diagram. Black points represent all spectroscopic galaxies in the redshift range $0.858 \leq z \leq 0.946$. The top two panels plot all members of the RCS 2319+00 structure with coloured symbols highlighting galaxies belonging to the numbered groups identified with the FOF algorithm as shown in Figure 3.2, divided into the core groups (top panel) and ≥ 5 member groups (middle panel). The bottom panel shows the comparison field sample from the large RCS IMACS spectroscopic campaign (R. Yan et al. 2012, in preparation). Lines represent the red-sequence slope at $z = 0.9$ (solid line; from Gilbank et al., 2008b) and ±0.2 mag of the red-sequence slope (dotted line). Note that no correction for redshift success has been applied to the colour–magnitude diagram.

two panels to highlight the cluster core groups (top panel) and the ≥ 5 member groups (middle panel). The bottom panel shows the colour–magnitude diagram of a comparison field sample, detailed below. It should be noted that the redshift success rate of the spectroscopic sample is a function of both the magnitude and colour for galaxies fainter than $z' \sim 22$ mag (see Figure 2.5), and is not accounted for in the colour–magnitude diagram. Faint blue galaxies have higher spectroscopic success rates in our data than faint red galaxies. This is due to the presence of more prominent emission lines, such as [OII]3727Å, in the bluer galaxies, which tend to be late-type galaxies (see Figure 1.1 for an example of early versus late-type galaxies) that are easier to identify in the low signal to noise data versus the harder to distinguish absorption features more common absorption features in the primarily early-type red galaxies.

Due to the incompleteness of our spectroscopic sample, we attempt a rough completeness correction when looking at the overall population distribution in the colour–magnitude diagram. Since the spectroscopic correction weights do not take into account the colour of the galaxies, we instead use the redshift success rates for bright ($z' \leq 22\,\mathrm{mag}$) and faint ($z' > 22\,\mathrm{mag}$) galaxies found in the right panel of Figure 2.5. We set the success rate of the bright galaxies conservatively at 70% from our 70%-80% redshift success rate for bright galaxies found in Section 2.3.2. For the faint galaxies, we define a colour cut at $R_c - z' = 1$ and find that bluer galaxies have a success of ∼50% while the redder galaxies have a redshift success of only ∼25%. We can use these rates to correct the faint galaxy numbers in Figure 3.6 up to the redshift success rate of the bright galaxies in order to better compare the populations. This is an oversimplification of the completeness correction, however it is sufficient given our small number statistics. Using all spectroscopic structure members corrected to the redshift success of bright galaxies and defining a rough limit for the red versus blue galaxies at –0.2 mag of the red-sequence line, we find 36%±3% of the galaxies are red and 64±4% of the structure members are blue galaxies, with Poisson errors.

We can compare these populations to the field in the same redshift range using a spectroscopic sample of galaxies derived from observations whose target cluster falls outside this redshift range in the RCS IMACS spectroscopic campaign (R. Yan et al. 2012, in preparation). We find 422 spectroscopically confirmed field galaxies that fit this criteria in the IMACS sample. The field sample is plotted in the bottom panel of Figure 3.6 with the red-sequence line again at $z = 0.9$ plotted for reference. Those galaxies populating the red-sequence make up only 18%±2% of the sample while the blue cloud is populated by 82%±4% of the comparison field sample. The limit on the depth of the spectroscopy is brighter for the field sample at $z' \sim 24\,\mathrm{mag}$ ($M_{z'} \sim -18.35$) compared to the limit of the RCS 2319+00 sample at $z' \sim 25\,\mathrm{mag}$ ($M_{z'} \sim -17.35$). As such, we can set the depth of the RCS 2319+00 structure to that of the field sample for better comparison. The fraction of red and blue galaxies in the structure to this brighter depth remains unchanged. One caveat to the field sample is that, though it is drawn from spectroscopic observations whose main target cluster lies outside of the supercluster range, there may exist groups and low-richness clusters within the supercluster range that have not yet been identified. Despite this, our supercluster galaxies show an excess red-sequence over the field population, as expected in clusters. To further investigate this excess we look at the identified structure from Section 3.2.

It can be seen that the cluster cores (Groups 2, 9, and 10) show a more prominent red-sequence than the groups, with the core groups having 77±13% red galaxies and only 23%±7% in the blue cloud, for all identified members down to the fainter $z' \sim 25$ mag limit. The large errors are due to the small numbers, even after correcting for the redshift success. The groups show a lower fraction of red-sequence galaxies at 37%±10%, with the percentage of blue cloud galaxies almost three times higher than those in the cores at 63%±13%. Though we do not expect to see significant differences between the populations given the small numbers of galaxies in our sample and the large errors, the populations are still not consistent within errors, only crossing at $\sim 2\sigma$. From this we infer that the two group categories contain galaxy populations that may be in slightly different stages of evolution.

In their study of the Cl1604 supercluster at $z \sim 0.9$, Lemaux et al. (2012) found that the fraction of their cluster and group galaxies in the red-sequence was identical at 47%, suggesting a similar level of processing in the two environments, differing from the results for RCS 2319+00. They also found that 70% of the red-sequence galaxies in their supercluster belong to the clusters and groups. Combined, the core and group members of the RCS 2319+00 supercluster account for only 38%±5% of the corrected red-sequence supercluster members, which again hints that some fraction of the isolated supercluster 'field' galaxies may belong to larger, as yet unidentified structures. In the supercluster isolated 'field' population, which accounts for 226 of our 302 supercluster members, 29%±3% of the corrected galaxies are red while the remaining 71%±5% are in the blue cloud region, consistent with the group fractions.

The interesting filamentary structure between Clusters A and B (Group 5) has eight of its nine identified members in the blue cloud and includes some of the faintest identified members so far, two of whom are also among the bluest galaxies currently identified in the overall structure. This is not surprising as Coppin et al. (2012) have shown that this region is undergoing an excess of star formation activity. If we remove this unique structure from our group category, the remaining $\geq$5 member groups contain 43%±12% red-sequence galaxies, still lower than the fraction of red-sequence galaxies in the cluster cores, though now consistent within $< 1.5\sigma$. This slightly higher group red-fraction is in closer agreement with the results of Lemaux et al. (2012) for both their groups and cluster galaxies. On average then, we think that the groups in our structure have undergone some processing, though less than the cluster core galaxies, with the filamentary structure standing out as a unique environment of blue, star-forming galaxies currently undergoing intense activity.

Recalling that the MC simulations run in Section 3.2.3 showed the possibility of one spurious 5–8 member FOF group, we look to see what effect this might have on the red-sequence fractions of the populations. The validity of the core groups is supported by the optical colour data and the X-ray detections and we are therefore confident that the FOF overdensities represent real groups. The filamentary structure is detected in the infrared and again we assume that its corresponding FOF group can therefore be assumed to trace a real structure. This leaves only one of the four remaining ≥ 5 member groups as the possible spurious structure detection. If we remove the galaxies belonging to a single group and reassess the fraction of red versus blue galaxies remaining for the group population, repeating the process until each group has been removed once, we find that the fraction of red and blue galaxies does not change significantly, with the fraction of red galaxies varying from 41% to 45% with errors of $\leq 14\%$, consistent with the previous results.

With the aid of the colour information, we can revisit the assignment of Group 9 as the core group of Cluster B over Group 6, the lower redshift group also consistent with the spatial position of the red-sequence overdensity and the X-ray emission. In Figure 3.6 it can be seen that all of the galaxies currently identified in Group 9 are red, while 50% of the identified galaxies in Group 6 are blue, closer to the fraction seen for the groups.

3.3.2 Colour Distribution in Different Environments

To further investigate the populations in the different environments and look for possible signs of the buildup of the red-sequence we look to the distribution of galaxy colours in the different density regions. Here we do not attempt to correct for the redshift success based on magnitude or for the galaxies' mass or luminosity differences, which will be investigated in Chapter 4. Instead, we normalize the number counts in the different populations to one in order to look at the relative colour distributions. In

Figure 3.7, we plot the normalized number counts of galaxies in the different environments, binned in colour and plotted as a difference over the normalized comparison field sample discussed above. Given the finite nature of filter bandpasses, converting the observed wavelength into a rest-frame wavelength of a source requires a correction factor, the k-correction, to connect the observation filter and what would be the emitted filter at the source redshift (Hogg et al., 2002). We k-correct the apparent magnitudes using the spectroscopic redshifts and version 4.2 of the kcorrect code by Blanton & Roweis (2007) to better compare the samples. The solid line shows the colour distribution in the cluster core galaxies over the field, the dashed line represents the ≥ 5 member, non-core groups with the filament removed, the dash-dotted line shows the filament galaxies and the triple-dot-dash line encompasses all remaining isolated supercluster 'field' members. The Poisson errors plotted are based on the parent population only, with no scaling applied when the difference between each population with the field population is found.

The isolated supercluster galaxies possess the expected bimodal distribution of blue and red galaxies over the field, with a distinct, underpopulated 'green valley', though $\sim 38\%$ of our spectroscopic cluster galaxies fall in this intermediate colour area. The core and group galaxies both show peaks in the red end of the histogram, as expected, with few blue galaxies and a deficit of 'green' galaxies compared to the field. The group galaxies do show a slight excess of galaxies at the bluest end of the distribution, though the large errors render the peak consistent with the comparison field at this colour.

The filament between Clusters A and B shows three peaks above the field: a small peak at the red sequence end; one populating the green valley; and a final excess at the bluest end of the colour distribution. The small number of filament galaxies currently in our spectroscopic sample (nine members) results in large errors

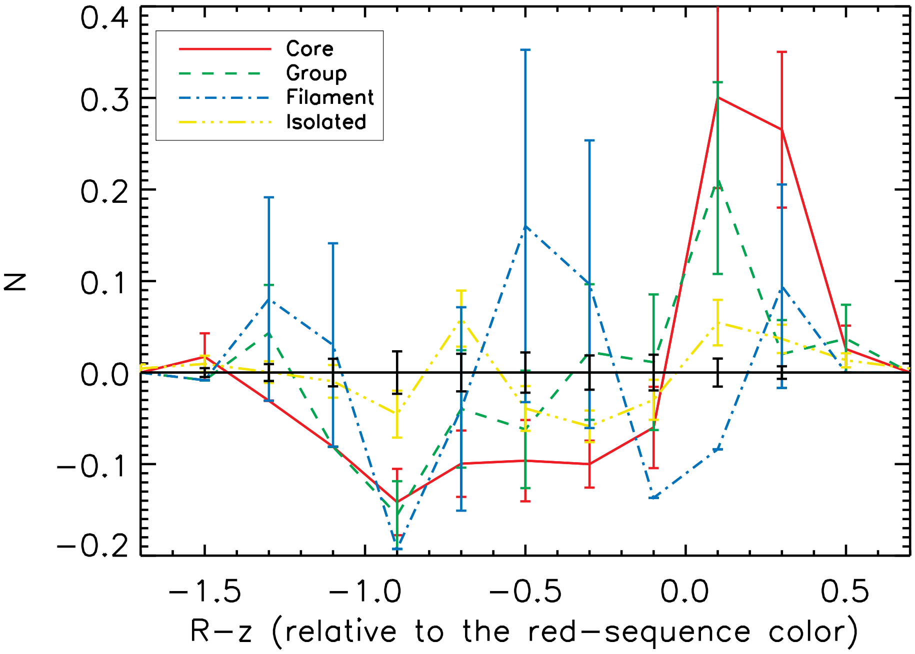

Figure 3.7 Number of galaxies in each environment normalized to one vs. $R_c - z'$ colour for the spectroscopically confirmed supercluster members plotted as a difference over the normalized comparison field sample. Errors given are Poisson errors found for each population. The solid line shows the colour distribution in the cluster core galaxies over the field, the dashed line represents the ≥ 5 member, non-core groups with the filament removed, the dash-dotted line shows the filament galaxies and the triple-dot-dashed line encompasses all remaining isolated supercluster 'field' members.

and therefore the three filament peaks are consistent with the field within the errors. We propose that, if the peal in the green galaxy population from the filament is real, these intermediate colour galaxies may in fact belong to a transient population in the process of migrating to the red-sequence, similar to those seen by Balogh et al. (2011) in their study of seven spectroscopically confirmed galaxy groups at $0.85 < z < 1$. They found that 30% of their confirmed group members populated this intermediate 'green' colour region and propose that these galaxies represent a transient population who have recently ceased their star formation and are in the midst of migrating from the blue cloud to the red-sequence. Currently, two thirds of the filament galaxies are found in this intermediate area of the colour–magnitude diagram versus the $\sim 45\%$

of field galaxies at this colour. Further studies with multiwavelength data on the RCS 2319+00 supercluster are needed to determine the properties of these galaxies, further motivating the research to follow in Chapter 4.

3.4 Luminosity Functions

We wish to put a rough estimate on the average mass of our identified groups in order to better trace the buildup of our supercluster and to place our groups in context with theories of hierarchical formation from semi-analytic models (e.g., McGee et al., 2009; Berrier et al., 2009; De Lucia et al., 2012; Cohn, 2012). The majority of our groups have too few spectroscopic members to compute reliable velocity dispersions and, as we have seen in Section 2.4.4, masses derived from velocity dispersions can carry large errors even with a larger sample. Instead, we attempt to estimate the mean mass of our groups by fitting luminosity functions (LFs) to two stacked group categories; the cluster cores and the potential infalling groups.

Luminosity functions measure the number of galaxies per volume in a given luminosity bin and can be used to test theories on the formation of galaxies, their evolution, and what role the environment plays on these factors. The faint-end of the luminosity function is populated by a mix of faint red and blue galaxies and slight variations in its slope can be used to help distinguish between different structure formation theories. A steeper faint-end slope may be indicative of the accretion of faint galaxies onto the group or cluster while a flatter slope would be expected in a relaxed cluster dominated by early-type galaxies (e.g., Goto et al., 2002; Propris et al., 2003; Goto et al., 2005; Zenteno et al., 2011). LFs can also be used to estimate the number of galaxies in each group or cluster by integrating the function to given luminosity limits. While cluster luminosity functions are generally constructed from background subtracted photometric catalogues, we attempt to measure the luminosity functions of the stacked clusters and groups in our supercluster through the recovered spectroscopic membership from the FOF search for substructure in the previous section.

We use the functional form of the Schechter function (Schechter, 1976) to fit the luminosity function,

$$\phi(M) = 0.4\ln(10)\phi^*(10^{0.4(M^*-M)})^{1+\alpha}\exp(-10^{0.4(M^*-M)}), \tag{3.3}$$

where α is the slope of the faint-end power-law, M^* is the characteristic magnitude and ϕ^* is the normalization of the Schechter function.

3.4.1 Luminosity Function of the RCS 2319+00 Supercluster Field

We first construct an LF for the full catalogue of 302 spectroscopically confirmed supercluster members in our 35×35 arcmin region to estimate the value of $M^*_{z'}$ and look at the shape of the faint-end slope. First, we convert the photometry of all cluster members to absolute magnitude $M_{z'}$ using,

$$M_{z'} = m_{z'} - 5\log\left[\frac{D_L(z)}{10\text{ pc}}\right] - K(z), \tag{3.4}$$

where $D_L(z)$ is the luminosity distance to our average supercluster redshift and the $K(z)$ variable refers to the k-correction. The k-correction was computed using version 4.2 of the kcorrect code by Blanton & Roweis (2007). Our apparent magnitudes ($m_{z'}$) have already been corrected for galactic dust extinction. The spectroscopic magnitude weights calculated in Section 2.3.2 are applied to each confirmed member with no geometric correction as we are looking at the statistics over the whole field and not at individual galaxy properties. The completeness-weighted spectroscopic members were then binned by absolute magnitude in 0.25 mag bins and the bins for each core or ≥ 5 member group were stacked. Fractional errors were added to the stacked, weighted number counts in each magnitude bin. The Schechter function was fit using

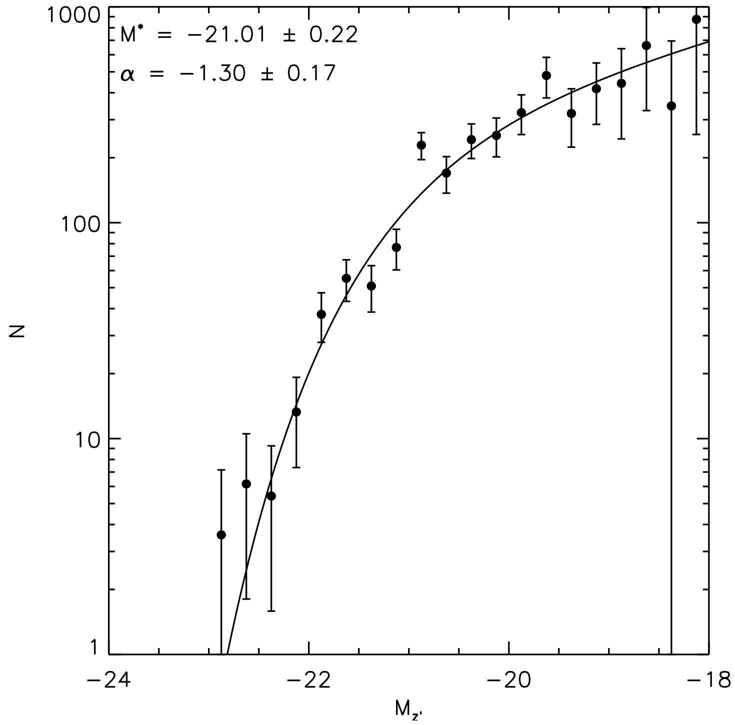

Figure 3.8 LF of the best-fit Schechter function to all completeness-corrected spectroscopic supercluster members in the 35×35 arcmin region.

the Levenberg–Marquardt algorithm for nonlinear least-squares fitting using the mpfit routine for IDL (Markwardt, 2009).

Figure 3.8 shows the LF for all weighted, spectroscopically confirmed members in the RCS 2319+00 supercluster. The BCGs from each cluster core were removed from the fitting so as not to influence the bright-end fit of the LF. The solid line shows the best fit Schechter function. The characteristic magnitude $M^*_{z'}$ is estimated to be $M^*_{z'} = -21.01 \pm 0.22$. This value is slightly lower than the value derived by Gilbank et al. (2008b) of $M^*_{z'} = -21.39$ at $z = 0.9$ using the passively evolving model on a fit to the LF of composite RCS clusters at $z = 0.4$. We note that our fitted value of the faint-end slope of $\alpha = -1.30 \pm 0.17$ is at the high-end of the values found with other galaxy clusters in the literature. The fit to the composite RCS clusters of Gilbank et al. (2008b) resulted in a faint-end slope of $\alpha = -0.94 \pm 0.04$. Lin et al.

(2004) used a composite K-band LF of 93 X-ray selected groups and clusters from the Two Micron All Sky Survey and found a faint-end slope is fit by a slope ranging as $-0.84 \leq \alpha \leq -1.1$. The closest agreement to our estimate of α was found by Zenteno et al. (2011), who measured an average faint-end slope of $\alpha \approx -1.2$ for their four SZ selected clusters in the r, g, i, and z-bands.

To construct our supercluster LF, we use the weighted number counts of all spectroscopically confirmed cluster members over the broad supercluster region rather than using background subtracted number counts from photometry in the much smaller radii of r_{500} (Lin et al., 2004), $0.5r_{200}$ (Gilbank et al., 2008b) or r_{200} (Zenteno et al., 2011) around groups and cluster cores as done in the previous studies. The steeper than average faint-end slope we find for RCS 2319+00 may therefore be reflective of the presence of infalling structures and individual galaxies in the lower density regions of the supercluster field. The addition of these lower density regions to our LF may also be the cause of the slightly lower characteristic magnitude found here compared to that found by Gilbank et al. (2008b). However, we must again note that our fit is based on an incomplete, completeness-corrected spectroscopic sample, which may also affect the shape of the LF. For these reasons, we choose to use the values for the $M^*_{z'}$ and α parameters found for the composite RCS galaxy clusters by Gilbank et al. (2008b) when looking at the LFs of the core and ≥ 5 member groups in the following section as they appear to be more representative of the denser cluster cores and groups than our fitted values from the broad supercluster field.

3.4.2 Luminosity Functions of the Cluster Cores and Groups

To construct the LFs of our stacked ≥ 5 member groups and the cluster cores recovered from the FOF output we follow the same methods described above for the whole supercluster member catalogue with the exception of the spectroscopic completeness weights, which were calculated using the photometric catalogue in a smaller radius around the mean group position (see Section 2.3.2 for details on the spectroscopic weight calculations) rather than the completeness weight for the full 35×35 arcmin field of view. This was done to simulate a smaller group radius of $\sim r_{200}$, which we initially set at 1.5 Mpc for the cluster cores, based on the values found for the clusters using the Evrard et al. (2008) relation (see Table 2.6) and an arbitrary radius of 1 Mpc for the ≥ 5 member groups. Since the LFs of our recovered groups and cluster cores are based on a small number of completeness-weighted spectroscopic sources per group, we find that fitting all three Schechter parameters simultaneously is not reliable. Instead, we fix the characteristic magnitude and faint-end slope to those measured for the composite RCS clusters by Gilbank et al. (2008b) of $M^*_{z'} = -21.39$ and $\alpha = -0.94$, as motivated above. For the stacked LF of the three core groups (2, 9, and 10) the BCGs were again removed from the fitting so as not to influence the bright-end fit.

The stacked luminosity functions are shown in Figure 3.9. The LF of the stacked cluster cores is shown as closed circles with the best-fit function plotted as a solid line. The open circles and dotted line show the results for the stacked ≥ 5 member groups. The dashed vertical line indicates the position of $M^*_{z'}$ for reference. The luminosity functions with fixed $M^*_{z'}$ and α were fit to ϕ^*, integrated to estimate the number of galaxies in the stacked groups, $N_{\rm gals}$, and then divided by the number of groups in the stacked LF as a proxy for the mean richness of the groups. We used two methods of estimating the group mass from the number of galaxies.

The first method employs the halo occupation number (HON), based on the halo occupation distribution (HOD); the probability distribution of finding N galaxies in a halo of mass M (e.g., Seljak, 2000; Benson, 2001; Berlind & Weinberg, 2002; Lin et al., 2004, 2006). In the HOD formalism, the HON is defined as $\langle N \rangle (M)$, the mean

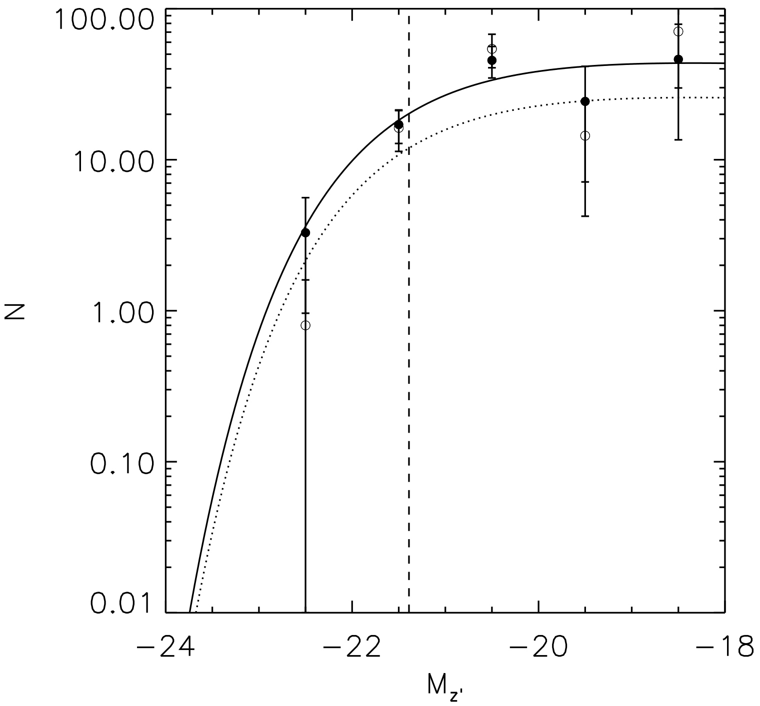

Figure 3.9 Stacked LFs for the three cluster cores in the supercluster from 1.5 Mpc completeness-corrected spectroscopic members found using the FOF algorithm (closed circles, solid line) and for the 1 Mpc completeness-weighted members in the five ≥ 5 member recovered groups (open circles, dotted line) in magnitude bins of ±0.5 mag. The curves show the best-fit Schechter functions using $M^*_{z'} = -21.39$ (vertical dashed line) and $\alpha = -0.94$ from Gilbank et al. (2008b).

number of galaxies per halo, and can be estimated by integrating the LF. Lin et al. (2004) used a sample of 93 X-ray-selected groups and clusters in the nearby universe to form a composite K-band LF and found an N_{500}–M_{500} scaling relation. Extending their work to $z = 0.9$, Lin et al. (2006) found no signs of evolution in the scaling relation. The $\Delta = 200$ form of the Lin et al. (2004) relation, as used by Zenteno et al. (2011) for their work on the LFs of SZ–selected clusters, becomes

$$N_{200} = (36 \pm 3) \left(\frac{M_{200}}{10^{14}\, h_{70}^{-1}\, M_{\odot}} \right)^{0.87 \pm 0.04} . \tag{3.5}$$

The N–M relation used is based on the number of galaxies within the viral radius of the group or cluster. Since we do not have that information available and our LFs are constructed from weighted spectroscopic samples with small numbers of known galaxies, we retain our 1.5 and 1 Mpc completeness corrections initially for these estimates for the cores and ≥ 5 member groups respectively. The total number of galaxies N_{200} is estimated from the integration of the luminosity function. Here the integration is done to a limit of $M^* + 2$.

Using the estimated N_{200} and its resulting mass, a new estimate of the virial radius r_{200} can be found and a new spectroscopic weighting for the galaxies can be performed to reflect this new radius. This is done iteratively until the resulting radius matches the input radius. The mass estimates with the initial and final radii vary by $< 0.1 \times 10^{14}\, M_\odot$, with the core mass decreasing slightly and the group mass increasing for the final, smaller radii. For the cluster cores, we find an average $N_{\rm gals} = 23.98$ and a mass estimate of $\sim 0.9 \times 10^{14} M_\odot$ using the Lin et al. (2004) N_{200}–M_{200} scaling relation with the galaxies completeness-weighted to an average virial radius of $\sim 0.7\,$Mpc. The mass estimated for the $\geq$5 member groups is over a factor of two lower at $\sim 0.4 \times 10^{14}\, M_\odot$ for $N_{\rm gals} = 11.55$ per group in a $\sim 0.5\,$Mpc radius.

The second method we use to estimate the masses of our groups from the stacked LFs involves the cluster and group richness estimate used with the SDSS maxBCG catalogue (e.g., Hansen et al., 2005, 2009; Becker et al., 2007; Johnston et al., 2007). In this case the richness, N_{200}, represents the number of red galaxies that are fainter than the BCG in an area that approximates r_{200}. N_{200} is first calculated for an arbitrary radius, which we take to be the 1.5 and 1 Mpc radii used above, and then calculated using the new r_{200} from the maxBCG N_{200}–r_{200} relations. Richness-size relations have been found for the maxBCG catalogue from both the radial density profiles of clusters (Hansen et al., 2005) and weak lensing (Johnston et al., 2007), with the weak lensing relation scaling to the cluster halo mass.

Due to our small numbers and completeness weighting, which is not dependant on colour information, we can not readily extract the red and blue galaxies into separate LFs to find different N_{gals} for the two populations. Instead, we use the rough percentage of red-sequence galaxies in each of the group categories found in Section 3.3.1 of ∼77% for the core groups and ∼33% for the ≥5 member groups. We used these percentages to scale the N_{gals} recovered from the LFs to an approximate N_{200} to be used with the maxBCG relations. For the cores, we find $N_{200} \sim 41.2$ from $r_{200} \sim 1.1$ Mpc and subsequent mass estimates of $\sim 6 \times 10^{14} M_{\odot}$ per cluster. For the ≥5 member groups we find $r_{200} \sim 0.6$ Mpc and $N_{200} \sim 6.7$, resulting in mass estimates of $\sim 5 \times 10^{13} M_{\odot}$ per group.

The average group mass estimates resulting from the different N–M scaling relations are relatively consistent, with the cluster cores having masses $\sim 10^{14} M_{\odot}$, an order of magnitude more massive than the $\gtrsim 10^{13} M_{\odot}$ estimates for the potential infalling groups. The mass estimate for the cluster cores of ~ 0.9–$6 \times 10^{14} M_{\odot}$ is consistent with those calculated from the spectroscopic velocity dispersions and the X-ray data of $10^{14.5}$–$10^{14.9} M_{\odot}$. From this we reason that the average group mass from our LFs of ~ 4–$5 \times 10^{13} M_{\odot}$ is a reasonable initial group mass estimate.

As a test, the LFs were also fit with only the faint-end slope set and allowing $M^{*}_{z'}$ to vary. This was done in order to check that any mass segregation between the denser cluster cores and the surrounding groups in the supercluster field did not cause the characteristic magnitude to shift drastically in the LFs of the stacked core/group galaxies (Figure 3.8). We found only slight changes in the value of $M^{*}_{z'}$ that did not result in any changes in the resulting average cluster core or group mass estimates.

3.4.3 Comparison to Theories of Hierarchical Structure Formation

In order to put our $\sim 10^{13} M_\odot$ recovered groups in context, we look to studies that employ semi-analytic techniques to retrieve galaxy merger tree information from N-body simulations in order to trace the merger history of clusters. In two recent studies by Berrier et al. (2009) and McGee et al. (2009), slightly differing results were obtained as to the fraction of galaxies in clusters today that were accreted onto the cluster as a member of a $\sim 10^{13}\, M_\odot$ group. Berrier et al. (2009) found that, of galaxies residing today in $10^{14.2}\ h^{-1}\, M_\odot$ clusters, $< 17\%$ were accreted in groups of ≥ 5 members, and $\sim 25\%$ from halos with masses of $\sim 10^{13}\ h^{-1}\, M_\odot$. For the same mass clusters, McGee et al. (2009) found a higher fraction of galaxies fell into the cluster from $\sim 10^{13}\ h^{-1}\, M_\odot$ groups, at $\sim$32%. The discrepancy in the results of the two studies is likely due to the different methods used to populate the dark matter halos with galaxies. The Berrier et al. (2009) study associates all subhalos above a certain mass with galaxies, with no robust stellar mass estimates. The McGee et al. (2009) study considers accretion onto the cluster halos as a function of the present halo and stellar mass of the infalling halos. At this point we do not have stellar mass estimates for our group and core member galaxies to compare to the merger tree studies but this will be investigated in Chapter 5.

Cohn (2012) also found that $\sim 30\%$ of galaxies in clusters with mass $\geq\ 10^{14}\, h^{-1}\, M_\odot$ at $z = 0.1$ had been accreted onto the final cluster as members of halos with $\geq\ 10^{13} h^{-1}\, M_\odot$, with the most massive cluster galaxies having a larger fraction coming from these groups. This work also found that the largest subgroups accreted onto clusters were aligned along the clusters major axis, which we see in Figure 3.2 in Groups 5 (the filamentary group between Clusters A and B), 6 (large group in the line of sight of Cluster B), and 13 (the large filamentary group seemingly falling into Cluster C).

Another study, by De Lucia et al. (2012), also used galaxy merger trees to study the accretion of galaxies onto clusters. While their study focuses primarily on the stellar mass of the galaxies accreted through different mass groups, they also find that a large fraction of the most massive cluster galaxies and about half of the low to intermediate stellar mass cluster members fell into the final cluster from $\sim 10^{13}\,M_{\odot}$ groups. These studies all suggest that some pre-processing of cluster galaxies in groups is occurring prior to accretion onto the final cluster.

The three clusters in RSC2319+00 are thought to be on a collision course to form a massive, $> 10^{15}\,M_{\odot}$ cluster by $z = 0.5$ (Gilbank et al., 2008a). If we consider Cluster A to be the most massive halo in our supercluster (based on the X-ray masses) and assign it as the final host halo in the eventual merging of the RCS 2319+00 supercluster, the spectroscopic members (as opposed to the completeness-corrected members) of the remaining $\sim 10^{13}\,M_{\odot}$ groups and clusters currently account for 22% of the spectroscopic cluster members. We recall that our other identified groups (<5 members) as well as some of our isolated supercluster field galaxies may in fact be identified as larger groups given further spectroscopy and, on the other hand, we may find a larger isolated galaxy population in the supercluster field so this percentage may change.

While comparing to these studies gives a general idea that our recovered groups likely represent real substructure in our supercluster that is destined to be accreted into the final cluster, a comparison to clusters at similar redshift and of similar final mass is more prudent. McGee et al. (2009) extended their study to trace the history of accretion onto galaxy groups and clusters at different redshifts. They determined that at $z = 1.0$ clusters with masses of $\sim 10^{14.5}\ h^{-1}\,M_{\odot}$ had ~36% of their galaxies accumulated through $> 10^{13}\ h^{-1}\,M_{\odot}$ halos. For Coma-like clusters of $\sim 10^{15}\,M_{\odot}$ at $z = 0.5$, which the RCS 2319+00 supercluster is predicted to form, they found that

$\sim 40\%$ of the cluster galaxies had been accreted through large halos over the merger history. Of more relevance is their result that by tracing the merger trees of the most massive $M_{\rm clus} \sim 10^{15.1}\ h^{-1}\, M_\odot$ galaxy clusters today, they were found to never have more than 17% of their galaxies in halos of mass 10^{13}–$10^{14}\ h^{-1}\, M_\odot$, which occurred at a lookback time of ~7 Gyr, about 0.3 Gyr more recently than the epoch at which we are viewing the RCS 2319+00 supercluster. In this context, our 22% of galaxies in the supercluster currently residing in groups with masses of 10^{13}–$10^{14}\, M_\odot$, though slightly high, is comparable to the McGee et al. (2009) findings. Again we reiterate our numbers are estimates based on incomplete spectroscopic coverage.

3.5 Summary of the Substructure Found in RCS 2319+00

Here we have attempted the trace out the substructure of the RCS 2319+00 supercluster, prompted in Chapter 2 by the multiwavelength indications of substructure in the supercluster field along with the close proximity of the three clusters in redshift and angular space, which makes conventional cluster member assignment difficult.

- We performed the DS test to begin tracing the substructure of the supercluster by looking for deviations from the global mean parameters in the supercluster field. We find evidence of substructure over the broad redshift range as well as within each separate redshift wall, with MC tests showing a very low probability that the substructure is false.

- To isolate specific structure, we used a modified FOF algorithm in an effort to associate supercluster galaxies with their parent clusters or groups.

- Comparing MC simulations to the FOF recovered overdensities in the real data suggests that groups found to have ≥ 5 members in our real data are tracing legitimate structure.

- Using the Millennium Simulation data we found that, while we believe we are tracing regions of true substructure, we may be assigning galaxies from multiple dark matter halos to a single subhalo.
- We find evidence of possible infalling groups and extended structure in the main clusters, with five ≥ 5 member groups plus the three cluster core groups, which we believe are tracing true structures.
- We spectroscopically confirm the presence of a filamentary structure spanning the area between Clusters A and B (Group 5) previously detected in the infrared by Coppin et al. (2012) to be forming stars at an SFR $\simeq 900 M_{\odot}$ yr^{-1} and building up significant stellar mass. The filament is detected in the DS test and using the FOF method.

An investigation of the CMR and colour distribution of the galaxies in the different density environments of the supercluster was performed.

- Of the galaxies identified as belonging to the three cluster cores, 77%±13% are red-sequence galaxies, with blue galaxies making up only 23%±7% of the population.
- In the ≥5 member groups with the unique filamentary structure excluded, 43%±12% of the galaxies fall on the red-sequence with over half of the population remaining in the blue cloud. This suggests that the group galaxies have undergone some processing to build up their red-sequence, though the remaining high fraction of blue galaxies would suggest less processing than the core galaxies.
- The filamentary structure between Clusters A and B has eight of its nine members below the red-sequence, with three distinct peaks in colour: one at the bluest colours; one in the green valley; and a small peak in the red-sequence of the colour–magnitude diagram. Despite the small numbers we propose that the 'green'

galaxies may belong to the transient population identified by Balogh et al. (2011) to be migrating from the blue cloud to the red-sequence.

We construct stacked LFs for the core and ≥5 member FOF groups from the spectroscopically weighted members to estimate average group richness and masses using two different methods: the HOD method and the maxBCG richness estimators.

- The LF derived masses from the stacked cores are $\sim 0.9\text{–}6 \times 10^{14} M_{\odot}$, consistent with the $\sim 10^{14.5}\text{–}10^{14.9} M_{\odot}$ cluster mass estimates from the multiwavelength data.
- The average ≥5 member group masses from the two methods are an order of magnitude less massive than the cluster cores, at $\sim 4\text{–}5 \times 10^{13} M_{\odot}$.
- Assigning Cluster A as the host halo of the eventual merged cluster, the remaining groups account for 22% of the galaxies currently confirmed as supercluster members. Compared to studies using semi-analytical derived merger trees on simulated cluster data, this fraction is slightly higher than the fraction seen at this epoch in massive, present-day clusters but not unrealistic given that all of the studies found a large fraction of ∼ 30% of surviving galaxies in present day clusters spent some time as members of $\sim 10^{13}\ h^{-1}\, M_{\odot}$ groups.

The mapped structure of the RCS 2319+00 supercluster defined in this chapter provides an abundance of different global density environments in which to study the effect of the environment on galaxy evolution: from the isolated supercluster field galaxies, along infalling groups and filaments, to the dense cluster cores. Though again we caution that the structure defined here is a lower limit on the possible groups present in the RCS 2319+00 supercluster field and 'isolated' supercluster galaxies may not actually be isolated given further spectroscopy. The addition of high-quality, multiwavelength photometric redshifts and supplementary spectroscopy will aid in limiting the mis-identification of the different density regions within the supercluster and add to our understanding of this unique, compact, high-redshift supercluster.

Chapter 4

The Distribution of Stars and Star Formation in RCS 2319+00

The following chapter is based on:

Witnessing the assembly of a massive galaxy cluster: the distribution of stars and star formation in the merging supercluster RCS 2319+00 at $z \sim 0.9$

A.J. Faloon, T.M.A. Webb, D. O'Donnell, A.G. Noble, A. Delahaye, J.E. Geach, E. Ellingson, R. Yan, D.G. Gilbank, L.F. Barrientos, H.K.C. Yee, and M. Gladders, to be submitted to ApJ

4.1 Introduction

This chapter presents a study of the stellar mass and star formation distribution in the RCS 2319+00 supercluster. Using data extracted from several studies in different observational bands on RCS-1 clusters, we have compiled a large multiwavelength catalogue for RCS 2319+00, whose data are outlined in Section 4.2. This catalogue includes the spectroscopy outlined in Section 2.3, mid infrared (MIR), near infrared (NIR), radio and X-ray imaging. In Section 4.3 we summarize the friends-of-friends (FOF) groups defined in Chapter 3, estimate the supercluster member stellar masses and star formation rates (SFRs), and discuss the possibility of AGN contamination of the MIR SFRs. The RCS 2319+00 supercluster and its FOF-identified global environments, in conjunction with the galaxy stellar masses and SFRs, allows us to study the evolution of galaxy properties at the same local densities in different sized parent halos in the merging structure. We look for signals of external environmental effects and internal, self-regulation of galaxy properties in the supercluster.

Section 4.4 presents a study of the stellar mass distribution as a function of the environment, both global and local. The SFR as a function of the environment follows in Section 4.5. We discuss the possible growth of stellar mass in the outskirts by investigating the star formation distribution of the cluster and take a closer look at the filamentary region. We briefly revisit the colours of galaxies in Section 4.6 by comparing the results for MIPS star-forming galaxies against those of the full supercluster sample found in Section 3.3.1. In Section 4.7 we investigate the SFR as a function of stellar mass in the different density regions, discussing the possibility of the quenching of the star formation population as a function of both the mass and environment. Finally, in Section 4.8 we offer a summary of the chapter's results.

4.2 Multiwavelength Data

The current study uses optical, MIR, NIR, radio, and X-ray data to analyze the distribution of star formation and stellar mass in the supercluster field. The multiwavelength coverage maps over the 35×35 arcminute area used in this study are shown in Figure 4.1. The individual observational runs are described briefly in Table 4.1 and in more detail in the following sections. The R_c and z' catalogue in the AB magnitude system, which derives from the RCS-1 cluster survey (Gladders & Yee, 2005), serves as the basis for the multiwavelength catalogue. We use a 35×35 arcminute region of the catalogue centered around the RCS 2319+00 supercluster.

4.2.1 Spitzer-MIPS Imaging

The supercluster field was imaged in the mid-infrared using the $24\,\mu$m Multiband Imaging Photometer for *Spitzer* (MIPS; Rieke et al., 2004) instrument through open

Table 4.1 Multiwavelength Observations of the RCS 2319+00 Supercluster Field.

	Band	Instrument	Depth	FOV	Reference
X-ray	0.3-7.0 keV	Chandra	$3.4\times10^{-15}\,\mathrm{erg\,s^{-1}\,cm^{-1}}$	$\sim$300 sq. arcmin	Hicks et al. (2008)
Optical	$\mathrm{R}_c z'$	MegaCam	24.7, 24.05 mag	1 sq. deg.	Gladders & Yee (2005)
NIR	K_s	WIRCam	21.8 mag	21.5×21.5 arcmin	Delahaye et al. (in prep.)
NIR	3.6, 4.5, 5.8, 8.0 μm	IRAC	4.2, 6.0, 27.0, 26.0 μJy	$\sim$300 sq. arcmin	Webb et al. (2013)
MIR	24 μm	MIPS	70 μJy	$\sim$300 sq. arcmin	Webb et al. (2013)
Radio	1.4 GHz	VLA	45 μJy	$>34\times34$ arcmin	Noble et al. (2012)

time proposal 30940. This was done as part of a MIR study of 45 RCS-1 galaxy clusters (Webb et al., 2013). The MIPS instrument has a point spread function (PSF) of ~ 6 arcseconds and a 5.4 square arcminute field of view, requiring three 2×2 mosaics to give ~ 10 square arcminute images around each cluster core. The MIPS coverage area is shown as an angled, L-shaped ~ 300 square arcminute area by the dark blue solid lines in Figure 4.1. With an integration time of 3200 seconds, the MIPS data reach an 80% completeness depth of $\simeq 70\,\mu$Jy, just under $L_{IR} \sim 5\times10^{10}\,L_\odot$ at the supercluster redshift assuming an IR luminous star-forming galaxy SED template (Chary & Elbaz, 2001; Dale & Helou, 2002). The reduction was performed using the MOPEX software from the Spitzer Science Center with further background subtraction achieved through IDL routines developed by Webb et al. (2013). The source positions were found using the PPP program (Yee, 1991) with the flux densities found using the aperture photometry program DAOPHOT (Stetson, 1987). For full details on the MIPS catalogue and observational set-up see Webb et al. (2013).

4.2.2 Spitzer-IRAC Imaging

Deep 4-channel imaging with the *Spitzer* InfraRed Array Camera (IRAC; Fazio et al., 2004) was taken with open time program 20754 to a depth of $\sim M^{*}{+}2$ at $z\sim0.9$. Each of the four channels (3.6, 4.5, 5.8, 8.0 μm) of the IRAC instrument were observed over a 5.2 square arcminute field of view simultaneously using InSb detectors for the

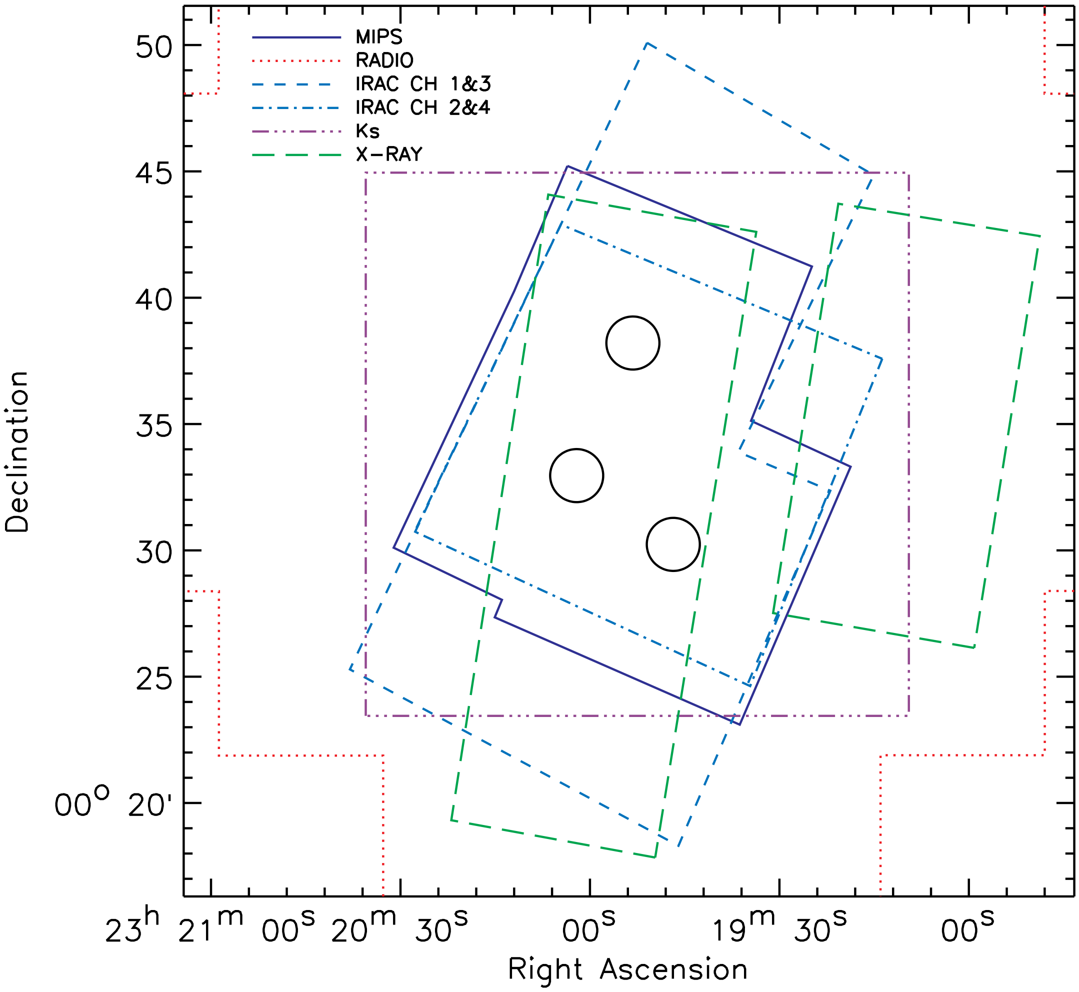

Figure 4.1 Multiwavelength coverage in a 35 x 35 arcmin area around the RCS 2319+00 supercluster field with the three cluster cores shown as solid black circles with a 0.5 Mpc radius. The coverage maps are: whole field - CFHT12K R_c and z'; dark blue solid lines - MIPS 24 μm; red dotted lines - VLA 1.4 GHz; light blue dashed lines - IRAC channels 1&3 (3.6 & 5.8 μm); dash-dot lines - IRAC channels 2&4 (4.5 & 8.0 μm); purple dash-dot-dot-dot lines - WIRCam K_s; green long-dashed lines - Chandra X-ray. Figure 2.1 in Chapter 2 details the mask layout of the five spectroscopic instruments in this field, which cover most of the area, concentrated in a 30 arcminute diameter around the center of the field.

two shorter wavelengths and Si:As detectors for the longer wavelengths. Dichronic beamsplitters separate the four wavelengths into pairs (channels 1 & 3, channels 2 & 4) that image different, non-overlapping areas of the sky. For this reason the fields of view for the four IRAC channels do not cover the same area, as seen in Figure 4.1.

The IRAC data were reduced using the IRACproc software suite (Schuster et al., 2006). The astrometry and photometry were found using the PPP software (Yee, 1991; Webb et al., 2013). The 3σ depths of the IRAC data are 4.2, 6.0, 27.0 and 26.0 μm for the four channels respectively.

4.2.3 VLA 1.4 GHz Imaging

Radio imaging at 1.4 GHz was obtained using the National Radio Astronomy Observatory's (NRAO) Very Large Array (VLA) in 'A' and 'B' configurations for a resolution of ~ 4.5 arcseconds. The observations spanned ~ 16 hours of integration time for a noise level of $\sim 15\,\mu\mathrm{Jy\,beam}^{-1}$. The Astronomical Imaging Processing System (AIPS) was used with standard tasks to calibrate and clean the images as well as extract the sources and determine flux densities (for details see Noble et al., 2012). The resulting radio map covers a $\sim 34 \times 34$ arcminute central region around Cluster A, with additional $\sim 20 \times 6$ arcminute regions along each side due to mosaicking, to a 3σ depth of $45\,\mu$Jy at the center of the map.

4.2.4 CHFT-WIRCam K_s imaging

Near-infrared imaging using the K_s filter (central wavelength of 2146 nm) on the Wide-field InfraRed Camera (WIRCam; Puget et al., 2004) was obtained through program ID 2010BC99 as part of the follow-up study of RCS-1 clusters begun in Webb et al. (2013). WIRCam contains four HAWAII-2RG detectors arranged in a 2×2 array for a total field of view of 21.5×21.5 arcminutes. The K_s imaging covers the three main cluster cores in the RCS 2319+00 supercluster (Figure 4.1) with an integration time of 600s, and reaches a depth of ~ 21.8 mag, in the AB magnitude system. The reduction, source detection and photometry will be described in detail in Delahaye et al. (in preparation).

4.2.5 Chandra X-ray Imaging

Chandra X-ray data from the Advanced CCD Imaging Spectrometer (ACIS) was obtained through observation programs 5750 (Cluster A), 7173 & 7174 (Cluster B) and 7172 (Cluster C) as part of an X-ray study of RCS-1 clusters (Hicks et al., 2008). Individual exposures ranged from 10-100 ks for a total exposure time of 74539 seconds over the coverage area. The X-ray data spans two rectangular mosaics; a larger region of $\sim 9 \times 25$ arcminutes covering the area around the three clusters, and a smaller $\sim 9 \times 12$ arcminute area west of the cluster cores (see the long dashed green regions in Figure 4.1). The complete details of the data reduction and point source detection are outlined in Hicks et al. (2008). The point-source sensitivity is $3.4 \times 10^{-15}\,\mathrm{erg\,s^{-1}\,cm^{-1}}$.

4.2.6 The Spectroscopic Catalogue

The extensive spectroscopic campaign, involving four optical spectrographs (Magellan: IMACS, VLT: VIMOS, FORS2, Gemini: GMOS-N) and one near-infrared spectrograph (Subaru: FMOS) has been described in Chapter 3. The full catalogue of 1961 high confidence galaxy redshifts found in the 35 x 35 arcminute field around the supercluster is used in the following analysis. In particular, we focus on the 302 galaxies that have been confirmed to lie in the broad $0.858 \leq z \leq 0.946$ redshift range containing the three cluster cores, the five infalling groups and three distinct redshift walls separated by ~ 65 Mpc from one another.

4.2.7 The Multiwavelength Catalogue

The extensive multiwavelength data on the RCS 2319+00 supercluster field has been compiled into a single catalogue containing all of the wavelength information available for each source. Astrometry may differ slightly between observational instruments, both due to instrument setup as well as the different wavelengths of the galaxy SED emitting from various regions of the galaxies (e.g., stellar light emitting in the optical and NIR versus the dust grains thermally emitting in the MIR). For this reason we must use matching between the different wavelength catalogues in order to compile multiwavelength information for each galaxy in the catalogue.

To match counterparts between different wavelengths, we choose matching radii based on tests that look for drop-off distances between catalogues. The majority of the catalogues are matched to the optical sources within ∼2 arcseconds, with the more accurate positions of the K_s-band data requiring a smaller match radius of only 1.25 arcseconds. In the case where there are multiple matches within the search radius, the closest match is chosen. All wavelengths, with the exception of the $24\,\mu$m data, are first matched to the optical catalogue before matching to other wavelengths should an optical counterpart not be available. The MIPS data are known to correlate well with the radio and so we match the broad, ~ 6 arcsecond PSF $24\,\mu$m sources first to within 2 arcseconds of the more accurate radio catalogue, before matching to the optical catalogue. The spectroscopic targets were all based on optical sources, despite the FMOS spectroscopy using the K_s-band coordinates for the NIR spectroscopy.

Future studies on the RCS 2319+00 supercluster will use the multiwavelength data described herein, as well as additional optical and infrared bands currently being observed and reduced, to isolate supercluster members through accurate photometric redshifts (Delahaye et al. in preparation). Here, we use only those 302 galaxies confirmed spectroscopically to lie in the supercluster redshift range of $0.858 \leq z \leq 0.946$ to study the properties of galaxies within different density environments in the supercluster.

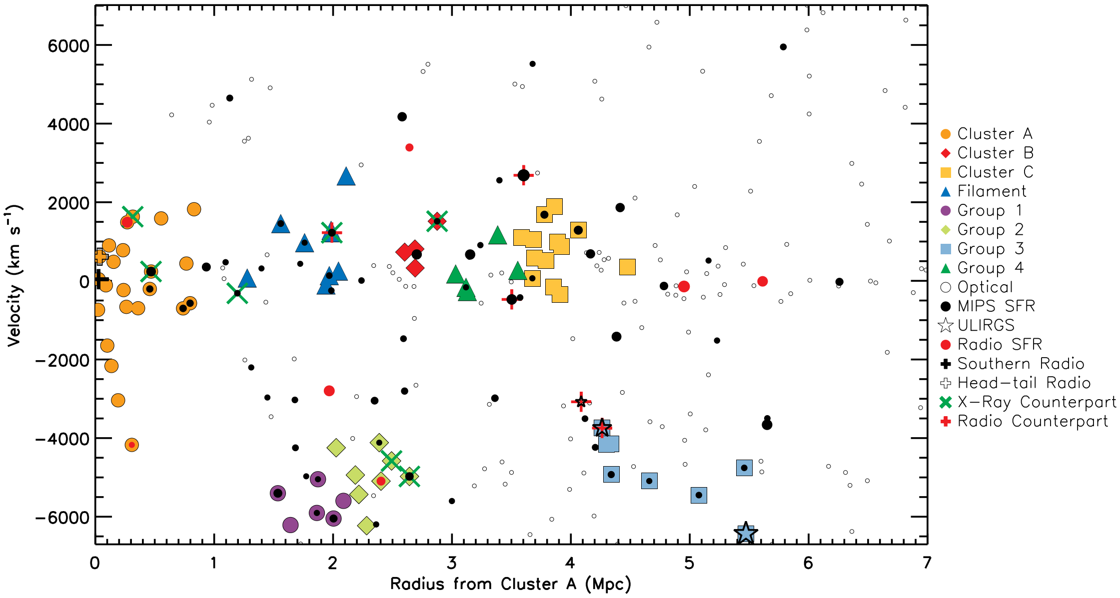

Figure 4.2 Relative velocity versus radius for all spectroscopically confirmed cluster members in the RCS 2319+00 supercluster relative to Cluster A. Cluster and group members identified through a friends-of-friends algorithm in Chapter 3 are highlighted. Those supercluster members with either MIPS or radio derived SFRs are indicated by solid black circles, with the size of the symbol increasing with increasing SFR. For the very highly star-forming radio galaxies in the core of Cluster A and the ULIRGs falling into Cluster C (see Figure 4.7 for the spatial distribution of galaxies), alternate symbols have been used so as not to overwhelm the plot. Open circles represent spectroscopic cluster members with no 24 μm or radio detection.

4.3 Analysis

4.3.1 The RCS 2319+00 Clusters and Groups

In Chapter 3, we used a friends-of-friends (FOF) algorithm to isolate the substructure of the RCS 2319+00 supercluster. Here we briefly outline those results and assign names to the ≥5 member FOF-identified groups that will be used in the analysis below. The relative velocity versus radius from Cluster A of all cluster members is shown in Figure 4.2 with the cluster core and group members highlighted. Table 4.2 summarizes the core and group names along with their former identification numbers in the FOF analysis from Chapter 3, the number of spectroscopic members in each

Table 4.2 Summary of Groups in the RCS 2319+00 Supercluster Field.

Core/Group Name	Previous ID	Spectroscopic members	$\sim z$	~RA	~DEC	Plot Color
Cluster A	2	23	0.901	23 19 53.20	+00 38 12.50	orange
Cluster B	9	4	0.905	23 20 02.10	+00 32 57.60	red
Cluster C	10	13	0.905	23 19 46.80	+00 30 14.30	yellow-orange
Filament	5	9	0.906	23 20 04.14	+00 35 31.29	blue
Group 1	7	6	0.865	23 19 50.34	+00 34 28.80	purple
Group 2	6	8	0.870	23 20 00.03	+00 28 25.54	light green
Group 3	13	8	0.870	23 20 03.90	+00 34 11.63	light blue
Group 4	1	5	0.903	23 19 26.86	+00 39 54.99	green

Note. Units of right ascension are hours, minutes, and seconds and units of declination are degrees, arcminutes, and arcseconds.

Note. Previous ID refers to the FOF association number given to each group in Figure 3.2 of Chapter 3.

group, and the mean group redshifts. Where there are ≥ 8 spectroscopic members, the group redshift listed is found using the biweight mean method of Beers et al. (1990). For groups with less than 8 members, the redshift listed is simply the mean of the members' spectroscopic redshifts. The right ascension and declination for the three cluster cores are taken from the peak of the clusters' X-ray emission (Hicks et al., 2008) while the group positions are given as the average position of the members. The plot colour listed refers to the colour used in subsequent figures that highlight the individual groups.

4.3.2 Stellar Masses

The K-band magnitude of a galaxy has been found to be well correlated to its stellar mass with little variance due to recent and current star formation history and, as such, the K-band luminosity can be used to estimate the galaxy stellar mass over a large redshift range (Kauffmann & Charlot, 1998; Kodama & Bower, 2003). At the supercluster redshift of $z \sim 0.9$ the IRAC-4.5 μm data samples the rest frame K-band and can therefore be used to estimate the stellar mass.

We follow the method of Bell et al. (2003) to estimate a K-band mass-to-light (M/L) ratio based on the rest frame K-band by using the rest frame galaxy colour. The equation for the M/L ratio is: $\log_{10}(\mathrm{M/L}) = a_\lambda + b_\lambda\,(\mathrm{colour})$, where we use the a_λ and b_λ parameters listed in Bell et al. (2003) for $\lambda = K_{rest}$. We use the R_c and z' magnitudes, k-corrected using version 4.2 of the kcorrect code by Blanton & Roweis (2007), to find the rest-frame $u - g$ colour. The IRAC-4.5 μm fluxes are converted to magnitudes and k-corrected with a band-shift out to $z = 1.045$, where the 4.5 μm data corresponds to rest-frame K-band at 2.2 μm. In addition to the k-correction of the IRAC magnitude we add an evolution correction for each galaxy based on colour (red: $0.9z$, blue: $0.6z$), as done by Gilbank et al. (2008b), to find the absolute magnitude and subsequent K-band luminosity. The M/L ratio found above is then applied to the luminosity to estimate the galaxy stellar mass. As the kcorrect uses a Chabrier IMF while the SFRs calculated in the next section are based on a Salpeter IMF, the stellar mass from the K-band luminosity, scaled by the M/L ratio, is further scaled by a factor of 1.65 to convert to a Salpeter IMF. The kcorrect code itself outputs a stellar mass estimate based on template data. A comparison of the kcorrect code stellar mass with those estimated from the colour and evolution corrected method above gave results ∼3 times lower consistently over the full mass range.

The IRAC-4.5 μm imaging reaches a completeness depth of 6 μJy. A 6 μJy IRAC source with red optical colours will result in a higher mass than that of a blue galaxy. The completeness level of 4.5 μm-derived stellar masses is therefore $\sim 7.3 \times 10^9\,M_\odot$, found for a red galaxy. Blue galaxies have IRAC derived masses complete to $\sim 5.8 \times 10^9\,M_\odot$. The M/L ratios carry uncertainties of 0.1-0.2 dex (Bell et al., 2003), however, since we are looking to compare trends within our own sample with all stellar masses calculated using the same colour correction method this should not effect our results.

Given that the IRAC-4.5 μm map does not cover the full area of the RCS 2319+00 supercluster field, stellar masses are found for only 144 of the 302 supercluster galaxies in this way. In order to increase the number of galaxies with stellar mass estimates, we attempt to calibrate the larger area K_s-band data to estimate stellar masses for additional supercluster members. To do this, we first find the stellar mass from rest-frame K-band using the four-channel IRAC data and the colour corrections over the full redshift sample of the 1961 galaxies in our spectroscopic redshift catalogue (i.e., using the 3.6 μm IRAC data for the $0.35 \leq z < 0.85$ galaxies, the 4.5 μm data for galaxies in the $0.85 \leq z < 1.35$ range and the 5.8 μm data for any galaxy with a redshift ≥ 1.35). We calculate stellar masses from the IRAC flux where available, with the appropriate k-correction band-shifts to rest-frame K-band depending on the given galaxy redshift. We use the corresponding rest-frame filters from the $R_c - z'$ data, given the galaxy redshift, to get the colour correction and evolution correction. The absolute rest-frame K-band magnitudes are scaled by the M/L ratio and the 1.65 factor, as above, to output stellar masses with a Salpeter IMF. We then use all spectroscopic galaxies with K_s magnitudes to find stellar masses, band-shifting the k-correction to $z = 0$ and using $R_c - z'$ colours. Again, we correct the final mass to a Salpeter IMF.

There are 438 spectroscopic galaxies in our full catalogue for which we have both observed K_s-band data and an IRAC detection in the appropriate channel, given the galaxy redshift, for a stellar mass estimate from rest-frame K-band. With these, we use a second order polynomial fit to find a relation between the stellar mass from rest-frame K-band to that from the observed K_s-band data of:

$$M_{\star,K_{rest}} = [(0.35 \pm 0.21) + (0.67 \pm 0.59)z + (0.37 \pm 0.40)z^2]M_{\star,K_s}. \tag{4.1}$$

This method gives stellar mass estimates for an additional 58 supercluster galaxies.

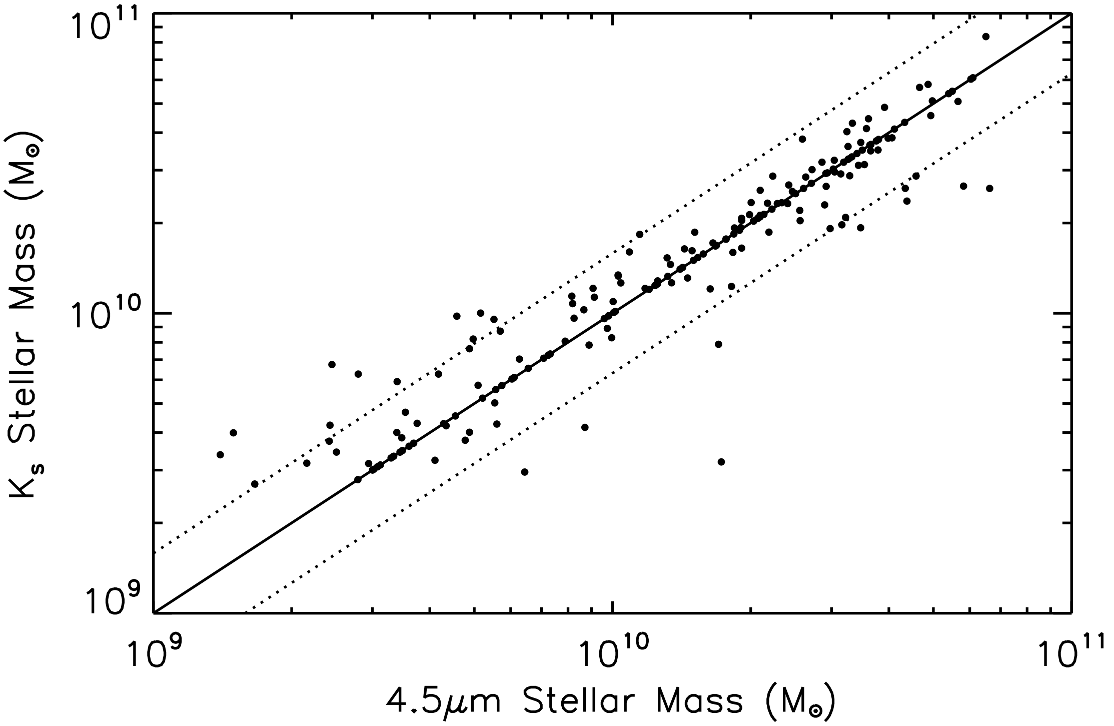

Figure 4.3 K_s–band derived stellar mass estimates vs. IRAC 4.5 μJy derived stellar masses for all cluster members with detections in both wavelengths. The 1:1 line is shown for comparison along with the 0.2 dex error associated with the M/L ratios, from the 1:1 line position, shown as dotted lines. K_s–band derived masses have been corrected to rest-band K at $z \sim 0.9$ using Equation 4.1.

With the K_s imaging complete to 21.8 mag, we achieve a lower completeness limit on the stellar mass of $\sim 2.3 \times 10^9\, M_\odot$, again derived using a red galaxy at $z = 0.9$.

To investigate the consistency of the IRAC versus K_s–band derived stellar masses, we use all sources within the cluster having detections in both the 4.5μm IRAC and K_s images and find the masses from both wavelengths as described above, with the K_s masses corrected using the second order fit found in Equation 4.1. These are plotted in Figure 4.3 with the 1:1 line shown for reference. We also plot the 0.2 dex error associated with the Bell et al. (2003) M/L ratios from the 1:1 line position, shown as dotted lines. The two mass estimates agree reasonably well, with the majority falling within the 0.2 dex errors of the 1:1 relation. From this we infer that our K_s–band derived masses will be comparable to the IRAC 4.5 μm stellar masses in this study.

4.3.3 24 μm Star Formation Rates

While the UV region of the galaxy spectrum is dominated by young stars, it can also be strongly obscured by dust, causing SFRs to be underestimated. The mid-infrared is sensitive to the stellar radiation that has been absorbed by the dust and re-emitted in the thermal infrared (Kennicutt, 1998). As such, it offers an ideal region of the spectrum from which to estimate unobscured galaxy SFRs.

At $z = 0.9$, the 24 μm emission corresponds to rest-frame $\sim$13 μm. This region of the spectrum contains polycyclic aromatic hydrocarbon (PAH) features, which recent studies suggest may have dust heating from alternate sources such as dusty active galactic nuclei (AGN) (eg. Daddi et al., 2007b; Papovich et al., 2007), intermediate age stars (Salim et al., 2009) or cooler, diffuse dust in the interstellar radiation field (Popescu et al., 2002), resulting in an overestimate of the SFR. In contrast, Rodighiero et al. (2010b) found that 24 μm estimated total IR luminosities are underestimated by $\sim$1.6 compared to *Herschel* PACS results for $0.5 < z < 1.0$ galaxies. Elbaz et al. (2010) see consistent results in the IR luminosities derived from 24 μm imaging and *Herscel* PACS and SPIRE fluxes for galaxies up to $z \sim 1.5$ for IR luminosities of $\sim 10^{10} - 10^{12}\,L_{\odot}$. Rieke et al. (2009) find that MIPS-24 μm-derived SFRs are accurate for $L_{IR} \geq 5 \times 10^{9}\,L_{\odot}$, but with a different L_{IR}-SFR conversion factor above $L_{IR} = 10^{11}\,L_{\odot}$. With all of the ambiguity as to the validity of MIPS-24 μm-derived SFRs, we choose to do as other studies have done (eg. Noble et al., 2013; Patel et al., 2011) and look at the *relative* differences in SFRs derived in this study.

The 24 μm SFR for each galaxy with a spectroscopic redshift is calculated by first converting the flux into a total infrared luminosity using the Chary & Elbaz (2001) spectral energy distribution (SED) templates. The infrared luminosity was converted to a SFR using the relation in Kennicutt (1998) of SFR $= 4.5 \times 10^{-44} L_{IR}$ (ergs/s). With an 80% completeness depth of 70 μJy in the MIPS data, we reach a lower SFR limit of $8\,M_\odot\,\mathrm{yr}^{-1}$ at $z = 0.9$.

There are 66 MIPS-24 μm galaxies found in the supercluster redshift range. Of these, 34 have infrared luminosities which classify them as luminous infrared galaxies (LIRG: $L_{IR} \geq 10^{11}\,L_\odot$, SFR $\sim 17\,M_\odot\,\mathrm{yr}^{-1}$ at $z \sim 0.9$), while three have luminosities placing them in the ultra-luminous IR galaxy range (ULIRG: $L_{IR} \geq 10^{12}\,L_\odot$, SFR $\sim 170\,M_\odot\,\mathrm{yr}^{-1}$ at $z \sim 0.9$). Local LIRGs and ULIRGs emit most of their energy in the IR, with the intense starburst activity most likely due to galaxy interactions and mergers (Sanders & Mirabel, 1996; Veilleux et al., 2002).

4.3.4 Radio Star Formation Rates

In normal radio galaxies not dominated by emission from active galactic nuclei (AGN) the majority of the radio continuum ($\sim$ 90%) is a result of massive, young stars ($M \sim 8\,M_\odot$, $\leq$ 30 Myr) whose core-collapse supernovae (SN) remnants accelerate relativistic electrons causing synchrotron radiation (Condon, 1992; Condon et al., 2002). Therefore the radio emission is a good tracer of the young stellar population in galaxies and can be used to estimate the galaxy SFR.

Table 4.3 Spectral Indices from Bondi et al. (2007) for $\sim$mJy Sources and Fomalont et al. (2006) for $\sim\mu$Jy Radio Galaxies.

1.4 GHz Flux (μJy)	α
$S < 75$	-0.87 ± 0.05
$75 \leq S < 100$	-0.78 ± 0.04
$100 \leq S < 150$	-0.61 ± 0.04
$150 \leq S < 500$	-0.46 ± 0.03
$500 \leq S$	-0.67 ± 0.05

Radio SFRs were computed by k-correcting the measured 1.4 GHz flux density using the relation $(1+z)\nu_o = \nu_e$ and the radio spectral index ($S_\nu \propto \nu^\alpha$). The spectral indices used are taken from Table 3 of Bondi et al. (2007) for ∼ mJy sources and from Fomalont et al. (2006) for ∼ μJy galaxies (see Table 4.3 for a summary). The corresponding luminosity was converted to a SFR using the relation of Condon et al. (2002),

$$\left(\frac{L_{1.4\ \mathrm{GHz}}}{\mathrm{W\,Hz^{-1}}}\right) \sim 4.6 \times 10^{21} \left[\frac{\mathrm{SFR}(M > 5M_\odot)}{M_\odot\,\mathrm{yr}^{-1}}\right]. \tag{4.2}$$

The 15 μJy depth of the data results in a lower limit on the radio SFR of 10 $M_\odot\,\mathrm{yr}^{-1}$. There are a total of fifteen radio members in the RCS 2319+00 structure over the full 35×35 arcminute region with spectroscopic coverage, with twelve falling in the MIPS-24 μm field of view.

Two of the radio supercluster members, located in the core of Cluster A, show extreme radio flux densities >1 mJy. One has extended radio flux and appears to be a head-tail source; an AGN with radio jets bent by the motion of the galaxy through the intracluster medium. If the radio emission was due solely to star formation this head-tail galaxy would have a SFR of 3900 $M_\odot\,\mathrm{yr}^{-1}$ while the other high flux radio galaxy, at a slightly more southern position, would have a SFR of 800 $M_\odot\,\mathrm{yr}^{-1}$. Radio galaxies with > 1 mJy flux are though to be powered primarily by AGN (Norris et al., 2006).

Sources with both 24 μm and radio counterparts allow for a direct comparison of their flux values. Of the twelve radio supercluster members within the MIPS field of view, five are found to have 24 μm counterparts. The galaxies and their information are listed in Table 4.4.

A comparison of the $\mathrm{SFR}_{24\mu\mathrm{m}}$ against the $\mathrm{SFR}_{1.4\mathrm{GHz}}$ gives an average ratio of 2.7 ± 1.4 for these five galaxies. Removing the two ULIRGs, this factor drops to 1.0 ± 0.4, with the ULIRGs having infrared SFRs 4.6 and 5.8 times larger than the

Table 4.4 RCS 2319+00 Supercluster Members with $24\,\mu$m and 1.4 GHz Detections

Source ID	z	Group	$L_{\rm IR}$ ($10^{11}\,L_\odot$)	SFR$_{24\mu\rm m}$ ($M_\odot\,\rm yr^{-1}$)	SFR$_{\rm 1.4GHz}$ ($M_\odot\,\rm yr^{-1}$)	q[a]	X-Ray [b] Detection
485V	0.881	···	1.4×10^{12}	242	53	1.21 ± 0.13	···
328B-FMOS	0.918	···	7.7×10^{11}	133	204	0.30 ± 0.04	···
382B	0.898	···	5.8×10^{11}	100	70	0.71 ± 0.12	···
465C	0.877	Group 3	2.3×10^{12}	402	70	1.27 ± 0.12	no
23V	0.909	Filament	2.5×10^{11}	43	48	0.61 ± 0.20	yes

[a] The MIR/radio correlation parameter $q = \log(f_{24\mu\rm m}/f_{\rm 1.4GHz})$, discussed in Appendix B

[b] Galaxies not in the field of view of the X-ray data are indicated by three dots

radio SFRs. The larger SFRs detected in $24\,\mu$m may be due to the intense starburst activity in the ULIRGs, which would enhance the MIR emission from the thermal dust while the radio emission remains suppressed, as the supernova activity follows from the star formation activity, but with a ∼30 Myr delay (Huynh et al., 2010a; Condon, 1992). Local ULIRGs have gas depletion timescales of 10–100 Myr (e.g., Solomon & Vanden Bout, 2005) with preliminary results on high-redshift luminous IR galaxies having consistent short lifetimes of ∼10 Myr for a $z = 2.6$ hyper-LIRG, starburst galaxy (Carilli et al., 2005) and ∼70 Myr for a $z = 1.2$ ultra-luminous merging galaxy (Frayer et al., 2008). Therefore, the probability that we are witnessing these ULIRGs at a time in their life when their radio emission has not yet been triggered is high, given the short star-forming lifetimes of the ULIRGs.

Figure 4.2 shows all supercluster galaxies with SFRs, either from the MIPS-$24\,\mu$m (66 galaxies - black symbols) or radio (7 galaxies - red symbols) flux densities, indicated by solid circles whose size increases with increasing SFR. The ULIRGs are shown as star, again with their size increasing with SFR (240, 400, and 510 $M_\odot\,\rm yr^{-1}$). The two strong radio galaxies, the Head-tail and Southern galaxies, are indicated with black crosses. For all IR star formation rate comparisons we use only the MIPS-detected supercluster galaxies, with the radio SFRs added in only as supporting data in looking at SFRs versus stellar mass. For this reason, we use the $24\,\mu$m SFRs for the five galaxies with both IR and radio SFRs.

4.3.5 AGN Contamination

MIPS 24 μm SFRs do not take into account any boosting of the flux from active galactic nuclei (AGN). Based on studies of the AGN population at high redshift we expect that the fraction of MIPS supercluster galaxies that are dominated by AGN is small. Fadda et al. (2010) found that the fraction of AGN dominated IR field galaxies at $z \sim 1$ is ~5% and that LIRGs at this redshift have an average spectrum consistent with starburst galaxies in the local Universe. A study of the AGN fraction in clusters by Martini et al. (2009) conclude that, though increasing with redshift, the AGN fraction is only 1.47% at $z \sim 0.8$. Another study, by Fu et al. (2010) found that at $z \sim 0.8$ AGN are missing in 24 μm galaxies with fluxes below 0.8 mJy and AGN only begin to dominate the IR emission in galaxies with > 1.2 mJy MIPS detections. Only the three supercluster ULIRGs have 24 μm fluxes above 0.8 mJy, with only two of those having >1.2 mJy fluxes. In Appendix B we look to the ancillary data to confirm a small AGN contamination of our MIPS supercluster galaxies and set a generous AGN contamination rate of ~7–10%. However, it is likely that only one or two of our 24 μm-derived SFRs are considerably boosted by AGN.

4.4 Stellar Mass as a Function of Environment

4.4.1 Mapping the Stellar Mass Distribution

In Figure 4.4 we plot the distribution of the stellar mass in the central 24×24 arcminute region of the RCS 2319+00 supercluster field over the red-sequence galaxy density contours from the R_c and z' photometry (L.F. Barrientos et al., in preparation). The K_s imaging covers a 21.5×21.5 arcminute region within this area while the IRAC 4.5 μm imaging (IRAC Channel 2&4, see Figure 4.1) covers a similar region and orientation as the MIPS field of view, which is shown with dotted lines in

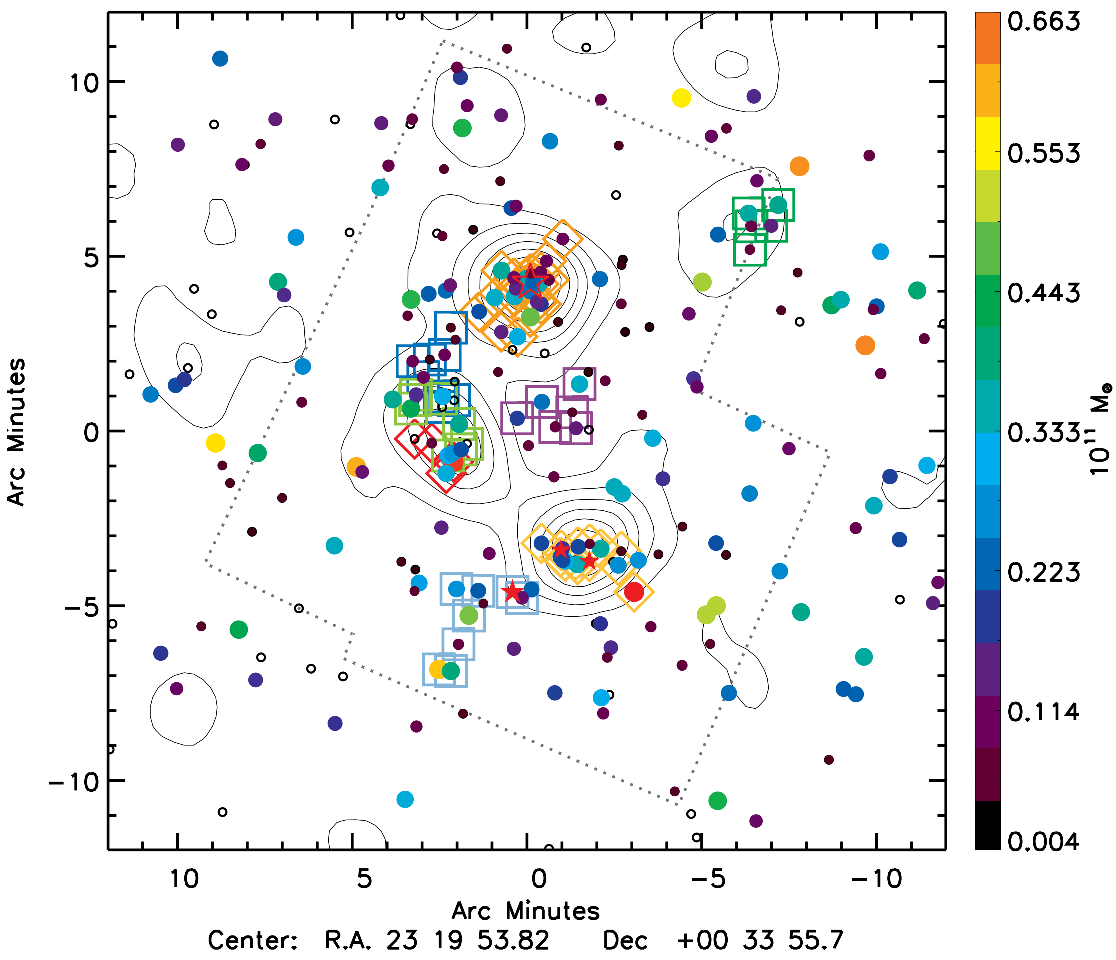

Figure 4.4 Distribution of the stellar mass in the central 24 × 24 arcminute region of the RCS 2319+00 supercluster field over the red-sequence galaxy density contours from the RCS-1 survey (L.F. Barrientos et al., in preparation). Symbol size and colour varies with stellar mass. Empty circles represent spectroscopically confirmed supercluster members with no stellar mass estimates. Open diamonds (squares) indicate galaxies belonging to the cluster cores (groups), with colours that match those listed for the groups in Table 4.2. The MIPS field of view is indicated by dotted lines.

the figure. The symbol size and colour varies with stellar mass. Open circles denote supercluster members that do not have detections in either the IRAC 4.5 μm imaging or the WIRCam K_s imaging. The most massive $\geq 10^{11}\,M_\odot$ galaxies are shown as red stars whose size increases with increasing stellar mass, with the most massive galaxy ($2.3 \times 10^{11}\,M_\odot$), located at the center of Cluster A, shown as an empty star.

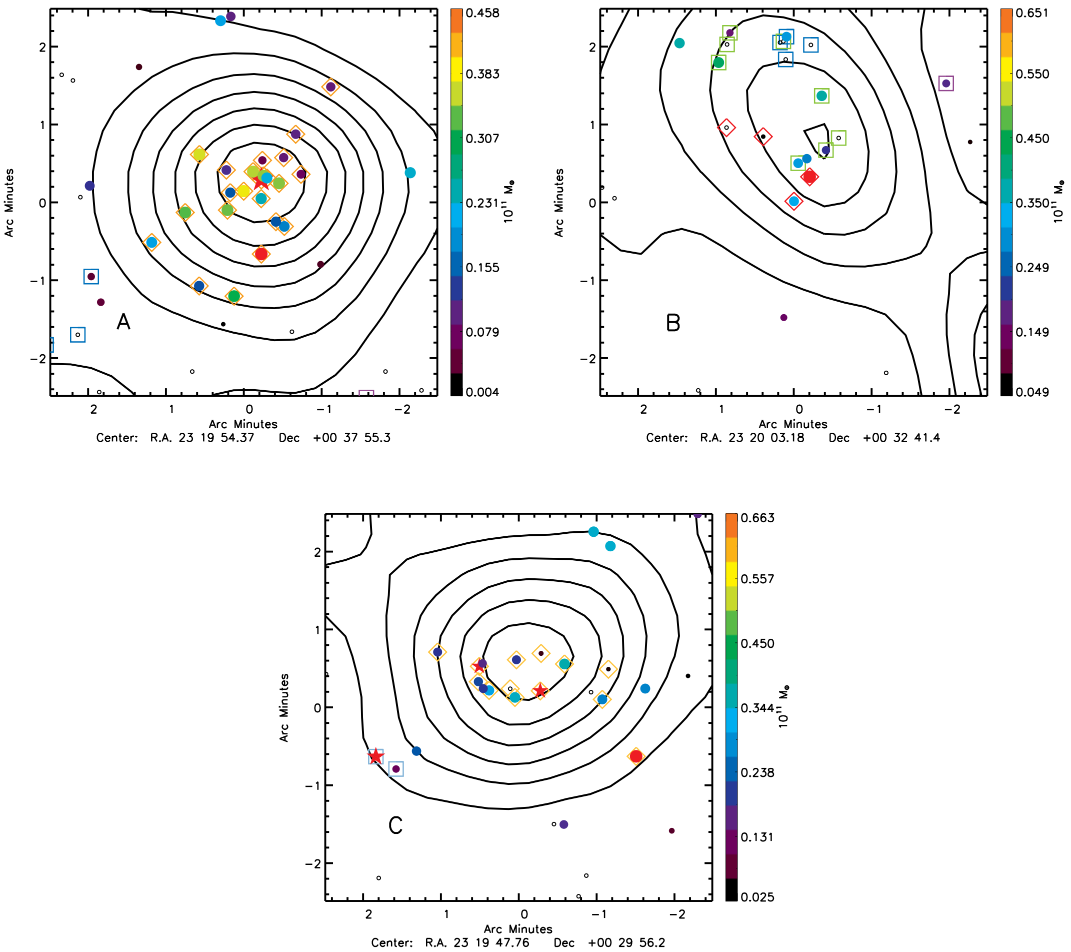

Figure 4.5 Zoomed distribution centered around the three cluster cores showing the stellar mass of spectroscopically confirmed galaxies over the red-sequence galaxy density contours. Symbols are the same as those in Figure 4.4.

The FOF-identified cluster core and group members are shown with diamonds and squares, respectively. Figure 4.5 shows the zoomed stellar mass distribution around the cluster cores.

We see indications that the massive galaxies are most prominent in high-density regions in the distribution of stellar mass in the cluster cores (Figure 4.5). One massive galaxy is found in Group 3, the filamentary group near Cluster C located in the lower redshift wall. This galaxy is one of our three ULIRGs, and has IRAC colours (see Figure B.1 in Appendix B) which classify it as an AGN, but with a radio

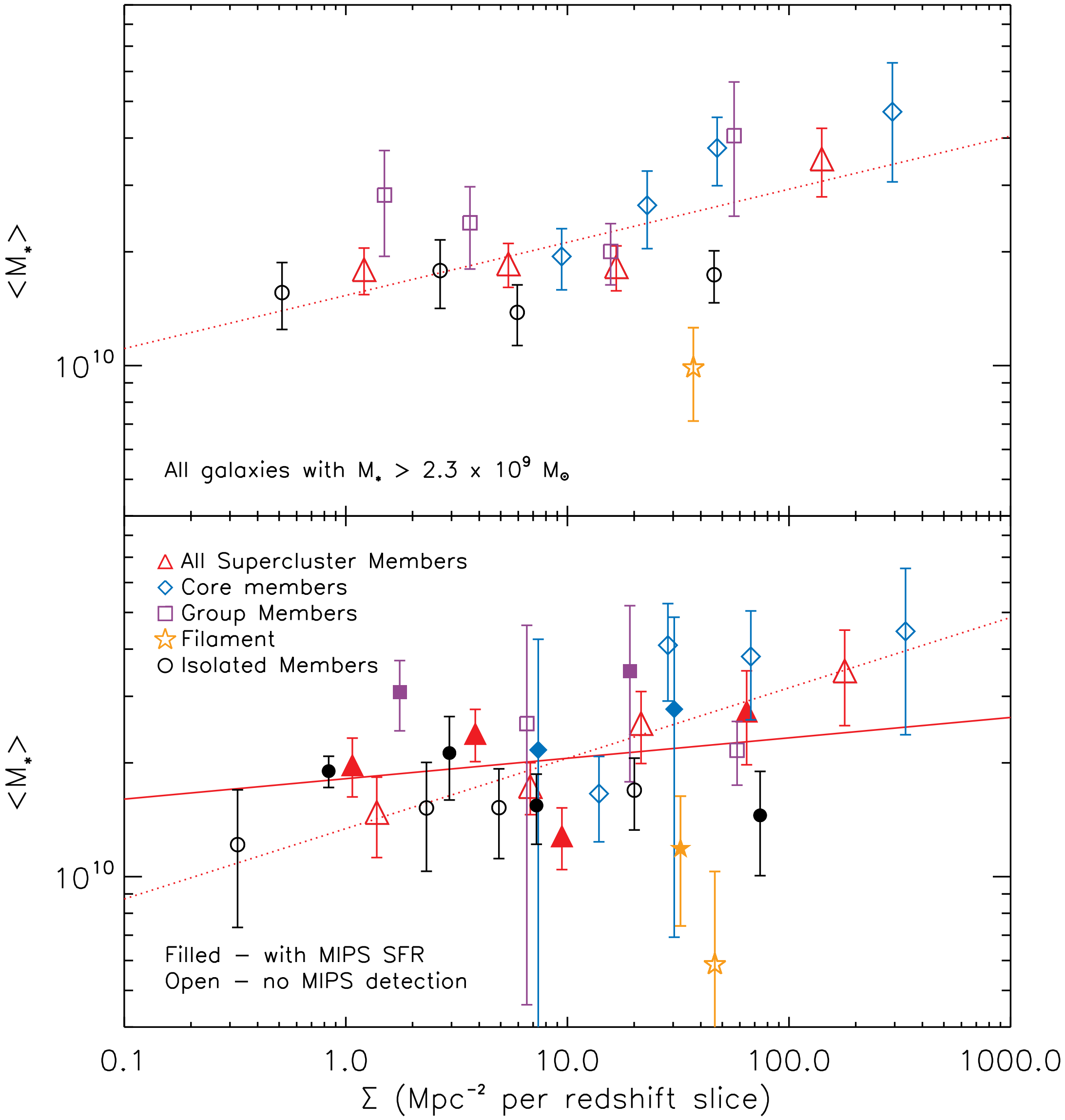

Figure 4.6 Stellar mass as a function of local galaxy density. Top: Average stellar mass over all galaxies with $M_* \geq 2.3 \times 10^9\,M_\odot$, binned in density so that each bin has the same number of galaxies. Errors are found using 100 bootstrap resamplings of the binned data. The best-fit line is shown over all supercluster galaxies. Bottom: Average stellar mass for the supercluster galaxies separated into the $24\,\mu$m detected star-forming (filled symbols, solid best-fit line) and non-SF (i.e., no MIPS detection; open symbols, dotted best-fit line) populations.

SFR ∼6 times lower than the MIR SFR.

We plot the stellar mass as a function of the local density in Figure 4.6. The local density is defined as the number of galaxies per Mpc^2 using the 5th nearest neighbour to define the distance limit. We also apply a limit on the redshift around each galaxy of $\pm 1500\,\mathrm{km\,s^{-1}}$ in an effort to minimize projection effects. For each cluster member with a stellar mass above the $2.3 \times 10^9\,M_\odot$ completeness limit we use the spectroscopic completeness correction weighting calculated over the MIPS imaging area, as done in Section 2.3.2, to interpolate the distance to the 5th nearest neighbour in the $\pm 1500\,\mathrm{km\,s^{-1}}$ redshift slice. The local density is then $\Sigma = N_{gals}/(\pi d^2)$, where N_{gals} is the sum of the spectroscopic completeness weights closest to 5 and d is the distance to that galaxy.

The top panel of Figure 4.6 shows the average stellar mass per density bin for each of the different FOF defined density categories as well as over all supercluster galaxies (red triangles) above the mass completeness limit in the MIPS field of view. The bins are chosen to contain an equal number of galaxies per bin per density category. All of the Filament galaxies are contained in a single bin due to the limited number of members. Minimizing the chi-squared statistic for the log-log plot gives a best-fit line over all galaxies that shows, on average, the stellar mass increasing with increasing local density at a slope of 0.14, with a 1σ error of ± 0.07.

The division of the supercluster members into their different density categories allows us to study the global environment (i.e., the mass of the halo in which the galaxies reside: field, group or cluster sized) in addition to the local environment. The core population shows a strong positive correlation between stellar mass and local density consistent with the overall trend, with a slope of 0.25 ± 0.15. The group and isolated supercluster galaxies, however, do not follow the positive correlation as well as the cores. The best-fit lines for both are consistent with a flat slope at 0.08 ± 0.12 and 0.01 ± 0.07 for the groups and isolated galaxies, though the group galaxies have mean stellar masses higher than their isolated counterparts at similar densities. The group galaxies do have higher masses in the highest density group bin but overall show no correlation with local density.

The Filament galaxies lie well below the best-fit line with the lowest average stellar mass and a higher than expected density. They contribute to the lower mean stellar mass of the second largest density bin in the full supercluster galaxy sample. This may be due to projection effects despite our efforts to minimize this using redshift slices. The Filament galaxies fall between Clusters A and B, which are in the same redshift wall (see Figure 4.2), and are along the line-of-sight of Group 2 and several isolated galaxies (see also Figure 4.4 and 4.5) that may be included in the redshift slices used for the calculation of local density around each galaxy.

In the bottom panel we divide the galaxies between the star-forming and the non-star-forming populations (SF galaxies - solid symbols, non-SF galaxies - open symbols) designated using the 24 μm-derived SFRs only for consistency. Again, the mean stellar mass per density bin over all supercluster galaxies is shown with red triangles. The non-SF galaxies show an increase in mean stellar mass with density with a best fit line of 0.19 ± 0.10. This trend is again consistent over the core environment. The groups do not contain enough non-SF members to fit the data, however their binned points are consistent with the overall slope, within errors. The isolated non-SF galaxies show a slight positive correlation, though at about half the slope of the overall and core populations at 0.08 ± 0.15.

The star-forming galaxies show no dependence of the stellar mass on environment and are consistent with a zero slope at 0.05 ± 0.13. The lack of correlation between the SF galaxies' stellar mass and local density is driven by the isolated supercluster galaxy population, which accounts for $\sim 62\%$ of the MIPS star-forming population in the supercluster (41/66). The best-fit line to the SF isolated galaxies is -0.07 ± 0.09.

The SF galaxies are lacking in the highest density bins in all global environments with the SF core, group, Filament and isolated members, all reaching local densities of only ∼20–30 Mpc^{-2} per redshift slice. The only exception to this is an isolated ULIRG in the line of sight of Cluster C, which has a local density of ∼380 Mpc^{-2} per redshift slice due to its proximity to both Cluster C and Group 3 (see Figure 4.2). This isolated ULIRG pulls the isolated galaxies to a higher local density bin then is representative of their overall population. Removing the ULIRG from the sample does not change the overall trend between stellar mass and local density, either in the isolated SF population or over the full SF population. The limited number of core and group SF galaxies (8 and 17 respectively) does not allow for an adequate view of their mass-density relations, though they are consistent with the overall SF galaxy trend of no increase in stellar mass with local density.

We note once again that the Filament population seems to be an outlier to the overall galaxy trends for stellar mass as a function of local density, with stellar mass falling below the trend for the other populations. In contrast to the results for the isolated galaxies, it is the non-star-forming Filament galaxies that show a larger disparity in stellar mass at similar density compared to the other FOF categories rather than the star-forming galaxies.

Summing up our results we find that overall, the galaxies in the RCS 2319+00 supercluster follow the expected mass segregation relation with increasing stellar mass at increasing local density. Dividing the members into their global environments retains this positive correlation, though with decreasing slopes from the core through group and isolated environments. Separating out the non-star-forming supercluster galaxies conserves the same correlations. In contrast, the star-forming galaxies show no correlation between their stellar mass and local galaxy density. We also note the lower overall stellar masses of the isolated galaxies compared to their similar local density core and group counterparts. As well, the Filament environments appears to be an outlier to all other global environments.

4.4.2 Discussion: Mass Segregation – Global Versus Local Density

The so called mass segregation scenario, where the stellar and halo mass of galaxies increases with local density, is a product of hierarchical model formation (e.g., Mo & White, 1996; Sheth & Tormen, 2002) and has been shown observationally (e.g., Scodeggio et al., 2009; Vulcani et al., 2012). Using a mix of cluster and field galaxy survey data Vulcani et al. (2012) and Vulcani et al. (2013) showed that the global environment had no statistical relevance on the shape of the mass function, concluding that the local density was the driving force in the stellar mass distribution.

In general our results for the RCS 2319+00 supercluster concur with this finding. The mean stellar mass in each of the FOF-designated global environments follows the same trend of increasing stellar mass with increasing local density as the full supercluster galaxy sample. On the other hand, though the limited galaxy numbers in our sample results in large errors we do see that, while the overall positive correlation is maintained between global environments, the least dense global environment, that of the isolated supercluster galaxies, has stellar masses consistently lower than the groups and cores at the same local densities. Also, though the isolated supercluster galaxies are consistent with the overall positive correlation within 2σ, we could also argue that there is no correlation between stellar mass and local density for this population.

As mentioned in the previous section, the larger positive correlation in the group environment is driven by the highest density bin. If we compare the isolated and group galaxies only to the same local densities of $\sim 20\,\mathrm{Mpc}^{-2}$, the group galaxies show a similar flat (even declining) relation with local density. Looking at the results in Figure 10 of the Vulcani et al. (2012) study shows that the highest density bins in their field samples are driving the positive correlations that are consistent with the cluster results. Their field samples, however, are contaminated by galaxy pairs and groups, and potentially by cluster galaxies not removed from the overall field samples. Thus the discrepancy between our study, where despite low numbers we see a hint of fracturing between the mass–density relation in the different global environments, and the Vulcani et al. (2012) results that see consistency in all environments, is likely due to our more rigorous definition of isolated supercluster galaxies. The relations seen for the different global environments are retained when removing all SF galaxies from the sample and looking at only those galaxies with no $24\,\mu$m detection.

Of interest is the apparent flat slope between average stellar mass and local density when isolating the star-forming population, despite the SF galaxies covering the full range of stellar masses (see Figure 4.9). The core and group SF galaxies have average stellar masses higher then the isolated galaxies in the same local density ranges. The discrepancy in stellar mass is not as strong for the non-SF galaxies. This perhaps is an indication that the global environment and not the local environment is playing a role in the mass-density relation for star-forming galaxies, whereas the local density is dominating the relation in the non-star-forming galaxies. To further test the relative influence of the global and local environment on galaxy mass in the RCS 2319+00 supercluster would require larger numbers of spectroscopic members to boost the statistics. Alternatively, well categorized samples of isolated, group and cluster galaxies over a larger sample of clusters would provide a thorough test of the deviations from mass-segregation that we see above.

4.5 Star Formation as a Function of Environment

4.5.1 Mapping the Star Formation in RCS 2319+00

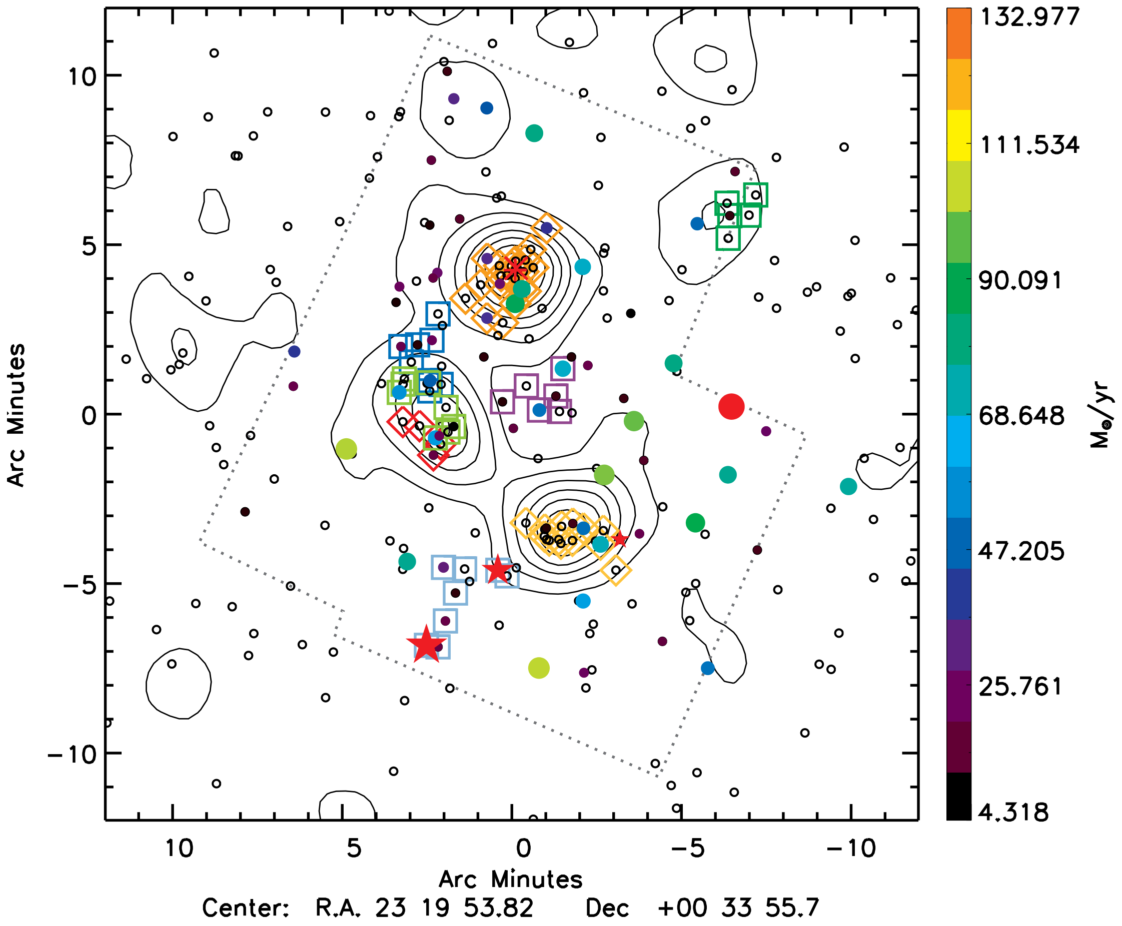

Figure 4.7 Distribution of the star formation in the RCS 2319+00 supercluster field. Symbol colour varies and size increases with increasing SFR. Red stars identify the three ULIRGs. Empty circles represent spectroscopically confirmed supercluster members that do not have detections in either the MIPS-24 μm imaging or the VLA 1.4 GHz data.

We plot the SFR distribution of all cluster members in Figure 4.7 for all galaxies with measured SFRs (66 MIPS and 7 radio galaxies in the 24×24 arcminute region plotted). We summarize the statistics of the 24 μm galaxies in Table 4.5 over the full supercluster (within the MIPS field of view) and divided into the different FOF density regions. Looking at only the 24 μm-derived SFRs we find that, of the 167 total cluster members in the MIPS field of view, the 66 MIPS galaxies make up ~40%±5% of the supercluster members. The fractions of galaxies detected in 24 μm in the various regions of the supercluster range from a high of ~ 52% in groups to a low of ~19% in the center of the cluster core regions. We note however, that due to the optical selection of our spectroscopic catalogue the fraction of star-forming galaxies may change in all regions of the superstructure field given additional confirmed cluster members. In fact, only six of the LIRG-level 24 μm supercluster members derive from the NIR FMOS spectrograph rather than the optical spectroscopy. Approximately one third of the 24 μm detected sources in the RCS 2319+00 field have z' magnitudes brighter than 22 mag, the magnitude range containing ~ 75% of all confident redshifts (see Section 2.3.1). Therefore, the majority of the MIPS sources are fainter in the optical than the level at which the spectroscopy is able to successfully yield confident redshifts.

If we look only at the LIRGs, at which level the MIPS data is 80% complete (i.e., above the 80% completeness limit of $8 M_{\odot}\,\mathrm{yr}^{-1}$), they account for 20%±3% of the supercluster galaxies, with the three ULIRGs accounting for only 2%±1% of the cluster population. We find that the LIRGs in our supercluster field are found predominantly in the less dense isolated supercluster galaxy population, with ~62% of the LIRGs found in these lower density regions. As noted in Chapter 3, further spectroscopic members may link more of the isolated supercluster population into larger groups, however, the fraction of unassociated supercluster galaxies is expected to remain high.

Figure 4.8 shows the stacked phase space diagrams of the core and group galaxies, where the relative velocity versus radius is from the cluster core/group center and mean redshift. Cluster members with SFRs are indicated by solid circles ($\mathrm{SFR}_{24\mu\mathrm{m}}$

Table 4.5 $24\,\mu$m Star Forming Galaxies in the Different Global Environments of the RCS 2319+00 Supercluster Within the MIPS Field of View

	$N_{\rm gals}$	$N_{24\,\mu{\rm m}}$	$N_{\rm LIRG}$	$N_{\rm ULIRG}$	$f_{24\,\mu{\rm m}}$	$f_{\rm LIRG}$	$f_{\rm ULIRG}$
All galaxies	167	66	34	3	0.40 ± 0.05	0.20 ± 0.03	0.02 ± 0.01
Core galaxies	40	8	6	0	0.20 ± 0.07	0.15 ± 0.06	···
≤0.5 Mpc[a]	32	6	4	0	0.19 ± 0.08	0.13 ± 0.06	···
>0.5 Mpc[b]	8	2	2	0	0.25 ± 0.18	0.25 ± 0.18	···
Groups[c]	33	17	7	2	0.52 ± 0.12	0.21 ± 0.08	0.06 ± 0.04
Filament	9	4	3	0	0.44 ± 0.22	0.33 ± 0.19	···
Isolated galaxies	94	41	21	1	0.44 ± 0.07	0.20 ± 0.05	0.01 ± 0.01

[a] FOF-identified cluster core galaxies within 0.5 Mpc of the X-ray cluster centers
[b] FOF-identified cluster core galaxies with radii > 0.5 Mpc to the X-ray cluster centers
[c] Includes all five FOF-identified groups, including the Filament

- black, $\rm SFR_{1.4GHz}$ -red) with their size increasing with SFR. The Xs indicate the galaxies with X-ray counterparts while the red crosses show the radio counterparts to $24\,\mu$m galaxies, with the high flux radio sources at the center of Cluster A shown with black crosses. These high-flux radio galaxies are likely strong AGN sources, however, they do not have $24\,\mu$m counterparts and therefore do not contaminate our MIPS population. The middle (bottom), left-hand panel shows that the fraction of all $24\,\mu$m (LIRG-level) core galaxies increases slightly with increasing cluster centric radius, though the errors are large due to small numbers. If we look at the overall fractions in the densest regions around the cores, those within 0.5 Mpc of the cluster centers (i.e., cumulative fraction over all radius bins $\leq$ 0.5 Mpc), we find that the fraction of $24\,\mu$m galaxies has remained consistent, dropping only slightly ($f_{\rm LIRG} \sim 0.13$, $f_{24\,\mu{\rm m}} \sim 0.19$).

About half of all identified group galaxies are star-forming ($f_{24\,\mu{\rm m}} \sim 0.52 \pm 0.12$). Due to the filamentary nature of many of the groups (see the spatial distribution in Figure 4.7) the radius from the average group center is not very meaningful, though we do see in Figure 4.8 that there are no LIRGs located in the spatial centers of the groups and that the ULIRGs in Group 3 are found at the ends of the filamentary structure.

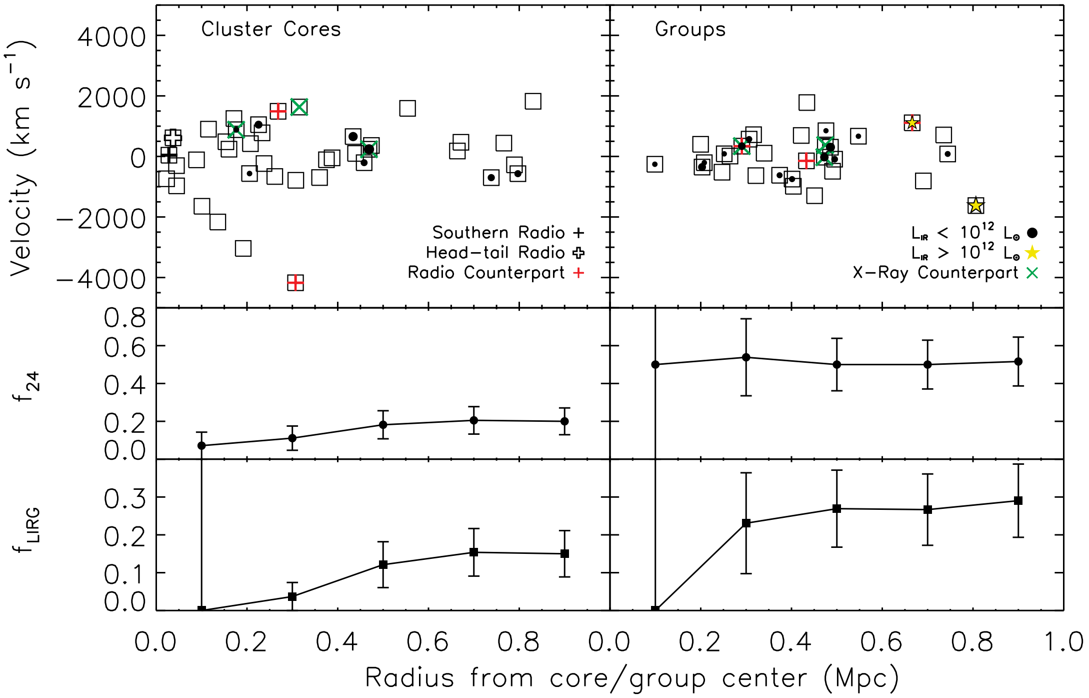

Figure 4.8 Top: Stacked relative velocity vs. core/group centric radius of members identified in the FOF groups. The centers of the cluster cores are determined by the peak of the cluster X-ray emission and the centers of the groups are determined by the average of the coordinates of the group members. The solid circles show galaxies with SFRs (black: 24 μm, red: 1.4 GHz) with symbol size increasing with increasing SFR and ULIRGs shown as yellow stars. MIPS galaxies with radio counterparts have red crosses and the green X marks denote galaxies with X-ray counterparts. Open squares are non-SF core/group galaxies. Middle: Fraction of MIPS-24 μm galaxies per radius bin with Poisson errors. Bottom: Fraction of LIRGs per radius bin.

In the supercluster field, MIPS galaxies account for ∼44% of the isolated cluster galaxies, though only about half of those have LIRG-level luminosities. Therefore, considering only LIRG-level SF galaxies, the fraction of SF galaxies in all density levels of the supercluster is consistent within errors at ∼20%, meaning the SFR-density relation at this luminosity level is flat for the supercluster. It is only upon adding the <LIRG-level SF galaxies that there appears to be a decline in the SF fraction at the highest densities, with only ∼20% of galaxies in the cluster cores being SF compared to the ∼45% in the group and isolated supercluster galaxies.

We note that we have not placed a mass limit on our star-forming population. However, as we will see in Section 4.7, only five star-forming galaxies have either no stellar mass estimate (one <LIRG-level galaxy in Group 2) or a stellar masses below the completeness limit (four isolated galaxies, only one having a LIRG-level IR luminosity). Therefore, the lack of stellar mass limit does not greatly affect the results, especially considering the large errors already associated with the SF fractions.

Reiterating the main results, we find that 40%±5% of all supercluster galaxies in the MIPS field of view are detected at 24 μm, with a 20%±3% contribution from LIRG-level galaxies and 2%±1% from the three ULIRGs. The fraction of LIRGs is consistent over our three density populations at ∼20%. A difference in the fraction of SF galaxies over the global environments is only detected when examining the fraction of all detected 24 μm galaxies, including those below the 80% MIPS completeness limit, with the primary location of star formation found to be at lower densities while avoiding the cluster cores.

4.5.2 Discussion: Growth in the Outskirts

There is conflicting evidence as to the preferential location for star-forming galaxies at $z \sim 1$. Some recent studies show that by redshift $z \sim 1$ the SFR-density relation flips from the local relation, with dominant sites of star formation moving to higher density regions (e.g., Cooper et al., 2008; Elbaz et al., 2007; Bai et al., 2007; Marcillac et al., 2007). Other studies, however, show evidence that the primary location of star-forming galaxies remains at lower densities at $z \sim 1$ (e.g., Patel et al., 2009, 2011; Koyama et al., 2010; Muzzin et al., 2012; Webb et al., 2013; Noble et al., 2013). Moreover, some studies have found no correlation between higher SFRs and the environment (e.g., Finn et al., 2010; Feruglio et al., 2010). In the zCOSMOS field, Caputi et al. (2009a) found that LIRGs preferred high density regions whereas

ULIRGs are found in less dense regions.

In RCS 2319+00, the overall number of LIRGs is highest in the isolated population, which contains just over half of the supercluster members, at three times the number over either the groups or cluster cores. Within each global environment, however, the fraction of LIRG galaxies remains consistent at ∼20%. The results of the RCS 2319+00 supercluster are therefore consistent with the studies showing that LIRGs prefer less dense regions as well as those showing that the fraction of galaxies with higher SFRs within each density level is independent of environment.

Our total 24 μm galaxy fraction in the cluster cores is consistent with other clusters at similar redshift. This is seen when comparing our ∼20% overall MIPS and LIRG fractions in the cluster cores to the ∼19% MIPS membership within $\sim r_{200}$ of a $z = 0.87$ cluster studied by Noble et al. (2013). In lower ($z = 0.165, 0.35$) and higher ($z = 0.8$) redshift superclusters and cluster/group systems, the fraction of SF galaxies is greatest in the groups and cluster outskirts compared to the denser cluster cores (e.g., Gallazzi et al., 2009; Tran et al., 2009; Koyama et al., 2010). Similarly, in higher redshift clusters the fraction of 24 μm cluster galaxies is seen to increase with increasing cluster centric radius (e.g., Finn et al., 2010) or relative velocity (Noble et al., 2013), indicating that SF galaxies are predominantly an infalling or recently accreted population. This is again consistent with the higher fraction of all MIPS supercluster galaxies in the group (∼52%) and infalling isolated (∼44%) galaxy populations of RCS 2319+00 compared to the cores (∼20%).

While we do not have a similar redshift field comparison sample over a consistent multiwavelength coverage area and depth to the RCS 2319+00 field that also includes spectroscopy, our results suggest that SF galaxies at $z \sim 1$ avoid the densest regions. This is consistent with the studies showing that the primary location for star formation remains at lower densities at $z \sim 1$, similar to the local SFR-density relation. Popesso et al. (2011), using two cluster systems in the process of forming (two groups merging at $z = 1.02$ and a $z = 0.73$ system of two clusters between two filaments) have suggested that the reversal in the SFR-density relation at $z \sim 1$ seen by some studies is a result of AGN that are found in high stellar mass galaxies in high density regions with high SFRs. They find a flattening of the relation once AGN are accounted for, similar to the results for the LIRG-level fractions found in this study, where we have already determined that the possible AGN boosting of our MIPS-derived SFRs is low (Section 4.3.5).

As mentioned in Section 1.6, the difference in results as to the nature of the SFR-density relation at $z \sim 1$ may be due to the different methods used in the various studies. For example, looking at the fraction of 24 μm galaxies in the different global environments, as done above, is consistent with the methods used in the studies of Bai et al. (2007), Marcillac et al. (2007) and Webb et al. (2013), who all compare MIPS fractions between cluster samples and the field. However, the first two studies, both finding a reversal in the SFR-density at $z \sim 1$, use specific members of clusters while the last uses statistical background subtraction over a large sample of clusters, finding no significant change in the SFR-density relation. Other studies use the mean SFR (e.g., Cooper et al., 2008; Elbaz et al., 2007) or mean SSFR (e.g., Cooper et al., 2008; Patel et al., 2009, 2011; Noble et al., 2013) versus local density to investigate the SFR-density relation. Even among a single study, for example that of Cooper et al. (2008), the two methods can give conflicting results, with the SSFR versus local density following the local universe relation while the SFR versus local density shows a reversal at higher redshift.

In the following sections we attempt to incorporate a variety of these methods to better understand the SFR-density relation in the RCS 2319+00 supercluster. We aim to test whether our current conclusion, that we see no change from the local to the

Table 4.6 Total SFR Estimates for the Different Substructures Within the MIPS Field of View

Group	$N_{\rm gals}$	$N_{24\,\mu{\rm m}}$	ΣSFR ($M_\odot$ yr^{-1})	ΣSFR$_{\rm Cor}$ ($M_\odot$ yr^{-1})	<SFR>[a] ($M_\odot$ yr^{-1} gal^{-1})	<SSFR> (Gyr^{-1} gal^{-1})
All Galaxies	167	66	3240	15890	49 (33)	2.6 (2.5)
Cluster A	23	4	180	800	45	2.3
Cluster B	4	1	15	110	15	0.5
Cluster C	13	3	120	640	41	2.0
CORE AVERAGE	···	···	110	520	40	2.0
Filament	9	4	90	530	22	2.2
Group 1	6	4	130	690	32	3.3
Group 2	8	2	60	400	30	1.0
Group 3	8	6	980	4070	163	2.8
Group 4[b]	2	1	10	52	10	1.1
GROUP AVERAGE	···	···	250	1150	74 (23)	2.6 (2.1)
Isolated Galaxies	94	34	1620	8580	41 (36)	2.7 (2.7)

[a] The mean SFR and SSFR per 24 μm galaxy is calculated based on the average over all SF galaxies per population rather than the average of the mean value given for each cluster/group. Values in parenthesis are averages calculated excluding the ULIRGs.

[b] Group 4 borders the MIPS area (see Figure 4.4, 4.7 or 4.11) and we therefore only include galaxies that fall within the 24 μm field of view

$z \sim 1$ SFR-density relation, will remain consistent when using different approaches to investigate the relation.

4.5.3 Total Star Formation Rate as a Function of Global Environment

Beyond looking at the location of the SF galaxies, we also look at the total SFR per density region to further gauge the role, if any, that the environment may play on the star formation activity of galaxies. Table 4.6 lists the total SFRs (ΣSFR) calculated per group and over all galaxies within the different density environments. Summing all star formation over each global environment serves to compare the amount of star formation activity in each environment where the fraction of SF galaxies may be similar (e.g., the ∼17–25% SF galaxy fraction in all cluster cores). Though we do not normalize based on cluster/group mass in the ΣSFR estimates, this should not affect the overall trends shown. A study by Goto (2005) on 115 $z \leq 0.09$ SDSS galaxy clusters found that the ΣSFR as well as the ΣSFR normalized by cluster mass and the fraction of blue galaxies in clusters were all independent of cluster virial mass.

Also listed in Table 4.6 are the estimates of the mean SFR (<SFR>) and mean

SSFR (<SSFR>) per 24 μm galaxy in each region. Looking at the mean SFR per star-forming galaxy in different areas extends the investigation of the distribution of SF galaxies in each environment from studying the fraction in each population to observing any increase or depression of the average star formation activity in those environments. Though some regions may show an increased fraction of SF galaxies, their ΣSFR and <SFR> may indicate reduced SF activity compared to areas with lower SF fractions. The SSFR, which is the SFR per unit stellar mass of a galaxy, gives an indication of the efficiency of the stellar mass build-up based on the current SFR, i.e., a lower stellar mass galaxy with similar SFR to a higher stellar mass galaxy is currently growing its mass at a more efficient, higher rate. Therefore the <SSFR> will give an indication of whether the average stellar mass build-up in the given environment is enhanced due to star formation.

The corrected total SFR ($\Sigma\mathrm{SFR}_{\mathrm{Cor}}$) is estimated using a simple correction factor applied to the ΣSFR of all galaxies to compensate for the incompleteness of the spectroscopy. This correction factor is found by taking the fraction of all galaxies within the MIPS field of view with 24 μm detections above the 70 μJy completeness limit over all of those with redshifts. This is similar to the magnitude factor of the spectroscopic completeness weighting used to find the local density in Section 4.4, though now over the MIR band rather than the z' optical component and for a single correction factor over the ΣSFR rather than unique weightings for each individual galaxy. For the $\Sigma\mathrm{SFR}_{\mathrm{Cor}}$ in each of the cores and groups, we use all MIPS galaxies above the completeness limit and use the area within r_{200} (cores) or 1 Mpc (groups) to find the localized correction factors.

The $\Sigma\mathrm{SFR}_{\mathrm{Cor}}$ varies greatly between the individual cluster cores and the different groups. Cluster A has a total SFR ∼7 times that of Cluster B, though it is more consistent with the $\Sigma\mathrm{SFR}_{\mathrm{Cor}}$ of Cluster C. This could again be due to the lack of spectroscopic members in Cluster B, discussed extensively in Chapters 2 and 3, though the correction factor applied should help account for the lack of member galaxies. The <SFRs> of the galaxies in Clusters A and B are consistent with one another. Cluster B, however, is based on a single MIPS member with a SFR lower by a factor of three than the other two cluster cores and requires more members in order to adequately compare its star-forming properties. This lower <SFR> based on a single SF galaxy is likely the reason for the low ΣSFR estimate.

The infalling groups show an even broader range of $\Sigma\mathrm{SFR}_{\mathrm{Cor}}$ and <SFR>. Group 4, the most distant group on the plane of the sky, seems to have had its star formation turned off, or perhaps not yet triggered. However, this group is on the edge of the MIPS field of view with only half of the group members falling within the MIPS area and therefore, as with Cluster B, the single $24\,\mu$m galaxy currently know may not be representative of the full group. Group 2 has a total SFR half that of Cluster A while Group 1's total SFR is similar to Cluster C. According to their elevated <SSFRs>, however, Groups 1 and 3 seem to be undergoing enhanced star formation. This is reflected in Group 3's inflated $\Sigma\mathrm{SFR}_{\mathrm{Cor}}$ but not to the same degree in the $\Sigma\mathrm{SFR}_{\mathrm{Cor}}$ of Group 1.

A study of $0.02 \leq z \leq 0.15$ Abell clusters by Mahajan et al. (2012) found increased <SFRs> were more probable in unrelaxed clusters that often housed starburst galaxies in the outskirts, with these clusters also showing higher ΣSFRs compared to more virialized clusters. Though Cluster A and C do not contain any ULIRGs, their strongest SF galaxies are found at radii of $\gtrsim 0.5$ (see Figures 4.2 and 4.7). Two ULIRGs are found at either end of the filamentary shaped Group 3. This may be indicative of these clusters and group being less dynamically relaxed than the other cluster and groups.

If we look at the overall SFR in the MIPS field of view over all cluster members, the combined core regions account for only ∼10% of the total star formation versus the ∼36% contribution from the groups and the ∼54% of star formation coming from the isolated supercluster galaxies on the outskirts of the clusters and groups, due to the larger fraction of 24 μm galaxies in these lower density regions. The average SSFR per galaxy is also highest in the isolated population, with the group average close to the isolated average, when including the ULIRGs, and both showing enhancement over the core galaxies, which have the lowest <SSFR>. This is again consistent with the primary location for star formation remaining at lower densities at $z \sim 1$, similar to the local SFR-density relation.

Over all 24 μm galaxies, the mean SFR is $\sim 49\,M_{\odot}\,\mathrm{yr}^{-1}$, or $\sim 33\,M_{\odot}\,\mathrm{yr}^{-1}$ if we exclude the three ULIRGs. This is higher than the <SFR> found by Marcillac et al. (2007) of $\sim 22\,M_{\odot}\,\mathrm{yr}^{-1}$ for non-AGN driven MIPS galaxies in a $z \sim 0.83$ galaxy cluster, with two merging X-ray peaks detected. However, Marcillac et al. (2007) use the galaxy templates of Dale & Helou (2002) to estimate L_{IR} while we use the Chary & Elbaz (2001) templates. This may result in differences in the SFRs, though tests on our own sample resulted in L_{IR} estimates $\sim 25\%$ higher when using the Dale & Helou (2002) templates as compared to the Chary & Elbaz (2001) templates. For this reason we believe we are seeing elevated SFRs in the RCS 2319+00 supercluster compared the the Marcillac et al. (2007) structure. The mean SFR of the dusty star-forming population in the isolated supercluster environment and the cores of RCS 2319+00 does not vary significantly. The two group ULIRGs boost the average SFR of dusty group galaxies to almost double the field and core level. Removing the ULIRGs, <SFR> in the groups is reduced to about half the core and isolated values.

Again we caution that the spectroscopic catalogue is derived mainly from optical spectroscopy and therefore the confirmed MIPS members are generally those that are brighter in the optical bands. This could mean that very dust-obscured star-forming galaxies that may add significant amounts of star formation to the populations are not included. Another issue may be that, though we are recovering the proper positions of groups in our FOF analysis, as noted in Section 3.2.4 we may be recovering members from a mixture of halos in that region, seen also by Farrens et al. (2011) in the FOF tests on their mock 2SLAQ simulation. If this is the case, the vast range of $\Sigma\mathrm{SFR}_{\mathrm{Cor}}$ we see in the groups may not be indicative of the true SFRs of that group's dark matter halo. We do however stress that the fraction of star-forming galaxies in RCS 2319+00 that do have spectroscopic redshifts have been studied in a uniform way over the full supercluster region.

We propose that the groups, whose $\Sigma\mathrm{SFR}_{\mathrm{Cor}}$, <SFRs> and <SSFRs> vary significantly, are in transitionary periods with some group galaxies having similar SF properties as field galaxies while others, accreted at earlier times perhaps, are more similar to cluster galaxies. The enhanced specific star formation in the galaxies in Groups 1 and 3 may be a result of galaxy mergers or gravitational tidal interactions (i.e., harassment) as galaxies accrete onto the groups, which could trigger enhanced bursts of star formation before quenching begins. This mechanism was proposed by Kocevski et al. (2011) for the infalling groups in the CL1604 $z \sim 0.9$ supercluster. In their study of the CL0016+16 $z = 0.55$ supercluster, Geach et al. (2011) find that, while there is an increased chance of tidal interactions which could trigger enhanced star formation in the infalling groups, there is no specific mechanism unique to the group environment causing the individual SFRs to be enhanced over the field. Given the long time-scales for groups and isolated supercluster galaxies on the outskirts of the cluster cores to accrete onto the final cluster, any enhanced star formation would likely cause the build up of significant stellar mass given that ram-pressure stripping, which can curtail star formation, is inefficient in the lower density intragroup and intracluster medium (e.g., Gunn & Gott, 1972; Moore et al., 1996).

4.5.4 Discussion: Star Formation in the Filament

Interestingly, the Filament has a relatively low <SFR> of only $\sim 22\,M_{\odot}\,\mathrm{yr}^{-1}$ and $\Sigma\mathrm{SFR}_{\mathrm{Cor}} = 530\,M_{\odot}\,\mathrm{yr}^{-1}$. This accounts for only ~60% of the star formation estimated by Coppin et al. (2012) using *Herschel* SPIRE imaging for the IR-bright region between Clusters A and B. The *Herschel* filament region is full of faint, low mass, hard to detect IR galaxies, many of which had to be stacked in the Coppin et al. (2012) study. These may not be compensated for in the corrected total SFR of the Filament group in our study since we are using galaxies detected in both the $24\,\mu$m map and the optical spectroscopy only, with the correction factor based on optical spectroscopy. The discrepancy is enhanced due to the fact that the Coppin et al. (2012) study uses stacked $250\,\mu$m flux at the positions of fourteen MIPS supercluster members spanning the broad region defined by the SPIRE map as an IR-bright filament. This region encompasses both Clusters A and B as well as the curved region where the Filament and Group 2 are found (see the group distributions in Figures 4.4 and 4.7). The combined, corrected total SFR of the FOF defined Filament and Group 2 gives a more consistent $\Sigma\mathrm{SFR}_{\mathrm{Cor}} \sim 930\,M_{\odot}\,\mathrm{yr}^{-1}$.

Fadda et al. (2008) identified a large-scale IR filament structure between a rich and a poor cluster at $z = 0.23$ and found that the fraction of highly star-forming IR galaxies in the filament is more than twice that of galaxies in the cluster cores and less dense outer regions. In the same $z = 0.23$ supercluster, Biviano et al. (2011) found that the cluster core region contained the lowest fraction of IR galaxies and had the lowest ΣSFR. This is not the case with our results of the higher redshift RCS 2319+00 supercluster and its IR filamentary region. While our fraction of SF galaxies in the FOF-identified Filament only (i.e., without the contribution of the Group 2 galaxies) is twice that of the cores, it is similar to the less dense isolated galaxies. The <SFR> of the Filament galaxies is also lower than the other regions of the supercluster.

The addition of Group 2 galaxies contributes only two additional MIR star-forming galaxies to the four from the Filament, with a new <SFR> $\sim$ 25 $M_{\odot}\,\mathrm{yr}^{-1}$. This lowers the filament LIRG fraction to $\sim$ 24% ±12%, consistent within errors to the core fraction (see Table 4.5). In addition, the total SFR of the cores, on average, is similar to that of the Filament population. Even with the addition of Group 2 the combined, corrected total SFR of the filament region of $\sim$ 930 $M_{\odot}\,\mathrm{yr}^{-1}$ is only ~17% higher than that of Cluster A at $\sim$ 800 $M_{\odot}\,^{-1}$.

Looking at the <SSFR> of the Filament galaxies, we find that the SFR per stellar mass is similar between the Filament and the average over the cluster cores, therefore showing no enhancement of star formation in the filament relative to the densest regions of the supercluster. Combining the Filament with Group 2 gives a <SSFR> = 2.1, again consistent with the cores and also consistent with the group average, when the ULIRGs are removed. As with the <SFR>, the <SSFR> of the filament is found to be lower than the isolated galaxies and the average over the full supercluster.

Unlike the IR filament in the $z = 0.23$ supercluster discussed above, we find no enhancement in the star-formation in the Filament region of RCS 2319+00, despite its presence in the *Herschel* SPIRE imaging. While the lack of evidence of enhanced activity in the Filament over the rest of the supercluster is consistent with the findings of Coppin et al. (2012), their results have the <SSFR> of the galaxies in the IR filament region being ~3 times higher than the cores, contrary to our results. Again, they use all galaxies within a broad, arcing region between Clusters A and B defined by the SPIRE map to calculate the properties of the *Herschel* filament.

4.6 The Colours of Star Forming Galaxies

The RCS 2319+00 supercluster was first found through the presence of it's red-sequence of early-type galaxies. In Section 3.3 we found that ∼36% of the 302 currently identified supercluster members lie along or above the red-sequence on the colour–magnitude diagram (see Figure 3.6). Separating the galaxies into their different density populations, the core galaxies were shown to have the expected high fraction of red galaxies at ∼77% while the groups contain only ∼43% red galaxies. The Filament has only one red galaxy out of its nine current confirmed galaxies. The isolated supercluster galaxies have the lowest red-sequence fraction at ∼29%. The increasing red galaxy fraction from the lowest to highest density environments in the supercluster is seen as evidence of different levels of processing as the galaxies evolve from the isolated outskirts of the supercluster, coalesce in groups and fall into the cluster cores.

We do not cover as large a field of view with the 24 μm data as the optical, nor do we reach a depth in the MIPS data to ensure that all dusty star formation is detected in the area covered. Therefore, we do not have corresponding MIPS information for all of the optical sources in the $R_c - z'$ colour magnitude diagram in Figure 3.6. We can, however, look at the colours of the MIPS star-forming population to see where they lie on the colour–magnitude diagram. The red-sequence is distinguished by a population of early-type, 'red and dead' galaxies with little to no star formation activity evident in the optical and UV whereas the blue–cloud is the location where the late-type, star-forming galaxies are found. The 24 μm data allows us to look for dust-enshrouded star formation in the red galaxy population not evident in the optical data.

In the overall 24 μm population of RCS 2319+00, ∼20% of the galaxies lie on or above the red-sequence. Limiting to the ≥LIRG luminosity population results in the same fraction of red galaxies. Correcting for the redshift success based on galaxy colour and magnitude, as done in Section 3.3, does not change the fraction of dust-obscured, star-forming galaxies. Dividing the MIPS galaxies into their different density environments, the only divergence from the ∼20% dusty, red fraction is found in the core galaxies, where only one of the eight SF galaxies, with a LIRG luminosity, lies along the red-sequence. This reiterates the value of the red-sequence in locating the cores of clusters through early-type galaxies while also showing that a simple optical colour cut does not accurately represent the star-forming and non-star-forming populations in galaxy clusters.

These results are in agreement with a study of 16 clusters over a redshift range of $0.6 < z < 0.8$ done by Finn et al. (2010), where 80% of the cluster LIRGs were found to be blue, with the rest occupying the red-sequence. The same study found that for those $24\,\mu$m galaxies on the red-sequence with *Hubble Space Telescope* morphologies the majority were normal spiral galaxies, red due to dust rather than AGN emission. This again favours our low AGN contamination of SF galaxies (Section 4.3.5).

A study by Wolf et al. (2009) on the A901/2 cluster system at $z = 0.17$ using HST morphologies from the STAGES (Gray et al., 2009) data set found a population of red spiral galaxies in the infall regions around groups and clusters, also consistent with the location of the dusty red galaxies in our sample. They found that the dusty red galaxies are optically passive spirals with SFRs lower than blue spirals at the same fixed masses. These passive spirals were found predominantly at stellar masses between $10^{10} - 10^{11}\,M_{\odot}$, in which mass range they constitute over half of the star-forming galaxies.

The lack of dusty, red galaxies in the cluster cores is consistent with the results of Koyama et al. (2008, 2010) on a merging structure at $z = 0.8$, where red MIR galaxies were also encountered in the intermediate density environments rather than the cluster core. They also find consistent optical colours over all galaxies as shown in Section 3.3, with the optical colours changing in groups in the ‘green valley’ between the bluer isolated galaxies and the redder cluster cores.

4.7 Star Formation as a Function of Stellar Mass

4.7.1 The Specific Star Formation Rates

Examining the SFR as a function of stellar mass along with local and global galaxy density information can help distinguish whether the star formation is preferentially quenched internally by stellar mass, externally by the environment, or a combination of both. If mass-quenching is the primary culprit of star formation quenching, the SF of galaxies above a characteristic stellar mass will be quenched at a rate proportional to their SFR (Peng et al., 2010) and we should see evidence of a decline in SFR as a function of mass. This is based on the evolution of the mass function of star-forming galaxies, seen to have a constant characteristic mass and therefore making the mass-quenching turnover rate a function of the SFR over the characteristic mass (Peng et al., 2010). An environmental star formation quenching effect will be evident by the decrease of a percentage of each population over all mass bins.

In Figure 4.9 we plot the SFR as a function of galaxy stellar mass in the top panel while the corresponding SSFR as a function of mass is shown in Figure 4.10. The number distribution of non-SF galaxies, shown as upper limits along the $8\,M_{\odot}\,\mathrm{yr}^{-1}$ 80% MIPS completeness line in the top panel of Figure 4.9, are separated into their different density regimes and plotted in the bottom panel. As expected, the isolated non-SF galaxies dominate at low masses while the core galaxies dominate the high mass bins. In order to tie in our environmental distribution we have highlighted our FOF-identified core, group and Filament members.

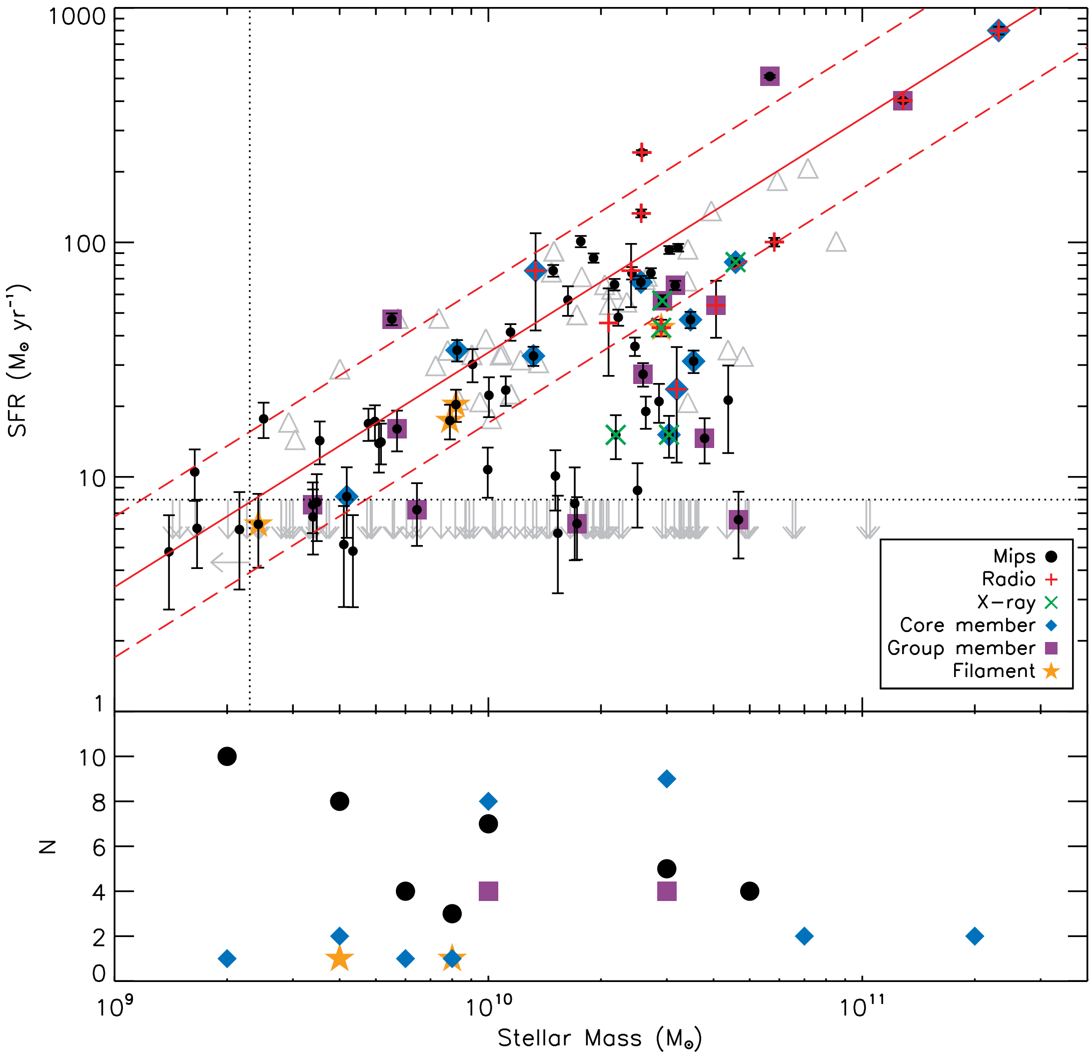

Figure 4.9 Top: SFR versus stellar mass for all confirmed MIPS, radio, K_s and IRAC 4.5 μm supercluster members in the MIPS field of view. All MIPS-detected galaxies are plotted as black filled circles. Radio counterparts are indicated with red-crosses. X-ray counterparts are indicated by green X marks. The SFR upper limit has been set at the MIPS 80% completeness limit of $8\,M_\odot\,\mathrm{yr}^{-1}$ (horizontal dotted line). FOF-identified core, group and Filament galaxies are highlighted with blue diamonds, purple squares and yellow stars. The stellar mass limit has been set at the completeness limit of $2.3 \times 10^9\,M_\odot$ (vertical dotted line). The red line is an arbitrary division line between the main sequence of SF galaxies, with 0.3 dex errors shown as dashed lines, and the apparent sub-main sequence (see Section 4.7.2). Grey triangles represent the comparison field sample. Bottom: The distribution of stellar mass for the galaxies not detected in 24 μm (grey upper limit arrows in top panel).

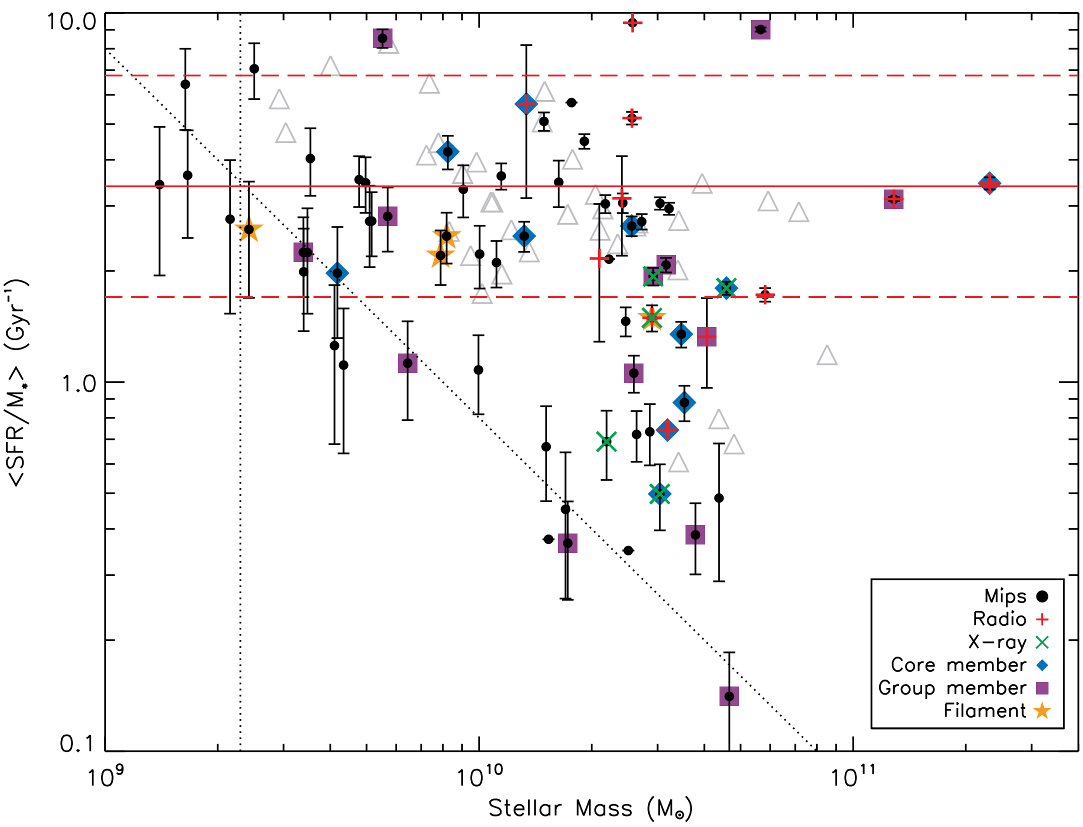

Figure 4.10 Specific SFR versus stellar mass for all confirmed MIPS, radio, K_s and IRAC 4,5 μm cluster members. Dotted lines show the completeness limits of the SFR and stellar mass. The red dashed line corresponds to the division between the main and sub-main sequence populations from Figure 4.9.

For comparison, we compile a field sample at similar redshift to RCS 2319+00, though not from a single field pointing. The field catalogue derives from the large RCS IMACS spectroscopic campaign (R. Yan et al. 2013, in preparation) in combination with the RCS MIPS cluster spectroscopy campaign undertaken with the two Gemini GMOS instruments. The combined spectroscopic field catalogue is cross-referenced with the full catalogue of RCS MIPS and IRAC cluster galaxies (Webb et al., 2013) to estimate SFRs and stellar masses. We choose cluster fields where the target cluster lies well outside the $0.8 < z < 1.0$ range to avoid contamination from cluster galaxies. This is done since these clusters have not all been well defined as of yet and we wish to have a true sample of field galaxies rather than galaxies falling into clusters from the field. IMACS sources are checked against a group catalogue (Yan et al., in preparation) and removed. However, no such catalogue currently exists for the more limited GMOS spectroscopic sample (10 of the 43 field galaxies) and therefore we note the possibility that these galaxies may belong to unidentified clusters or groups. The field galaxies, with stellar masses and SFRs calculated in the same way as the supercluster sample, are plotted as grey triangles.

4.7.2 Evidence for a 'Quenched' Population?

Star-forming galaxies are known to follow a 'main sequence' out to $z \sim 2$ in both SFR versus stellar mass and, consequently, SSFR as a function of stellar mass. Galaxies at each stellar mass bin occupy a limited SFR range ($\sigma \lesssim 0.3$ dex; e.g. Daddi et al., 2007a; Elbaz et al., 2007; Noeske et al., 2007; Salim & Lee, 2012) and have a slightly declining slope in the related SSFR-mass correlation. This main sequence is evident in both our supercluster galaxies and the comparison field sample, however we see a sharp turn-over in the SFR at stellar masses between $\sim 2 - 5.5 \times 10^{10}\,M_\odot$ in our supercluster galaxies. This is inconsistent with most studies, including the results of Koyama et al. (2010) on the merging structure at $z = 0.8$, where they find their cluster galaxies fall along the main sequence.

Hints of this bimodal distribution, with a distinct main and sub-main sequence of galaxies as a function of stellar mass, have been seen by Noble et al. (2013) in a cluster at $z = 0.872$. With stellar masses and SFRs estimated using different methods between the two studies, we can not directly compare the samples but note instead the trends in the two data sets. The Noble et al. (2013) sub-main sequence is a subset of lower, quenched SF galaxies that follow a relatively flat slope as a function of stellar mass, though their cluster lacks the collection of higher stellar mass members seemingly in the process of having their star formation quenched. We also see indications of this flat quenched population along the SFR completeness limit line at a similar SFR to their sub-main sequence sample.

With measurements of age available from the 4000Å break, which we do not have access to due to the lower quality of our spectroscopy, Noble et al. (2013) find that the majority of the older galaxies lie within the sub-main sequence while the younger galaxies are found to follow the main sequence. Using the $R_c - z'$ colour information in RCS 2319+00 as a proxy for the transition between active blue and passive red galaxies, the sub-main sequence does seem to represent an older population, with ∼60% of the sub-main sequence galaxies above both the mass and SFR completeness limits having red colours. Keeping in mind the ∼80% blue fraction in the MIPS star-forming population, this represents a large fraction of the dusty red galaxies in the supercluster. Only ∼8% of the main sequence galaxies have red colours, again suggesting that the main sequence represents a younger population than the sub-main sequence.

Other studies by Vulcani et al. (2010) and Finn et al. (2010) on galaxies in clusters over a redshift range of $0.4 < z < 0.8$ find that cluster galaxies, though lying along what appeared to be a similar trend as the main sequence, had SFRs lower on average than their field comparison galaxies at the same stellar masses (i.e., not as distinct a bimodal distribution as seen here and in the Noble et al. (2013) study). Though the Finn et al. (2010) study did not have statistically significant numbers, the Vulcani et al. (2010) work found that there was a $\sim 10-25\%$ population of the cluster galaxies at the reduced SFRs (∼2x lower) compared to the field and they suggest that this is evidence of the transition from active SF galaxies to passive galaxies in the clusters. They also note that the SSFR-mass relation, while again showing a declining trend in both the field and cluster galaxies, is steeper for the clusters, meaning the difference in the cluster and field populations is more evident at high mass. They take this to

Table 4.7 Fraction of Galaxies in the Sub-Main Sequence Trend Within the MIPS Field of View

SFR ($M_\odot\,\mathrm{yr}^{-1}$)	> 0	≥ 8	≥ 8	no SFR cut	≥ 8	No SFR cut[a]
M_* ($M_\odot$)	No M_* cut	$\geq 2.3 \times 10^9$	$< 2 \times 10^{10}$	$< 2 \times 10^{10}$	$\geq 2 \times 10^{10}$	$\geq 2 \times 10^{10}$
All galaxies	0.32 ± 0.07	0.28 ± 0.07	0.09 ± 0.06	0.71 ± 0.10	0.44 ± 0.12	0.69 ± 0.11
Core galaxies	0.33 ± 0.17	0.33 ± 0.17	0	0.76 ± 0.21	0.50 ± 0.25	0.81 ± 0.20
Groups[b]	0.41 ± 0.16	0.33 ± 0.17	0	0.67 ± 0.24	0.50 ± 0.25	0.69 ± 0.23
Isolated galaxies	0.29 ± 0.08	0.26 ± 0.09	0.13 ± 0.09	0.70 ± 0.12	0.40 ± 0.16	0.65 ± 0.16
Comparison Field	···	0.09 ± 0.05	···	···	0.25 ± 0.13	···

[a] Includes all galaxies with a stellar mass estimate, including those with no SFR estimate

[b] Includes all five FOF-identified groups, including the Filament

mean that the environment has a bigger influence on the SFR in higher mass galaxies. We see similar results with our sample of high mass galaxies having a higher fraction of SF galaxies in the sub-main sequence than the lower mass supercluster galaxies.

We separate out the main and sub-main sequence galaxies with an arbitrary limit chosen to isolate the SFR turnover feature and the lower SFR galaxies. This line is at a constant SSFR of $1.7\,\mathrm{Gyr}^{-1}$, plotted as the solid red line in Figures 4.9 and 4.10. The main sequence derived from field galaxy samples at $z \sim 1$ and $z \sim 2$ have been found to have slightly smaller slopes of 0.9 (Elbaz et al., 2007; Daddi et al., 2007a). We add red-dashed lines on both plots at 0.3 dex from our main sequence line, the error often associated with the main sequence to divide between the main and sub-main sequence populations. Table 4.7 summarizes the fraction of sub-main sequence galaxies found for various mass and SFR limits, defined in the column headings.

The two separate deviations from the main sequence we see may be evidence of both mass-quenching and environment-quenching effects. The turn-over in SFR for $M_* \gtrsim 2 \times 10^{10}\,M_\odot$ galaxies, which is seen to lesser extent in the comparison field sample, could be evidence of mass-quenching. Environment-quenching is seen in the fact that the SFR has been quenched for a subset ($\sim 17-18\%$) of the group (3 out of 17 SF group galaxies) and isolated (7 out of 42) supercluster galaxies due to the density of the environments in which they reside. The fraction of SF galaxies that fall below the main sequence trend is consistent at $\sim 30\%$ over all density regions within the supercluster given the Poisson errors, which increase for the cores and groups due to small numbers. This is three times the fraction of comparison field galaxies in the sub-main sequence, which all lie above the $M_* \geq 2 \times 10^{10}\,M_\odot$ turn-over mass.

The consistency of the SFR-stellar mass distribution between different global environments in the supercluster is in agreement with the results of Biviano et al. (2011) on a $z = 0.23$ supercluster system. They suggest that this uniformity between different density regions in their system is indicative of similar modes of star formation in all environments of the supercluster. A similar lack of environmental trends within the cluster field is seen by Koyama et al. (2010) for the merging cluster/sub-cluster system at $z = 0.8$. Though they do not have sufficient group data for statistical significance, the Vulcani et al. (2010) study finds that the group galaxies in their study follow the field galaxies in their SFR-mass correlation, in contrast to our findings, the Biviano et al. (2011) study and the Koyama et al. (2010) results, all on merging systems. The Vulcani et al. (2010) study posits that, if this group similarity to the field galaxy SFR-mass correlation is true for larger samples, it would mean that strangulation as a means of SFR quenching would not be occurring in group environments. The difference in the Vulcani et al. (2010) groups and the groups found in this study and the Biviano et al. (2011) and Koyama et al. (2010) studies is that the Vulcani et al. (2010) groups are their own systems, rather than belonging to merging structures. This suggests that the difference in the overall density of the regions surrounding the groups in the different studies may play a role in the SFR-mass relation, with groups in higher density merging cluster fields showing different environmental effects to those in isolated field environments.

Below the mass of the apparent SFR-turnover, there are only two isolated galaxies that lie above the SFR completeness limit. Only two group galaxies and an additional four isolated galaxies have measured SFRs that lie below the completeness level, meaning the majority of the identified SF galaxies in this mass range (approximately three quarters) are on the main sequence. At the mass limit of the SFR turn-over, the fraction of SF galaxies in the sub-main sequence remains consistent over all density regions, with a higher fraction of ∼45% compared to the $\sim 30\%$ of galaxies in the sub-main sequence over the full mass range. This is approximately twice the fraction of SF comparison field galaxies in the sub-main sequence over this stellar mass limit, indicating that some difference exists between the denser supercluster regions and the field at $z \sim 0.9$. These results are consistent with the results of Wolf et al. (2009) who found that over half of the star-forming galaxies in the $10^{10} - 10^{11}\,M_\odot$ stellar mass range in their sample were passive red spirals in the infalling regions around groups and clusters having lower SFRs compared to blue spirals in the same stellar mass range.

Taking into consideration all galaxies with stellar mass estimates above the $M_* \geq 2 \times 10^{10}\,M_\odot$ limit (i.e., including those with no $24\,\mu$m detection) shows that the number of massive galaxies below the main sequence increases from $\sim 60\%$ to $\sim 70\%$ to $\sim 80\%$ in the isolated, group and core supercluster population, perhaps hinting at a combination of environmental-quenching and mass-quenching in the high-mass cluster galaxies. Though again the errors are large, leading to consistent fractions throughout all cluster populations.

Noble et al. (2013) raised the possibility that the sub-main sequence galaxies could be AGN, with feedback causing the quenching of the SFR in these galaxies. They refer to the Peng et al. (2012) study, which posits powerful quasar feedback as a rapid quenching mechanism. Though we found in Section 4.3.5 that the possibility of AGN contamination boosting our MIPS SFRs was low, we did note an estimated, corrected AGN fraction of galaxies at a 7-10%. Interestingly, it can be seen in Figure 4.9 that the only X-ray counterparts to SF galaxies are found above the mass limit set for

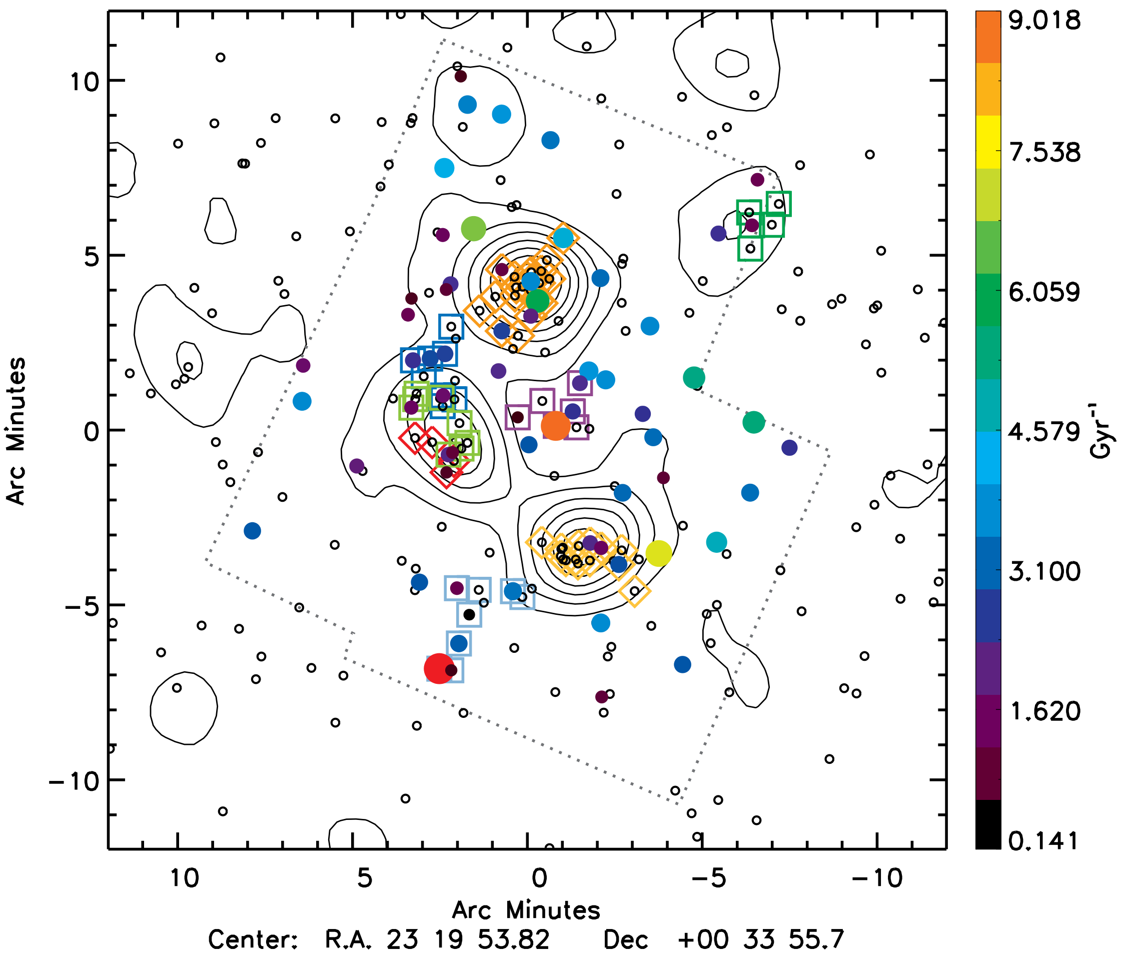

Figure 4.11 Distribution of specific-SFR in the RCS 2319+00 supercluster field. Symbol colour, shape and size follows Figures 4.4 and 4.7.

the SFR turn-over, with three of the five X-ray galaxies in the sub-main sequence and the other two very close to the division line. As well, the majority of the radio counterparts, while predominantly in the main sequence, are found above the SFR turn-off mass limit. This gives weight to the argument that AGN feedback may be responsible for quenching the SFRs in the high-mass column of the sub-main sequence of galaxies.

4.7.3 Global Trends in the Specific Star Formation Rates

In this section we look at the specific-SFR as a function of density. Figure 4.11 shows the distribution of SSFR in the supercluster field. Once again, it can be seen that the close proximity in the distribution of our clusters and groups makes it difficult to study the SSFR as a function of the cluster or group centric radius, as done in other studies (e.g., Noble et al., 2013; Muzzin et al., 2012; Lu et al., 2012). Instead we again look at the local density. In Figure 4.12 we plot the SSFR as a function local galaxy density with the density measured as in Section 4.4.1. The plot shows the average SSFR over all supercluster galaxies (open triangles) and for SF cluster galaxies (solid triangles) binned in density. The binned average SSFR for the different global environments is also plotted. The errors on the <SSFR> for all galaxies (over all density regimes) represent the range between the summed SFR over stellar mass of cluster galaxies assuming an upper limit of SFR=8 $M_{\odot}\,\mathrm{yr}^{-1}$ for all members with no MIPS detection (upper limit) and the integrated SSFR over all galaxies assuming zero SF for all non-detected cluster members (lower limit). The symbols are plotted as the average between the two limits.

The best-fit trend for the star-forming supercluster population shows a slight positive correlation between the SSFR with density, having a slope of 0.08 ± 0.10. This slight positive trend in <SSFR> with local density for SF galaxies differs from other studies (e.g., Noble et al., 2013; Muzzin et al., 2012; Lu et al., 2012). One explanation for the contradicting results may be due to the different measures of local density used, such as the cluster centric radius as a proxy for density in the latter two studies. Looking back at Table 4.6 we recall that the <SSFR> over the global environments, when averaged over all cores/groups within each global environment bin, showed values of ∼2.0–2.6 $\mathrm{Gyr}^{-1}\,\mathrm{gal}^{-1}$ but varied between values of ∼0.5–3.3 $\mathrm{Gyr}^{-1}\,\mathrm{gal}^{-1}$ when looking at individual cores and groups. Considering the SF galaxies separated into

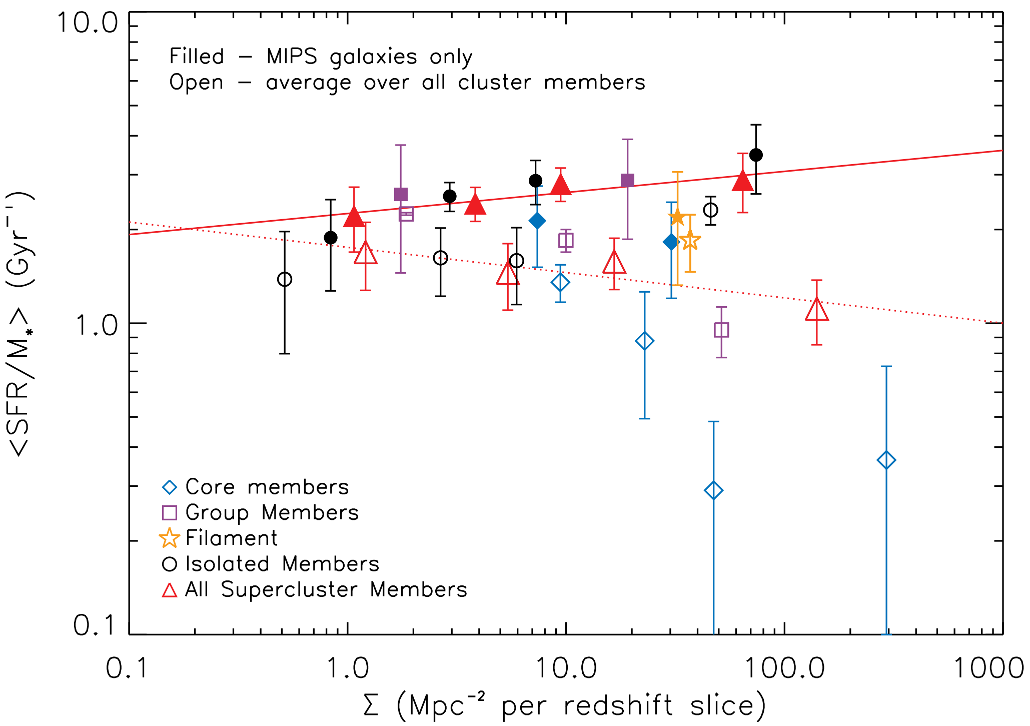

Figure 4.12 Specific-SFR as a function local galaxy density for all supercluster members (open symbols) and over the star-forming population only (solid symbols). Best-fit trends for the full supercluster samples are shown.

global environments in Figure 4.12, we see that the isolated and group environments drive the increasing <SSFR> with density, whereas the core galaxies show the expected decreasing trend seen in the other cluster studies. The current result seems to suggest that there is enhanced SF activity as a function of local density in the outskirts of the supercluster, in the groups and isolated environments. This would appear to contradict our previous results that the SFR-density relation at $z \sim 1$ retains the local correlation of higher star-formation activity avoiding the densest regions.

There does, however, appear to be a negative correlation between <SSFR> and density when considering all supercluster galaxies, both star-forming and non star-forming. The best-fit slope of -0.08 ± 0.10 is consistent with the results of Noble et al. (2013) for their $z = 0.872$ cluster as well as a study by Patel et al. (2009) on a $z = 0.834$ cluster using stacked MIPS detections. The decreasing trend of the SSFR over all galaxies with local density is also consistent with our findings in Section 4.5, where we saw that the total fraction of MIPS galaxies is approximately double in the groups and isolated galaxies compared to the denser cluster cores. This is also seen when we divide the galaxies into their global environments, with the average SSFR over all core galaxies falling lower than the group and isolated galaxies at similar densities. We once again see an interesting reversal in the relation when looking only at the isolated galaxy environment, where there is a slight increase in density with increasing <SSFR>, similar to the correlation seen for the SF population.

The SF Filament galaxies, in one density bin due to small numbers, lie along the best-fit line for the full SF sample within errors. The binned Filament galaxy bin lies slightly above the average over the full sample. From this we can infer that the Filament lies in a transitional state between the higher, possibly induced star-formation regions of the supercluster outskirts in the isolated and group populations and the less actively star-forming regions in the dense cluster cores.

The integrated SSFR (shown as the lower limits on the binned data over all SF and non-SF galaxies) is representative of the current fraction of known star-forming galaxies in each density bin, while assuming the completeness limit of $8\,M_{\odot}\,\mathrm{yr}^{-1}$ for all galaxies not detected in MIPS (upper limits) gives the maximum fraction possible. Therefore, the excess of the Filament bin over the full galaxy sample trend is expected, since we have already found the fraction of MIR galaxies to be twice as high in the Filament compared to the cores (see Table 4.5), which have similar high local densities. This maximum fraction also shows that, though the SF population seems to contrast the SFR-density relation of the local universe, the overall supercluster sample is consistent with the local relation.

4.8 Summary of the Mass and Star Formation Distribution

We have presented a multiwavelength study of the $z = 0.9$ RCS 2319+00 supercluster, concentrating on spectroscopically confirmed MIR supercluster members and their close environments in an attempt to detangle the role of the global versus local environment on the galaxy stellar mass and star formation. Here we summarize our main findings.

With respect to the stellar mass distribution as a function of the environment, we find that the stellar mass of the full RCS 2319+00 supercluster galaxy population increases with increasing local density with a slope of 0.14 ± 0.07, as expected due to mass segregation.

- Over the global environments, the isolated supercluster members show a flatter relation and have systematically lower stellar masses then their counterparts in the cores and groups at similar local densities.
- While isolating the non-SF galaxies results in a positive mass-density correlation of 0.19 ± 0.10, the SF galaxies seem to show no correlation in their stellar mass with local density, having a slope of 0.05 ± 0.13.
- The SF galaxies do not cover the full local density range and the highest local density bins appear to drive the positive correlation for the overall and non-SF population, so we conclude that the lack of correlation for the SF population is due to SF galaxies avoiding the highest local densities.

Investigating the distribution of star formation in the different global environments shows that the RCS 2319+00 supercluster at $z \sim 0.9$ follows the local SFR-density relation.

- In the MIPS field of view 40% ±5% of supercluster galaxies are detected at

$24\,\mu$m. LIRG-level galaxies make up 20% ±3% of the cluster population while the three ULIRGs account for 2% ±1% of the supercluster galaxies.

- The LIRG-level SFR-density relation is flat over our three density regimes at ~20% (isolated: 20% ±5%, groups: 21% ±8%, cores: 15% ±6%).

- Taking into account all MIPS detected galaxies, the SFR-density relation in RCS 2319+00 is consistent with the local relation, with the primary location of star formation being at lower densities, avoiding the densest regions in the cluster cores.

- The $\Sigma\mathrm{SFR}_{\mathrm{cor}}$ over the supercluster reiterates that the main region for star formation is in the outskirts, with $\sim$ 54% or the total SFR occurring in the isolated galaxies, $\sim$ 36% happening in groups, and only a $\sim$ 10% contribution to the total SFR from the cluster cores.

- The variable $\Sigma\mathrm{SFR}_{\mathrm{cor}}$ values for the different groups suggest different stages of star formation activity, with some group galaxies showing similarities to the isolated population while others seem to be further along in their evolution, showing similarities to the core galaxies.

- The increase in <SSFR> for isolated galaxies and half of our groups indicate enhanced SFR in those populations over the full supercluster membership and may be indicative of tidal interactions or galaxy mergers causing bursts of star formation as the galaxies are accreted.

- The Filament, initially identified by Coppin et al. (2012) from SPIRE *Herschel* imaging, shows a lower <SFR> per SF galaxy compared to the full cluster sample at only $\sim 22\,M_\odot\,\mathrm{yr}^{-1}$ and a lower $\Sigma\mathrm{SFR}_{\mathrm{cor}}$ of only $\sim 529\,M_\odot\,\mathrm{yr}^{-1}$ compared to the estimated $900\,M_\odot\,\mathrm{yr}^{-1}$ from Coppin et al. The addition of Group 2 galaxies, in the same region defined in the Coppin et al. study, results in a more consistent $\Sigma\mathrm{SFR}_{\mathrm{cor}} \sim 930\,M_{\odot}\,\mathrm{yr}^{-1}$. As with the *Herschel* results, we find that the Filament shows no significant enhancement in star formation over the cluster cores.

We find evidence of a bimodal distribution in the SFR and SSFR versus stellar mass of the MIPS supercluster galaxies.

- Along with the known main sequence of SF galaxies we see a sub-main sequence population below a SSFR of $\sim$1.7 Gyr^{-1}. There is an apparent sharp turnover in SFR at stellar masses between $\sim$2–5.5 $\times 10^{10}\,M_{\odot}$ and a subset of lower, quenched SFR galaxies that follow a relatively flat slope as a function of stellar mass along the SFR completeness limit line.

- The flat slope portion of our proposed sub-main sequence is similar to that seen by Noble et al. (2013) in a cluster at $z = 0.872$ and we posit that it is a result of environment-quenching, with $\sim$ 17–18% of the group and isolated galaxies in this subset population.

- The higher stellar mass section of the sub-main sequence, with an apparent suppression of SFR at $\gtrsim 2 \times 10^{10}\,M_{\odot}$, seems to be a unique feature in the literature and is not visible in the current data of the Noble et al. (2013) cluster. Despite the large errors due to small numbers, we propose that mass-quenching is contributing to the suppression of the star formation in the supercluster, along with the apparent environment-quenching over the full stellar mass range.

- The presence of X-ray and radio galaxies in the high mass column of sub-main sequence galaxies lends credence to the suggestion by Noble et al. (2013) that the sub-main sequence galaxies may be quenched by AGN feedback, though we find that the likelihood of AGN contaminating the MIR SFRs is low.

The <SSFR> versus local density over all galaxies is consistent with other studies, showing a negative correlation. Despite this, we see an interesting increasing trend in <SSFR> with local density when studying the star-forming supercluster population.

- The star forming galaxies show a slight positive correlation in the SSFR-density dependence of 0.08±0.10, driven by the isolated and group global environments. These infalling regions may be experiencing a period of enhanced star formation as they accrete onto the larger group or core halos.
- The star forming Filament galaxies lie between the higher isolated and group galaxy <SSFRs> and the lower core <SSFRs>, suggesting that the Filament is in a transitional state of star formation activity between the group and core global environments.
- The full galaxy sample shows a negative correlation of -0.08 ± 0.10, consistent with the local SFR-density relation.

The RCS 2319+00 supercluster presents a unique opportunity to study different density regions within a massive, merging structure. The extensive spectroscopic campaign presented in Chapter 2 and the substructure defined in Chapter 3 allow for the study of the distribution of stars and star formation in the RCS 2319+00 supercluster both as a function of the local and the global environment. With the addition of accurate photometric redshifts, currently underway, to further trace the substructure of the supercluster and add additional members to each density population, we will be able to further clarify the role of dusty star-forming galaxies in the supercluster environment.

Chapter 5

The Current and Future Mass Content of the Supercluster

THE FOLLOWING CHAPTER IS BASED ON:

The current and future mass content of the $z \sim 0.9$ RCS 2319+00
supercluster: Exploring the fate of the merged cluster

A.J. Faloon, T.M.A. Webb, D. O'Donnell, A.G. Noble, A. Delahaye, J.E. Geach, E. Ellingson, R. Yan, D.G. Gilbank, L.F. Barrientos, H.K.C. Yee, and M. Gladders, to be submitted to ApJ

5.1 Introduction

In this chapter we look at the total current and possible future mass content of the RCS 2319+00 supercluster. In Section 5.2 we outline the data used in Section 5.3 to investigate the current stellar and halo mass content of the supercluster and its component cluster cores and groups. The results are presented in Section 5.4. The data are also used to explore the possible fate of the stellar mass in the supercluster. We estimate the total future stellar and halo mass content by interpolating the stellar mass build-up given continuous star formation over estimated gas depletion timescales. This is done in order to investigate the role of the currently star forming galaxies on the descendent cluster and discuss in Section 5.5 the relative mass build-up in each global environment before reaching a final, single merged cluster. These results are compared to theories of hierarchical structure formation. Finally, we offer a summary of the results of this study in Section 5.6.

5.2 Data

In Chapter 2 we found that there are 302 spectroscopically identified members in the RCS 2319+00 supercluster. Of these, 203 have stellar masses derived from the *Spitzer* IRAC 4.5 μm and K_s-band imaging, as outlined in Section 4.3.2. From the *Spitzer* MIPS–24 μm data, we calculated galaxy SFRs in Section 4.3.3, finding 66 IR star forming galaxies in the MIPS field of view. Figure 4.1 shows the layout of the IRAC, K_s, and MIPS imaging and their overlapping regions. In addition to the stellar mass and SFR estimates of our cluster members, we also have the completeness information from the full spectroscopic catalogue (Section 2.3.2), which can be used in relation to each of the above wavelengths to estimate the appropriate correction factors. The combination of these data are used in this chapter to investigate the current and potential future stellar and halo mass content of the supercluster.

5.3 Stellar and Halo Mass Estimations

5.3.1 Total Stellar Mass at $z = 0.9$

We estimate the total stellar mass for the supercluster by summing the stellar mass of all spectroscopically confirmed supercluster galaxies in the K_s-band imaging region. To compensate for spectroscopic incompleteness we use a correction factor found by taking the fraction of all galaxies within the K_s band field-of-view with a K_s or 4.5 μm detection above the completeness limits ($K_s = 21.8$ mag, 4.5 $\mu\text{m} = 6\,\mu$Jy) over all of those with redshift. This is similar to the magnitude factor of the spectroscopic completeness weighting used in Section 2.3.2, though now over the NIR bands rather than the z' optical component and for a single correction factor over the whole mass rather than unique weightings for each individual galaxy. As there are known systematic errors in our stellar mass estimates (see Section 4.3.2) and we are only interested in looking at overall trends in the different density environments, we choose to use the single correction factor, found to be 4.92, to give an estimate of the total expected stellar mass if we had 100% spectroscopic coverage. The results for the stellar mass estimates for the full cluster, as well as the contribution from each of the different density populations, are shown in the top left section of Table 5.1.

5.3.2 Total Halo Mass at $z = 0.9$

The halo mass of the supercluster and its substructures can be estimated using a conversion between the stellar and halo mass. Behroozi et al. (2010) found that the stellar mass–halo mass (SM-HM) relation can be fit using functional forms consistent with a power-law at lower stellar masses and a sub-exponential for high stellar masses, with a transition point around a characteristic stellar mass. We use the best-fit functional form of the relation shown in equation 21 of Behroozi et al. (2010);

$$\begin{aligned}\log_{10}(M_h(M_*)) \;=\; & \log_{10}(M_1) \;+\; \beta \log_{10}\left(\frac{M_*}{M_{*,0}}\right) \\ & + \frac{(\frac{M_*}{M_{*,0}})^{\delta}}{1+(\frac{M_*}{M_{*,0}})^{-\gamma}} \;-\; \frac{1}{2}. \end{aligned} \tag{5.1}$$

The five parameters of the relation are: the characteristic halo mass (M_1), characteristic stellar mass ($M_{*,0}$), the faint-end power-law for low mass galaxies (β), the sub-exponential for the massive galaxies (δ), and the transition width (γ). The parameters of the SM-HM relation are scaled using the best-fit values in Table 2 of the Behroozi et al. (2010) paper for $0 < z < 1$ galaxies with full systematic error allowances for the mass estimates. We employ the scaling relations found in equation 22 of Behroozi et al. (2010);

$$\log_{10}(M_1(a)) = M_{1,0} + M_{1,a}(a-1), \tag{5.2}$$

$$\log_{10}(M_{*,0}(a)) = M_{*,0,0} + M_{*,0,a}(a-1), \tag{5.3}$$

$$\beta(a) = \beta_0 + \beta_a(a-1), \tag{5.4}$$

$$\delta(a) = \delta_0 + \delta_a(a-1), \tag{5.5}$$

$$\gamma(a) = \gamma_0 + \gamma_a(a-1), \tag{5.6}$$

with the scale factor $a = 1/(1+z)$ set for $z = 0.9$. To find the total halo mass we first find the halo mass of each individual galaxy using the Behroozi et al. (2010) SM-HM relation and then sum them to find the total. We again correct the total halo mass with the spectroscopic completeness correction factor found above. The results for the halo mass estimates for the full cluster and each density population is shown in the top right section of Table 5.1.

5.3.3 Stellar and Halo Mass of Groups and Clusters

We are interested in looking at the individual and average group masses in the RCS 2319+00 supercluster. To do this, we calculate the total stellar and halo masses for each core and group as above, but with a spectroscopic correction factor for the mass based on regions around each group rather than the larger field of view. We use the galaxies within the spectroscopically derived r_{200} for cores and within a 1 Mpc radius for the groups to find the new correction factors. This is done so as to compensate for the different spectroscopic coverage around each group (see Figure 3.2 in Section 3.2.2 for the spectroscopic target density contours in relation to the FOF cores and groups). The stellar and halo mass estimates for each core and group are listed in Table 5.2.

Table 5.1 Total Stellar and Halo Mass Estimates for the RCS 2319+00 Supercluster Members

	M_* ($10^{12}\,M_\odot$)	$M_{*,\mathrm{cor}}$[a] ($10^{12}\,M_\odot$)	% of $M_{*,\mathrm{Tot}}$[b]	$< M_* >$[c] ($10^{10} M_\odot$ gal^{-1})	M_{Halo}[d] ($10^{14} M_\odot$)	$M_{\mathrm{Halo,cor}}$ ($10^{14}\,M_\odot$)	% of $M_{\mathrm{Halo,Tot}}$	$< M_{\mathrm{Halo}} >$ ($10^{12}\,M_\odot$ gal^{-1})
Over the full K_s-band field of view ($\sim$ 21.5 × 21.5 arcmins)								
Cores	1.3	6.2	29	3.3	1.7	8.2	44	4.4
Groups	0.7	3.5	16	2.4	0.6	2.7	15	1.9
Isolated	2.4	11.8	55	1.7	1.5	7.5	41	1.1
TOTAL	4.4	21.6	···	2.1	3.7	18.4	···	1.8
Over the MIPS 24 μm field of view								
Cores	1.3	6.2	41	3.3	1.7	8.1	56	4.4
Groups	0.7	3.2	21	2.5	0.5	2.6	18	1.9
Isolated	1.2	5.9	38	1.4	0.8	3.7	26	0.9
TOTAL	3.1	15.3	···	2.1	3.0	14.4	···	2.0
Final mass of current supercluster members using gas depletion timescales over the MIPS 24 μm field of view[e]								
Cores	1.5	7.3	33	3.9	2.5	12.1	48	6.5
Groups	0.8	4.0	18	3.1	0.8	4.0	15	3.0
Isolated	2.2	10.7	49	2.6	1.8	8.9	36	2.2
TOTAL	4.5	22.0	···	3.0	5.1	25.1	···	3.5

[a] Stellar mass corrected for spectroscopic incompleteness using the fraction of all $K_s/4.5\,\mu$m sources over those with redshifts.

[b] Percentage of the total supercluster M_* in each density regime.

[c] Mean M_* per galaxy given as the total, uncorrected stellar mass over the number of galaxies in each population with measured M_*.

[d] Total halo mass calculated by summing the estimated halo mass of each galaxy, found using the Behroozi et al. (2010) SM-HM relation.

[e] With stellar mass added assuming constant SFRs for 700 Myr for the all MIPS galaxies with the exception of the ULIRGs, whose added stellar mass is based on constant SFRs for 50 Myr.

5.4 Total Stellar and Halo Mass in the Supercluster

5.4.1 Total Mass Distribution in RCS 2319+00

The total supercluster stellar and halo mass estimates are summarized in Table 5.1. The top section of the table corresponds to the mass estimates over the full $\sim$ 21.5 × 21.5 arcmin region covered by the K_s imaging ($\sim$10 × 10 Mpc). We find that the total estimated stellar mass of the RCS 2319+00 supercluster galaxies, with the spectroscopic correction factor of 4.92 applied, is $\sim 2.2 \times 10^{13}\,M_\odot$. The corresponding halo mass over all regions of the supercluster is estimated at $1.8 \times 10^{15}\,M_\odot$.

Looking at the different global environments identified by the FOF groups, the three cluster cores collectively contribute $\sim$ 29% of the total stellar mass of the cluster, however, their contribution to the total halo mass is higher, at $\sim$ 44%. This is due to the fact that about half of the highest stellar mass galaxies, above the characteristic stellar mass for the supercluster redshift of $M_* = 2.9 \times 10^{10}\,M_\odot$, are located in the cluster cores and therefore fall on the sub-exponential end of the SM-HM relation.

The group galaxies are fairly consistent in their mass contribution, containing ∼15-16% of the total stellar and halo mass. As seen in Figure 4.6 of Section 4.4.1, the isolated supercluster galaxies dominate the low mass regime and, as such, their stellar mass contribution of ∼55% of the total mass drops to a ∼41% contribution in the overall halo mass of the supercluster.

Within the different density environments, we see that the overall mean stellar and halo mass of the supercluster galaxies increases with increasing global density. We have defined the mean masses in each population as the total, uncorrected mass over the number of supercluster galaxies with measured mass in that population. This rising stellar mass in the increasingly dense global environments is expected due to the mass segregation scenario, seen in the results of the stellar mass relation to local density found in Section 4.4.1. In Figure 4.6, we also found that the global environments followed increasing local density bins as expected, with the isolated galaxies in the lowest local densities, followed by the group and core galaxies, with overlap in local density when transitioning from one global environment to the next. On average, the isolated galaxies have a halo mass of $M_{\rm Halo} \sim 1.1 \times 10^{12}\, M_\odot$, with the average mass increasing for the infalling group galaxies to $M_{\rm Halo} \sim 1.9 \times 10^{12}\, M_\odot$ before reaching the highest average halo masses in the cluster cores at $M_{\rm Halo} \sim 4.4 \times 10^{12}$.

5.4.2 Mass Estimates of the Substructures in the Supercluster

The results of the total mass per cluster core and group are summarized in Table 5.2. Summing the corrected halo masses of the three clusters gives a combined mass of $7.5 \times 10^{14}\, M_\odot$, $\sim 10\%$ lower than that found using the correction factor over the full field of view. The combined group mass agrees well with the previous estimate at $2.7 \times 10^{14}\, M_\odot$.

Table 5.2 Total Stellar and Halo Mass Estimates for the Cluster Cores and Groups

Group	M_* ($10^{11}\,M_\odot$)	$M_{*,\rm cor}$ ($10^{11}\,M_\odot$)	$M_{\rm Halo}$ ($10^{13}M_\odot$)	$M_{\rm Halo,cor}$ ($10^{13}\,M_\odot$)
Cluster A	7.1	31.5	11.9	52.8
Cluster B	1.0	6.3	2.4	4.5
Cluster C	4.6	20.2	4.0	17.7
Core Average	4.2	19.3	5.5	25.0
IR Filament	0.6	3.1	0.4	2.0
Group 1	0.9	3.7	0.6	2.2
Group 2	1.4	8.5	0.8	5.0
Group 3	3.3	15.3	3.2	14.9
Group 4	9.5	5.4	0.6	3.3
Group Average	1.4	7.2	1.1	5.5

Note. The corrected mass estimates are derived for spectroscopically corrected regions within radii corresponding to the r_{200} values estimated in Table 2.6 using the Evrard et al. (2008) method for the cluster cores and within an arbitrary 1 Mpc radius around each group.

The estimated halo masses for Clusters A, B and C of $5.28, 0.45$ and $1.77 \times 10^{14}\,M_\odot$ can be compared to the mass estimates from the spectroscopic measurements and the cluster X-ray emission. The virial mass estimates from the spectroscopic velocity dispersions around each cluster core found in Section 2.4.4 are $11.9 \pm 6.9, 10.5 \pm 10.0$ and $2.5 \pm 1.9 \times 10^{14}\,M_\odot$ for Clusters A, B and C respectively. The large errors are due to the limited number of spectroscopic members available to estimate the velocity dispersions. The X-ray masses found by Hicks et al. (2008) for the three clusters are $6.4^{+1.0}_{-0.9}, 4.7^{+0.9}_{-1.4}$, and $5.1^{+0.8}_{-0.8} \times 10^{14}\,M_\odot$.

We find reasonable agreement for the three mass estimates for Cluster A when taking the low end of the spectroscopic mass range. We also note the halo mass estimate is in good agreement with the weak lensing mass for Cluster A of $5.8^{+2.3}_{-1.6} \times 10^{14}\,M_\odot$ found by Jee et al. (2011). The halo mass estimate for Cluster C is consistent with the dynamical measurement but $\sim$2–3 times lower than the X-ray estimate.

Cluster B remains an outlier in the measurements for the halo mass as it was for the virial mass estimate from spectroscopy. This is again due to the fact that both studies use only the confirmed cluster members, which are lacking in numbers for Cluster B compared to the other two cluster cores (See Figure 3.2 in Chapter 3 for the spectroscopic target density layout).

In Section 3.4 the approximate average halo mass for the cluster cores and infalling groups in the RCS 2319+00 supercluster was found through use of luminosity functions (LFs) in conjunction with the Halo Occupation Distribution (HOD) and richness estimates. The cluster cores were found to have halo masses of ~ 0.9–$6 \times 10^{14}\, M_\odot$, consistent with the spectroscopically derived masses of ~ 8, ~ 6 and $\sim 3 \times 10^{14}\, M_\odot$ for the Clusters A, B and C. The average core halo mass estimated here of $2.5 \times 10^{14}\, M_\odot$ agrees well with the LF derived estimates.

The average group halo mass from the LF method is ~ 4–$5 \times 10^{13}\, M_\odot$, consistent with the $\sim 10^{13}\, M_\odot$ infalling groups found in simulated cluster data and semi-analytically derived merger trees. Since the average core mass and the halo mass estimates for Clusters A and C are consistent with the masses derived by other methods, we expect the halo mass estimates for the groups to also offer reasonable mass measurements. In the groups, the estimated halo masses are found to be of order $10^{13}\, M_\odot$, as expected based on the average mass derived from the LFs in Chapter 3, for all but Group 3. The average group halo mass is $5.5 \times 10^{13}\, M_\odot$.

Group 3 is a filamentary shaped group that appears to be falling towards Cluster C from the lower redshift wall (See Figures 4.2 and 4.7) and contains two of the three highly star forming ULIRGs. Its estimated halo mass of $1.5 \times 10^{14}\, M_\odot$ places it more in the cluster mass regime rather than the group category. Looking at the red-sequence galaxy density maps from the RCS-1 survey (Gladders & Yee, 2005), shown for the redshift slice centered at $z = 0.895$ in Figure 2.6, we do not see a significant peak in red-sequence galaxies at the location of Group 3, which would be indicative of a typical cluster core. At the next slice down in redshift, centered at $z = 0.758$, we see a slight increase in red galaxies in the red-sequence density map, though no more so than the rest of the supercluster region. This is not surprising given that in Chapter 4 we found six of the eight currently identified members of Group 3, including the two ULIRGs, are star forming, with only four found in Figure 3.6 to fall on or near the red-sequence. Therefore, though Group 3 has a cluster-sized mass of $\sim 10^{14}\,M_{\odot}$, it does not present as a typical cluster core with an established red-sequence population, but rather a large group that we are witnessing in a state of high activity.

If we remove Group 3 from the list as an outlier, the new average mass for the groups is $3.1 \times 10^{13}\,M_{\odot}$. The results show that we are again finding that the groups are approximately an order of magnitude lower in mass than the clusters, consistent with the mass of halos for which some studies using semi-analytical merger trees have predicted pre-processing to be an important factor prior to accretion onto the final halo (e.g., De Lucia et al., 2012; McGee et al., 2009; Cohn, 2012; Berrier et al., 2009, see Section 5.5.1).

5.5 Discussion: The Possible Fate of RCS 2319+00

5.5.1 The Fate of the RCS 2319+00: Final Merged Mass Estimates

Gilbank et al. (2008a) estimate the merger rate of the three cluster cores and predict that the RCS 2319+00 supercluster will merge to form a $\sim 10^{15}\,M_{\odot}$ sized cluster by $z \sim 0.5$. Though the three cores are estimated to have merged by this epoch, we do not assume that all galaxies in either the cores or the groups and isolated regions will be within the virial radius of the final cluster by this point. We aim to investigate the relative mass build-up in the different global environments based on the current activity in the galaxies.

We use the SFR measurements from Chapter 4 to interpolate a rough estimate of the final stellar and halo mass of the currently identified supercluster population in order to study the relative mass distributions between epochs. To do this we assume a constant SFR for the SF galaxies for a timescale based on estimates of the gas depletion timescales for star-forming galaxies.

Gas depletion timescales are based on the star-formation efficiency (SFE), which is a measure of a galaxy's SFR over the mass of the molecular gas reservoir available for star formation. The gas depletion timescale, τ_{gas}, is the inverse of the SFE. Studies of star-forming galaxies and ULIRGs at low and high redshifts have estimated the SFE from compact CO line emission. Local ULIRGs have been found to have an average gas depletion timescale of $\sim$10–100 Myr (e.g., Solomon & Vanden Bout, 2005; Magdis et al., 2012), while a $z = 1.2$ ULIRG was found to have a depletion time of ~ 70 Myr (Frayer et al., 2008), and $z \sim 2$ ULIRGs show a range of timescales of 17–96 Myr (Yan et al., 2010). We therefore use an average gas depletion timescale of $\sim$50 Myr for the three supercluster ULIRGs. For the LIRG and sub-LIRG MIPS galaxies, we use an estimate of ~ 700 Myr for the star formation lifetime, the average gas depletion timescale from a study of $0.5 < z < 2$ main-sequence galaxies (Magdis et al., 2012).

Using the current SFRs and the gas depletion timescales above, we interpolate the stellar mass build-up of the current supercluster members as they continue to merge on their path towards a single, massive cluster. This will likely give an upper limit to the final stellar mass of these galaxies. For one thing, we are using the same estimate based on the full gas depletion timescales with no knowledge of the current stage within the lifetime of the star formation at which these galaxies are detected. Also, the average depletion timescale does not take into account any further quenching or boosting of the SFRs.

The new, approximate stellar mass is converted to a halo mass as before. For the scale factor, and consequently the five parameters of the SM-HM relation, we use the estimated merger redshift of $z = 0.5$ in order to investigate the possible fate of the current supercluster members in the final cluster. As this is just an exercise to give a rough estimate of the total, final mass of the merged cluster from the current supercluster members we do not attempt to add any additional galaxies that may fall from the background or foreground field into the supercluster field, groups or cores between $z = 0.9$ and $z = 0.5$. The only correction is using the spectroscopic completeness as before, which is based on the current cluster membership.

Calculation of the halo mass at $z = 0.5$ from the increased stellar mass results in increased halo masses compared to $z = 0.9$ despite the lack of additional galaxy halos through mergers to boost the halo mass. Though the bulk of the halo mass accretion is thought to be due to the accretion of dark matter halos through mergers, a study by Genel et al. (2010) on the growth of dark matter halos found that smooth accretion of dark matter not previously bound in smaller halos accounts for $\sim$40% of the halo mass increase. The Behroozi et al. (2010) scaling relation is based on halo mass functions from simulations and overall cosmological constraints that contain uncertainties including the inability to account for the effect of subhalos below the resolution of the simulation data and uncertainties on the gas physics that can affect the dark matter halo mass. The increase in halo mass between epochs shown above without the addition of galaxy mergers is a result of the scaling relation determined by the halo mass and galaxy stellar mass functions at different epochs used in Behroozi et al. (2010).

For a better comparison of the stellar and halo mass at $z = 0.9$ to that predicted with the continued, constant star formation of the galaxies in the supercluster, we limit the total mass estimates to the area covered by the MIPS field of view only, found in the middle section of Table 5.1. The spectroscopic correction factor applied to the mass estimates is slightly lower in the 24 μm region, at 4.87. The main difference in the mass in the MIPS field of view comes from the loss of isolated galaxies outside of this area.

Comparing between the mass estimates at the supercluster redshift and the interpolated mass at $z \sim 0.5$, summarized in the bottom of Table 5.1, we find that the total halo mass located in the current core galaxies rises by $\sim$50% from $\sim 8.1 \times 10^{14}\, M_{\odot}$ to $\sim 1.2 \times 10^{15}\, M_{\odot}$. This is in line with the predicted final cluster mass at $z \sim 0.5$. The group galaxies will add an additional $4.0 \times 10^{14}\, M_{\odot}$ to the overall supercluster mass by by this redshift, and if they have all merged within the virial radius of the final cluster core, the combined halo mass of the cores and groups would be $\sim 1.6 \times 10^{15}\, M_{\odot}$. This does not take into account any mass increase due to any of the currently isolated galaxies falling onto the cluster. These isolated supercluster galaxies can fall into the cluster core either on their own or as part of a group; through accretion onto the currently identified infalling groups or by joining together in new group-sized halos ($M_{\rm Halo} \sim 10^{13}\, M_{\odot}$). The $8.9 \times 10^{14}\, M_{\odot}$ contribution of all of the isolated galaxies to the merged cluster would still be within the predicted $\sim 10^{15}\, M_{\odot}$ mass. Therefore, no decrease in star formation between the two epochs needs to occur so as to reduce the mass-contribution of the galaxies in the final cluster, even if all isolated galaxies have fallen into the cluster core by $z = 0.5$.

5.5.2 Comparison with Theories of Hierarchical Structure Formation

To investigate the merger scenario in more depth, we can once again look to compare the RCS 2319+00 supercluster to studies using galaxy merger tree information based on the hierarchical structure formation theory, as done in Section 3.4.3. In a study using semi-analyic model merger tree information to look at the accretion of galaxies onto groups and clusters, McGee et al. (2009) found that, regardless of final cluster mass, the number of isolated galaxies destined to fall into the clusters show similar distributions throughout the accretion history of the clusters. At a look-back time of 10 Gyr, the isolated galaxies contribute $\sim$55% of the cluster progenitor population, with this fraction decreasing by $\sim$5–6% per Gyr. In the case of RCS 2319+00, at a look-back time of $\sim$ 7.5 Gyr, $\sim$40% of the final merged cluster galaxies should still be found as isolated galaxies. In the MIPS field of view, the 94 isolated cluster galaxies account for $\sim$ 56% of the total supercluster membership of 167 galaxies. This higher fraction than that predicted by the McGee et al. (2009) study again suggests that as high as $\sim$30% of our currently identified isolated supercluster galaxies over the full field may in fact belong to as yet unidentified groups. At $z \sim 0.5$, the McGee et al. (2009) results suggest that $\sim$30% of the total cluster galaxies will continue to persist as isolated galaxies, meaning only about half of the currently identified isolated galaxies will have merged into groups or directly onto the cluster by that epoch.

If $\sim$30% of the identified isolated galaxies in RCS 2319+00 do belong in as yet identified groups, then the results for the stellar mass-density relation shown in Figure 4.6 and the SSFR versus local density in Figure 4.12 may be affected. In terms of the mass-density relation, we would expect the highest local density isolated galaxies are the most likely unidentified group members, so the highest density bins of the group population would likely reduce in average stellar mass given that the isolated population shows lower average stellar masses then the groups at the same local densities. This would result in the group environment being more consistent with a flat mass-density relation and show a larger difference between the group and core global environments, consistent with pre-processing. It is more difficult to determine what would become of the isolated population. If the higher mass galaxies in the highest local density bins of the isolated population are in fact members of groups, then the mass-density relation for the isolated population would decrease at higher densities, becoming more consistent with no correlation between mass and local density in this environment or even becoming slightly negative. If the lowest stellar mass isolated galaxies at the higher local densities belong to groups, then the isolated population would show a slightly positive correlation between mass and density and would be more consistent with the overall supercluster trend.

Looking at the SSFR relation with local density, the star-forming isolated and group global populations would not likely change with the shift of 30% of the isolated galaxies onto the group population as they are quite consistent. In the overall supercluster population, however, we would estimate that a change in the group and isolated fractions would increase the average SSFR of group galaxies at the highest local densities, as the isolated population shows a high SSFR in its highest local density bin. This would again result in the group population deviating further from the core population and be further evidence of pre-processing in group environments. The isolated population could either change to show a more prominent diversion from the overall population with an increased slope, or have its increasing correlation with local density flattened out, depending on the local densities of the galaxies that would shift to the group population.

McGee et al. (2009) also conclude that environmental processes acting on $M_{\rm Halo} \sim 10^{13}\,h^{-1}\,M_\odot$ groups occur over > 2 Gyr time scales. Therefore, given the ~ 3.4 Gyr time-scale for the RCS 2319+00 supercluster to merge into a Coma-sized cluster, there is sufficient time for the pre-processing of the already identified groups as well as some pre-processing in the as yet unformed groups. This would again suggest that the SFR of galaxies in these populations will have time to be quenched, in whole or in part, before the groups amalgamate into the cluster core.

The McGee et al. (2009) study also found that the group galaxies accreted onto the final cluster are more massive on average than those that fall in from smaller groups or as individual galaxies, concurrent with the mass segregation scenario. We see evidence of this between global environments when looking at the final stellar mass after gas depletion, as we did for the $z = 0.9$ mass results. The average stellar masses of the three environments increase by ∼86% in the isolated population, to $2.6 \times 10^{10}\,M_{\odot}$, ∼24% in the group population to $3.1 \times 10^{10}\,M_{\odot}$, and by ∼18% in the core population to $3.3 \times 10^{10}\,M_{\odot}$.

A similar N-body simulation study by Cohn (2012) found that approximately 30% of cluster galaxies at $z = 0.1$ had undergone some form of pre-processing in $M_{\mathrm{Halo}} \geq 10^{13}\,h^{-1}\,M_{\odot}$ groups, including a large fraction of the most massive final cluster galaxies. This is consistent with results from De Lucia et al. (2012), also using galaxy merger trees, who find that a large fraction of the most massive cluster galaxies ($M_{*} \sim 10^{11}\,M_{\odot}$) and about half of the low to intermediate mass members ($M_{*} \sim 10^{9} - 10^{10}\,M_{\odot}$) fell into the final cluster from $\gtrsim 10^{13}\,M_{\odot}$ groups. The mass of these group galaxies were not found to increase significantly after first becoming satellites of the groups, since the transition fraction between blue, active galaxies to red, passive galaxies after accretion by $\sim 10^{13}\,M_{\odot}$ size halos was found to be 60% for high stellar mass galaxies ($M_{*} \sim 10^{10.5} - 10^{12}$), increasing to 80-90% for higher mass halos ($M_{\mathrm{Halo}} \sim 10^{14.5}\,M_{\odot}$). The transition fraction, and therefore the quenching fraction, is lower for lower stellar mass galaxies, at 30-50% in the group sized halos, and 60-75% in cluster sized halos. They also find that 40-60% of galaxies first became satellites when falling onto the final cluster rather than first being accreted onto smaller groups. Berrier et al. (2009) find a higher fraction of ∼70% of galaxies that are accreted onto clusters from the field with no prior group pre-processing.

The results of the mean stellar masses in each density regime, set by the gas depletion timescale estimates and listed above, are consistent with these studies.

The primarily lower mass, isolated galaxies show the largest increase in the stellar mass build-up, at ∼86%, compared to the lower mass build-up for the already higher mass group and core galaxies with mean values increasing only ∼24% and ∼18%. In addition, we found in Chapter 4 an apparent sub-main sequence of galaxies in the RCS 2319+00 supercluster, with lower than expected star formation rates as a function of stellar mass (see Figure 4.9). The majority of the sub-main sequence star-forming galaxies were found at higher stellar masses, with a turn over to lower star formation above $\sim 2 \times 10^{10}\, M_{\odot}$. This seemingly quenched star forming population at higher stellar masses, when added to the non-star forming galaxy populations, was found to contain ∼60%, ∼70%, and ∼80% of the isolated, group and core galaxies respectively, though with large errors of 15%–20% (see Table 4.7). These increasing sub-main sequence fractions in the increasing density levels correspond well with the De Lucia et al. (2012) results for the transition fractions from active to passive galaxies in halos of increasing size.

Another test of the pre-processing of galaxies in groups was seen in Section 3.3 when looking at the fraction of red-sequence galaxies in each population as well as the colour distribution of the galaxies in the different environments in Figure 3.7. The highest red-sequence fraction was found in the cluster cores at ∼77%, followed by the ∼37% red fraction in the group galaxies and the ∼29% fraction in the isolated population. Along with this we found that the group galaxies, and in particular the Filament galaxies, showed a population of green, transient galaxies in the process of migrating to the red-sequence. Though the groups as a whole show few galaxies in the green valley, a closer look at the colour-magnitude diagram in Figure 3.6 shows that Groups 1 and 3 (labeled as groups 7 and 13 in the FOF results) have the highest population of green galaxies, after the Filament. This would suggest that they are in a different stage in their pre-processing from blue to red galaxies compared to the other groups and cores. This is consistent with the results shown in Table 4.6 in Section 4.5.2, which shows the mean SSFR in these galaxies is higher than those in Groups 2 and 4 as well as Clusters B and C. Cluster A has a similar mean SSFR to that of the Filament, which has the lowest between itself and Groups 1 and 3. The Filament also has the highest fraction of green galaxies versus blue galaxies and therefore is probably in a later stage of pre-processing.

These theoretical studies all suggest that some pre-processing of cluster galaxies in groups is occurring prior to accretion onto the final cluster. They also suggest that quenching will begin upon accretion onto a group or directly onto the cores, with higher mass galaxies having a higher quenching fraction. We see evidence of this pre-processing in RCS 2319+00; through the fraction of galaxies in each density regime that fall below the main sequence of star forming galaxies, with the increasing average mass per galaxy in the increasingly dense global environments both at $z = 0.9$ and at the end of the gas depletion timescales, and with the colours of the galaxies in the groups showing different blue to red transitions.

5.6 Summary of the Current and Future Mass Content

In this chapter we have investigated the current mass content of the RCS 2319+00 supercluster and found an estimated total stellar mass of all galaxies, from the isolated infalling galaxies through to the dense cluster cores of $2.16 \times 10^{13}\,M_\odot$, with a corresponding halo mass of $1.84 \times 10^{15}\,M_\odot$. The core galaxies contribute only $\sim 29\%$ of the stellar mass yet account for $\sim 44\%$ of the total halo mass, due to the higher average stellar mass of core galaxies over group and isolated galaxies. The isolated galaxies in the supercluster field, on the other hand, account for only $\sim 41\%$ of the halo mass but make up the majority, at $\sim 55\%$, of the stellar mass content.

The estimated halo mass of each cluster core of $5.28, 0.45$ and $1.77 \times 10^{14}\,M_\odot$ for

Clusters A, B and C are consistent with the masses derived from the spectroscopic velocity dispersions, though those carried large errors. Cluster A has a mass consistent with the X-ray and weak lensing mass estimates for the cluster while Cluster C is found to have a corrected halo mass 2–3 times lower than the X-ray estimate. Cluster B remains an outlier, with its estimated halo mass an order of magnitude lower than the X-ray value. The average core halo mass of $2.5 \times 10^{14}\,M_{\odot}$ agrees well with the masses derived through the LF methods in Chapter 3 of 0.9–$6{\times}10^{14}\,M_{\odot}$.

The groups are found to have masses on the order of $10^{13}\,M_{\odot}$, as expected from the average group LF estimates of 4–$5{\times}10^{13}\,M_{\odot}$ and consistent with the halo size of groups thought to be important in the pre-processing of galaxies in theoretical models. The only outlier is Group 3, a filamentary group falling in towards Cluster C that contains two of the three identified ULIRGs in the supercluster. It has a higher estimated halo mass of $1.5 \times 10^{14}\,M_{\odot}$ more consistent with a cluster mass, however it contains a high fraction of star forming galaxies not consistent with an established red-sequence seen in typical cluster cores.

Approximating the final merged cluster mass of the supercluster at $z \sim 0.5$ from the star formation rates found at $z = 0.9$ using gas depletion timescales, we find that the core galaxies will contribute a halo mass of $\sim 1.2 \times 10^{15}\,M_{\odot}$ to the final cluster. The additional $\sim 4.0 \times 10^{14}\,M_{\odot}$ found in the infalling groups at this epoch would be well within the estimated $\sim 10^{15}\,M_{\odot}$ cluster mass should some or all of the groups have merged with the parent cluster by then. The isolated galaxies, who may be accreted within the 3.75 Gyr timeframe either individually or having first been accreted onto group sized halos, will contribute a halo mass of $8.9 \times 10^{14}\,M_{\odot}$ over the cluster field. This value, however, does not take into account any enhancement or quenching of the star formation as the isolated galaxies accrete onto either groups or directly onto the cores.

The fractions of galaxies at $z = 0.9$ below the main sequence of star forming galaxies in each density population found in Chapter 4 are consistent with the theoretical studies showing increasing transitions between active star forming galaxies and passive galaxies from the lowest to highest density regions. The increasing average mass per galaxy in the increasingly dense global environments, both at $z = 0.9$ and after depletion of all the molecular gas, and therefore a cessation of star formation, is also consistent with the theoretical models.

We conclude that the mass estimates in this section for the cluster cores and groups are consistent with others presented in this thesis. The current and predicted mass distribution in the supercluster agrees well with theoretical models that predict pre-processing in $\sim 10^{13}\,M_{\odot}$ group environments. This, in addition to other indications of pre-processing in groups throughout the thesis, suggest that we are witnessing varying degrees of galaxy pre-processing in the identified groups as the fall towards the dense cluster cores in the RCS 2319+00 supercluster.

Chapter 6

Conclusions and Future Work

6.1 Thesis Conclusions

This thesis has presented a large-scale study on the unique, compact, high-redshift RCS 2319+00 supercluster at $z = 0.9$. We are witnessing this supercluster as it is in the process of merging to form a massive $\sim 10^{15}\,M_{\odot}$ cluster by $z \sim 0.5$, as predicted by Gilbank et al. (2008a). In Chapter 1, we offered a brief overview of hierarchical structure in the universe, motivating the importance of studying superclusters at high redshift as they present ideal laboratories to test galaxy evolution in different global regions within a single large-scale structure.

We first compiled an extensive spectroscopic redshift catalogue on the supercluster field in Chapter 2. 302 spectroscopic members were confirmed to lie within three distinct galaxy sheets surrounding the supercluster, separated from one another by only $\Delta\, z = 0.03$ in redshift (∼65 Mpc). The spectroscopically derived cluster mass estimated from velocity dispersions of $\sim 8, \sim 6$ and $\sim 3 \times 10^{14}\,M_{\odot}$ are comparable to existing X-ray mass estimates as well as the weak lensing mass for Cluster A.

The unique compactness of these three clusters both in redshift space and in angular separation makes RCS 2319+00 an excellent laboratory for studying cluster mergers. This tight proximity however, with the clusters lying $< 3\,$Mpc from their nearest neighbour, makes assigning cluster members to their parent cores using conventional methods very difficult. As such, we traced the structures in the supercluster region in Chapter 3 using a friends-of-friends algorithm, identifying five infalling groups in addition to the three cluster cores. One of these groups is a filamentary structure stretching between two of the three cluster cores and corresponds well with the position of an IR-bright filament region found by Coppin et al. (2012) using *Herschel* data.

Analysis of the galaxy colours found ~80% of the galaxies in the cores lie along the red-sequence, as expected from cluster theories. The red galaxy fraction in groups is lower at $\sim 40\%$, consistent with the red fraction over the full supercluster field. The distribution of group galaxy colours lies between those of the isolated galaxies and the core galaxies, with blue, green and red galaxies populating the groups to varying degrees. Three groups, including the Filament, show higher green galaxy fractions and we propose they are in a transitional state between isolated and core galaxies, indicating that there is likely some galaxy pre-processing occurring in the infalling groups. Richness estimates from stacked luminosity function fits result in average group mass estimates consistent with $\sim 10^{13}\,M_\odot$ halos. Currently, 22% of our confirmed members reside in $\gtrsim 10^{13}\,M_\odot$ groups/clusters destined to merge onto the most massive cluster, in agreement with the massive halo galaxy fractions important in cluster galaxy pre-processing in N-body simulation merger tree studies.

In Chapter 4, multiwavelength data was combined with the spectroscopic catalogue in order to study to distribution of stellar mass and star formation in the supercluster. Using the confirmed members and their FOF associations as isolated, group or core galaxies we investigated the role of both the local and global environment on the stellar mass and star formation rate of cluster galaxies. The stellar mass versus local density was found to show no correlation when isolating the star forming galaxies, in contrast to the expected mass segregation where the most massive galaxies populate the densest regions, which is seen for the full supercluster sample. The lack of correlation is driven by the isolated star forming galaxies. Their average stellar masses are lower than their counterparts in the groups and cores at the same local densities. The isolated galaxies contribute a large fraction of galaxies to each density bin over the full star-forming sample and therefore drive the total average stellar masses down for the high density bins, flattening out the full trend. From this we infer that the global environment may be playing a role in the mass-density relation for star-forming galaxies rather than the local density, which dominates the relation for non-star-forming galaxies whose mass-density correlation follows the expected mass-segregation scenario.

We analyzed the SFR-density relation in a variety of ways; looking at the fraction of star-forming galaxies in each global environment, comparing total SFR measurements and examining the mean SSFRs in each population. We found that the RCS 2319+00 supercluster follows the local SFR-density relation, with the star formation primarily located in the lower density, infalling isolated and group regions. An analysis of the <SSFR> versus local density suggests some enhancement in the star formation activity in the denser regions of these groups and isolated outskirt galaxies. This increased activity may be induced as these galaxies accrete onto larger group or core halos.

Though we see evidence of enhanced star-formation in the densest regions of the groups and isolated galaxies, there is also evidence of both environment-quenching and mass-quenching in RCS 2319+00. This is found through a bimodal distribution in the SFRs with respect to stellar mass. Despite the presence of the known star-forming galaxy main sequence, where SFR increases with stellar mass, a sub-main sequence population of partially quenched star forming galaxies is also apparent below the main sequence trend. The sub-main sequence itself seems to be divided between a subset of galaxies along a relatively flat SFR containing $\sim 17-18\%$ of the group and isolated galaxy population, due to environment-quenching, and a region of apparent mass-quenching, where we see a sharp turn-over in SFR at higher stellar masses in all global populations. The fraction of all galaxies, both star-forming and non-star-forming, in the high mass region of the sub-main sequence shows signs of increasing as a function of global populations with $\sim 60\%$, $\sim 70\%$ and $\sim 80\%$ of the isolated, group and core galaxies in the sub-main sequence above $2 \times 10^{10}\, M_{\odot}$. This suggests a combination of environment and mass-quenching occurring at these masses, though our small numbers do not yield statistically significant results. The results are also consistent with studies of galaxy merger tress from N-body simulations, where the transition fraction from star-forming to passive galaxies increases in halos of increasing mass.

To better relate the structure in the merging RCS 2319+00 supercluster to simulations using hierarchical formation models, we investigate both the total current and possible future stellar and halo mass distributions in Chapter 5. We compared the current to final mass estimates, using star formation depletion timescales based on estimates for LIRGs and ULIRGs to estimate the final stellar mass. Our results show agreement with theoretical work in that the average mass build-up after accretion into a group or cluster halo is reduced with respect to the isolated infalling galaxies. This again suggests that pre-processing of the galaxies is occurring in the infalling groups before their final accretion onto the cluster halos.

The main results of this work show that the different global environments defined within the merging RCS 2319+00 supercluster at $z = 0.9$ are experiencing different evolutionary effects. Indications of enhanced star-formation in the highest local density regions of the isolated and group global environments could be due to a triggering of star formation as galaxies are first accreted onto the outskirts of the groups and clusters. We see signs of external environmental quenching of a percentage of star-forming galaxies in the group and isolated regions in the flat portion of the sub-main sequence, suggesting pre-processing in these regions. Internal mass quenching occurs in star-forming galaxies in all global populations of the supercluster, with approximately half of all star-forming galaxies in each population with stellar masses $\geq 2 \times 10^{10}\,M_\odot$ having lower SFRs than expected from the star-forming main-sequence. Over the full supercluster population, the quenching fractions in the high stellar mass galaxies increase from the lowest density global regions in the isolated infalling population, through the group environments, with the highest quenching fractions occurring in the cluster cores. The $z = 0.9$ RCS 2319+00 supercluster follows the predictions of semi-analytic merger tree studies, with evidence of pre-processing of the star-formation activity and galaxy stellar mass in group environments before accretion onto the cluster cores, which contain massive, primarily passive galaxies.

6.2 Future Work: RCS 2319+00

Additional work on estimating the merger rates and possible fate of the supercluster members identified in this study is planned to further explore the role of infalling groups on the star formation activity in the galaxies. Attempting to place constraints on the merger timescales may shed light on why some of our groups appear to be have enhanced star formation activity while others show signs of star-formation quenching.

Using the multiwavelength catalogue described in Chapter 4, along with a few additional wavelengths of data (the g, i, and J bands from CFHT), collaborators are currently working on compiling a large photometric redshift catalogue spanning the RCS 2319+00 field. The full spectroscopic catalogue compiled herein of 1961 good confidence galaxy redshifts in the region is being used to examine the accuracy of the photometric results. The new photometric redshift supercluster member list is being used by collaborators to trace the substructure once more, again using a FOF analysis. The larger errors in redshift estimates from photometric techniques means that the spatial separation of the galaxies within broader redshift slices is used in the analysis. The additional galaxy numbers with photometric redshifts will help combat the small number statistics we find using only spectroscopic members.

Other studies currently underway by collaborators using the spectroscopic catalogue from Chapter 2 include a study of the far-infrared properties of the supercluster galaxies in a *Herschel* SPIRE map of the supercluster and an analysis of spectral lines to look for signatures of AGN in the both the supercluster and the foreground field.

6.3 Future Work: Global versus Local Environments in Large Surveys

In order to confirm and quantify galaxy pre-processing in group environments large samples of well characterized spectroscopic galaxies in wide field studies and large cluster samples are needed. Wide-field surveys with well characterized galaxy environments can allow for the study of global and local environmental effects over large scales. Results from consistent analysis of different cluster environments over a large range in mass and redshift would help characterize the effects of pre-processing on cluster galaxies in the hierarchical formation model. Work is currently underway on a large cluster sample over a broad redshift and mass range using similar techniques as defined in this thesis on the RCS 2319+00 supercluster.

A large spectroscopic sample has been assembled on the 45 RCS-1 clusters ranging in redshift from $0.2 \leq z \leq 1.0$ that have been previously targeted with the *Spitzer* MIPS instrument and used for statistical analysis of cluster MIPS fractions (Webb et al., 2013). The spectroscopy has been combined from three large campaigns. Half of the clusters have spectroscopic coverage from the large survey of RCS-1 clusters using the Magellan IMACS spectrograph (see Section 2.2.1 for details). The spectroscopic survey using the CFH-MOS and Magellan-LDSS2 spectrographs done for the PhD research of Kris Blindert (Blindert, 2006) covers a third of the clusters. A third of the data is also covered by a survey using the twin Gemini telescopes' GMOS North and South instruments. This cluster sample has been observed in multiple wavelengths, similar to the RCS 2319+00 field, so as to extract galaxy photometric redshift estimates, stellar masses and star-formation rates for use in evolutionary studies.

The GMOS spectroscopic campaign was designed to target 24 μm sources in the cluster fields specifically, versus the optically selected targets from the other two surveys. The IDL-based redshift finding program employed for the VIMOS, FMOS and GMOS-N data in RCS 2319+00 (Section 2.2) was originally written for the use with this GMOS spectroscopic survey.

The goal of the spectroscopic campaign is to first estimate cluster velocity dispersions and virial masses, which is underway. The plan is to then carry out similar structure finding on the RCS-1 clusters as done in Chapter 3 to look for infalling groups in the smaller cluster systems and search for evidence of other cluster-cluster mergers. Two potential merging cluster systems have already been found in the preliminary analysis of the data, one at $z \sim 0.63$ and the other at $z \sim 0.87$. With the aid of defined global environments in clusters and potential merging structures over the large redshift range of the RCS-1 clusters, we can delve deeper into the role of the global versus local environment in driving galaxy evolution.

Appendix A

Foreground Structures in the RCS 2319+00 Field

With the vast amount of spectroscopically confirmed redshifts available on the supercluster field region we are able to search for foreground and background structures. In Figure 2.3 we identified five potential foreground redshift peaks that have close photometric red-sequence overdensities in the RCS catalogue at $z \sim 0.28$, 0.45, 0.53 and 0.76. The presence of the redshift peaks, in conjunction with the red-sequence overdensities, leads us to surmise that there may be foreground clusters or groups present in the RCS 2319+00 field.

To look for structure in these redshift peaks we applied the same friends-of-friends algorithm used on our supercluster in Section 3.2.2 on broad redshift slices around each redshift peak. The redshift ranges used are indicated for each of Figures A.1a-d, where we plot all redshifts in that range as blue and red lines indicating the relative velocity to the central redshift of the slice (blue shifted or red shifted respectively). The plots are all centered on $23^{\mathrm{h}}19^{\mathrm{m}}52^{\mathrm{s}}.8 + 00^{\circ}34'12''$, with the contours of the closest photometric red-sequence density profile map to each redshift range shown for comparison. The FOF identified groups are indicated by same coloured boxes, as done in Figure 3.2.

In the lowest redshift peak at $z \sim 0.28$ (Figures A.1a) we recover an 8 member group with an average redshift of $z = 0.278$ corresponding to the position of the largest red-sequence density peak near this redshift. This may represent a foreground cluster. The redshift slice around $z \sim 0.45$ has one 6 member group but no real correspondence to the red-sequence profile in the same redshift space and may therefore belong to an isolated group. Three of the recovered groups in the redshift peak at $z \sim 0.53$

follow the red-sequence significance peaks, with the largest peak correlating with an 18 member recovered group with an average redshift of $z = 0.529$. We suspect that this peak represents a foreground cluster. The final foreground slice we tested around $z \sim 0.76$ results in several FOF groups, including three with 5, 6 and 8 members. Though some of the smaller groups in this redshift range lie along red-sequence density peaks, the larger groups do not. This slice also shows the contamination of the red-sequence galaxy distribution from neighbouring redshift slices. This is evident from the appearance of the three distinct, high significance peaks of the RCS 2319+00 supercluster at $z = 0.9$ already contaminating the lower redshift slice.

The large multiwavelength campaign underway on the RCS 2319+00 supercluster region covers the area of these foreground structures to varying degrees depending on the wavelength. We will be able to use the multiwavelength catalogues generated for the supercluster to study these foreground objects in more depth. A study in underway by collaborators to create an accurate photometric redshift catalogue that will be used to further corroborate and investigate these potential foreground groups and clusters.

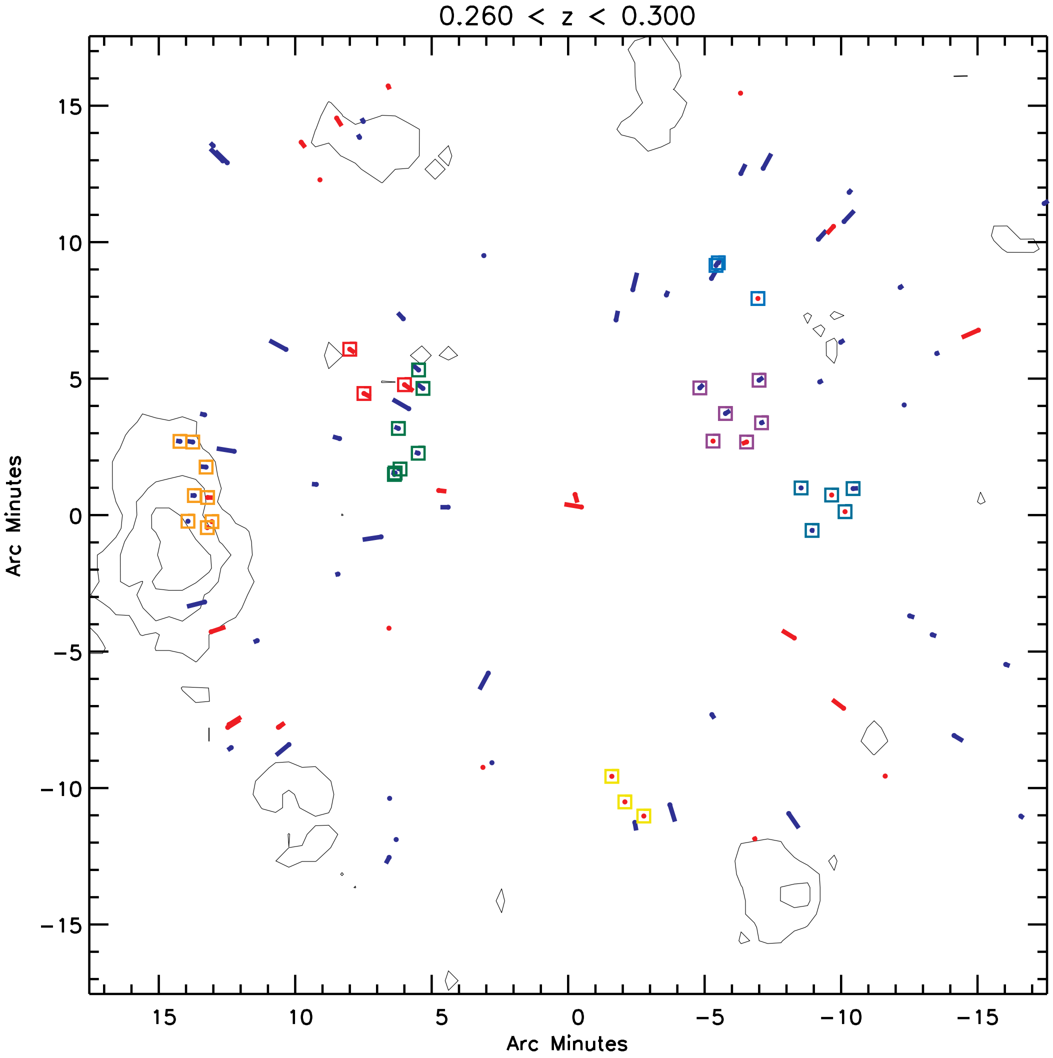

Figure A.1a Distribution of galaxies in the foreground redshift peaks seen in Figure 2.3. All foreground galaxies within the given redshift range are plotted as relative velocities (blue and red lines for blue and red-shifted galaxies) to the mean redshift. The closest corresponding red-sequence density profile contours are shown. FOF identified groups are identified as same coloured boxes. The redshift range for this panel is $0.26 \leq z \leq 0.30$, corresponding to the $z \sim 0.28$ peak in the redshift histogram.

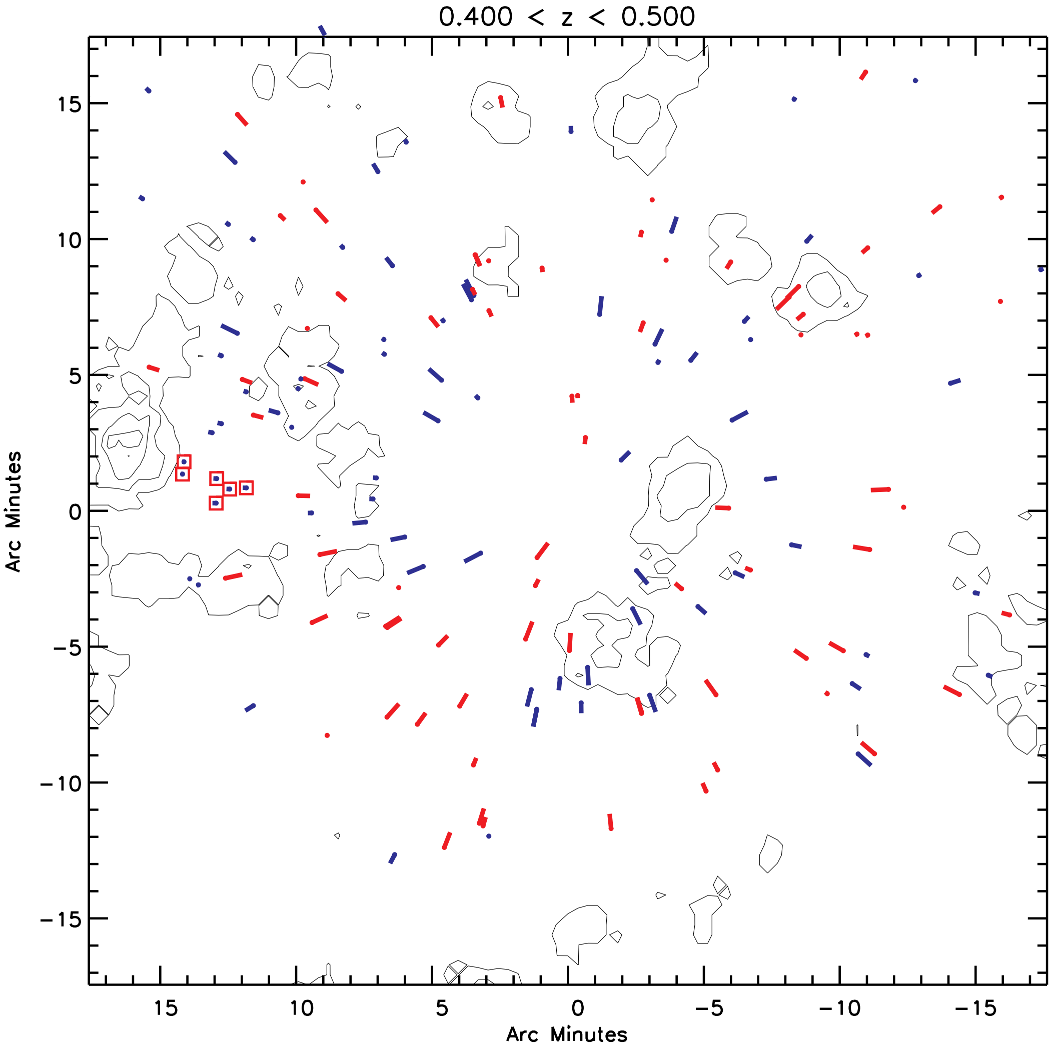

Figure A.1b Same as Figure A.1a, with a redshift range of $0.40 \leq z \leq 0.50$ covering the $z \sim 0.45$ peak in the redshift histogram.

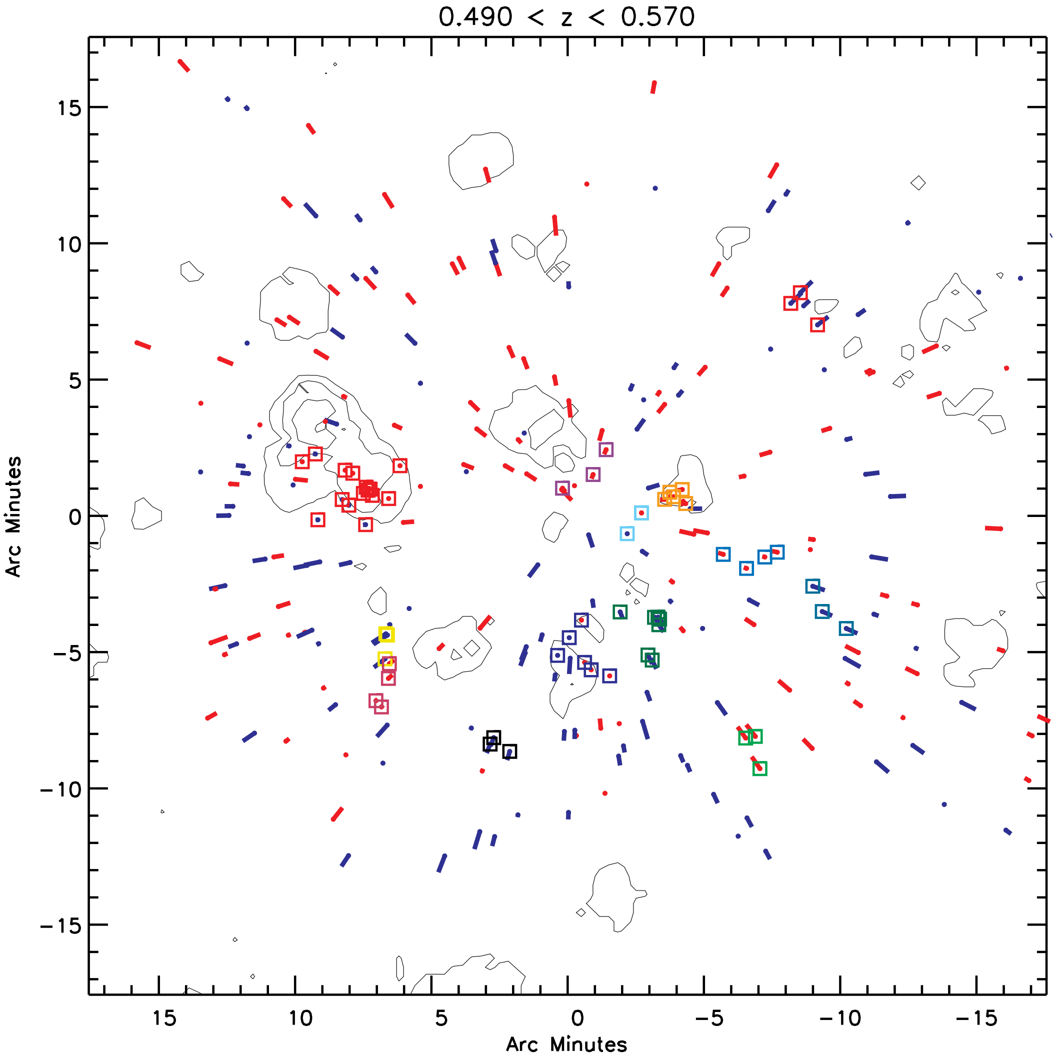

Figure A.1c Same as Figure A.1a, with a redshift range of $0.49 \leq z \leq 0.57$ covering the $z \sim 0.53$ peak in the redshift histogram.

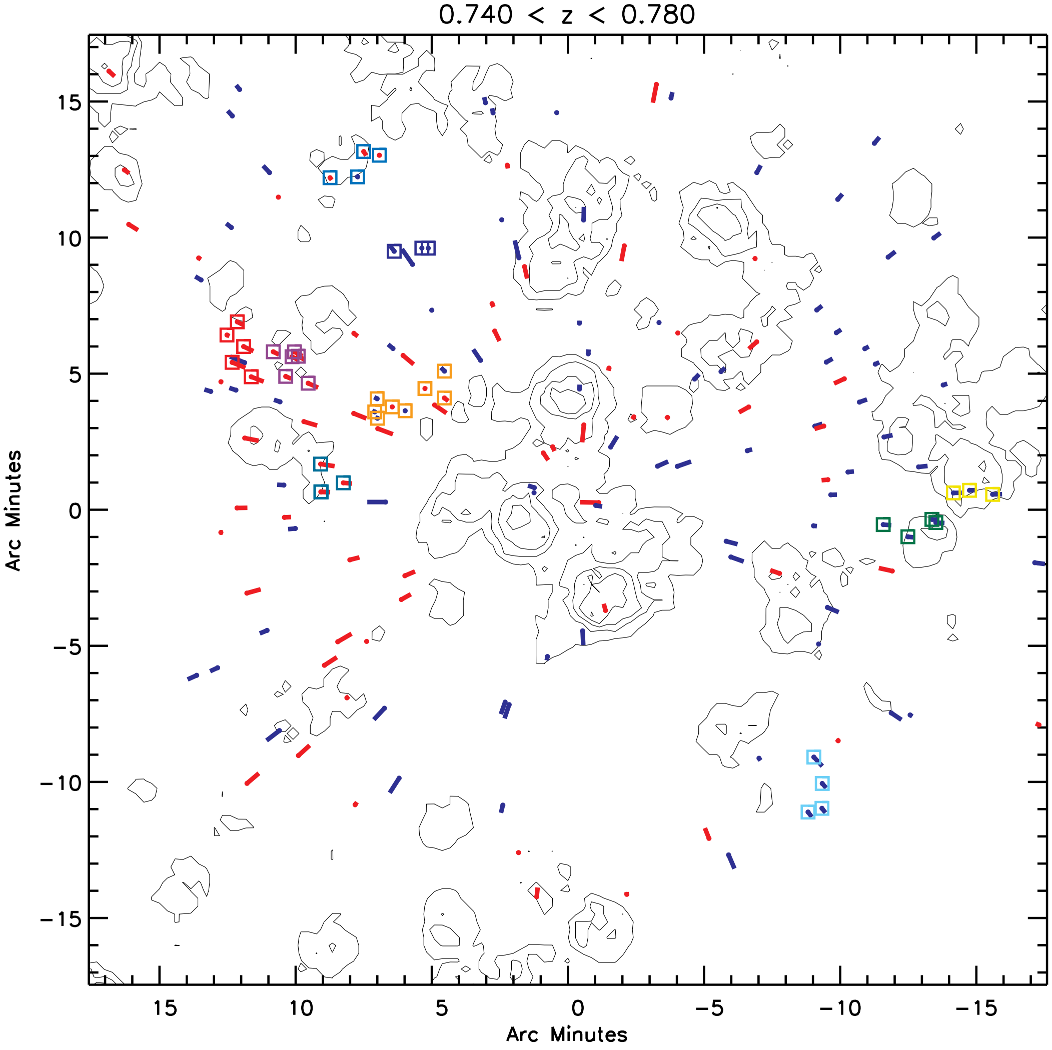

Figure A.1d Same as Figure A.1a, with a redshift range of $0.74 \leq z \leq 0.78$ covering the $z \sim 0.76$ peak in the redshift histogram.

Appendix B

AGN Contamination

In Chapter 4 we briefly discussed the possibility of MIPS 24 μm SFRs being boosted by active galactic nuclei (AGN). There we summarized the results of other studies showing little contamination from AGNs in clusters at $z \sim 1$. Here we look at the ancillary data compiled on the RCS 2319+00 supercluster and use it to assess in more detail the potential AGN contamination of the MIPS SFRs.

X-ray and Radio Emission

The *Chandra* X-ray data covers the majority of the MIPS field of view. The fraction of AGN in clusters from X-ray sources is found to increase with redshift, however, by $z \sim 0.6$ Eastman et al. (2007) find this fraction has increased to only ∼2%. In the RCS 2319+00 supercluster, X-ray point source detections are found for only seven member galaxies, five of which have 24 μm fluxes. Only one galaxy has X-ray, MIR and radio flux detections. The lack of radio and X-ray detections for the majority of our MIPS sources seems to indicate low AGN contamination.

The few sources with both MIR and radio counterparts allow for a direct comparison of their flux values. A MIR/Radio correlation exists for star-forming (SF) galaxies that is consistent to $z \sim 2$. Different studies find values of the correlation $q = \log(f_{24\mu\mathrm{m}}/f_{1.4\mathrm{GHz}})$ of ∼0.5–1.3 (e.g., Appleton et al., 2004; Ibar et al., 2008; Beswick et al., 2008; Huynh et al., 2010a; Rieke et al., 2009; Boyle et al., 2007). Using all 26 galaxies in our RCS 2319+00 field that have both 24 μm and radio flux along with spectroscopic redshifts, we find a correlation $q = 0.70 \pm 0.38$. AGN would result in $q < 0$.

Table 4.4 lists the q values of the five $24\,\mu$m/1.4 GHz supercluster galaxies, which all lie above zero. The two ULIRGs have a higher fraction than the star-forming correlation we find, though consistent with the higher correlations of other studies. U et al. (2012) found that 60% of local ULIRGs are found to be AGN. However, studies of ULIRGs at high redshifts show that while they may contain an AGN component, the majority of the emission is due to star formation, with their MIR spectrum comparable to local starbursts rather than local ULIRGs (Farrah et al., 2008). Based on the q value and the Farrah et al. (2008) results, the $24\,\mu$m SFR of the ULIRGs are likely not significantly boosted by the presence of an AGN. The X-ray/radio/MIPS galaxy located in the Filament has a q value that lies right along the MIR/radio correlation relation, which would argue against significant AGN contamination despite the additional X-ray detection. The other three galaxies also lie within the errors of our value for the MIR/radio correlation and are therefore likely not dominated by emission from AGN.

Mid-IR Color Diagnostic

For the majority of the MIPS supercluster members for which we do not have radio or X-ray counterparts (86%), we can look to the IRAC colours to help determine possible AGN contamination. Of the 100 supercluster members with detections in all four IRAC bands, 44 belong to our MIPS population. The IRAC colours are plotted in Figure B.1 with the proposed AGN selection region of Lacy et al. (2004) shown with dotted lines. Even within this broad AGN selection region we find that only ten of our MIPS supercluster galaxies, including two of the ULIRGs and two of the X-ray counterparts, would be classified as AGN.

For MIPS galaxies with IRAC detections missing in one or two bands, either due to no detection or due to the differences in the fields of view of the IRAC channel 1&3

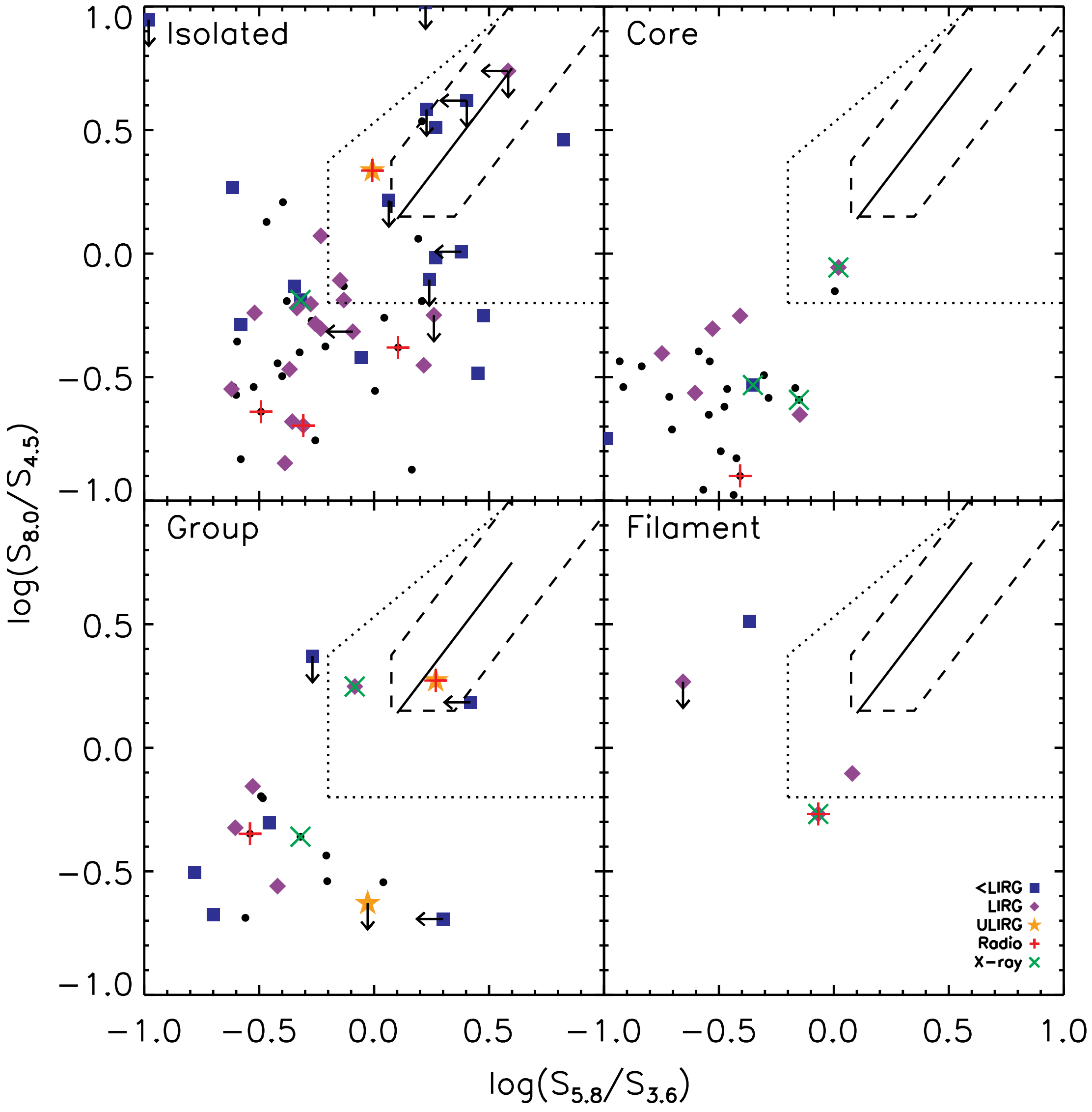

Figure B.1 IRAC colour-colour plot of supercluster members, divided by density within the supercluster using the FOF designations from Chapter 2. The dotted lines represent the AGN selection region defined in Lacy et al. (2004, 2007) while the dashed lines enclose the reduced AGN selection criteria found by Donley et al. (2012) to better isolate AGN with less contamination from purely star-forming galaxies. The solid line is a perfect power law with α=-0.5 to -3.0. MIPS galaxies with IRAC detections missing in one or two bands are show with the limits of the colours using the completeness limits of the four IRAC bands.

and channel 2&4 images, we show the limits of the colours given the completeness limits of the four IRAC bands (4.2, 6.0, 27.0 and 26.0 μm for the 3.6, 4.5, 5.8 and

8.0 μm channels respectively; Noble et al., 2012). This adds fifteen galaxies to the colour-colour plots. Seven of the MIPS sources with colour limits lie within the Lacy et al. (2004) AGN selection region, only one having LIRG luminosity, with an additional isolated MIPS galaxy having a 5.8/3.6 μm colour and 8.0/4.5 μm colour limit that could move it within the AGN criteria boarders.

Though Lacy et al. (2007) found only a minimal contamination (8%) in the AGN selection region from star-forming galaxies for their sample of 24 μm luminous AGN and quasars, Donley et al. (2012) found high contamination by SF galaxies in the same region using COSMOS-selected SF and AGN galaxies up to $z \sim 2.5$. The Donley et al. (2012) study used the IRAC colours of composite SED templates for $0 < z < 3$ starburst and AGN galaxies along with the hard-band detected X-ray AGN in the XMM-COSMOS galaxies to further limit the AGN selection region on the IRAC colour-colour plot, as indicated by the dashed lines on Figure B.1. Of our ten MIPS galaxies in the Lacy et al. (2007) AGN selection region, only two remain within the more rigid criteria defined by Donley et al. (2012). Looking at the MIPS galaxies with colour limits, two are within the smaller AGN selection region, with an additional three falling along a colour line with limits that allow for AGN classification.

AGN Summary

From the methods employed above we can conclude that there is little evidence of significant AGN boosting of the IR SFRs in our 66 MIPS-detected supercluster galaxies. We attempt to correct for 24 μm cluster members with no X-ray or radio detection and without detections in all four IRAC bands. We assume 2-3 AGN in our sources from the ancillary data tests discussed above and we set a generous AGN contamination rate at $\sim 7-10\%$. This incorporates two of the ULIRGs, including the isolated one just outside the border of the Donley et al. (2012) AGN selection region, which we have already determined are most likely starburst galaxies according to the Farrah et al. (2008) study of high-redshift ULIRGs. Their SFR is therefore probably not dominated by the presence of AGN. In addition, Elbaz et al. (2010) used data from *Herschel* in the GOODS-North field and found that two thirds of the galaxies that are identified as AGN have dust temperatures similar to pure star-forming galaxies. They suggest that the IR emission of the AGN is therefore dominated by star formation, which happens simultaneously with the AGN activity.

In the case that there are a few additional <ULIRG luminosity 24 μm supercluster members that contain AGN, the IR-derived star formation from the majority of these would not be boosted by the AGN and therefore would not affect our results. So, though we allow for an upper limit on the AGN contamination rate of 7–10% at most, only one of two of our MIPS-derived SFRs may be significantly affected by the presence of an AGN.

Appendix C

Radio-faint 24 μm Sources and 24 μm-Faint Radio Sources

Using the multiwavelength data, we find that the majority of the MIPS supercluster members (61/66) have no radio counterpart, with ~72% of those (44/61) having 24 μm derived SFRs above the 1.4 GHz completeness limit of 10 $M_\odot\,\mathrm{yr}^{-1}$. The lack of radio counterparts is similar to results of previous studies. Huynh et al. (2010a) found only three out of 60 sources detected in 24 μm in their $0.75 < z < 1.00$ redshift bin of galaxies in the Hubble Deep Field South (HDF-S) had 1.4 GHz counterparts. Only four of the 41 MIPS structure members in a study of a proto-cluster filamentary region comprising three groups at $z = 1.016$ by Elbaz et al. (2007) were detected at 1.4 GHz.

The apparent radio emission suppression could be a result of lower radio emission than at $z \sim 0$ due to inverse Compton scattering interactions with the CMB at higher redshifts causing electrons to lose energy or due to lower magnetic field strengths compared to the local universe (e.g., Huynh et al., 2010a; Mao et al., 2011). Another possibility is that the MIR emission is boosted above the radio emission for some of the radio nondetection cases due to strong bursts of star formation that, as discussed in Section 4.3.4, may precede the supernova activity responsible for the radio emission by $\sim$ 30 Myr.

Infrared-faint radio sources (IFRS) have been found by previous studies (e.g., Norris et al., 2006, 2007; Middelberg et al., 2008; Huynh et al., 2010a) to be high flux radio sources of a few hundred μJy to several mJy at 1.4 GHz with very faint or nondetected IR counterparts. For intermediate redshifts of $z \sim 1$ explanations put forth to describe the lack of IR emission by these studies include the sources being highly obscured radio galaxies, radio lobes of close but undetected radio galaxies, or an as yet unknown class of galaxies.

Of our seven radio galaxies in the MIPS field of view not detected in $24\,\mu$m, only two, the Head-tail and Southern Radio sources in the core of Cluster A, have flux densities above 1 mJy and are likely AGN dominated galaxies. The other five galaxies have 1.4 GHz flux densities ranging from $\sim 32 - 120\,\mu$Jy, with four having IRAC detections in all four bands, contrary to the IFRS population where no IR detections or only very faint detections are available. Only one of these, a member of Group 2, has IRAC fluxes above the completeness limits in all four channels. The other three MIPS-faint radio galaxies with detections in the 4 IRAC channels have one or both of the $5.8\,\mu$m and $8.0\,\mu$m detections below the 3σ completeness limits. The IRAC colours of the $24\,\mu$m-faint radio sources place them outside of the AGN region on the IRAC colour-colour diagram (see Figure B.1). Two are located in Cluster A and the final two are assigned to the isolated supercluster field.

Also contrary to most IFRSs, these five MIPS-faint radio galaxies have reasonably bright optical counterparts, with the faintest having a z' magnitude of 21.65. All of the radio cluster members with no MIPS detections have $R_c - z'$ colours that place them on or above the red-sequence line on the colour magnitude diagram (Figure 3.6). A study by Richards et al. (1999) on radio sources in the Hubble Deep Field found that $\sim 20\%$ of the μJy radio sources had no counterpart in the I-band imaging (to a limit of 25 mag) but these optically faint radio sources had $I - K$ colour limits that also identified them as red galaxies. For the intermediate redshift of this study, the explanations for the optically faint radio sources given by Richards et al. (1999) are consistent with those mentioned above, of highly obscured radio-loud starburst/AGN or jets from neighbouring galaxies.

Another possible explanation is a deficit of the $24\,\mu$m emission of these galaxies due to low metallicities. A lower metal content in a sample of nearby galaxies has been found to cause reduced emission from the PAH bands responsible for the 24 μm emission at $z \sim 1$ (Engelbracht et al., 2005; Madden et al., 2006). This could be the cause of the deficit in the 24 μm detections of these galaxies, while they remain visible in the lower MIR bands not affected by PAHs. The combination of the IRAC colours, the red optical colours, the detection of the lower MIR bands and the lower than IFRS radio fluxes present in these galaxies leads us to believe that at least four of our remaining five 24 μm-faint radio sources are most likely low metallicity star forming galaxies.

References

Appenzeller, I., Fricke, K., Fürtig, W., et al. 1998, The Messenger, 94, 1

Appleton, P. N., Fadda, D. T., Marleau, F. R., et al. 2004, ApJS, 154, 147

Bahcall, N. 1988, ARA&A, 26, 631

Bahcall, N., Dong, F., Hao, L., et al. 2003, ApJ, 25, 814

Bahcall, N., & Soneira, R. 1983, ApJ, 270, 20

—. 1984, ApJ, 277, 27

Bahcall, N. A. 1999, in Formation of Structure in the Universe, ed. A. Dekel & J. P. Ostriker, 135

Bai, L., Marcillac, D., Rieke, G. H., et al. 2007, ApJ, 664, 181

Baldry, I. K., Balogh, M. L., Bower, R. G., et al. 2006, MNRAS, 373, 469

Baldwin, J., Phillips, M., & Terlevich, R. 1981, PASP, 93, 5

Balogh, M., Baldry, I., Nichol, R., & Al., E. 2004a, ApJ, 615, L101

Balogh, M., Schade, D., Morris, S. L., et al. 1998, ApJL, 504, L75

Balogh, M., Eke, V., Miller, C., et al. 2004b, MNRAS, 348, 1355

Balogh, M. L., Morris, S. L., Yee, H. K. C., Carlberg, R. G., & Ellingson, E. 1997, ApJ, 488, L75

—. 1999, ApJ, 10, 54

Balogh, M. L., Wilman, D., Henderson, R. D. E., et al. 2007, MNRAS, 374, 1169

Balogh, M. L., McGee, S. L., Wilman, D., et al. 2009, MNRAS, 398, 754

Balogh, M. L., Mcgee, S. L., Wilman, D. J., et al. 2011, MNRAS, 412, 2303

Barnes, J., & Hernquist, L. 1991, ApJ, 370, L65

Barro, G., Pérez-González, P. G., Gallego, J., et al. 2011, ApJS, 193, 30

Baugh, C. M. 2006, RPPh, 69, 3101

Baum, W. 1959, PASP, 71, 106

Becker, M. R., Mckay, T. A., Koester, B., et al. 2007, ApJ, 669, 905

Beers, T., Flynn, K., & Gebhardt, K. 1990, AJ, 100, 32

Behroozi, P. S., Conroy, C., & Wechsler, R. H. 2010, ApJ, 717, 379

Bell, E., McIntosh, D., Katz, N., & Weinberg, M. 2003, ApJS, 149, 289

Bell, E. F. 2003, ApJ, 586, 794

Bell, E. F., & de Jong, R. S. 2001, ApJ, 550, 212

Bell, E. F., Zheng, X. Z., Papovich, C., et al. 2007, ApJ, 663, 834

Bell, E. F., Wolf, C., Meisenheimer, K., et al. 2004, ApJ, 608, 752

Benson, A. J. 2001, MNRAS, 325, 1039

Berlind, A. A., & Weinberg, D. H. 2002, ApJ, 575, 587

Bernardi, M., Sheth, R. K., Nichol, R. C., Schneider, D. P., & Brinkmann, J. 2005, AJ, 129, 61

Berrier, J. C., Stewart, K. R., Bullock, J. S., et al. 2009, ApJ, 690, 1292

Bertin, E. 2006, ASPCS, 351, 112

Bertin, E., & Arnouts, S. 1996, A&AS, 117, 393

Bertin, E., Mellier, Y., Radovich, M., & Missonnier, G. 2002, ASP Conference Series, 281, 228

Beswick, R. J., Muxlow, T. W. B., Thrall, H., Richards, A. M. S., & Garrington, S. T. 2008, MNRAS, 385, 1143

Binggeli, B. 1982a, A&A, 53, 41

—. 1982b, A&A, 107, 338

Binney, J., & Tremaine, S. 1994, Galactic Dynamics (Princeton University Press)

Biviano, A., Fadda, D., Durret, F., Edwards, L. O. V., & Marleau, F. 2011, A&A, 532, A77

Biviano, A., Murante, G., Borgani, S., et al. 2006, A&A, 456, 23

Blanton, M., Hogg, D., Bahcall, N., & Al., E. 2003, ApJ, 592, 819

Blanton, M., & Roweis, S. 2007, AJ, 133, 734

Blindert, K. 2006, PhD thesis, University of Toronto

Bode, P., & Ostriker, J. 2003, ApJS, 145, 1

Böhringer, H., Schuecker, P., Guzzo, L., et al. 2004, A&A, 425, 367

Bolzonella, M., Miralles, J., & Pello, R. 2000, A&A, 363, 476

Bolzonella, M., Pozzetti, L., Zucca, E., et al. 2010, A&A, 524, A76

Bond, J., Kofman, L., & Poposyan, D. 1996, Nature, 380, 603

Bondi, M., Ciliegi, P., Venturi, T., et al. 2007, A&A, 527, 519

Book, L. G., & Benson, A. J. 2010, ApJ, 716, 810

Bosch, F. V. D., Tormen, G., & Gioco. 2005, MNRAS, 359, 1029

Bourne, N., Dunne, L., Ivison, R. J., et al. 2011, MNRAS, 410, 1155

Bower, R. G., Lucey, J., & Ellis, R. 1992, MNRAS, 254, 601

Boyle, B. J., Cornwell, T. J., Middelberg, E., et al. 2007, MNRAS, 376, 1182

Brammer, G. B., van Dokkum, P. G., & Coppi, P. 2008, ApJ, 686, 1503

Brodwin, M., Ruel, J., Ade, P. A. R., et al. 2010, ApJ, 721, 90

Bruzual, A. 1983, ApJ, 273, 105

Bruzual, G., & Charlot, S. 2003, MNRAS, 344, 1000

Butcher, H., & Oemler, A. 1978, ApJ, 219, 18

—. 1984, ApJ, 285, 426

Calzetti, D., Kennicutt, R., Engelbracht, C., et al. 2007, ApJ, 666, 870

Caputi, K. I., Kovač, K., Bolzonella, M., et al. 2009a, ApJ, 691, 91

Caputi, K. I., Lilly, S. J., Aussel, H., et al. 2009b, ApJ, 707, 1387

Carilli, C. L., Solomon, P., Vanden Bout, P., et al. 2005, ApJ, 618, 586

Carlberg, R., Yee, H., Ellingson, E., et al. 1996, ApJ, 462, 32

—. 1997, ApJL, 485, L13

Cen, R., Miralda-Escude, J., Ostriker, J., & Rauch, M. 1994, ApJ, 437, L9

Chary, R., & Elbaz, D. 2001, ApJ, 556, 562

Cohn, J. D. 2012, MNRAS, 419, 1017

Coia, D., Mcbreen, B., Metcalfe, L., et al. 2005, A&A, 431, 433

Colless, M., Dalton, P. G., Maddox, S., et al. 2001, MNRAS, 328, 1039

Condon, J. 1992, ARA&A, 30, 575

Condon, J. J., Cotton, W. D., & Broderick, J. J. 2002, ApJ, 124, 675

Cooper, M. C., Newman, J. A., Weiner, B. J., et al. 2008, MNRAS, 383, 1058

Coppin, K. E. K., Geach, J. E., Webb, T. M. A., et al. 2012, ApJ, 749, L43

Costa-Duarte, M. V., Sodré Jr, L., & Durret, F. 2011, MNRAS, 411, 1716

Cowie, L., Songaila, A., Hu, E., & Cohen, J. 1996, ApJ, 112, 839

Croton, D. J., Springel, V., White, S. D. M., et al. 2006, MNRAS, 365, 11

Cuillandre, J.-C., Luppino, G., Starr, B., & Isani, S. 2000, SPIE, 4008, 1010

Daddi, E., Dickinson, M., Morrison, G., et al. 2007a, ApJ, 670, 156

Daddi, E., Alexander, D. M., Dickinson, M., et al. 2007b, ApJ, 670, 173

Dale, D. A., & Helou, G. 2002, ApJ, 576, 159

Danese, L., De Zotti, G., & Di Tullio, G. 1980, A&A, 82, 322

Davis, M., Efstathiou, G., Frenk, C., & White, S. 1985, ApJ, 292, 371

Davis, M., Faber, S. M., Newman, J., et al. 2003, SPIE, 4834, 161

De Lucia, G., Kauffmann, G., Springel, V., et al. 2004a, MNRAS, 348, 333

De Lucia, G., Weinmann, S., Poggianti, B. M., Aragón-Salamanca, A., & Zaritsky, D. 2012, MNRAS, 1292, 1277

De Lucia, G., Poggianti, B., Aragon-Salamanca, A., et al. 2004b, ApJL, 610, L77

de Vaucouleurs, G. 1971, ApJS, 5, 233

Désert, F., Boulanger, F., & Puget, J. 1990, A&A, 237, 215

Donley, J., Rieke, G. H., Perez-Gonzalez, P. G., & Barro, G. 2008, ApJ, 687, 111

Donley, J. L., Koekemoer, A. M., Brusa, M., et al. 2012, ApJ, 748, 142

Donoso, E., Yan, L., Tsai, C., et al. 2012, ApJ, 748, 80

Drake, A. B., Simpson, C., Collins, C. a., et al. 2013, MNRAS, 433, 796

Dressler, A. 1980, ApJ, 236, 351

Dressler, A., & Shectman, S. A. 1988, AJ, 95, 985

Dressler, A., Oemler Jr, A., Couch, W., et al. 1997, ApJ, 490, 577

Dressler, A., Bigelow, B., Hare, T., et al. 2011, PASP, 123, 288

Eastman, J., Martini, P., Sivakoff, G., et al. 2007, ApJ, 664, L9

Egami, E., Rex, M., Rawle, T. D., et al. 2010, A&A, 518, L12

Einasto, J., Einasto, M., Tago, E., et al. 2007a, A&A, 462, 811

Einasto, J., Hütsi, G., Einasto, M., & Al., E. 2003, A&A, 405, 425

Einasto, M., Liivamagi, L., Tago, E., et al. 2011a, A&A, 5, 532

Einasto, M., Liivamägi, L. J., Saar, E., et al. 2011b, A&A, 535, A36

Einasto, M., Einasto, J., Tago, E., et al. 2007b, A&A, 464, 815

Einasto, M., Vennik, J., Nurmi, P., et al. 2012, A&A, 540, A123

Elbaz, D., Daddi, E., Borgne, D. L., et al. 2007, A&A, 468, 33

Elbaz, D., Hwang, H. S., Magnelli, B., et al. 2010, A&A, 518, L29

Ellingson, E., Lin, H., Yee, H., & Carlberg, R. 2001, ApJ, 547, 609

Engelbracht, C. W., Gordon, K. D., Rieke, G. H., et al. 2005, ApJ, 628, 29

Evrard, A. E., Bialek, J., Busha, M., et al. 2008, ApJ, 672, 122

Fadda, D., Biviano, A., Marleau, F. R., Storrie-lombardi, L. J., & Durret, F. 2008, ApJ, 672, L9

Fadda, D., Yan, L., Lagache, G., et al. 2010, ApJ, 719, 425

Faloon, A. J. 2008, Msc thesis, McGill University

Faloon, A. J., Webb, T. M. A., Ellingson, E., et al. 2013, ApJ, 768, 104

Farrah, D., Lonsdale, C. J., Weedman, D. W., et al. 2008, ApJ, 677, 957

Farrens, S., Abdalla, F. B., Cypriano, E. S., Sabiu, C., & Blake, C. 2011, MNRAS, 417, 1402

Fazio, G. G., Hora, J. L., Allen, L. E., et al. 2004, APJS, 154, 10

Fernandez-Soto, A., Lanzetta, K., Chen, H.-W., Pascarelle, M., & Yahata, N. 2001, ApJS, 135, 41

Feruglio, C., Aussel, H., Le Floc'h, E., et al. 2010, ApJ, 721, 607

Finn, R. A., Desai, V., Rudnick, G., et al. 2010, ApJ, 720, 87

Fomalont, E. B., Kellermann, K. I., Cowie, L. L., et al. 2006, ApJS, 167, 103

Font, a. S., Bower, R. G., McCarthy, I. G., et al. 2008, MNRAS, 389, 1619

Frayer, D., Koda, J., Pope, A., et al. 2008, ApJ, 680, L21

Fu, H., Yan, L., Scoville, N. Z., et al. 2010, ApJ, 722, 653

Gal, R. R., Lemaux, B. C., Lubin, L. M., et al. 2008, ApJ, 684, 933

Gal, R. R., & Lubin, L. M. 2004, ApJL, 607, L1

Gallazzi, A., Bell, E. F., Wolf, C., et al. 2009, ApJ, 690, 1883

Gao, L., Frenk, C. S., Boylan-Kolchin, M., et al. 2011, MNRAS, 410, 2309

Gao, L., White, S. D. M., Jenkins, A., Stoehr, F., & Springel, V. 2004, MNRAS, 355, 819

Geach, J. E., Ellis, R. S., Smail, I., Rawle, T. D., & Moran, S. M. 2011, MNRAS, 413, 177

Geach, J. E., & Papadopoulos, P. P. 2012, ApJ, 757, 156

Geach, J. E., Smail, I., Ellis, R. S., et al. 2006, ApJ, 649, 661

Geach, J. E., Hickox, R. C., Diamond-Stanic, A. M., et al. 2013, ApJ, 767, L17

Genel, S., Bouché, N., Naab, T., Sternberg, A., & Genzel, R. 2010, ApJ, 719, 229

Gilbank, D., Yee, H., Ellingson, E., et al. 2008a, ApJL, 677, L89

Gilbank, D. G., Yee, H. K. C., Ellingson, E., et al. 2007, AJ, 134, 282

—. 2008b, ApJ, 673, 742

Giocoli, C., Tormen, G., Sheth, R. K., & Bosch, F. C. V. D. 2010, MNRAS, 404, 502

Girardi, M., & Biviano, A. 2004, in Merging Processes in Galaxy Clusters, ed. L. Feretti, I. Gioia, & G. Giovannini (Dordrecht: Kluwer), 39–77

Gisler, G. R. 1978, MNRAS, 183, 633

Gladders, M., Hoekstra, H., Yee, H., Hall, P., & Barrientos, L. 2003, ApJ, 593, 48

Gladders, M., & Yee, H. 2000, AJ, 120, 2148

—. 2005, ApJS, 157, 1

Goto, T. 2005, MNRAS, 356, L6

Goto, T., Okamura, S., Mckay, T. A., et al. 2002, PASJ, 54, 515

Goto, T., Postman, M., Cross, N. J. G., et al. 2005, ApJ, 621, 188

Gralla, M. B., Sharon, K., Gladders, M. D., et al. 2011, ApJ, 737, 74

Gray, M. E., Wolf, C., Barden, M., et al. 2009, MNRAS, 393, 1275

Greene, C. R., Gilbank, D. G., Balogh, M. L., et al. 2012, MNRAS, 425, 1738

Gregory, S., & Thompson, L. 1978, ApJ, 222, 784

Gregory, S., Thompson, L., & Tifft, W. 1981, ApJ, 243, 411

Gunn, J., & Gott, J. G. 1972, ApJ, 176, 1

Haines, C. P., Merluzzi, P., Mercurio, A., et al. 2006, MNRAS, 371, 55

Haines, C. P., Pereira, M. J., Sanderson, A. J. R., et al. 2012, ApJ, 754, 97

Hansen, S. M., McKay, T. A., Wechsler, R. H., et al. 2005, ApJ, 633, 122

Hansen, S. M., Sheldon, E. S., Wechsler, R. H., & Koester, B. P. 2009, ApJ, 699, 1333

Hicks, A., Ellingson, E., Bautz, M., et al. 2008, ApJ, 680, 1022

Hilton, M., Stanford, S. A., Stott, J. P., et al. 2009, ApJ, 697, 436

Hogg, D., Baldry, I., Blanton, M., & Eisenstein, D. 2002, Arxiv preprint astro-ph/0210394, 1

Hogg, D. W. 1999, Arxiv preprint arXiv: astro-ph/9905116, 1, 1

Hogg, D. W., Blanton, M. R., Brinchmann, J., et al. 2004, ApJ, 6-1, L29

Homeier, N. L., Mei, S., Blakeslee, J. P., et al. 2006, ApJ, 647, 256

Hook, I., Jø rgensen, I., Allington-Smith, J., et al. 2004, PASP, 116, 425

Hou, A., Parker, L. C., Harris, W. E., & Wilman, D. J. 2009, ApJ, 702, 1199

Hou, A., Parker, L. C., Wilman, D. J., et al. 2012, MNRAS, 421, 3594

Hsieh, B., Yee, H., Lin, H., & Gladders, M. 2005, ApJS, 158, 161

Huchra, J., & Geller, M. 1982, ApJ, 257, 423

Huynh, M. T., Gawiser, E., Marchesini, D., Brammer, G., & Guaita, L. 2010a, ApJ, 723, 1110

Huynh, M. T., Norris, R. P., Siana, B., & Middelberg, E. 2010b, ApJ, 710, 698

Ibar, E., Cirasuolo, M., Ivison, R., et al. 2008, MNRAS, 386, 953

Iwamuro, F., Moritani, Y., Yabe, K., et al. 2012, PASJ, 64, 59

Jee, M. J., Dawson, K. S., Hoekstra, H., et al. 2011, ApJ, 737, 59

Joeveer, M., & Einasto, J. 1978, MNRAS, 357

Johnson, O., Best, P., & Almaini, O. 2003, MNRAS, 343, 924

Johnston, D., Sheldon, E. S., Wechsler, R. H., et al. 2007, Arxiv preprint arXiv: 0709.1159v1

Jones, C., Forman, W., Vikhlinin, A., et al. 2008, in Lecture Notes in Physics: A Pan-Chromatic View of Clusters of Galaxies and the Large-Scale Structure, Vol. 740, 31–69

Juneau, S., Dickinson, M., Alexander, D., & Salim, S. 2011, ApJ, 736, 104

Kauffmann, G., & Charlot, S. 1998, MNRAS, 297, L23

Kauffmann, G., Colberg, J. M., Diaferio, A., & White, S. D. M. 1999, MNRAS, 307, 529

Kauffmann, G., Heckman, T. M., White, S. D. M., et al. 2003a, MNRAS, 341, 54

Kauffmann, G., White, S. D. M., Heckman, T. M., et al. 2004, MNRAS, 353, 713

Kauffmann, G., Heckman, T., White, S., et al. 2003b, MNRAS, 341, 33

Kennicutt, R. C. 1998, ARA&A, 36, 189

Kennicutt Jr, R. 1998, ApJ, 498, 541

Kimura, M., Maihara, T., Iwamuro, F., et al. 2010, PASJ, 62, 1135

Kinney, A. A., Calzetti, D., Bohlin, R., et al. 1996, ApJ, 467, 38

Kocevski, D. D., Lemaux, B. B. C., Lubin, L. L. M., et al. 2011, ApJ, 736, 38

Kodama, T., & Bower, R. 2003, MNRAS, 346, 1

Kolokotronis, V., Basilakos, S., & Plionis, M. 2002, MNRAS, 331, 1020

Koyama, Y., Kodama, T., Shimasaku, K., et al. 2010, MNRAS, 403, 1611

—. 2008, MNRAS, 391, 1758

Krick, J. E., Surace, J. A., Thompson, D., et al. 2009, ApJ, 700, 123

Lacey, C. G., & Cole, S. 1993, MNRAS, 262, 627

Lacki, B. C., & Thompson, T. A. 2010, ApJ, 717, 196

Lacy, M., Petric, A. O., Sajina, A., et al. 2007, ApJ, 133, 186

Lacy, M., Storrie-Lombardi, L., Sajina, A., et al. 2004, ApJS, 154, 166

Larson, D., Dunkley, J., Hinshaw, G., et al. 2011, ApJS, 192, 16

Larson, R., & Tinsley, B. 1978, ApJ, 219, 46

Larson, R., Tinsley, B., & Caldwell, C. 1980, ApJ, 237, 692

Le Fevre, O., Saisse, M., Mancini, D., et al. 2003, SPIE, 4841, 1670

Le Floc'h, E., Papovich, C., Dole, H., Bell, E. F., & Lagache, G. 2005, ApJ, 632, 169

Lee, J., & Evrard, A. 2007, ApJ, 657, 30

Lemaux, B. C., Gal, R. R., Lubin, L. M., et al. 2012, ApJ, 745, 106

Lemson, G., & the Virgo Consortium. 2006, Arxiv preprint arXiv: astro-ph/0608019v2

Lemze, D., Postman, M., Genel, S., et al. 2013, Arxiv preprint arXiv :1308.1675v1

Lerchster, M., Seitz, S., Brimioulle, F., et al. 2011, MNRAS, 411, 2667

Liang, Y. C., Hammer, F., Flores, H., et al. 2004, A&A, 423, 867

Lidman, C., Iacobuta, G., Bauer, A. E., et al. 2013, MNRAS

Liivamägi, L. J., Tempel, E., & Saar, E. 2012, A&A, 539, A80

Lilly, S. J., Le Fevre, O., Hammer, F., & Crampton, D. 1996, ApJ, L1

Lin, Y.-T., Mohr, J., & Stanford, S. 2004, ApJ, 610, 745

Lin, Y.-T., Mohr, J. J., Gonzalez, A. H., & Stanford, S. A. 2006, ApJL, 650, L99

Liu, H. B., Hsieh, B. C., Ho, P. T. P., Lin, L., & Yan, R. 2008, ApJ, 681, 1046

Loh, Y., Ellingson, E., Yee, H. K. C., et al. 2008, ApJ, 680, 214

Lokas, E. L., Wojtak, R., Gottlober, S., Mamon, G. A., & Prada, F. 2006, MNRAS, 367, 1463

Lopez-Cruz, O., Barkhouse, W. A., & Yee, H. K. C. 2004, ApJ, 614, 679

Lotz, J. M., Davis, M., Faber, S. M., et al. 2008, ApJ, 672, 177

Lu, T., Gilbank, D. G., Balogh, M. L., & Bognat, A. 2009, MNRAS, 399, 1858

Lu, T., Gilbank, D. G., McGee, S. L., Balogh, M. L., & Gallagher, S. 2012, MNRAS, 420, 126

Lu, T., Gilbank, D. G., Balogh, M. L., et al. 2010, MNRAS, 403, 1787

Lubin, L., Postman, M., Oke, J., et al. 1998, ApJ, 116, 584

Lubin, L. M. L., Brunner, R., Metzger, M. M. R., Postman, M., & Oke, J. 2000, ApJL, 531, L5

Madau, P., Ferguson, H. C., Dickinson, M. E., et al. 1996, MNRAS, 283, 1388

Madden, S. C., Galliano, F., Jones, A. P., & Sauvage, M. 2006, A&A, 446, 877

Magdis, G. E., Daddi, E., Béthermin, M., et al. 2012, ApJ, 760, 6

Mahajan, S., Raychaudhury, S., & Pimbblet, K. a. 2012, MNRAS, 427, 1252

Maier, C., Lilly, S. J., Zamorani, G., et al. 2009, ApJ, 694, 1099

Mancone, C., Gonzalez, A., Brodwin, M., et al. 2010, ApJ, 720, 284

Mao, M. Y., Huynh, M. T., Norris, R. P., et al. 2011, ApJ, 731, 79

Marcillac, D., Rigby, J. R., Rieke, G. H., & Kelly, D. M. 2007, ApJ, 654, 825

Markwardt, C. B. 2009, in ASP Conf. Ser. 411, Astronomical Data Analysis Software and Systems XVIII, ed. D. A. Bohlender, D. Durand, & P. Dowler, Vol. 411, San Francisco, CA, 251–254

Martini, P., Sivakoff, G. R., & Mulchaey, J. S. 2009, ApJ, 701, 66

McGee, S. L., Balogh, M. L., Bower, R. G., Font, A. S., & McCarthy, I. G. 2009, MNRAS, 400, 937

Mehrtens, N., Romer, A. K., Hilton, M., et al. 2012, MNRAS, 423, 1024

Mei, S., Holden, B. P., Blakeslee, J. P., et al. 2009, ApJ, 690, 42

Michaowski, M. J., Dunlop, J. S., Cirasuolo, M., et al. 2012, A&A, 541, A85

Middelberg, E., Norris, R. P., Cornwell, T. J., et al. 2008, ApJ, 135, 1276

Mo, H. J., & White, S. 1996, MNRAS, 282

Moore, B., Governato, F., Quinn, T., Stadel, J., & Lake, G. 1998a, ApJL, 499, L5

Moore, B., Katz, N., Lake, G., Dressler, A., & Oemler, Jr, A. 1996, Nature, 379, 613

Moore, B., Lake, G., & Katz, N. 1998b, ApJ, 495, 139

Moore, B., Lake, G., Quinn, T., & Stadel, J. 1999, MNRAS, 304, 465

Moster, B. P., Somerville, R. S., Maulbetsch, C., et al. 2010, ApJ, 710, 903

Murphy, E. J. 2009, ApJ, 706, 482

Muzzin, A., Wilson, G., Lacy, M., Yee, H. K. C., & Stanford, S. A. 2008, ApJ, 686, 966

Muzzin, A., Wilson, G., Yee, H. K. C., et al. 2012, ApJ, 746, 188

Nakata, F., Kodama, T., Shimasaku, K., et al. 2005, MNRAS, 357, 1357

Nardini, E., Risaliti, G., Watabe, Y., Salvati, M., & Sani, E. 2010, MNRAS, 405, 2505

Navarro, J., Frenk, C., & White, S. 1995, MNRAS, 275, 56

—. 1996, ApJ, 462, 563

Navarro, J., & White, S. 1996, ApJ, 462, 563

Nelan, J. E., Smith, R. J., Hudson, M. J., et al. 2005, ApJ, 632, 137

Nichol, R. C., Miller, C. J., Balogh, M. L., et al. 2003, ApJ, 584, 210

Noble, A. G., Webb, T., Muzzin, A., et al. 2013, ApJ, 768, 118

Noble, A. G., Webb, T. M. A., Ellingson, E., et al. 2012, MNRAS, 419, 1983

Noeske, K., Weiner, B., Faber, S., Papovich, C., & Koo, D. 2007, ApJ, 660, L43

Noh, Y., & Cohn, J. 2011, MNRAS, 000

Norris, R., Afonso, J., Appleton, P., et al. 2006, ApJ, 132, 2409

Norris, R. P., Tingay, S., Phillips, C., et al. 2007, MNRAS, 378, 1434

Norris, R. P., Afonso, J., Cava, A., et al. 2011, ApJ, 736, 55

Oort, J. 1983, ARA&A, 21, 373

Osterbrock, D. E. 1960, ApJ, 132, 325

Papadopoulos, P. P., van der Werf, P. P., Xilouris, E. M., et al. 2012, MNRAS, 426, 2601

Papovich, C., Rudnick, G., Le, E., et al. 2007, ApJ, 668, 45

Papovich, C., Momcheva, I., Willmer, C. N. A., et al. 2010, ApJ, 716, 1503

Patel, S. G., Holden, B. P., Kelson, D. D., Illingworth, G. D., & Franx, M. 2009, ApJ, 705, L67

Patel, S. G., Kelson, D. D., Holden, B. P., Franx, M., & Illingworth, G. D. 2011, ApJ, 735, 53

Peebles, P. J. E. 1980, The large-scale structure of the universe (Princeton University Press)

Peng, Y.-j., Lilly, S. J., Renzini, A., & Carollo, M. 2012, ApJ, 757, 4

Peng, Y.-j., Lilly, S. J., Kovač, K., et al. 2010, ApJ, 721, 193

Pimbblet, K. A., & Jensen, P. C. 2012, MNRAS, 426, 1632

Pinkney, J., Roettiger, K., Burns, J. O., & Bird, C. M. 1996, ApJS, 104, 1

Poggianti, B. M., Desai, V., Finn, R., et al. 2008, ApJ, 684, 888

Polletta, M., Weedman, D., & Hönig, S. 2008, ApJ, 675, 960

Popescu, C., Tuffs, R., Volk, H., Pierini, D., & Madore, B. 2002, ApJ, 567, 221

Popesso, P., Rodighiero, G., Saintonge, A., et al. 2011, A&A, 532, A145

Postman, M., Lubin, L., & Oke, J. 1998, AJ, 116, 560

—. 2001, AJ, 122, 1125

Propris, R. D., Colless, M., Driver, S., Al, E., & De Propris, R. 2003, MNRAS, 342, 725

Puget, P., Stadler, E., Doyon, R., et al. 2004, SPIE, 5492, 978

Rasia, E., Ettori, S., Moscardini, L., et al. 2006, MNRAS, 369, 2013

Rasia, E., Meneghetti, M., Martino, R., et al. 2012, NJPh, 14, 055018

Richards, E. A., Formalont, E. B., Kellermann, K. I., et al. 1999, ApJ, 526, 73

Rieke, G. H., Alonso-Herrero, A., Weiner, B. J., et al. 2009, ApJ, 692, 556

Rieke, G. H., Young, E. T., Engelbracht, C. W., et al. 2004, ApJ, 154, 25

Rodighiero, G., Vaccari, M., Franceschini, A., et al. 2010a, A&A, 515, A8

Rodighiero, G., Cimatti, A., Gruppioni, C., et al. 2010b, A&A, 518, L25

Rosati, P., Stanford, S., Eisenhardt, P. R., et al. 1999, AJ, 118, 76

Rudnick, G. H., Tran, K.-V., Papovich, C., Momcheva, I., & Willmer, C. 2012, ApJ, 755, 14

Ryden, B. 2003, Introduction to cosmology (Addison Wesley: San Francisco, CA, USA)

Saintonge, A., Tran, K.-v. H., & Holden, B. P. 2008, ApJ, 685, L113

Salim, S., & Lee, J. C. 2012, ApJ, 758, 134

Salim, S., Dickinson, M., Michael Rich, R., et al. 2009, ApJ, 700, 161

Salmi, F., Daddi, E., Elbaz, D., et al. 2012, ApJ, 754, L14

Sanchis, T., Lokas, E. L., & Mamon, G. A. 2004, MNRAS, 347, 1198

Sanders, D. B., & Mirabel, I. F. 1996, ARA&A, 34, 749

Sarazin, C. L. 1988, X-ray emission from clusters of galaxies (Cambridge University Press, Cambridge, England)

Sarazin, C. L. 2002, in Merging Processes in Galaxy Clusters, ed. L. Feretti, I. M. Gioia, & G. Giovannini (Netherlands: Springer), 1–38

Schechter, P. 1976, ApJ, 203, 297

Schirmer, M., Hildebrandt, H., Kuijken, K., & Erben, T. 2011, A&A, 532, A57

Schuster, M. T., Marengo, M., & Patten, B. M. 2006, SPIE, 6270, 65

Scodeggio, M., Vergani, D., Cucciati, O., et al. 2009, A&A, 501, 21

Scoville, N., Aussel, H., Benson, A., et al. 2007, ApJS, 172, 150

Seljak, U. 2000, MNRAS, 318, 203

Sheth, R. K., & Tormen, G. 2002, MNRAS, 329, 61

Shim, H., Im, M., Lee, H. M., et al. 2011, ApJ, 727, 14

Sifon, C., Menanteau, F., Hasselfield, M., et al. 2012, arXiv:1201.0991v1, 15

Skrutskie, M. F., Cutri, R. M., Stiening, R., et al. 2006, AJ, 131, 1163

Small, T., Ma, C., Sargent, W., & Hamilton, D. 1998, ApJ, 492, 45

Smith, G. P., Haines, C. P., Pereira, M. J., et al. 2010, A&A, 518, L18

Smoot, G., Bennett, C., Kogut, A., et al. 1992, ApJ, 396, L1

Snyder, G. F., Brodwin, M., Mancone, C. M., et al. 2012, ApJ, 756, 114

Sobral, D., Best, P. N., Smail, I., et al. 2011, MNRAS, 411, 675

Solomon, P., & Vanden Bout, P. 2005, ARA&A, 43, 677

Spergel, D., Verde, L., Peiris, H., et al. 2003, ApJS, 148, 175

Springel, V., Frenk, C., & White, S. 2006, Nature, 440, 1137

Stern, D., Eisenhardt, P., Gorjian, V., et al. 2005, ApJ, 631, 163

Stetson, P. B. 1987, PASP, 99

Swinbank, a. M., Edge, a. C., Smail, I., et al. 2007, MNRAS, 379, 1343

Takey, A., Schwope, A., & Lamer, G. 2011, A&A, 534, A120

Tanaka, M., Finoguenov, A., Kodama, T., et al. 2009, A&A, 505, L9

Tanaka, M., Kodama, T., Arimoto, N., et al. 2005, MNRAS, 362, 268

—. 2006, MNRAS, 1552, 1551

Tomczak, A. R., Tran, K.-V. H., & Saintonge, A. 2011, ApJ, 738, 65

Tran, K.-V. H., Saintonge, A., Moustakas, J., et al. 2009, ApJ, 705, 809

Tran, K.-V. H., Papovich, C., Saintonge, A., et al. 2010, ApJ, 719, L126

U, V., Sanders, D. B., Mazzarella, J. M., et al. 2012, ApJS, 203, 9

van Dokkum, P. G., Franx, M., Kelson, D. D., et al. 1998, ApJ, 714

Veilleux, S., Kim, D., & Sanders, D. 2002, ApJ, 143, 315

Verdugo, M., Lerchster, M., Böhringer, H., et al. 2012, MNRAS, 421, 1949

Vijayaraghavan, R., & Ricker, P. M. 2013, Arxiv preprint arXiv:1308.1311v1, 000

Visvanathan, N., & Sandage, A. 1977, ApJ, 216, 214

Vulcani, B., Poggianti, B. M., Finn, R. A., et al. 2010, ApJ, 710, L1

Vulcani, B., Poggianti, B. M., Fasano, G., et al. 2012, MNRAS, 420, 1481

Vulcani, B., Poggianti, B. M., Oemler, A., et al. 2013, A&A, 550, A58

Walcher, J., Groves, B., Budavári, T., & Dale, D. 2010, Ap&SS, 331, 1

Wang, L., Farrah, D., Oliver, S. J., et al. 2013, MNRAS, 431, 648

Watabe, Y., Risaliti, G., Salvati, M., et al. 2009, MNRAS, 396, L1

Webb, T. M. A., O'Donnell, D., Yee, H. K. C., et al. 2013, AJ, 146, 84

Wetzel, A. R., Tinker, J. L., & Conroy, C. 2012, MNRAS, May, 1

White, M., Cohn, J. D., & Smit, R. 2010, MNRAS, 408, 1818

White, S., & Rees, M. 1978, MNRAS, 183, 341

White, S. D. M., & Frenk, C. S. 1991, ApJ, 379, 52

Wolf, C., Aragón-Salamanca, A., Balogh, M., et al. 2009, MNRAS, 393, 1302

Wray, J. J., Bahcall, N. A., Bode, P., Boettiger, C., & Hopkins, P. F. 2006, ApJ, 652, 907

Xue, Y.-J., & Wu, X.-P. 2000, ApJ, 538, 65

Yan, L., Tacconi, L. J., Fiolet, N., et al. 2010, ApJ, 714, 100

Yang, X., Mo, H. J., & van den Bosch, F. C. 2009, ApJ, 695, 900

Yee, H. 1991, PASP, 103, 396

Yee, H., & Ellingson, E. 2003, ApJ, 585, 215

Yee, H., Ellingson, E., Abraham, R., et al. 1996a, ApJS, 102, 289

Yee, H., Ellingson, E., & Carlberg, R. 1996b, ApJ, 102, 269

Yee, H., Morris, S., Lin, H., et al. 2000, ApJS, 129, 475

York, D., Adelman, J., Anderson Jr., J., et al. 2000, AJ, 120, 1579

Yun, M. S., Aretxaga, I., Ashby, M. L. N., et al. 2008, MNRAS, 389, 333

Zandivarez, A., Martinez, H., & Mercha, M. E. 2006, ApJ, 650, 137

Zenteno, A., Song, J., Desai, S., et al. 2011, ApJ, 734, 3